Lawrence Berkeley Laboratory
UNIVERSITY OF CALIFORNIA

CHEMICAL BIODYNAMICS DIVISION

Electron Spin Echo Spectroscopy of Photosynthesis

R.D. Britt
(Ph.D. Thesis)

March 1988

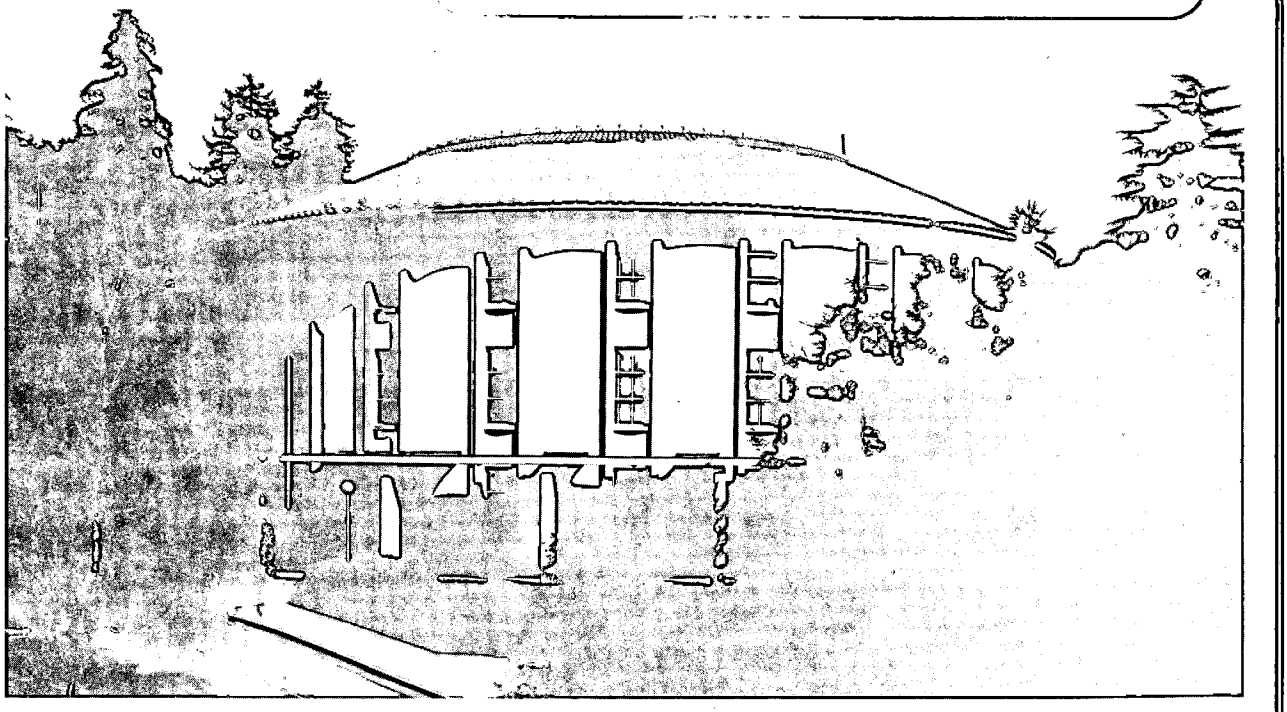

Prepared for the U.S. Department of Energy under Contract DE-AC03-76SF00098

DISCLAIMER

LBL-25042

Electron Spin Echo Spectroscopy of Photosynthesis

R.D. Britt
(Ph.D. Thesis)

Lawrence Berkeley Laboratory
University of California
Berkeley, CA 94720

March 1988

Electron Spin Echo Spectroscopy of Photosynthesis

Ralph David Britt

Abstract

The initial light-driven electron transfer event in plant photosynthesis creates an electron-deficient pigment molecule with sufficient oxidative potential to strip electrons from water. The process of photosynthetic water oxidation releases molecular oxygen as a byproduct. The water oxidation process is cyclic, with intermediate states designated S_0 through S_4. Each photo-oxidation of the primary pigment induces a transition in the cycle. Molecular oxygen is released after four photo-oxidation events, and the complex resets to the least oxidized state, S_0. The water oxidation chemistry is performed by a membrane-bound protein complex containing the transition metal Manganese. The structure of the Mn complex has been partially characterized by X-ray spectroscopy and electron paramagnetic resonance (EPR).

We have constructed a high-power pulsed EPR spectrometer to perform Electron Spin Echo (ESE) experiments on the Mn complex. Details of the design and construction of this instrument are presented. In particular, we are interested in measuring the magnetic dipolar and electric quadrupolar parameters of paramagnetic nuclei magnetically coupled to the Mn complex. High power microwave pulses induce quantum mechanical coherences in the nuclear spin sublevels. Interference effects due to these sublevel coherences can be measured by monitoring the amplitude of the ESE signal as a function of the interval between the applied microwave pulses. Fourier analysis of the resulting Electron Spin Echo Envelope Modulation (ESEEM) reveals the nuclear sublevel splittings. ESEEM effects for spin I=1/2 and I=1 nuclei are discussed in detail.

The ESEEM technique has provided details of the chemical environment of ^{1}H, ^{2}H, and ^{14}N nuclei in the vicinity of the photosynthetic Mn cluster. The specific ^{14}N sublevel frequencies observed indicate Mn coordination to an imidizole group from a histidine residue. We discuss possible roles for coordinated imidizole in the functioning of the water oxidation complex. Additional ^{14}N modulation is observed when oxygen evolution is inhibited by ammonia. The increase in ^{14}N modulation may result from directly coordinated ammonia. ESEEM studies following incubation in $^{2}H_2O$ buffers indicate water coordination to Mn in the S_2 state. However, water

does not bind to Mn during the $S_1 \rightarrow S_2$ transition. The coordinated water may be present in the least-oxidized state, S_0, or water may bind during the $S_0 \rightarrow S_1$ transition.

We also present ESEEM data on di-μ-oxo bridged Mn(III)Mn(IV) dimers with 2,2,-bipyridine or 1,10-phenanthroline terminal ligands. The ^{14}N ESEEM frequencies observed for these Mn mixed valence complexes are analyzed in detail.

To my parents for years of love and support

and to my dear wife Anne for all her affection

Acknowledgements

It has been a great pleasure to work under the direction of Dr. Melvin P. Klein. Mel is not only an excellent scientist, but also one of the finest gentlemen I have known. Mel's excellent insights have contributed to every stage of this work. I thank Mel for providing a stimulating environment where I have been able to actively explore my ideas and interests.

I also thank Prof. Kenneth Sauer for his support in these research efforts. Ken has greatly aided these research efforts with his vast knowledge of photosynthesis and chemistry. His contributions have been enormous. I also thank Prof. Carson Jeffries for sponsoring my work through the physics department and for his help in reviewing my work.

The faculty at N. C. State gave me an excellent start in physics. In particular, I thank Profs. Edward R. Manring and Jan F. Schetzina. At Berkeley, Prof. Paul Richards and Steve McBride helped me make the transition from physics student to experimental physicist.

Mel and Ken always have many excellent students, postdocs, and visitors in their laboratories, and these people have been good colleagues and companions. David Gooden introduced me to the many new concepts of biophysical chemistry. I also thank David for teaching me X-ray spectroscopic techniques, and for being a good friend.

John McCracken was also a student when I came to the Calvin lab. I thank John for his insights into magnetic resonance spectroscopy and for a multitude of amusing anecdotes during the time that we were both in the Calvin Lab. I also thank John for hours of useful long distance telephone conversations about electron spin echo techniques, and for letting me dismantle his superheterodyne spectrometer the afternoon he left Berkeley.

I have also benefited greatly from my association with Vittal Yachandra. Vittal's immense knowledge of biophysical chemistry and wonderful teaching ability have influenced me greatly. I also appreciate Vittal's insight into a manifold of subjects outside our sometimes narrow focus of science.

I also owe many thanks to Ann McDermott. Ann was always willing to spend a few moments answering my naive questions. I also thank her for innumerable cappuccino adventures. Ann's presence in the laboratory has made a big difference,

both in terms of scientific productivity and general spirit.

I thank Ron Guiles for his insights into photosynthesis and inorganic chemistry, as well as for meaningful discussions of Star Trek. Jim Cole also helped me in many ways, particularly with his excellent knowledge of the photosynthesis literature. I also note that Jim's uncanny ability to portray Zombies in action. I thank Sue Dexheimer for many useful physics discussions, as well as for introducing me to Anne. Vickie DeRose, Trish Maxson, and Ishita Mukerji have all been good friends and colleagues.

It has also been a pleasure working with Jean-Luc Zimmermann in the last year. I only regret that I may never live in Paris. Peter "Plate-O'-Shrimp" Sandusky has been a good friend. I thank him for many fine discussions, ranging from details of photosynthesis to the seizure of Fort Sumter. I have also had the pleasure to work with Greg Karczmar, Alan Koretsky, Tom Pratum, Sun Un, and Sarah Tabbutt.

Gary Smith has been a good friend and advisor for all matters electronic. I thank Gary not only for his many useful suggestions on computers and computer interfacing, but also for his fine tales about fast cars, motorcycles, and F-86's. When I become a father I will always keep Gary in mind. Phil Eggers and Mike Press have also been great help in keeping everything on track.

I also thank David Perlman for years of friendship, and particularly for the "Lady Di" speech. Steve McBride and Madeleine Leullier have been good friends. I thank them for their companionship over the years.

Most of all I thank my parents for being patient with their hyperactive child and Anne for loving him as an adult.

This work was supported by the Director, Office of Energy Research, Office of Basic Energy Sciences, Division of Energy Conversion and Conservation of the Department of Energy, under contract DE-AC03-76SF00098, and by a grant from the United States Department of Agriculture (85-CRCR-1-1847).

Abbreviations

ADP	adenosine diphosphate
ATP	adenosine triphosphate
Bchl	bacteriochlorophyll
Bipy	2,2'-bipyridine
Chl	chlorophyll
CW EPR	continuous wave electron paramagnetic resonance
Cyt	cytochrome
DCMU	3-(3,4-dichlorophenyl)-1,1-dimethylurea
ENDOR	electron nuclear double resonance
EPR	electron paramagnetic resonance
ESE	electron spin echo
ESEEM	electron spin echo envelope modulation
EXAFS	extended X-ray absorption fine structure
FID	free induction decay
HEPES	n-2-hydroxyethylpiperazine-n'-2-ethanesulfonic acid
MES	2[n-morpholino]ethanesulfonic acid
NADP	nicotinamide-adenine dinucleotide phosphate
NMR	nuclear magnetic resonance
NQR	nuclear quadrupole resonance
Phen	1,10-phenanthroline
PPBQ	phenyl-*p*-benzoquinone
PSI	Photosystem I
PSII	Photosystem II
Q	quality factor
Tris	2-amino-2-hydroxymethylpropane-1,3-diol
TWT	travelling wave tube
WOC	water oxidation complex of PSII

Table of Contents

Chapter IV
ESEEM of Mixed Valence Mn Compounds

Chapter V
Electron Spin Echo Studies of Mn in Photosystem II

Chapter I – Introduction to Electron Spin Echo Spectroscopy in Photosynthesis

Photosynthesis is the process by which plants and certain bacterial species convert photon energy into chemical energy. The resultant chemical energy is used to drive biochemical reactions. Photosynthesis thus provides the ultimate source of energy for the earth's life processes. Higher plants also release molecular oxygen as a byproduct of the photosynthetic reactions. Photosynthetic oxygen evolution produces essentially all of the O_2 in our atmosphere.

The initial event of a photosynthetic reaction is the absorption of a photon by a special pigment molecule. This energy absorption promotes the pigment molecule into an excited electronic state. The reduction potential of this electronically excited state is sufficient to cause the spontaneous transfer of an electron to a nearby "acceptor" molecule, which in turn becomes a strong reducing agent. The initial pigment molecule is left in an electron deficient state and thus acts as a strong chemical oxidant. The creation and immediate stabilization of this photon-induced chemical energy is the essence of photosynthesis.

In higher plants the process of photosynthesis generates an oxidizing agent sufficiently powerful to remove electrons from water. Water acts as a source of electrons in a flow pattern which ultimately results in the reduction of atmospheric carbon dioxide to a variety of fixed carbon species. The result of the photosynthetic process may be represented by a simple equation

$$6CO_2 + 6H_2O \xrightarrow{h\nu} C_6H_{12}O_6 + O_2 \qquad (I-1)$$

where electrons from H_2O are used to reduce the CO_2 to a reduced carbon species, here represented by a simple sugar ($C_6H_{12}O_6$). Molecular oxygen is released as a byproduct of this reaction. This molecular oxygen is used as an electron sink in the complementary biological process of respiration.

The process of photosynthetic water oxidation is catalyzed by a complex assembly of proteins and cofactors. The first row transition metal manganese serves an important role in this enzymatic chemistry. Manganese ions involved in water oxidation chemistry undergo electronic oxidation in the process and can be observed in an electron paramagnetic form. This thesis discusses the results of a set of magnetic resonance experiments on this paramagnetic species and synthetic chemical analogues. The goal of this research is to further our knowledge of the chemical structure of this

Mn site and its role in photosynthetic water oxidation. The specific magnetic resonance technique, electron spin echo spectroscopy, is introduced in Section 2 of this chapter. Electron spin echo spectroscopy provides a sensitive measure of the chemical environment of the Mn ions involved in the water oxidation process. We begin our discussion with a more more detailed description of photosynthesis and the biological processes of water oxidation and oxygen evolution.

Section 1 – Introduction to Photosynthesis and Photosynthetic Water Oxidation

The pigment-protein complexes in which photosynthetic charge separations occur are known as reaction centers. The reaction center pigment molecules are bound in the matrix formed by the surrounding protein. The reaction center pigment-protein assemblies are incorporated into membrane complexes. An important function of the photosynthetic reaction centers is to establish proton gradients across these membranes. Such proton gradients are used to drive the phosphorylation of adenosine diphosphate (ADP) into high-energy adenosine triphosphate (ATP). The electronic oxidation-reduction reactions also follow a vectorial arrangement with respect to the membrane, with oxidizing and reducing species formed on opposite sides.

Associated with the photosynthetic reaction centers are accessory "antenna" proteins which contain additional light-gathering pigments. The special pigments where photo-induced charge separation occur are actually minority components. There are typically several hundred antenna pigment molecules for each reaction center. This antenna arrangement greatly increases the cross section for photon gathering. The absorption of a photon by an antenna pigment promotes the molecule into an excited electronic state. The electronic excitation may be transferred to other nearby pigment molecules. In such fashion the resultant "exciton" wanders about the antenna complex until reaching the special pigments which perform charge separation, at which point the exciton energy is converted into chemical energy. Given the large size of the antenna complex, it is very important that the energy transfer processes occur with great speed and efficiency. The details of the mechanisms for energy transfer are not fully understood. In some cases the excitons are probably delocalized over several pigment molecules. Transfer of excitation energy over a distance of many nanometers requires a relatively long range mechanism such as the inductive resonance transfer described by Förster (1965). Studies into the exact nature of the energy transfer mechanisms form a major area of current research (Sauer, 1986; Knox, 1986; Holzwarth, 1986; Geacintov and Breton, 1986; Breton, 1986; and Scheer, 1986).

The principal pigments employed in higher plant photosynthesis are chlorophylls (*Chl*). Bacterial photosynthetic organisms utilize the related bacteriochlorophyll (*Bchl*) molecules which absorb slightly longer wavelength light. Carotenoid molecules also serve a light gathering function in plants. Many species of algae employ open-chain tetrapyrroles known as bilins as antenna pigments. Good introductions to the organization and function of the various pigment complexes in different photosynthetic

organisms are provided by Clayton (1980) and by Thornber (1986).

Optical and magnetic resonance studies have provided much information about the structure of photosynthetic reaction centers. The most detailed structural information has come from analysis of X-ray diffraction patterns obtained from crystallized bacterial reaction centers. Deisenhofer and Michel presented the first of these X-ray determined reaction center structures with their work on the purple bacterium *Rhodopseudomonas viridis* (Deisenhofer et al., 1984; Deisenhofer et al., 1985; Michel et al., 1986b; Michel and Deisenhofer, 1986) An X-ray structure of the related *Rhodobacter sphaeroides* reaction center has also been reported (Chang et al., 1986).

Rhodobacter sphaeroides and *Rhodopseudomonas viridis* are examples of purple nonsulfur bacteria. These bacteria employ a single photosystem. This photosystem is used to promote a cyclic flow of electrons. A cartoon illustrating the patterns of electron and proton flow is provided as Figure I-1. The initial charge separation occurs out of a "special pair" of *Bchl* molecules called P_{960} in *R. viridis*. Norris et al. (1971) had proposed such an arrangement of two strongly interacting molecules to explain the narrow EPR linewidth observed for the cation radical P^+ produced by the charge separation. The resulting photoelectron is passed to a bacteriopheophytin (*Bpheo*) molecule denoted I within about 5 ps (Parson and Holten, 1986). The electron is passed from I^- to a quinone acceptor designated Q_a (menaquinone in *R. viridis* and ubiquinone in *R. sphaeroides*) in about 200 ps. At this stage the charge separation is fairly stable. The $P^+IQ_a^-$ state has a back-reaction time of about 100 ms vs. about 10 ns for the state P^+I^- (Wraight and Clayton, 1974). The electron is then passed to a ubiquinone designated Q_b, on the time scale of 100 μs (Dutton, 1986). In the meantime, P^+ has become re-reduced via electron donation from a cytochrome (*Cyt*) complex. The state with Q_b singly reduced is very stable with respect to back-reaction, and the resultant Q_b^- species also remains strongly bound in the reaction center. The system remains in this state until another photo-driven charge separation occurs, allowing Q_b^- to receive a second electron. This doubly reduced Q_b^{-2} picks up two protons from the cytoplasm side of the membrane, and the resultant quinol Q_bH_2 is released from its binding pocket, to be replaced by a fully oxidized ubiquinone from a quinone pool existing within the membrane. The singly reduced semi-quinone does not exist as a stable molecule within the pool. The "two-electron gate" formed by the double reduction of Q_b couples the intrinsically one-electron process of photo-induced charge separation to the two-electron oxidation-reduction chemistry preferred

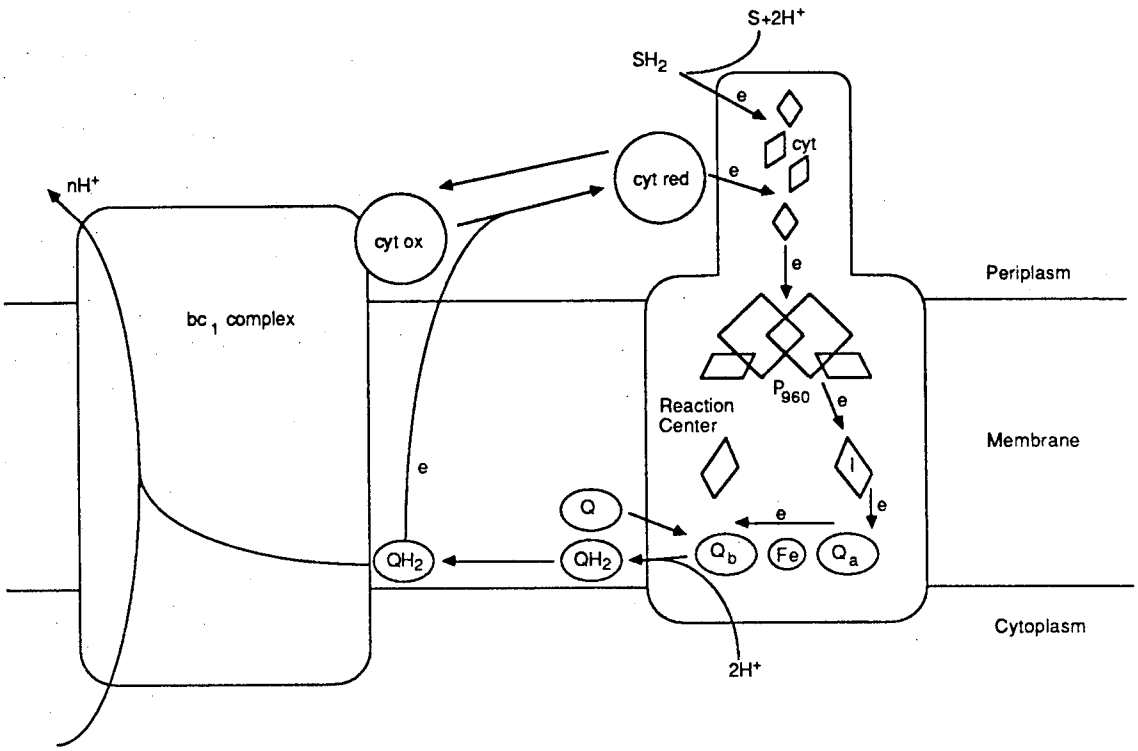

Figure I-1 Electron and proton flow patterns for the photosystem of *Rhodopseudomonas viridis* (adapted from Michel and Deisenhofer, 1986). The reaction center is incorporated into the photosynthetic membrane. Electrons are transferred from the photoexcited *Bchl* special pair P_{960} to a nearby *Bpheo I* and then to the menaquinone Q_a. After two electrons are transferred to the secondary ubiquinone Q_b the doubly reduced Q_b^{-2} receives two cytoplasmic protons and leaves the binding pocket as a membrane-soluble quinol. The released quinol is replaced in the binding pocket by a quinone from the quinone/quinol pool within the photosynthetic membrane. The quinol is in turn oxidized by the membrane-bound bc_1 complex. The released protons are pumped to the periplasmic side of the membrane, and the resulting electrons are used to reduce water-soluble cytochromes. These water-soluble cytochromes in turn reduce the reaction center cytochromes initially oxidized by the P_{960}^{+} cation following the initial photo-induced electron transfer. External electrons may also enter the photosynthetic cycle through the reaction center bound cytochromes. Such electrons typically originate from easily oxidizable sulfur compounds.

by quinones (Vermeglio, 1977; and Wraight, 1977).

The quinone pool operates at a dynamic equilibrium between the quinol and quinone forms. The quinol form acts as a substrate for another membrane-bound protein system known as the bc_1 complex. The bc_1 complex is a quinol-cytochrome c oxidoreductase enzyme. The quinols are oxidized back to the quinone form by the bc_1 complex. The protons are translocated to the periplasm side of the membrane. The electrons are used to reduce water-soluble cytochrome c proteins. These soluble cytochromes diffuse within the periplasm, and act to re-reduce the reaction center bound cytochromes which have been oxidized in re-reducing the $Bchl$ special pair after the initial photo-induced electron transfer. Thus the cyclic electron transfer loop is closed. The net result of the cyclic pattern is the absorption of two photons to pump two protons across the photosynthetic membrane. The proton gradient drives the synthesis of ATP through yet another membrane bound enzyme called the coupling factor complex (Melandri and Venturoli, 1986).

The cyclic electron flow pattern may be complemented by the injection of electrons from easily oxidizable reduced sulfur compounds such as H_2S. It is thought that these electrons enter the cycle through the bound cytochromes of the reaction center (Dutton, 1986). However the P^+ oxidant formed by photo-induced charge separation in the purple bacteria is not strong enough to draw electrons from H_2O. Water oxidation can be performed only by the Photosystem II reaction center of cyanobacteria and higher plants. We will address the topic of photosynthetic water oxidation later in this introduction.

The previous description of bacterial photosynthesis is somewhat simplified. In particular the biological regulation of the quinone/quinol and water-soluble cytochrome pools is quite complex. For example, components such as the bc_1 and coupling factor complexes are also used in the process of respiration when the bacteria are supplied with oxidizable substrates such as succinate. More complete reviews on various aspects of bacterial photosynthesis may be found in Clayton, 1980; Hoff, 1982; Parson, 1982; Parson and Ke, 1982; Dutton, 1986; and Norris and Van Brakel, 1986.

At this juncture we return to focus on details of the reaction center structure as determined by X-ray crystallography. The *R. viridis* reaction center contains four protein subunits. The three subunits designated L, M, and H are involved in binding the photosynthetic cofactors. The fourth subunit is a c-type cytochrome which contains four covalently bound heme groups. This cytochrome is not present in the

R. sphaeroides crystals. The *L*, *M*, and *H* protein subunits and the bound pigments form a beautifully symmetric complex, with a 2-fold rotation axis passing through the *Bchl* special pair and out through a non-heme Fe which bridges the two quinones. This symmetry element is readily visible in Figure I-2, a drawing of the prosthetic groups of the *R. viridis* reaction center (Michel and Deisenhofer, 1986). Each of the *L* and *M* subunits contains five membrane-spanning α-helices. The α-helices of *L* are mapped onto the α-helices of M through the C_2 symmetry group. The smaller *H* subunit presents only one membrane spanning helix. The major portion of *H* forms a cap over the *L* and *M* components on the cytoplasmic side of the membrane. In *R. viridis* the cytochrome protein tightly binds to the opposite (periplasmic) side, with the four heme groups forming an approximately linear chain with one heme relatively close ($\approx$21 Å) to the *Bchl* special pair.

The *Bchl* special pair is found in a hydrophobic pocket formed by *L* and *M*. The two *Bchl* molecules are covalently attached to the proteins by Mg ligation to two histidines, one from *L* and one from *M*. The macrocycles of the two *Bchl* molecules lie in nearly parallel planes, with close stacking of the pyrrole rings I. Two accessory *Bchl* molecules are located near the special pair, with their orientations also following the 2-fold symmetry seen throughout the complex. It is currently unclear what role these accessory pigments play in the photosynthetic process. The two *Bpheo* molecules are located in hydrophobic pockets in *L* and *M*, again following the 2-fold symmetry. The menaquinone Q_a of *R. viridis* is bound only to the *M* subunit. The quinone Q_b is not present in the *R. viridis* X-ray crystal structure. However, inhibitor molecules like 1,10-O-phenanthroline bind to the *L* subunit at a position related to the Q_a site by the C_2 symmetry group. This positioning of the secondary quinone is confirmed in the *R. sphaeroides* X-ray structure, where the native ubiquinone Q_b is present and well resolved. A Fe^{+2} ion lies along the C_2 axis between Q_a and Q_b . Q_a forms a hydrogen bond to a histidine from *M* which is also a ligand to the Fe^{+2} ion. Although it is appealing to envision this Fe ion being involved in electron transport between Q_a and Q_b, it can be completely removed in *R. sphaeroides* without greatly reducing electron transport rates (Debus et al., 1985).

The apparent structural C_2 symmetry of the reaction center does not carry over to functional symmetry, because electrons are initially transferred to Q_a and only subsequently to Q_b. Subtle deviations from structural symmetry must be responsible for this functional asymmetry. For example, the *Bchl* and *Bpheo* phytyl side chains

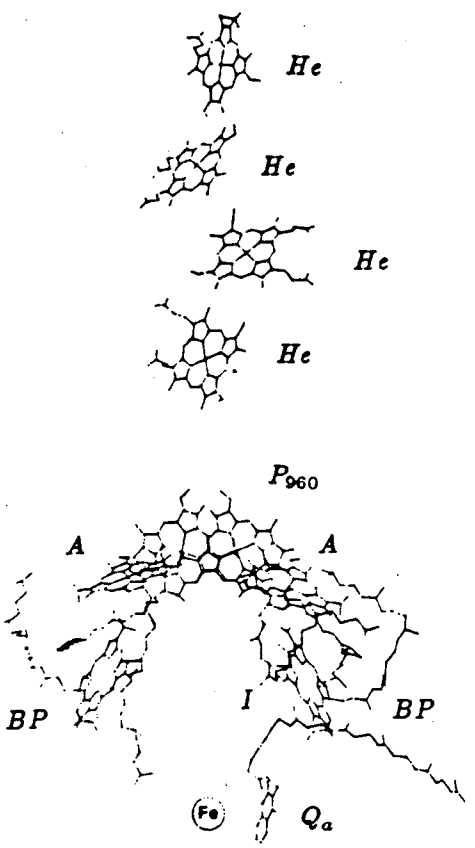

Figure I-2 Diagram of the prosthetic groups of the *Rhodopseudomonas viridis* reaction center (Michel and Deisenhofer, 1986). This diagram shows the 2-fold symmetry structure of the reaction center. The symmetry axis is oriented vertically within the plane of the page. The two *Bchl* molecules which form the special pair P_{960} are shown with their stacked pyrrole rings. P_{960} is flanked by the two additional "accessory" *Bchl* molecules (*A*). The 2-fold symmetry is maintained in the positioning of the *Bpheo* molecules (*BP*). Electrons are transferred through the *Bpheo* molecule denoted *I*. The secondary quinone Q_b is not present in the *R. viridis* reaction center crystal. Thus, only the tightly bound menaquinone Q_a is displayed in the figure. The *R.sphaeroides* structure (Chang et al., 1986) shows the ubiquinone Q_b in a position related to that of Q_a by the 2-fold symmetry seen in the other cofactors. The Fe^{+2} ion is on the axis of symmetry between the two quinone sites. Four heme groups are shown in the figure. They are the functional groups of the donor cytochromes, and are arranged in a roughly linear fashion with the closest heme about 21 Å from the special pair.

are not rigorously positioned according to the 2-fold symmetry. Small differences in protein composition may also play a role in the functional asymmetry. For example, a negatively charged glutamic acid located near one of the *Bpheo* moieties may affect the relative electron transfer rates to the two symmetrically located *Bpheo* molecules. There is also a *M* subunit tryptophan which effectively bridges the *L* subunit *Bpheo* and Q_a, and could help facilitate rapid electron transfer along this path. With the crystal structures at hand, and with the application of molecular biology techniques such as site-directed mutagenesis, it will be very interesting to see what can be learned about such "fine-tuning" of reaction center function in the coming years.

Unlike the purple bacteria, green plants and cyanobacteria operate with two distinct photosystems. Photosystem I (PSI) operates at a relatively low midpoint potential and generates a strongly reducing species which acts to donate electrons ultimately to the pyridine nucleotide coenzyme $NADP^+$ (nicotinamide-adenine dinucleotide phosphate). The resulting NADPH is employed in the dark reactions of the Calvin cycle to reduce CO_2. Two equivalents of NADPH and three equivalents of ATP are required to assimilate one equivalent of CO_2 (Clayton, 1980, Ch. 11). Photosystem II (PSII) operates at a much more positive midpoint potential. The "hole" created by the PSII charge separation is a very strong oxidant, and drives the electrochemistry required to strip electrons from H_2O. Both plant photosystems use higher photon energies ($\approx$1.8 eV) than does the photosystem of the purple bacteria ($\approx$1.4 eV). The extra photon energy serves to span the greater range of redox potential over which plant photosynthesis operates. The overall pattern of electron flow in higher plant photosynthesis is suggested by the *Z*-scheme of Hill and Bendall (1960), such as illustrated in Figure I-3. Redox active components of plant photosynthesis are positioned vertically to represent their approximate midpoint potentials (pH=7.0).

The Photosystem I reaction center is represented on the right side of the *Z*-scheme. The PSI reaction center is structurally rather different from the purple bacterial reaction center. The exact chemical nature of the primary donor P_{700} is uncertain. EPR and optical evidence originally suggested a *Chl a* dimer as the molecular identity of P_{700} (Norris et al., 1971; Schaffernicht and Junge, 1981; den Blanken and Hoff, 1983). However, EPR experiments with ^{13}C enriched samples (Wasielewski et al. 1981a) and proton ENDOR measurements (O'Malley and Babcock, 1984) have suggested a *Chl a* monomer origin for the primary donor. Wasielewski et al. (1981b) suggested that ring V of *Chl a* is modified to the enol form in P_{700}. Of additional interest is

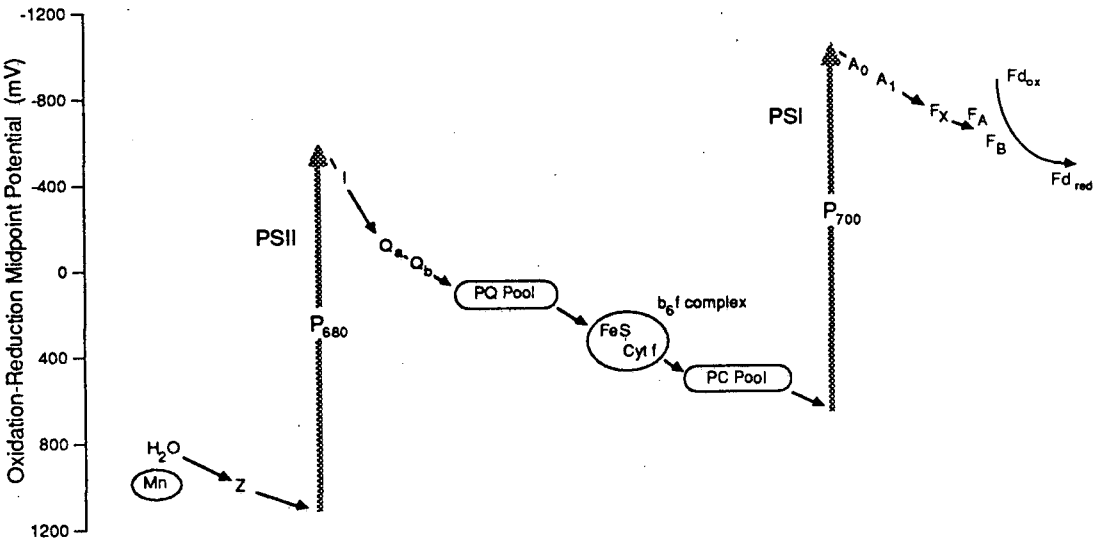

Figure I-3 Z-scheme of Hill and Bendall (1960) representing non-cyclic electron flow in higher plant photosynthesis. The diagram shows redox active components of the photosynthetic membranes. The vertical position of each component represents its approximate midpoint potential (pH=7.0). This Z-scheme representation illustrates photosynthetic electron flow from the water oxidation side of PSII to the ferredoxin reduction on the acceptor side of PSI. Cyclic flow is also possible, primarily via the *cyt* b_6f-mediated reduction of plastocyanin by the water-soluble ferredoxin.

the discovery of a chloro-*Chl a* derivative found in stoichiometric ratios with P_{700} (Scheer et al., 1983). The first electron acceptor A_0 operates at a very low potential and is most likely a *Chl* molecule (Swarthoff et al., 1982; and Fajer et al., 1980). The EPR properties of the secondary acceptor A_1 show that is not a *Chl* molecule (Sétif et al., 1984). The molecular identity of A_1 is still an open question, though there is evidence suggesting Vitamin K_1 (Brettel et al. 1987). The stable electron acceptors in PSI are Fe-S centers rather than quinones. The center denoted F_X is probably the first of these Fe-S centers to be reduced after the photo-induced charge separation. The electron is then passed to F_A and/or F_B. It is not clear whether these two acceptors operate in parallel or in series (Rutherford and Heathcote, 1985; Sétif and Mathis, 1986). Ferredoxin, a water soluble 2Fe-2S protein, shuttles electrons from these terminal acceptors to the ferredoxin-NADP oxidoreductase enzyme. This enzyme is the catalytic site of $NADP^+$ reduction. These reactions occur on the stromal side of the photosynthetic membrane.

The core structure of Photosystem II is very similar to the structure of the purple bacterial reaction center (Diner, 1986). The primary donor, called P_{680}, is probably a special pair of strongly coupled *Chl a* molecules. The primary acceptor is *Pheo a*. The two-electron gate formed by Q_a and Q_b is also present in PSII. In PSII reaction centers Q_a, Q_b, and the membrane soluble quinone pool are all composed of plastoquinone. The protons used in the reduction of Q_b to the quinol form are taken from the exterior of the photosynthetic membrane. We also note the strong amino acid sequence homology between the *D*1 and *D*2 proteins of PSII and the *L* and *M* proteins of the the reaction centers of purple bacteria (Hearst, 1986).

Although the structure of PSII is analogous to the structure of the reaction centers of purple bacteria, there is a number of important differences. The PSII primary donor operates with higher energy photons, and products resulting from the photo-induced charge separation of P_{680} span a greater range of oxidation-reduction potential. In particular, the oxidizing product P_{680}^+ is sufficiently powerful to drive the oxididation of water. P_{680}^+ is not re-reduced by a cytochrome as in the bacterial centers. A redox active tyrosine denoted Z serves this function in PSII reaction centers (Barry and Babcock, 1987; Boska and Sauer, 1983; Boska et al., 1983). This species Z serves as an electron transfer intermediate between the water oxidation complex and P_{680}^+. We will shortly return to discuss the water oxidation complex.

The interaction between PSI and PSII is mediated by a plastoquinol:plastocyanin

oxidoreductase called the *cyt* b_6f complex (Ort, 1986). The *cyt* b_6f complex is also membrane bound and contains as redox components several cytochromes and the high-potential Rieske Fe-S center (Hauska, 1986). Its function is very similar to that of the bc_1 complex of the purple bacteria. Quinol molecules produced through the reduction of quinones via the two-electron gate on the acceptor side of PSII are in turn oxidized by the *cyt* b_6f complex. Protons are pumped into the interior of the photosynthetic membrane. The electrons are used to reduce a small water-soluble Cu protein called plastocyanin, which serves a function analogous to that of the water-soluble cytochrome in the purple bacteria. Reduced plastocyanin transports electrons to PSI and probably directly re-reduces P_{700}^+ (Haehnel, 1986). Thus, the plastoquinone pool, the *cyt* b_6f complex, and plastocyanin link PSII and PSI reaction centers and provide a path for electrons stripped from water to enter the PSI-mediated reduction of $NADP^+$. The *cyt* b_6f complex also may oxidize the water-soluble ferredoxin reduced by PSI reaction centers. In this manner electrons may be transferred back to P_{700}^+, thus providing a cyclic electron transport path driven by the PSI reaction centers.

The organization of the photosynthetic membrane and its major components is quite interesting. The photosynthetic membranes of higher plants are called thylakoid membranes. The chloroplasts are rather full with the highly-invaginated thylakoid. The aqueous chloroplast matrix external to the thylakoids is called the stroma. The region interior to the thylakoid membrane is called the lumen. Electron micrographs show an interesting organization to the thylakoid membranes (Staehelin, 1986). In certain regions the membranes are appressed into tight disks, known as grana stacks. These grana stacks are rich in PSII reaction centers. Approximately 85% of PSII centers are found in these appressed portions of the thylakoid membrane. PSI centers are primary found in the unappressed, or stromal regions, of the thylakoid. The *cyt* b_6f complex is evenly distributed among the two regions. The coupling factor complex is located in the unstacked regions and at the boundaries of the grana stacks (Staehelin, 1986).

The segregation of the PSI and PSII reaction centers requires the transportation of electron equivalents over relatively long distances. From the measured dimensions of the grana stacks we can estimate the minimum distance for electron transfer to be at least 100 nm. We note that the PSI and PSII reaction centers and the *cyt* b_6f complex are too large to readily diffuse such large distances in the membrane on the timescale ($\approx$2 ms) of intersystem electron transport (Ort, 1986). The lateral communication of reducing equivalents between PSII reaction centers and *cyt* b_6f complexes

is performed by the membrane soluble plastoquinone/plastoquinol pool. Electrons are transported between *cyt* b_6f complexes and PSI reaction centers by plastocyanin, which is small (MW=10.5 kDa) and diffuses rapidly in the aqueous space of the lumen. We note that diffusion of these components is not the rate-limiting step for intersystem electron transfer. In steady-state conditions the plastoquinone/plastoquinol pool is almost completely reduced while the plastocyanin pool is almost completely oxidized. This shows that the oxidation of plastoquinol by the *cyt* b_6f complex is the rate-limiting step.

We now return to the donor side of PSII and the major focus of this thesis, the mechanism of photosynthetic water oxidation. We begin with a short examination of electrolytic water oxidation. The oxidation of water can be represented by the half-reaction

$$2H_2O \rightarrow 4e^- + 4H^+ + O_2 \qquad (I-2)$$

The evolution of one molecule of O_2 requires the removal of four electrons from water. The average reduction potential of the four electron steps is +0.81 eV at pH 7.0. Figure I-4 illustrates the individual steps for the reaction, with either hydrogen peroxide H_2O_2 or atomic oxygen O as intermediates (Radmer and Cheniae, 1977; George, 1965). The first step, $H_2O \leftrightarrow HO + H^+ + e^-$, requires 2.3 V. Another large potential increase is required to produce atomic oxygen in the next step. A more conservative oxidation path produces H_2O_2 as the second product, with another moderate step to produce O_2^- after the third electron oxidation.

PSII operates with photons of wavelengths as long as 680 nm. The energy of a 680 nm photon is 1.8 eV. There is not enough energy available from a single photon absorption to promote a 2.3 V oxidation such as shown in step 1. However the average oxidation value of 0.81 V is within reach of a single photon event. This argues for the presence of a "buffering" system which increments a modest oxidation increase for each electron donated to the photo-oxidized P_{680}^+. After a given number of electron oxidation steps this water oxidation complex (WOC) will have acquired sufficient oxidative potential to perform the full oxidation of water. The biological mechanism to translate a number of independent one-electron oxidation events into a concerted four-electron oxidation is analogous to the previously described two-electron gate demonstrated for quinone reduction.

A great advance in understanding such a water oxidation mechanism came from the interpretation of experiments measuring the kinetics of oxygen evolution following

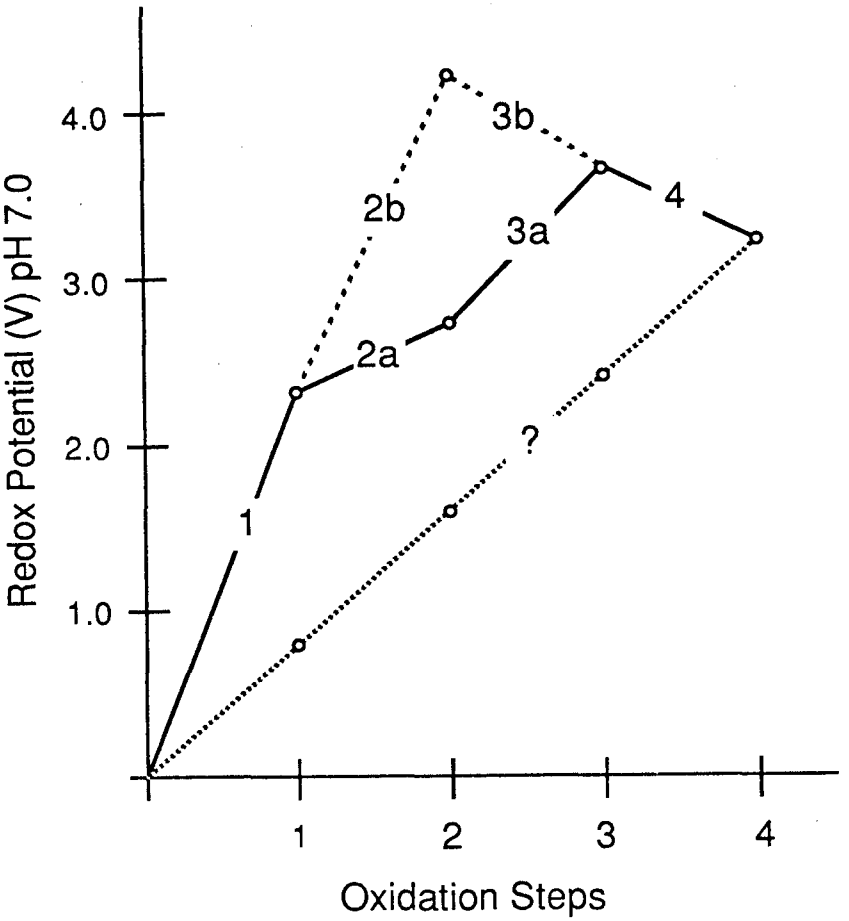

Figure I-4 Redox potentials of the individual electron redox couples for the full oxidation of water to molecular oxygen at pH 7.0 (adapted from Radmer and Cheniae, 1977). Two distinct pathways are shown. The solid line passes through a hydrogen peroxide intermediate. The dashed line employs an atomic oxygen intermediate. The oxidation- reduction couples indicated on the figure are

(1) $H_2O \leftrightarrow HO + H^+ + e^-$

(2a) $HO + H_2O \leftrightarrow H_2O_2 + H^+ + e^-$

(3a) $H_2O_2 \leftrightarrow O_2^- + 2H^+ + e^-$

(4) $O_2^- \leftrightarrow O_2 + e^-$

(2b) $HO \leftrightarrow O + H^+ + e^-$

(3b) $O + H_2O \leftrightarrow O_2^- + 2H^+ + e^-$

(?) Path of minimum energy per step (0.81 V/e^-)

short light flashes. Joliet et al., (1969) described the pattern of oxygen evolution following a series of short $\approx 10\mu s$ saturating flashes applied to previously dark-adapted suspensions of spinach chloroplasts or algae. The result was a remarkable period-four oscillation of oxygen evolution vs. flash number. Figure I-5 shows such a pattern as measured for spinach chloroplasts by Babcock (1973). The quantity of evolved oxygen is maximal after the third flash, with repeated maxima after successive four flash intervals. The oxygen evolution vs. flash pattern eventually dephases and reaches a steady state value. These experiments demonstrate that the number of independent photo-oxidation steps required to oxidize water is four.

Kok et al. (1970) reproduced the flash pattern results of Joliot et al. and devised a kinetic model to explain the data. This "S-state" model is illustrated in Figure I-6. In the Kok S-state model each PSII reaction center acts as an independent unit in the oxidation of water. The least oxidized state of the water oxidation complex is denoted S_0. The photo-oxidized P_{680}^+ is re-reduced by an electron donated by the water oxidation complex. The resulting oxidized WOC state is denoted S_1. The successive single-oxidation products of the water oxidation complex are denoted S_2, S_3, and S_4. The S_4 state is a sufficiently strong oxidant to fully oxidize the two water molecules. Molecular oxygen is released, and the WOC resets to the S_0 state.

The details of the experimental oxygen evolution flash pattern are explained by supposing both S_0 and S_1 to be stable in the dark. S_1 is formed by the deactivation of states S_2 and S_3, while S_0 is formed by the deactivation of the state S_4 via oxygen evolution. After short term dark adaptation, the system is thus approximately 60% in the S_1 state, resulting in maximal oxygen evolution after the third flash. By letting the system dark adapt a second time following a single flash, Kok et al. were able to concentrate the water oxidation complex into the S_1 state. Subsequent flashes showed almost no oxygen evolved after the first two flashes and an even larger maximum after the third flash. The slow dephasing of the oxygen evolution oscillations is simply explained by a nonzero probability of "misses" and "double hits" leading to a loss of S-state coherence. We note that Figure I-6 elaborates somewhat on the original Kok cycle. The oxidation of the S-states is explicitly shown as occurring through the redox active tyrosine Z. Also, the measured pattern of protons released into the lumen is added (see review by Godvindjee et al., 1985).

The oxygen evolution vs. flash number experiments and the subsequent Kok S-state model are important for several reasons. They show that four photo-oxidized

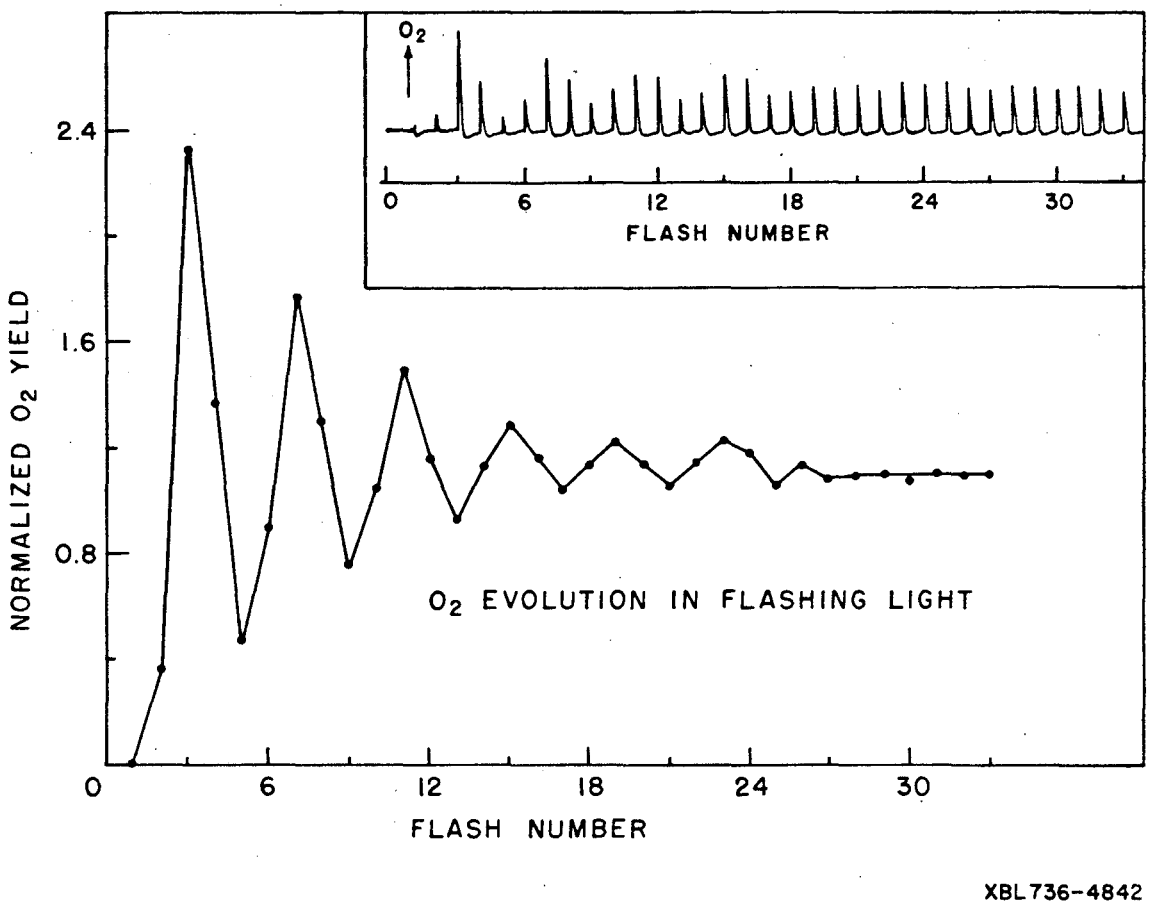

Figure I-5 Oxygen evolution as a function of flash number (Babcock, 1973). In this experiment 21 μs saturating flashes spaced 1 s apart are applied to a chloroplast suspension. The inset figure shows the experimental trace of the fast oxygen electrode voltage. The large figure shows the normalized oxygen yield averaged over a series of eight experiments.

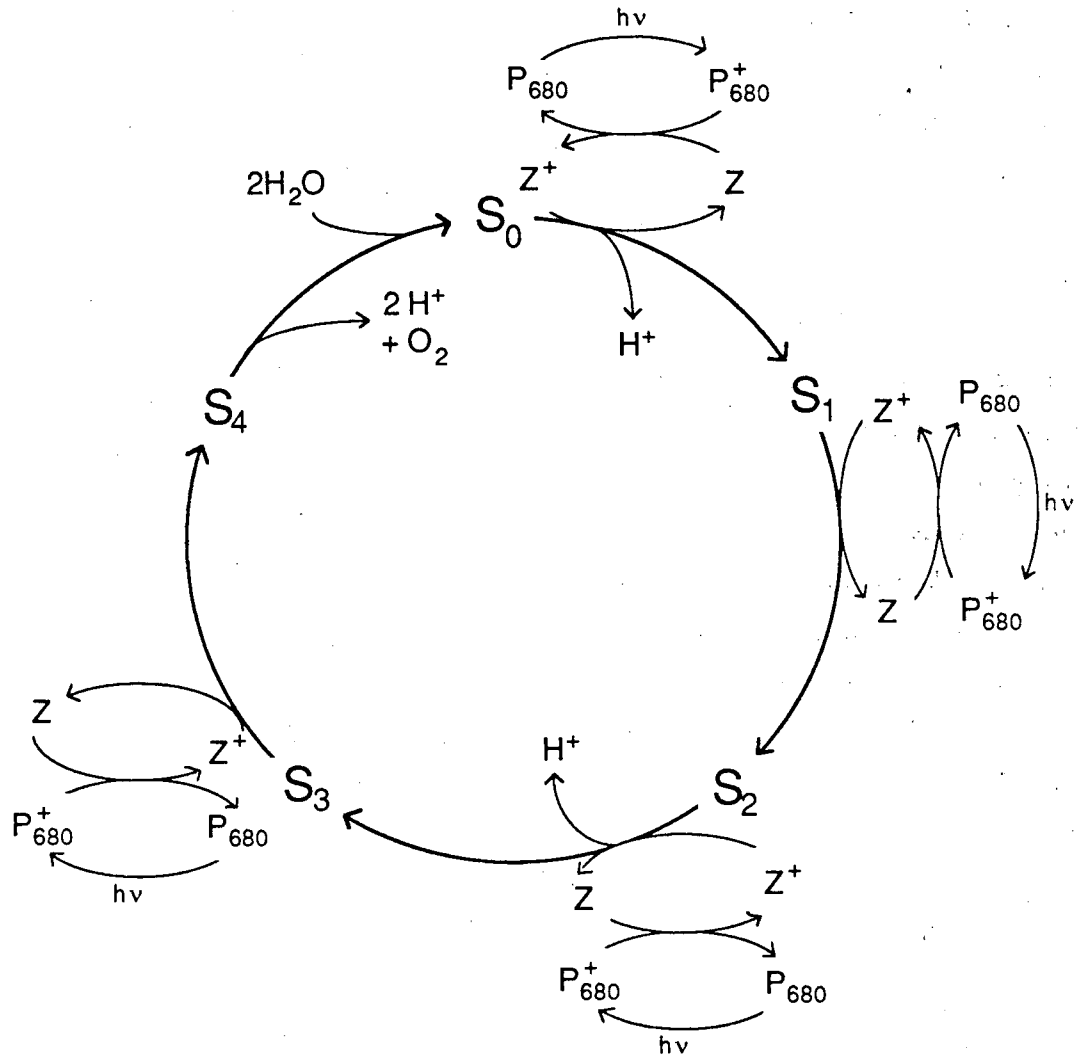

Figure I-6 Kok S-state scheme (Kok et al., 1970). The water oxidation center undergoes four successive oxidations, each coupled to the photo-oxidation of P_{680} through the redox active tyrosine Z. The resulting states of successive oxidation are denoted S_1, S_2, S_3, and S_4. Molecular oxygen is spontaneously released following the fourth oxidation step, and the cycle resets to the state S_0. The figure also shows the measured pattern of proton release in the cycle (Govindjee et al., 1985). The entrance of the two water molecules at the S_0 stage is only included to balance the cycle. The stages at which water molecules are inserted into the S-state cycle are not yet known.

equivalents are needed to oxidize two molecules of water. The experiments also reveal that each PSII reaction center has its own water oxidation center. Such an arrangement was later demonstrated by the isolation of small PSII-enriched thylakoid membrane fragments with integral high rates of oxygen evolution (Berthold et al., 1981). This may be contrasted to a hypothetical organization employing a separate pool of water oxidation enzymes supplied with diffusing oxidizing equivalents produced by a pool of PSII reaction centers. Finally, the Kok S-state scheme has provided a useful working model for subsequent investigations into photosynthetic water oxidation.

Over the years sufficient evidence has accumulated to demonstrate that the transition metal manganese plays a key role in the enzymatic action of the water oxidizing complex. Early experiments of growing algae on low levels of Mn revealed dimunition of oxygen evolving capability (Pirson, 1937). Later experiments led to a localization of Mn function to PSII. Kessler et al. (1957) showed that Mn deficiency led to a decrease in PSII luminescence. Cheniae and Martin (1966) demonstrated loss of oxygen evolution by releasing Mn via heat shock techniques. Cheniae and Martin (1970) arrived at a stoichiometry of four Mn per PSII reaction center. This ratio of four Mn ions per PSII reaction center is also seen in the purified PSII membrane fragments (Yocum et al., 1981). Many biochemical studies from the late 1960's through the 1970's confirmed the role of Mn in photosynthetic oxygen evolution. (These are reviewed particularly well by Radmer and Cheniae (1977)). However there was no direct spectroscopic evidence providing details of the structural or functional role of Mn during this time. Fortunately this situation changed in the 1980's. Results from X-ray spectroscopy and EPR have provided a great deal of information about the structure of PSII Mn and its function in photosynthetic water oxidation.

The earliest X-ray spectroscopic results were reported by Kirby et al. (1981). They reported the extended X-ray absorption fine structure (EXAFS) for Mn in chloroplast preparations. Mn EXAFS were recorded for native chloroplasts and chloroplasts treated with alkaline *Tris* buffer to inactivate water oxidation capability. The difference between the EXAFS of the untreated and the inactivated chloroplasts was taken to represent the EXAFS of the active pool of Mn. The results were shown to be similar to the EXAFS of di-μ-oxo-bridged Mn model systems. Yachandra et al. (1986a) reported Mn EXAFS of purified photosystem II membrane fragments. With these cleaner preparations difficult difference techniques were not required. These EXAFS studies show a metallo-organic cluster with at least two Mn atoms separated by 2.7 Å.

A later report shows the identical structure to be present in PSII membranes poised in both the S_1 and S_2 states (Yachandra et al., 1987). High resolution Mn X-ray edge spectra show a distinct oxidation of Mn corresponding to the transition from the S_1 to the S_2 state (Goodin et al., 1984)

The other major spectroscopic breakthrough was the discovery of a low temperature Mn EPR signal in spinach chloroplasts by Dismukes and Siderer (1981). This Mn EPR signal presents $\approx$19 Mn hyperfine lines (see Figure V-1). The spectrum is similar to that observed for antiferromagnetically coupled mixed-valence Mn dimers. Dismukes and Siderer demonstrated that this Mn EPR signal is associated with the S_2 state of the water oxidation complex. Chapter V presents details of experiments characterizing this Mn EPR signal and describes the results of our electron spin echo experiments on this Mn signal. The remainder of this chapter provides a brief introduction of the techniques of electron spin echo spectroscopy.

Section 2 – Electron Spin Echo Spectroscopy

In this section we provide a qualitative introduction to Electron Spin Echo spectroscopy (ESE). Further general introduction may be obtained from a number of good review articles (Kevan, 1979; Mims, 1972c; Mims and Peisach, 1979; Mims and Peisach, 1981). A more detailed view of ESE is provided in Chapter II.

Electron Paramagnetic Resonance (EPR) is an important tool for studying structure and function of paramagnetic molecules in biological systems. EPR has played a particularly important role in the study of photosynthesis, where light-induced electron transfer results in the appearance of a number of electron paramagnetic species, including both organic radicals and transition metal systems with unpaired d-orbital electrons. EPR studies typically reveal g-values, linewidths, and large hyperfine couplings. However, weak hyperfine and superhyperfine couplings may be masked under the broad EPR lineshapes that are typically observed.

The EPR linewidths in biological systems are rarely limited by the effects of homogeneous broadening. A number of mechanisms give rise to inhomogeneous broadening, typically causing the EPR linewidth to be much larger than the uncertainty principle limit of $\approx 1/T_2$. The effects of such broadening are seen in Figure I-7, which illustrates an inhomogeneously broadened line composed of a near-continuum of individual "spin-packets". Each spin packet represents a microscopic site with a certain resonant frequency and a homogeneous linewidth $\approx 1/T_2$.

There are numerous sources of inhomogeneous broadening. Transition metal centers typically present anisotropic g-tensors. Biological samples are generally not available as single crystals, therefore the EPR lineshape may largely be determined by the powder pattern resulting from averaging the g-tensor over all orientations. This can result in total linewidths as large as several thousand Gauss. Even in the absence of g-anisotropy, other factors introduce inhomogeneous broadening. One common source of inhomogeneity results from the presence of unresolved hyperfine coupling. An electron site interacting with k classes of inequivalent nuclei, with n_k nuclei of spin I_k in each class, has an EPR signal split into N lines, with

$$N = \prod_{k=1}^{k} (2n_k I_k + 1). \qquad (I-3)$$

Electrons in biological systems are typically weakly magnetically coupled to a large number of protons, giving rise to a manifold of densely spaced spin packets. Unresolved ^{14}N couplings also often broaden lines. Additionally, random mechanical and

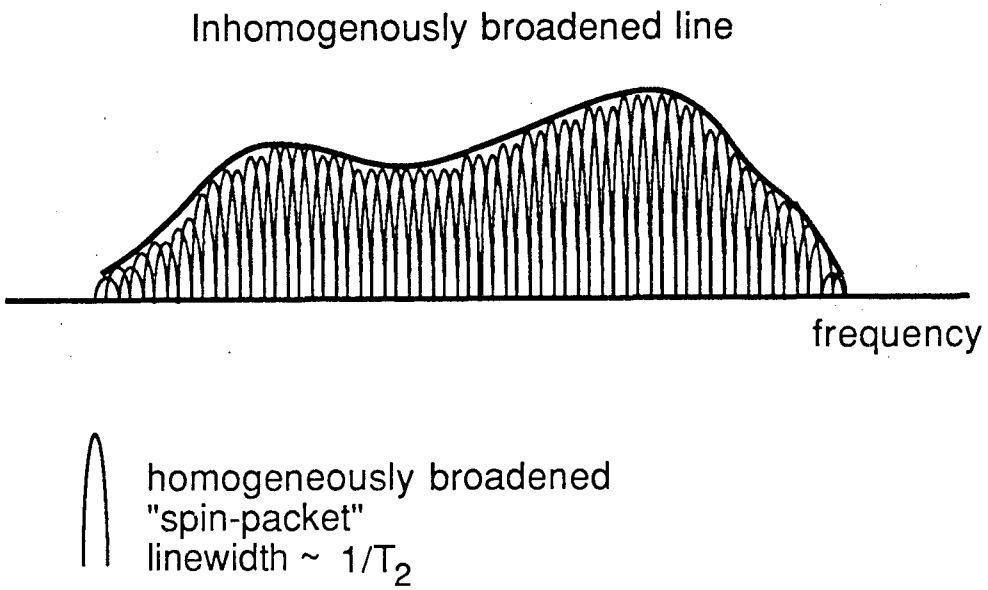

Figure I-7 Effect of inhomogeneous broadening on EPR lineshape. The overall lineshape is determined by the summation of a near-continuum of individual "spin-packets", each resonating at a characteristic frequency and with a homogeneous linewidth determined by the uncertainty principle.

electrical strains act to broaden EPR lines. All of these factors limit the resolution available with conventional continuous wave (cw) EPR and provide motivation for introducing versatile pulsed EPR techniques which can extract information normally masked by the effects of inhomogeneous broadening.

The simplest pulsed EPR experiment consists of applying a single resonant microwave pulse to rotate the electron spin by 90°. The resulting free induction decay (FID) formally contains the same information available by taking the cw EPR spectrum. This is the basis for routine pulsed NMR spectroscopy. However the linewidths in the NMR cases are typically many orders of magnitude smaller than the EPR linewidths. For example, a "narrow" EPR signal in a biological sample may be present as a Gaussian envelope of spin packets with a total linewidth of approximately 10 Gauss. The corresponding frequency bandwidth of such a signal would be about 30 MHz. If we could uniformly excite this line with a 90° pulse, the FID would last only about 30 ns and would be totally obscured in the pulse ringdown. Many EPR signals are on the order of hundreds to thousands of Gauss in width, and the FID obtained for such signals would contain information about only the limited excitation profile of the 90° pulse. Of course, in practice these FID's would also be obscured by ringdown. The EPR applications of FID spectroscopy are thus limited to samples with narrow, well-defined lines, and have no apparent role in our studies of photosynthetic oxygen evolution. However broad EPR signals may often be studied with Electron Spin Echo techniques, which effectively remove the contributions of inhomogeneous broadening.

The simplest spin echo experiment is the 2-pulse Hahn echo (Hahn, 1950). The mechanism of the 2-pulse spin echo experiment is illustrated in Figure I-8. The $\{x, y, z\}$-axis system shown represents a reference frame rotating with respect to the laboratory at an angular frequency ω_0 equal to the Larmor frequency of a spin packet in the center of an inhomogeneously broadened line. The equilibrium situation shown in (a) exists before the application of the first microwave pulse. The magnetization $\vec{M}$ lies along the z-axis, defined by the externally applied dc magnetic field $\vec{H}_0$. A 90° pulse is then applied using a microwave pulse in the laboratory which has a magnetic field component $\vec{H}_1$ along the y-axis of the rotating frame. After the 90° pulse, the magnetization $\vec{M}$ lies along the x-axis of the rotating frame (b). The system is then allowed to precess freely for a time τ (c). During this precession time, the magnetization dephases in the xy-plane. Only spin packets with precisely the rotating frame frequency remain along the x-axis. Packets with lower and higher

frequencies precess away from the x-axis, and apparent xy-plane coherence is lost. This coherence loss is measured in the lab frame as a diminution of the induction signal. Application of a 180° pulse rotates the spins into the configuration shown in (d). The packets continue their previous rates of precession in the rotating frame, and after an additional time τ the spins rephase (e). The resulting evanescent coherence is known as a spin echo.

The time sequence of the 2-pulse spin echo is shown in Figure I-9a. The 90° pulse is followed by the free precession time τ before the application of the 180° pulse. The spin echo is formed at time τ after the 180° pulse. Figure I-9b shows a 3-pulse "stimulated" echo sequence, where two 90° pulses separated by τ are followed by a third 90° pulse at time T. The stimulated echo occurs at time τ after the third 90° pulse.

The origin of the 3-pulse stimulated echo is seen in Figure I-10. Figure I-10a shows the equilibrium lineshape as a function of frequency. The first 90° pulse rotates magnetization onto the x-axis, just as in Figure 1-8b. The second 90° pulse is applied after a dephasing time τ. Spin packets with Larmor frequencies very close to ω_0 will remain along the x-axis during the dephasing time, and the second pulse will rotate them onto the z-axis with a negative projection. These spins are thus flipped by 180°. The same rotation will occur for all spin packets which have precessed an integral number of cycles in the xy-plane in the precession time τ. In contrast, spin packets which have precessed in the xy-plane by odd multiples of 180° will be reoriented onto the positive z-axis by the 90° pulse. The net result of the first two 90° pulses is to induce a modulation of the z-component of magnetization with respect to frequency, as shown in Figure I-10b. The period of this modulation is $\Delta\omega = 2\pi/\tau$. The third 90° pulse simply induces a FID of this modulated line, the result being the stimulated echo. We note that after the first two 90° pulses the echo information is stored along the longitudinal z-axis and, therefore, disappears on the timescale of T_1 rather than T_2. As a result, 3-pulse echoes generally persist to relatively long values of T as compared to the more rapid decay of 2-pulse echoes with increasing τ.

Both the 2-pulse and 3-pulse spin echo sequences effectively negate the effects of inhomogeneous broadening. We may take advantage of this fact to observe effects which would be totally obscured by large inhomogeneities. The energy splittings available for study with spin echo spectroscopy are on the order of the homogeneous linewidths of the individual spin packets. In particular, we will be studying

Figure I-8 The formation of a 2-pulse spin echo. The $\{x, y, z\}$-axis system represents a rotating frame with angular velocity ω_0 equal to the Larmor frequency of a spin packet at the center of the inhomogeneously broadened line. $\vec{H}_0$ is the DC magnetic field along the z-axis, and $\vec{H}_1$ is a rotating frame magnetic field component of the applied microwave pulse of laboratory frequency $\omega_0/2\pi$.

(a) Equilibrium situation with the magnetization $\vec{M}$ aligned with $\vec{H}_0$.

(b) After 90° pulse, with $\vec{M}$ rotated onto the x-axis of the rotating frame.

(c) After free precession period of duration τ. Magnetization dephases in the xy-plane due to inhomogeneous broadening. Spin packets labeled "1" and "2" precess in the counter-clockwise direction as seen from the positive z-axis. The spin packet labeled "3" is perfectly on resonance and remains along the x-axis. Spin packets labeled "4" and "5" precess in the clockwise direction.

(d) After 180° pulse applied at time τ. The spin packets are flipped such that rephasing begins. All spin packets maintain their same precession frequencies, and begin reconverging.

(e) After time τ following 180° pulse. All packets are fully converged, resulting in a spin echo.

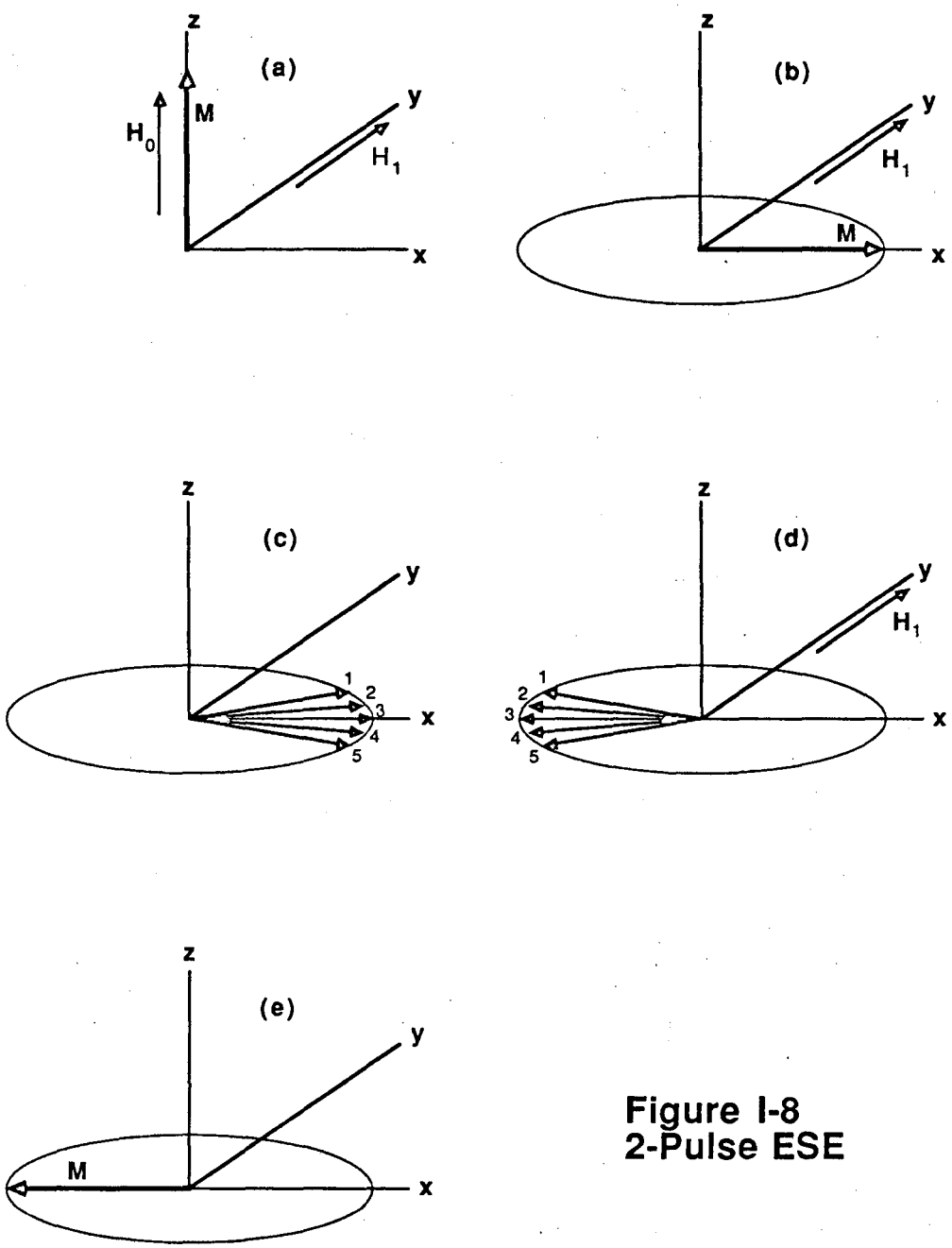

Figure I-8
2-Pulse ESE

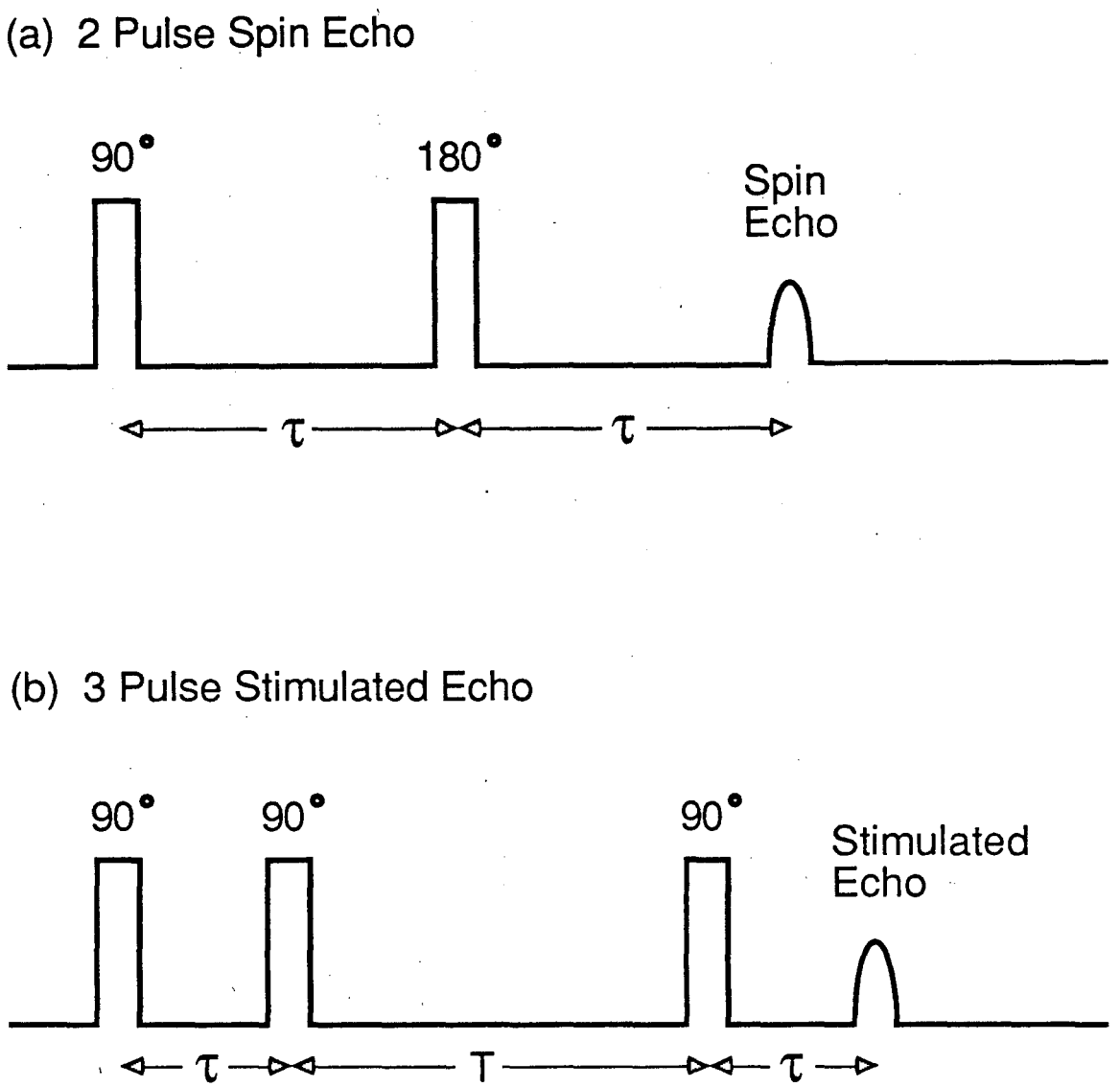

Figure I-9 2-pulse and 3-pulse spin echo sequences. The 2-pulse sequence is shown in (a). A 90° pulse is followed by a free precession period of duration τ, at which time a 180° refocussing pulse is applied. The 2-pulse spin echo is formed at time τ after the refocussing pulse. The 3-pulse sequence is show in (b). This stimulated echo sequence begins with two 90° pulses separated by time τ. A third 90° pulse follows at time T after the second pulse. The stimulated echo forms at time τ after this third pulse.

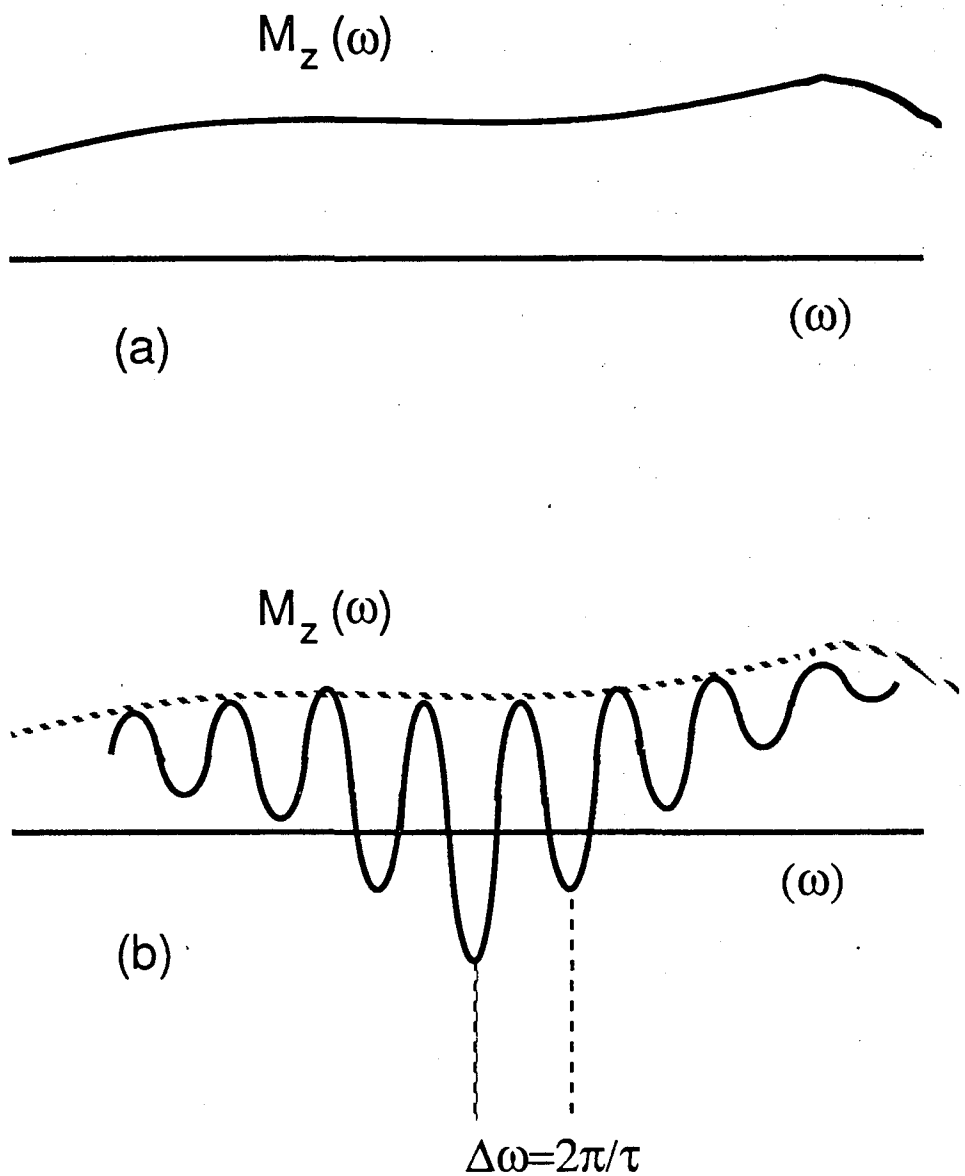

Figure I-10 Mechanism of 3-pulse stimulated echo. The initial equilibrium magnetization as a function of frequency is shown in (a). Modulation is induced in $\vec{M}_z$ by the first and second 90° pulses as shown in (b). The FID of this modulated envelope forms the stimulated echo.

small superhyperfine couplings to nearby paramagnetic nuclei through the technique of Electron Spin Echo Envelope Modulation (ESEEM).

Figure I-11 shows the energy level of an electronic spin in a magnetic field, with further splitting due to interaction with a paramagnetic spin $1/2$ nucleus. The EPR transition results from electron spin flips, i.e. $\Delta m_s = \pm 1$ transitions. Simultaneous nuclear flips are forbidden in the absence of electron-nuclear interaction. Therefore only the solid-line $\Delta m_i = 0$ transitions connect the upper and lower manifolds. This situation differs when anisotropic hyperfine or electric quadrupolar interactions are present. In these cases the $\Delta m_i = \pm 1$ transitions, shown with dashed lines, may become partially allowed. The microwave pulses which cause the electronic transitions now also induce coherences within the nuclear sublevels. As the interpulse time in a spin echo experiment is varied, these induced coherences produce interference effects with characteristic frequencies representing the intervals in the nuclear sublevels. Fourier analysis of the resultant echo "envelope" explicitly reveals these sublevel frequencies. A detailed analysis of this electron spin echo envelope modulation is the subject of Chapter II.

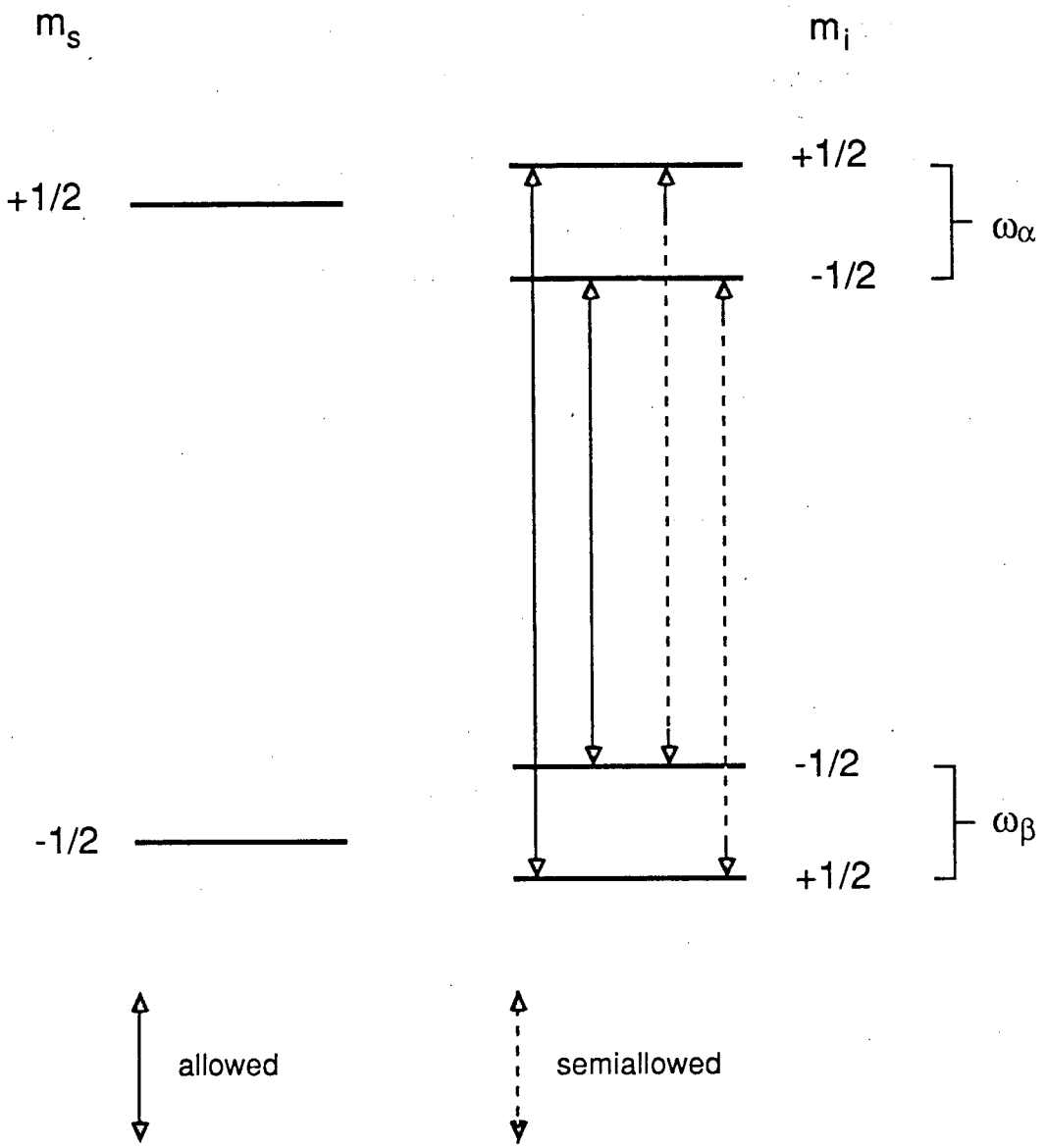

Figure I-11 Level splitting for $S = 1/2, I = 1/2$ electron-nuclear system. The left side shows the Zeeman splitting of the electronic levels. Interaction with the $I = 1/2$ nucleus is shown on the right, with each electronic level split into two sublevels. In the limit of zero electron-nuclear interaction, only the solid-line $\Delta m_i = 0$ transitions are allowed. However non-zero hyperfine and quadrupole couplings may induce simultaneous transitions $\Delta m_i = \pm 1$, as shown in dashed lines. The resulting sublevel coherences give rise to electron spin echo envelope modulation.

Chapter II – Electron Spin Echo Envelope Modulation

In this chapter we describe in more detail the processes of electron spin echo spectroscopy, focussing primarily on the mechanism of Electron Spin Echo Envelope Modulation (ESEEM). The general methods for describing the envelope modulation were presented by Mims (1972a,b). The more specific description in Sections 1 and 2 largely follow a review article by Mims (1972c). Kevan (1979) offers another review of the processes of ESEEM. Less mathematical presentations are offered by Mims and Peisach (1979, 1981) with an emphasis on biological applications.

Section 1 – Density Matrices and Spin Echo Formation

The ESEEM results are derived with the density matrix formalism to account for statistical mixtures of quantum mechanically "pure" states. The short density matrix review presented below can be supplemented by any quantum mechanics text. For a "pure" state we can write the state vector at time t as

$$|\psi(t)\rangle = \sum_n c_n(t)|u_n\rangle, \qquad (II-1)$$

where $\{|u_n\rangle\}$ is an orthonormal basis set. The coefficients $c_n(t)$ meet the normalization condition

$$\sum_n |c_n(t)|^2 = 1. \qquad (II-2)$$

We introduce the density operator $\rho(t)$ as

$$\rho(t) = |\psi(t)\rangle\langle\psi(t)| \qquad (II-3)$$

with matrix elements

$$\rho_{pn}(t) = \langle u_p|\rho(t)|u_n\rangle = c_n^*(t)c_p(t). \qquad (II-4)$$

The coefficient normalization condition $(II-2)$ can be rewritten

$$\sum_n |c_n(t)|^2 = \sum_n \rho_{nn}(t) = Tr\ \rho(t) = 1. \qquad (II-5)$$

The expectation value $\langle A\rangle(t)$ of an observable A can be found from

$$\langle A\rangle(t) = Tr\{\rho(t)A\}. \qquad (II-6)$$

From the Schrödinger equation we can derive an expression for the time evolution of the density operator:

$$\frac{d}{dt}\rho(t) = \frac{1}{i\hbar}\left[\mathcal{H}(t), \rho(t)\right], \qquad (II-7)$$

where $\mathcal{H}(t)$ is the system Hamiltonian.

We can generalize the density operator to a situation with a statistical mixture of states. We can describe the statistical system by a set of uncorrelated states $\{|\psi_i\rangle\}$ with a corresponding set of probabilities $\{p_i\}$. We now define a new density operator ρ which is the average of the set of pure state density operators $\{\rho_i\}$; that is

$$\rho = \sum_i p_i \rho_i. \qquad (II-8)$$

Since the sum of the statistical probabilities $\{p_i\}$ is unity, it is easy to generalize the conservation of probability equation $(II-5)$ to the ensemble average situation to give

$$Tr\ \rho(t) = 1. \qquad (II-9)$$

In a like fashion, we can show that equation $(II-6)$ for finding expectation values and equation $(II-7)$ for the time evolution of the density operator can be generalized to the statistical case.

We start off our treatment of ESEEM by using the density matrix formalism to follow the formation of an electron spin echo in an isolated electronic system with inhomogeneous broadening. The ESEEM effects will be added in Section 2. This treatment of the simple spin echo follows that of Mims (1972c). We will use the familiar Pauli matrices to represent the $S = 1/2$ basis set, where $\vec{S} = 1/2\ \vec{\sigma}$, and

$$\sigma_x = \begin{pmatrix} 0 & 1 \\ 1 & 0 \end{pmatrix} \qquad \sigma_y = \begin{pmatrix} 0 & -i \\ i & 0 \end{pmatrix} \qquad \sigma_z = \begin{pmatrix} 1 & 0 \\ 0 & -1 \end{pmatrix}. \qquad (II-10)$$

The electronic Zeeman Hamiltonian polarizes the spin system, so we can write the initial equilibrium density matrix:

$$\rho_0 = Z^{-1} \begin{pmatrix} e^{-\frac{1}{2}g\beta H/kT} & 0 \\ 0 & e^{\frac{1}{2}g\beta H/kT} \end{pmatrix}, \qquad (II-11)$$

where the partition function Z is given by

$$Z = e^{\frac{1}{2}g\beta H/kT} + e^{-\frac{1}{2}g\beta H/kT}. \qquad (II-12)$$

The initial density matrix can be rewritten in terms of the Pauli matrices:

$$\rho_0 = \alpha\sigma_z, \qquad (II-13)$$

with

$$\alpha = -tanh\left(\frac{1}{2}g\beta H/kT\right), \qquad (II-14)$$

and where we have discarded the term of the density matrix which represents the unpolarized fraction of the spins.

We introduce inhomogeneous broadening by writing the laboratory frame Hamiltonian for an individual spin packet j as

$$\mathcal{H}_L = \mathcal{H}_0 + \Delta\mathcal{H}_j, \qquad (II-15)$$

where the $\Delta\mathcal{H}_j$ term represents the component responsible for the time-independent frequency shift of the spin packet. A packet in the center of the line has $\Delta\mathcal{H}_j = 0$ and precesses at an angular velocity ω_0 which is equal to the angular frequency of the applied microwave magnetic field. We can transfer into the "interaction picture" Hamiltonian associated with the rotating frame by simply dropping the $\mathcal{H}_0$ term. If the rotating frame y-axis is defined by the direction of the microwave magnetic field component H_1 (see Figure I-4), we can write the rotating frame Hamiltonian for a spin packet as

$$\mathcal{H}_R = \Delta\mathcal{H}_j + \frac{1}{2}g\beta H_1\sigma_y. \qquad (II-16)$$

This Hamiltonian can be simplified further if we assume the magnitude of H_1 is much greater than the total width of the inhomogeneous line, for then during a pulse we can approximate

$$\mathcal{H}_{Pulse} = \Delta\mathcal{H}_j + \frac{1}{2}g\beta H_1\sigma_y \approx \frac{1}{2}g\beta H_1\sigma_y. \qquad (II-17)$$

During free precession time we can reduce (II-16) to

$$\mathcal{H}_{Free} = \Delta\mathcal{H}_j. \qquad (II-18)$$

Over a period in which the Hamiltonian of a system is constant, we can simply integrate equation (II-7) to give

$$\rho(t+t_1) = R\ \rho(t_1)\ R^{-1}, \qquad R = exp(-i\mathcal{H}t/\hbar), \qquad (II-19)$$

where R is a generalized rotation operator. We can write such a rotation operator R for the 90° pulse:

$$R_{\pi/2} = exp\left(-i\frac{1}{2}\sigma_y(\pi/2)\right) = exp\left(-i\sigma_y(\pi/4)\right) = (1/\sqrt{2})(I - i\sigma_y), \quad (II-20)$$

where we have employed the Pauli matrix identity $exp(i\sigma_y\theta) = Icos\theta + i\sigma_y sin\theta$. Similarly, the rotation operator for the 180° pulse is written

$$R_\pi = exp\left(-i\frac{1}{2}\sigma_y(\pi)\right) = exp(-i\sigma_y(\pi/2)) = -i\sigma_y. \quad (II-21)$$

The free precession time τ introduces phase factors due to the inhomogeneous broadening. If ω_j is the precession frequency of the jth spin packet in the rotating frame, and we define $\omega_j = \lambda_+ - \lambda_-$ for the packet, we can write

$$R_\tau = \begin{pmatrix} e^{-i\lambda_+\tau} & 0 \\ 0 & e^{-i\lambda_-\tau} \end{pmatrix}. \quad (II-22)$$

With each of the evolution operators specified, we can now show how the density matrix is transformed in each stage. The operator $R_{\pi/2}$ changes the initial density matrix ρ_0 as

$$\rho_{\pi/2} = R_{\pi/2}\,\rho_0\,R_{\pi/2}^{-1} = \frac{\alpha}{2}\begin{pmatrix} 1 & -1 \\ 1 & 1 \end{pmatrix}\begin{pmatrix} 1 & 0 \\ 0 & -1 \end{pmatrix}\begin{pmatrix} 1 & -1 \\ 1 & 1 \end{pmatrix}^{-1} = \alpha\sigma_x. \quad (II-23)$$

This is simply the mathematical statement that the 90° pulse has flipped the magnetization to along the x-axis. In a similar fashion, The density matrix after free precession for time τ is

$$\rho_\tau = R_\tau\,\rho_{\pi/2}\,R_\tau^{-1} = \alpha\begin{pmatrix} 0 & e^{-i(\lambda_+-\lambda_-)\tau} \\ e^{i(\lambda_+-\lambda_-)\tau} & 0 \end{pmatrix}, \quad (II-24)$$

explicitly showing the precession in the xy-plane of an arbitrary spin packet. The 180° pulse effectively interchanges the off-diagonal elements

$$\rho_\pi = R_\pi\,\rho_\tau\,R_\pi^{-1} = \alpha\begin{pmatrix} 0 & e^{i(\lambda_+-\lambda_-)\tau} \\ e^{-i(\lambda_+-\lambda_-)\tau} & 0 \end{pmatrix}. \quad (II-25)$$

The final operator allows free precession for a time $\tau + t$. The resulting density matrix is given by

$$\rho_{\tau+t} = R_{\tau+t}\ \rho_{\pi}\ R_{\tau+t}^{-1} = \alpha \begin{pmatrix} 0 & e^{-i(\lambda_+ - \lambda_-)t} \\ e^{i(\lambda_+ - \lambda_-)t} & 0 \end{pmatrix}. \qquad (II-26)$$

We see that the previous phase factors have "echoed out", and that at time $t = 0$ we have complete rephasing with full coherence in the xy-plane.

The observable of interest is the xy-plane magnetization $M_+ = 1/2(M_x + iM_y)$. The expectation value is given by the application of equation II-6:

$$\langle M^+ \rangle(\tau + t) = Tr\{\rho(\tau + t)M^+\} = M_0 Tr\left\{\rho(\tau + t)(\sigma_x + i\sigma_y)\right\}. \qquad (II-27)$$

Evaluation of the trace and summation over the spin packets gives

$$M(\tau + t) = -\sum_j M_{0,j} exp(i\omega_j t), \qquad (II-28)$$

which is simply the expression for the back-to-back free induction decays which form the spin echo.

Section 2 – ESEEM for I=1/2 Nuclei

We now add the ESEEM effects by introducing interactions with paramagnetic nuclei. The general formalism is due to Mims (1972a,b). We begin with the simplest case of an $I = 1/2$ nucleus coupled to the $S = 1/2$ electron. The description in this section is slightly less general than the most formal presentation referenced above, and more closely follows the Mims review (1972c). The more general formalism will be utilized in Section 4.

For the $S = 1/2, I = 1/2$ system, we can generally write

$$\mathcal{H}_T = \mathcal{H}_e + \Delta\mathcal{H}_j + \mathcal{H}_i + \mathcal{H}_{ei}, \qquad (II-29)$$

where $\mathcal{H}_T$ is the complete system Hamiltonian; with components $\mathcal{H}_e$, the electronic Zeeman term; $\Delta\mathcal{H}_j$, the inhomogeneous broadening term; $\mathcal{H}_i$, the nuclear Zeeman term; and $\mathcal{H}_{ei}$, the electron-nuclear hyperfine coupling term. The eigenvalues for $\mathcal{H}_T$ are shown in Figure II-1. The eigenstates $|a\rangle$ and $|b\rangle$ are the two substates corresponding to $m_s = 1/2$, with frequency difference ω_{ab}. Likewise, substates $|c\rangle$ and $|d\rangle$ correspond to $m_s = -1/2$, with a frequency difference ω_{cd}. Mims allows for two transition probabilities connecting substates. In the limit of zero hyperfine coupling, the transitions v are allowed $\Delta m_i = 0$ transitions, and the transitions u are un-allowed $\Delta m_i = \pm 1$ transitions. The hyperfine coupling may mix the substates, allowing for a non-zero branching ratio between the substates. We will later calculate explicitly the branching ratios. First, we generalize the matrix operators from the previous section to include the sublevels.

The branching ratios between sublevels during pulses can be accounted for by introducing a unitary 2×2 submatrix

$$U = \begin{pmatrix} v & u \\ -u^* & v* \end{pmatrix}. \qquad (II-30)$$

This 2×2 matrix U is the $I = 1/2$ specific version of the general unitary M-matrices introduced by Mims (1972a,b) to account for state mixing. We include the 2×2 submatrix U in forming our rotation operators. For example, we may generalize our previous expression $(II-21)$ for R_π as

$$R_\pi = \begin{pmatrix} 0 & U \\ -U^\dagger & 0 \end{pmatrix} = \begin{array}{c} \\ |a\rangle \\ |b\rangle \\ |c\rangle \\ |d\rangle \end{array} \begin{array}{c} \begin{array}{cccc} |a\rangle & |b\rangle & |c\rangle & |d\rangle \end{array} \\ \begin{pmatrix} 0 & 0 & v & u \\ 0 & 0 & -u^* & v^* \\ -v^* & u & 0 & 0 \\ -u^* & -v & 0 & 0 \end{pmatrix} \end{array}. \qquad (II-31)$$

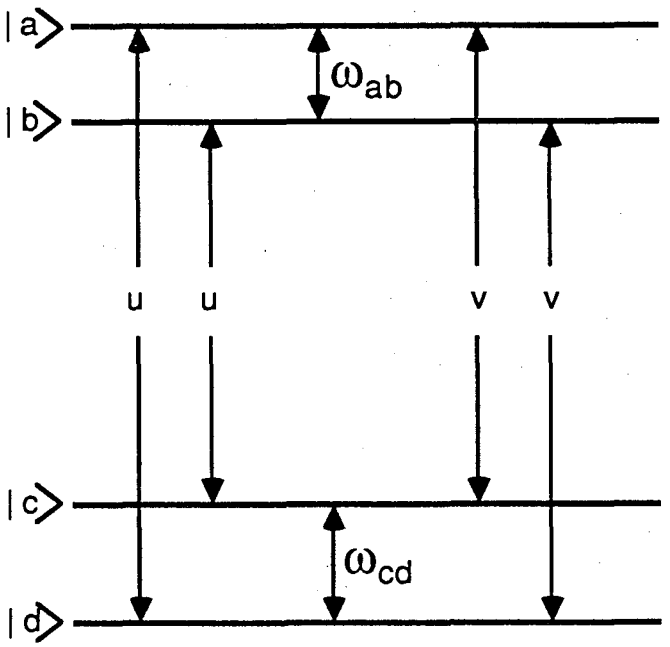

Figure II-1 Level scheme for calculating ESEEM parameters. The eigenstates $|a\rangle$ and $|b\rangle$ are the two substates corresponding to $m_s = 1/2$, with frequency difference ω_{ab}. Likewise, substates $|c\rangle$ and $|d\rangle$ correspond to $m_s = -1/2$, with a frequency difference ω_{cd}. Two separate transition probabilities u and v are used to calculate the branching ratios during electronic transitions.

We can see by inspection that this provides the correct 4×4 unitary matrix. The diagonal elements are zero, as are terms connecting $|a\rangle$ to $|b\rangle$ and $|c\rangle$ to $|d\rangle$, meaning that transitions occur fully between the two different m_s manifolds. The placement and composition of the U matrices gives the transition ratios shown in Figure II-1. In a similar fashion we can write the 90° pulse operator

$$R_{\pi/2} = 1/\sqrt{2} \begin{pmatrix} I & U \\ -U^\dagger & I \end{pmatrix}, \qquad (II-32)$$

where I is the 2×2 identity matrix. We also need the operator $M_+ = \frac{1}{2} g\beta(\sigma_x + i\sigma_y)$, which can be written

$$M_+ = g\beta \begin{pmatrix} 0 & U \\ 0 & 0 \end{pmatrix}. \qquad (II-33)$$

In the assumed limit where the electron Zeeman interaction dominates the total Hamiltonian, i.e. $\mathcal{H}_T \approx \mathcal{H}_e$, we can rewrite the initial density matrix

$$\rho_0 = \alpha \begin{pmatrix} I & 0 \\ 0 & -I \end{pmatrix}. \qquad (II-34)$$

Finally we need the matrix operator for the free precession times. We still have the $\lambda_\pm$ frequencies from the inhomogeneous broadening term $\Delta\mathcal{H}_j$. In addition we have the sublevel splitting frequencies. If λ_i is the frequency difference introduced to the state $|i\rangle$ by the nuclear Zeeman and hyperfine terms, we can write

$$R_\tau = \begin{pmatrix} P & 0 \\ 0 & Q \end{pmatrix}, \qquad (II-35)$$

where we define the 2×2 matrices P and Q as

$$P = \begin{pmatrix} e^{-\lambda_a \tau} & 0 \\ 0 & e^{-\lambda_b \tau} \end{pmatrix} e^{-\lambda_+ \tau} \qquad Q = \begin{pmatrix} e^{-\lambda_c \tau} & 0 \\ 0 & e^{-\lambda_d \tau} \end{pmatrix} e^{-\lambda_- \tau}. \quad (II-36)$$

With these matrix representations we can calculate the evolution of the density matrix as before. At time $\tau + t$ after the 180° refocussing pulse we can write

$$\rho(\tau + t) = R_{\tau+t} R_\pi R_\tau R_{\pi/2}\ \rho_0\ R_{\pi/2}^{-1} R_\tau^{-1} R_\pi^{-1} R_{\tau+t}^{-1}. \qquad (II-37)$$

We use the density matrix to calculate $\langle M_+ \rangle$ as in equation II-27. If the inhomogeneous linewidth is large compared to the superhyperfine splittings, we can factor the results into two terms. The first term gives the echo shape from the large inhomogeneous broadening and is again given by equation II-28. The second term results from

the discrete superhyperfine coupling and depends on the frequencies ω_{ab}, ω_{cd}, and the interpulse time τ. The resulting factorization gives

$$M(\tau + t) = \left[-\sum_j M_{0,j} exp(i\omega_j t) \right] \times E_{mod}(\tau). \qquad (II-38)$$

The modulation term E_{mod} can be evaluated in terms of the submatrices as

$$E_{mod}(\tau) = 1/4\ Tr(QU^\dagger PUQ^\dagger U^\dagger P^\dagger U). \qquad (II-39)$$

This expression was evaluated by Mims (1972a) with results

$$E_{mod}(\tau) = |v|^4 + |u|^4 + |v|^2|u|^2 \Big[2cos(\omega_{ab}\tau) + 2cos(\omega_{cd}\tau) - cos(\omega_{ab} - \omega_{cd})\tau - cos(\omega_{ab} + \omega_{cd})\tau \Big]. \qquad (II-40)$$

We see explicitly the modulation of the echo by the superhyperfine frequencies, as well as by their sums and differences.

To calculate the amplitude of the modulation we must find the values of u and v. This requires us to be more explicit with the elements of the Hamiltonian given by equation II-29. We assume that the electronic Zeeman is the dominant component. Thus there is no mixing of $m_s = 1/2$ and $m_s = -1/2$ in the eigenstates $|a\rangle$, $|b\rangle$, $|c\rangle$, and $|d\rangle$. Each of the eigenstates represents a single projection of the electronic spin with a superposition of the two nuclear spin projections. For example, we can write

$$|a\rangle = c_1|+,+\rangle + c_2|+,-\rangle, \qquad (II-41)$$

where the notation is abbreviated so that $|+,-\rangle$ denotes the state with $m_s = 1/2$ and $m_i = -1/2$. The other effect of considering the electronic Zeeman dominant limit is that we can discard terms of the hyperfine coupling tensor not involving S_z. We can also form a rotation about the nuclear z-axis so as to eliminate the $S_z I_y$ term. We are left with the simple sublevel Hamiltonian

$$\mathcal{H}_T/\hbar = \omega_S S_z + \omega_I I_z + A S_z I_z + B S_z I_x, \qquad (II-42)$$

with electron Zeeman, nuclear Zeeman, and two hyperfine terms. The BS_zI_x term mixes nuclear spin states in forming the eigenstates $|a\rangle$, $|b\rangle$, $|c\rangle$, and $|d\rangle$ of the total Hamiltonian $\mathcal{H}_T$. The Hamiltonian for the two $m_s = 1/2$ sublevels becomes

$$\frac{1}{\hbar}\mathcal{H}_{(m_s=1/2)} = \omega_I I_z + \frac{1}{2} A I_z + \frac{1}{2} B I_x, \qquad (II-43)$$

and can be diagonalized by a rotation operator $e^{-iI_y\eta}$, where $\eta = tan^{-1}(B/(A + 2\omega_I))$. We can write the eigenstates as

$$\begin{aligned} |a\rangle &= cos(\eta/2)|+,+\rangle + sin(\eta/2)|+,-\rangle \\ |b\rangle &= -sin(\eta/2)|+,+\rangle + cos(\eta/2)|+,-\rangle \end{aligned} \qquad (II-44)$$

The frequency difference ω_{ab} is given by

$$\omega_{ab} = \left\{(B/2)^2 + [(A/2) + \omega_I]^2\right\}^{1/2}. \qquad (II-45)$$

A similar rotation by ς about the nuclear y-axis diagonalizes

$$\frac{1}{\hbar}\mathcal{H}_{(m_s=-1/2)} = \omega_I I_z - \frac{1}{2}AI_z - \frac{1}{2}BI_x, \qquad (II-46)$$

where $\varsigma = tan^{-1}(B/(A - 2\omega_I))$. This results in

$$\begin{aligned} |c\rangle &= cos(\varsigma/2)|-,+\rangle + sin(\varsigma/2)|+,-\rangle \\ |d\rangle &= -sin(\varsigma/2)|-,+\rangle + cos(\varsigma/2)|+,-\rangle \end{aligned} \qquad (II-47)$$

with

$$\omega_{cd} = \left\{(B/2)^2 + [(A/2) - \omega_I]^2\right\}^{1/2}. \qquad (II-48)$$

The values of u and v can now be obtained by operating on these explicit eigenvectors with the electronic 180° rotation operator $-i\sigma_y$ and comparing the results with equation II-31. This gives values

$$u = sin\left[(\eta - \varsigma)/2\right], \qquad v = cos\left[(\eta - \varsigma)/2\right]. \qquad (II-49)$$

We can now place known amplitudes into equation II-40, giving

$$\begin{aligned} E_{mod}(\tau) = 1 - \frac{k}{2} + \frac{k}{4}\Big[&2cos(\omega_{ab}\tau) + 2cos(\omega_{cd}\tau) \\ &- cos(\omega_{ab} - \omega_{cd})\tau - cos(\omega_{ab} + \omega_{cd})\tau\Big], \end{aligned} \qquad (II-50)$$

or the more compact equivalent expression

$$E_{mod}(\tau) = 1 - 2k\ sin^2\left(\frac{\omega_{ab}\tau}{2}\right) sin^2\left(\frac{\omega_{cd}\tau}{2}\right). \qquad (II-51)$$

The modulation depth parameter k is given by

$$k = \left(\frac{\omega_I B}{\omega_{ab}\omega_{cd}}\right)^2. \qquad (II-52)$$

We can evaluate the expression for the depth parameter k in several limits. The I_x component of the hyperfine coupling, B, must be non-negligable to induce the necessary branching. The modulation depth falls off as ω_I^2 in the low field limit where $\omega_I \ll A, B$. In the opposite limit of $\omega_I \gg A, B$; k is proportional to $(1/\omega_I)^2$. Maximum modulation is achieved when the nuclear Zeeman frequency is on the order of the hyperfine frequency.

If we assume the hyperfine coupling arises from a contact component, a, and a classical magnetic dipole-dipole coupling component, we can further specify our parameters

$$\begin{aligned} A &= a + \frac{g g_n \beta \beta_n}{\hbar r^3}(3cos^2\theta - 1) \\ B &= \frac{g g_n \beta \beta_n}{\hbar r^3}(3cos\theta\ sin\theta). \end{aligned} \qquad (II-53)$$

These assumptions are often valid for proton couplings.

We often have more than one nucleus interacting with an electron site. Mims (1972a) has shown that the modulations are multiplicative, that is

$$E_{mod\ N} = \prod_i^N E_{mod\ i}. \qquad (II-54)$$

We can follow the same procedure used to derive the 2-pulse ESEEM pattern to calculate the modulation in the 3-pulse stimulated echo experiment. The density matrix at time $t + \tau$ after the third pulse is

$$\rho(\tau + t) = R_{\tau+t} R_{\pi/2} R_T R_{\pi/2} R_\tau R_{\pi/2}\ \rho_0\ R_{\pi/2}^{-1} R_\tau^{-1} R_{\pi/2}^{-1} R_T^{-1} R_{\pi/2}^{-1} R_{\tau+t}^{-1}. \quad (II-55)$$

The resulting modulation is given by

$$\begin{aligned} E_{mod}(\tau, T) = 1 - \frac{1}{2}k\Big\{ & sin^2\frac{1}{2}\omega_{ab}\tau\Big[1 - cos\omega_{cd}(\tau + T)\Big] \\ & + sin^2\frac{1}{2}\omega_{cd}\tau\Big[1 - cos\omega_{ab}(\tau + T)\Big]\Big\}. \end{aligned} \qquad (II-56)$$

The depth modulation parameter k is the same as in the 2-pulse case. Of significant note is the elimination of sum and difference terms in the envelope modulation. If Fourier analysis is performed with $\tau + T$ as the time variable, only the principal superhyperfine frequencies result. This is very useful for simplifying the ESEEM patterns in complex situations. The resolution is also often superior in 3-pulse studies because the envelope duration is not limited by the often short phase memory of the

system. An additional important aspect of the 3-pulse ESEEM is the suppression effect observed when τ is set to a multiple of $2\pi/\omega_{ab}$ or $2\pi/\omega_{cd}$. The modulation from one interval can be eliminated by setting τ to the period multiple of the other interval.

Section 3 – ESEEM for I=1 Nuclei with Small Quadrupole Coupling

For nuclei with nuclear spin $I \geq 1$, we must include the electric quadrupolar effects in ESEEM calculations. For biological studies, we will typically study ^{2}H and ^{14}N nuclei. The quadrupole couplings for ^{2}H are typically small, in fact reasonable results may sometimes be obtained by neglecting the quadrupolar effects entirely. The situation is entirely different for the ^{14}N nucleus. Quadrupolar couplings for ^{14}N are typically on the order of a few MHz.

Mims calculated the ESEEM observed for $I = 1$ nuclei in the limit of vanishing quadrupole coupling (1972a). These expressions are useful for applications to deuteron modulation, though generally inadequate for ^{14}N studies. In this case the unitary submatrix M becomes a 3×3 matrix. If ω_α and ω_β are the splittings in the upper and lower manifolds in the absence of quadrupole effects and Δ represents a small quadrupole correction, we can write the four transition frequencies as $\omega_{ab} = \omega_\alpha + \Delta$, $\omega_{bc} = \omega_\alpha - \Delta$, $\omega_{de} = \omega_\beta + \Delta$, and $\omega_{ef} = \omega_\beta - \Delta$. If the quadrupolar contribution to the M-matrix can be neglected, a closed form solution can be obtained. This is a limiting assumption, but since experimental frequencies can be obtained more accurately than amplitudes in this type of experiment, this approximation is valid in many cases. The expression for the 2-pulse modulation takes on awesome proportions:

$$
\begin{aligned}
&E_{mod}(\tau) = \\
&\left(1 - \frac{4}{3}k + \frac{3}{4}k^2\right) + \left(\frac{2}{3}k - \frac{1}{2}k^2\right)\left(cos\omega_{ab}\tau + cos\omega_{bc}\tau + cos\omega_{de}\tau + cos\omega_{ef}\tau\right) \\
&- \left[\frac{1}{6}k - \frac{1}{6}k^2 + \frac{1}{6}(1-k^2)^{1/2}\right]\Big[cos(\omega_{ab}+\omega_{de})\tau + cos(\omega_{ab}-\omega_{de})\tau \\
&\qquad + cos(\omega_{bc}+\omega_{ef})\tau + cos(\omega_{bc}-\omega_{ef})\tau\Big] \\
&- \left[\frac{1}{6}k - \frac{1}{6}k^2 + \frac{1}{6}(1-k^2)^{1/2}\right]\Big[cos(\omega_{bc}+\omega_{de})\tau + cos(\omega_{bc}-\omega_{de})\tau \\
&\qquad + cos(\omega_{ab}+\omega_{ef})\tau + cos(\omega_{ab}-\omega_{ef})\tau\Big] \\
&+ \frac{1}{4}k^2(cos\omega_{ac}\tau + cos\omega_{df}\tau) - \frac{1}{24}k^2\Big[(cos(\omega_{ac}+\omega_{df})\tau + cos(\omega_{ac}-\omega_{df})\tau\Big] \\
&- \frac{1}{12}k^2\Big[(cos(\omega_{de}+\omega_{ac})\tau + cos(\omega_{de}-\omega_{ac})\tau \\
&\qquad + (cos(\omega_{df}+\omega_{ab})\tau + cos(\omega_{df}-\omega_{ab})\tau \\
&+ (cos(\omega_{df}+\omega_{bc})\tau + cos(\omega_{df}-\omega_{bc})\tau \\
&\qquad + (cos(\omega_{ef}+\omega_{ac})\tau + cos(\omega_{ef}-\omega_{ac})\tau\Big].
\end{aligned}
\tag{II-57}
$$

An equation of similar complexity was also derived for the 3-pulse case.

This expression can be greatly reduced in the limit of zero quadrupole effects, where $\omega_{ab} = \omega_{bc} = \omega_\alpha$, and $\omega_{de} = \omega_{ef} = \omega_\beta$:

$$
E_{mod}(\tau) = 1 - \frac{16}{3}k\ sin^2\left(\frac{\omega_\alpha\tau}{2}\right)sin^2\left(\frac{\omega_\beta\tau}{2}\right) + \frac{16}{3}k^2 sin^4\left(\frac{\omega_\alpha\tau}{2}\right)sin^4\left(\frac{\omega_\beta\tau}{2}\right).
\tag{II-58}
$$

If the k^2 term can be ignored, this reduces to the same expression as for the $m_s = 1/2$ case, but with modulation greater by a factor of 8/3. Thus the ESEEM sensitivity is almost three times greater for a deuteron than for a proton.

Section 4 – ESEEM for I=1 Nuclei with Large Quadrupole Coupling

The ESEEM results of Section 3 are valid when the quadrupolar couplings are very small and add negligible contribution to the semi-forbidden $\Delta m_i \neq 0$ transitions. This is not a reasonable assumption in many situations, particularly for the ^{14}N nucleus. Quadrupolar couplings for ^{14}N are typically on the order of a few MHz. Since the Zeeman, hyperfine, and electric quadrupole effects may be energetically comparable, we cannot take a perturbation approach to calculating ESEEM frequencies and amplitudes.

The most general sublevel Hamiltonian will include both isotropic and anisotropic components of hyperfine coupling. However, if we assume that the isotropic component is dominant, the sublevel Hamiltonian is greatly simplified. In the high-field limit where electron states are not mixed by the hyperfine couplings, we can treat the isotropic hyperfine and the nuclear Zeeman as colinear, with two effective Zeeman field values given by

$$\nu_{ef} = |\nu_i \pm a/2| \,. \qquad (II-59)$$

The analysis of the ESEEM frequencies then becomes equivalent to the analysis of Nuclear Quadrupole Resonance (NQR) frequencies in the presence of an arbitrary magnetic field (Astashkin et al. 1984). This limit is often valid for ^{14}N ligands to transition metal centers.

We therefore begin by examining the energy levels which result for an $I = 1$ nucleus in a magnetic field. The Hamiltonian $\mathcal{H}$ for the system may be written as

$$\mathcal{H} = \mathcal{H}_Q + \mathcal{H}_M, \qquad (II-60)$$

with $\mathcal{H}_Q$ and $\mathcal{H}_M$ the magnetic dipole and electric quadrupole Hamiltonian terms. Two limiting cases have been extensively studied. If the Zeeman energy resulting from the applied field is much larger than the quadrupole splittings, $\mathcal{H}_Q$ can be treated as a perturbation on the eigenstates of $\mathcal{H}_M$. This case is analyzed in detail by Cohen and Reif (1957). This is the regime in which NMR studies of $I > 1/2$ nuclei are performed. The other extreme, with Zeeman effects small compared with zero-field quadrupolar splittings, can likewise be treated by perturbation theory, with $\mathcal{H}_M$ acting on the eigenstates of $\mathcal{H}_Q$. This is the subject of the review of Das and Hahn (1958), and is the regime where most NQR experiments are performed.

The intermediate field case is more difficult, because perturbation approaches are invalid. As previously described, this is the most common regime for ^{14}N ESEEM

studies. Quadrupolar frequencies for ^{14}N are typically in the range 0 to 5 MHz. The Zeeman splitting for X band experiments is on the order of 1 MHz. The isotropic hyperfine coupling for ESEEM-observable ^{14}N ranges up to about 10 MHz. We have taken the approach of numerically diagonalizing the sublevel Hamiltonian to calculate the ESEEM frequencies.

We start with the pure quadrupole interaction, with the quadrupole moment in a field gradient with principal values eq_{xx}, eq_{yy}, and eq_{zz}. The ordering of the principal axes is chosen such that

$$|q_{xx}| \leq |q_{yy}| \leq |q_{zz}|. \qquad (II-61)$$

For an $I = 1$ nucleus, the quadrupolar Hamiltonian $\mathcal{H}_Q$ may be written

$$\mathcal{H}_Q = K\left[3I_z^2 - I^2 + \eta(I_x^2 - I_y^2)\right], \qquad (II-62)$$

where

$$K = \frac{e^2qQ}{4h}, \qquad (II-63)$$

with Q is defined as the scalar quadrupole moment for the specific nucleus, $q = q_{zz}$, and the asymmetry parameter η defined by

$$\eta = \left|\frac{q_{xx} - q_{yy}}{q_{zz}}\right|. \qquad (II-64)$$

The eigenvalues corresponding to this zero-field Hamiltonian are $(1+\eta)K$, $(1-\eta)K$, and $-2K$ (Casabella and Bray, 1958). The corresponding NQR frequencies are

$$\begin{aligned} \nu_+ &= (3+\eta)K \\ \nu_- &= (3-\eta)K\,. \\ \nu_0 &= 2\eta K \end{aligned} \qquad (II-65)$$

We now add an external magnetic field with spherical angles θ and φ relative to the quadrupolar principal axes. We define the frequency ν_i resulting from this field with no quadrupolar contributions as

$$\nu_i = \frac{g_n\mu_n H}{h}, \qquad (II-66)$$

and generalize to include an isotropic hyperfine component by introducing $\nu_{ef} = |\nu_i \pm a/2|$ as in equation II-59. Two sets of eigenfrequencies corresponding to the upper and lower electronic manifolds will be obtained with the two different values

of ν_{ef}. The Hamiltonian for a single sublevel manifold can be written in matrix form (Casabella and Bray, 1958; Muha, 1980),

$$\mathcal{H} = \begin{pmatrix} K(1+\eta) & \nu_{ef}\sin\theta\cos\varphi & \nu_{ef}\cos\theta \\ \nu_{ef}\sin\theta\cos\varphi & -2K & -i\nu_{ef}\sin\theta\sin\varphi \\ \nu_{ef}\cos\theta & -i\nu_{ef}\sin\theta\sin\varphi & K(1-\eta) \end{pmatrix}. \qquad (II-67)$$

A trigonometric solution to the resulting secular equation has been provided by Muha (1980). A graphical solution may also be found (Astashkin et al., 1984; Flanagan and Singel, 1987), following an approach developed for analysis of EPR triplet spectra (Kottis and Lefebvre, 1963). The graphical solutions are useful for determining eigenfrequency ranges and obtaining information about the angular dependence of various transition frequencies. Our approach is to diagonalize the 3×3 Hermitian matrix numerically to obtain the three resultant eigenvalues. These eigenvalues can then be plotted as a function of effective field to show the general splitting of the quadrupolar energy states with an applied field. The effective field is expressed in frequency units so that calculations are applicable to any $I = 1$ nuclei. Figure II-2 shows the result of such a calculation over an effective field range of 0.0 to 8.0 MHz. This specific calculation was performed for e^2qQ =4.5 MHz, $\eta = 0.35$, $\theta = 30°$, and $\varphi = 60°$.

In general, we will be studying non-crystalline samples. It is therefore necessary to average the eigenfrequency results over the unit sphere in order to obtain the results for a uniform angle distribution of quadrupolar axes. We have therefore written a FORTRAN program which calculates the angle average of the three possible transitions between the three eigenlevels. The symmetry of the Hamiltonian requires both θ and φ to be incremented only between 0 and 90°. Both angles are stepped in 0.5° increments. The three eigenfrequencies obtained for each set of θ and φ are summed in a 1000 point frequency histogram. The summed values are weighted by $\sin\theta$ to average properly over the unit sphere.

Figure II-3 shows the powder pattern eigenfrequencies obtained when the electric quadrupole interaction is large compared to the magnetic interaction. The precise values used in this calculation are e^2qQ/h =4.5 MHz, $\eta = 0.35$, and $\nu_{ef} = 0.1$ MHz.

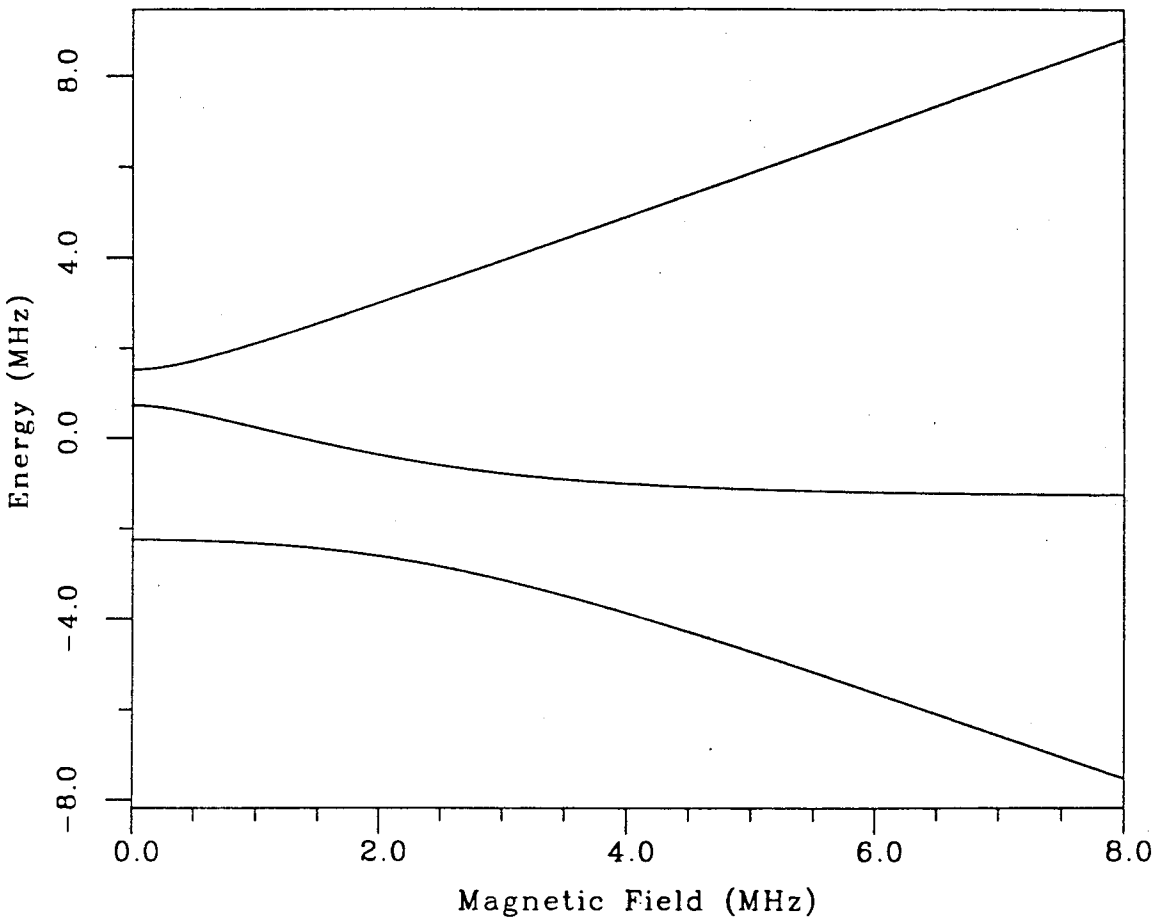

Figure II-2 Energy level splitting for $I = 1$ nucleus over a effective field range of 0 to 8.0 MHz, and e^2qQ =4.5 MHz, $\eta = 0.35$, $\theta = 30°$, $\varphi = 60°$

The three peaks are all sharp and well-defined, and they occur close to the zero-field quadrupolar frequencies. Perturbation theory treatment of this region is covered by Das and Hahn (1958). Figure II-4 shows the results in the opposite regime, with the magnetic interaction much greater than the quadrupolar interaction. The quadrupolar couplings which lead to this simulation are the same as in Figure II-3; e^2qQ/h =4.5 MHz and η =0.35. The value of ν_{ef} is increased to 25 MHz. This regime is also easily treated by perturbation theory (Cohen and Reif, 1957), with the pure Zeeman eigenstates $\{|+1\rangle, |0\rangle, |+1\rangle\}$ as the zeroth order basis. The broad powder pattern centered about 25 MHz results as the sum of the spherical averages of the two $\Delta m = 1$ transitions. This pattern is centered about effective field frequency ν_{ef} through first-order perturbation by the quadrupolar interaction. Small shifts in the pattern position may occur through second order in the quadrupolar perturbation. The turning points in the powder pattern occur at $\pm(1-\eta)3e^2qQ/8h$, $\pm(1+\eta)3e^2qQ/8h$, and $\pm 3e^2qQ/8h$ relative to ν_{ef}. The $\Delta m = 2$ transition at 50 MHz is quite sharp, because there are only second-order quadrupole effects for this single transition.

For an $I = 1$ nucleus there are six possible ESEEM frequencies. As previously described, in the limit of purely isotropic hyperfine coupling these frequencies will be determined by the quadrupolar parameters and the two effective field values, $\nu_{ef} = |\nu_i \pm a/2|$, with each of the two electronic manifolds contributing one of the effective field values and three eigenfrequencies. Unless the quadrupolar couplings are exceptionally small, ^{14}N ESEEM will not occur in the high-field limit, for the isotropic hyperfine couplings would necessarily be very large and the sublevel intervals will be too large to simultaneously excite with a microwave pulse. The quadrupolar dominated limit may be obtained in one of the electronic manifolds if $|\nu_i| \approx |a/2|$. However, the majority of our ESEEM experiments occur in the intermediate regime.

Figure II-5 shows the powder pattern results obtained by varying ν_{ef} while keeping the quadrupolar parameters fixed. The values of e^2qQ =4.5 MHz and η = 0.35 are identical to the previous examples. The value of ν_{ef} is incremented from 0.1 to 6.0 MHz. The most striking feature of these patterns is the rapid broadening of the two low-frequency transitions when the effective Zeeman interaction becomes non-negligible. Under these conditions only the single high-frequency transition is likely to be observed in an ESEEM experiment. This "double-quantum" transition corresponds to the $(m_s = -1) \leftrightarrow (m_s = +1)$ transition in the high field limit. The transition contains increasing NQR ν_+ character as the effective field is decreased.

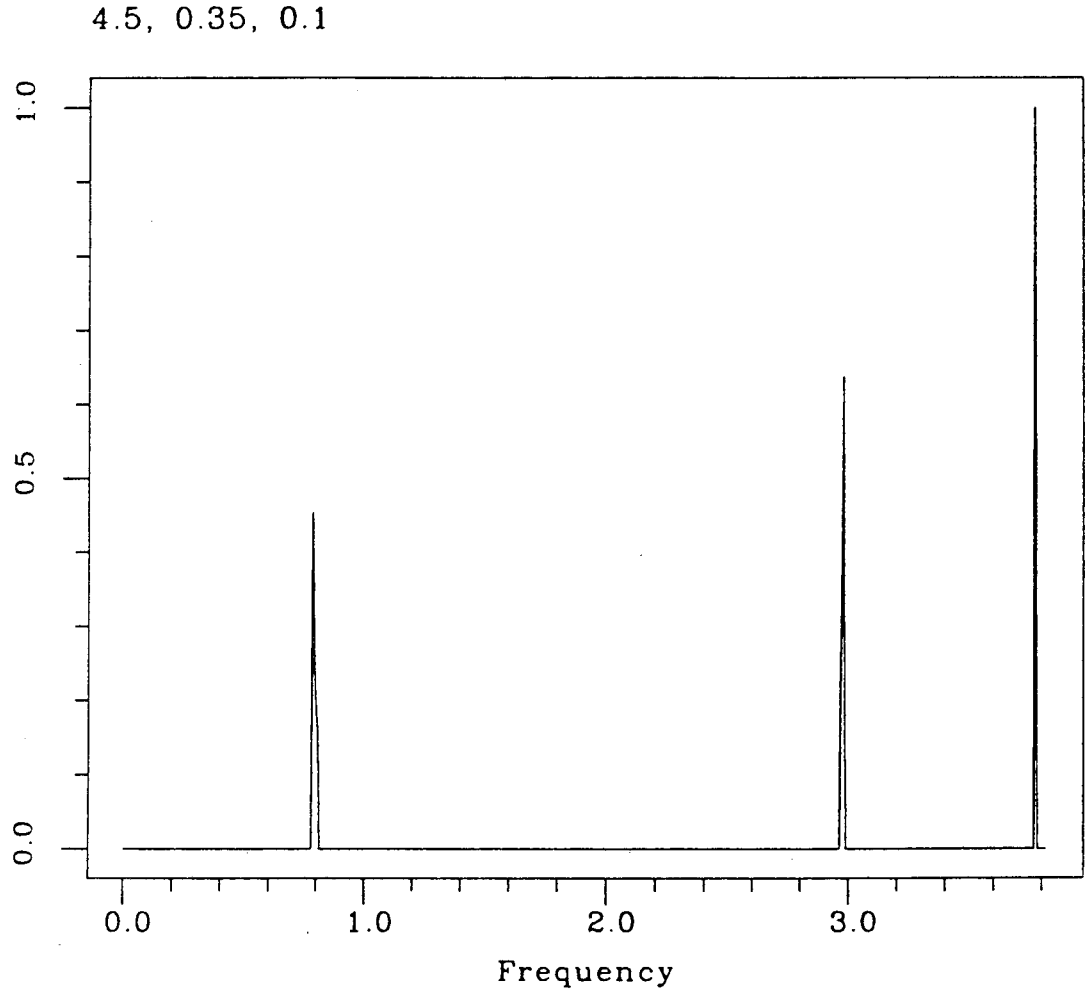

Figure II-3 Powder pattern near zero effective field with quadrupolar interactions dominating. Simulation parameters are e^2qQ =4.5 MHz, η = 0.35, and ν_{ef} = 0.1 MHz.

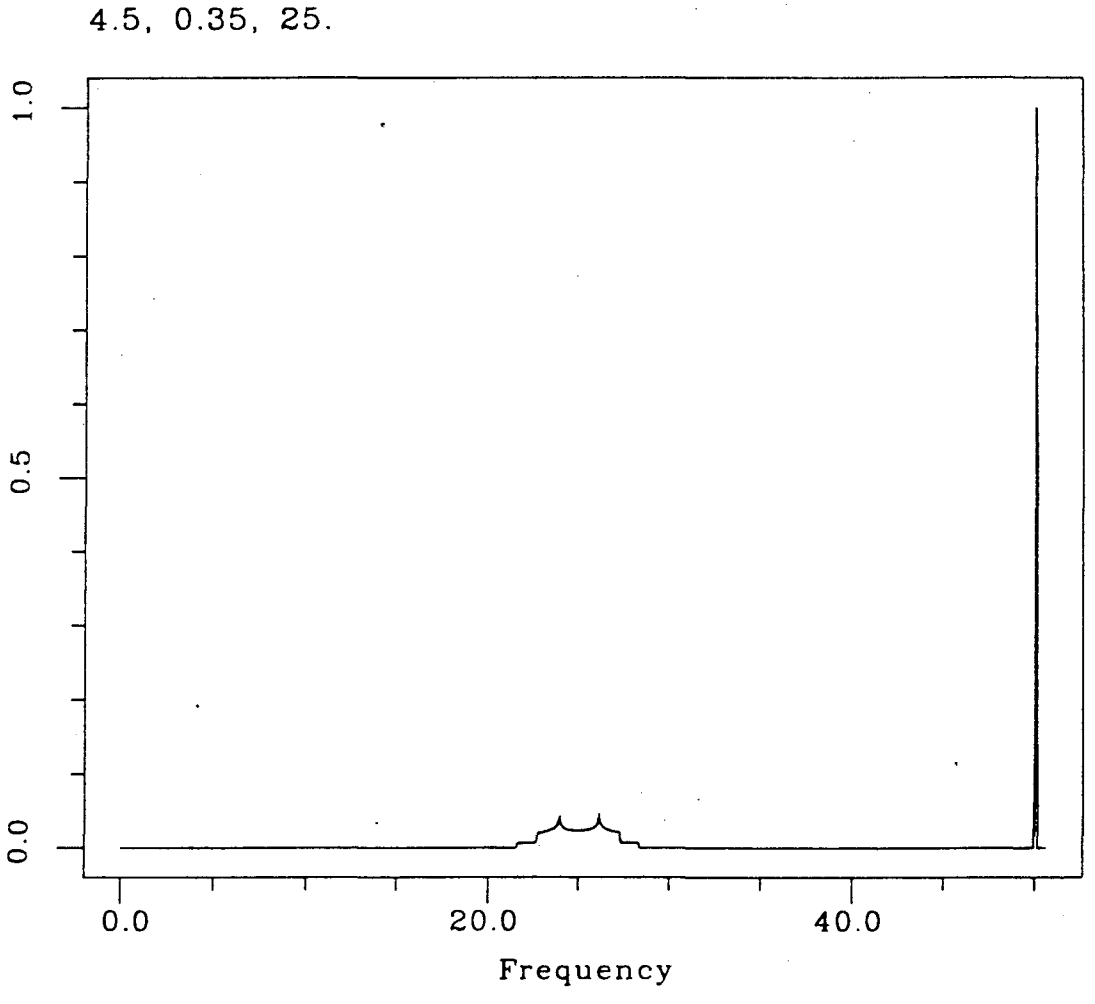

Figure II-4 Powder pattern in high field limit where the magnetic interaction is much larger than the electric quadrupolar interaction. Simulation parameters are e^2qQ =4.5 MHz, $\eta = 0.35$, and $\nu_{ef} = 25.0$ MHz.

Figure II-5 Effect of varying ν_{ef} on $I = 1$ eigenfrequency powder patterns. The quadrupolar parameters are e^2qQ =4.5 MHz and $\eta = 0.35$ for all simulations. The values of ν_{ef} are:

(a) 0.1 MHz
(b) 0.5 MHz
(c) 1.0 MHz
(d) 2.0 MHz
(e) 3.0 MHz
(f) 4.0 MHz
(g) 5.0 MHz
(h) 6.0 MHz

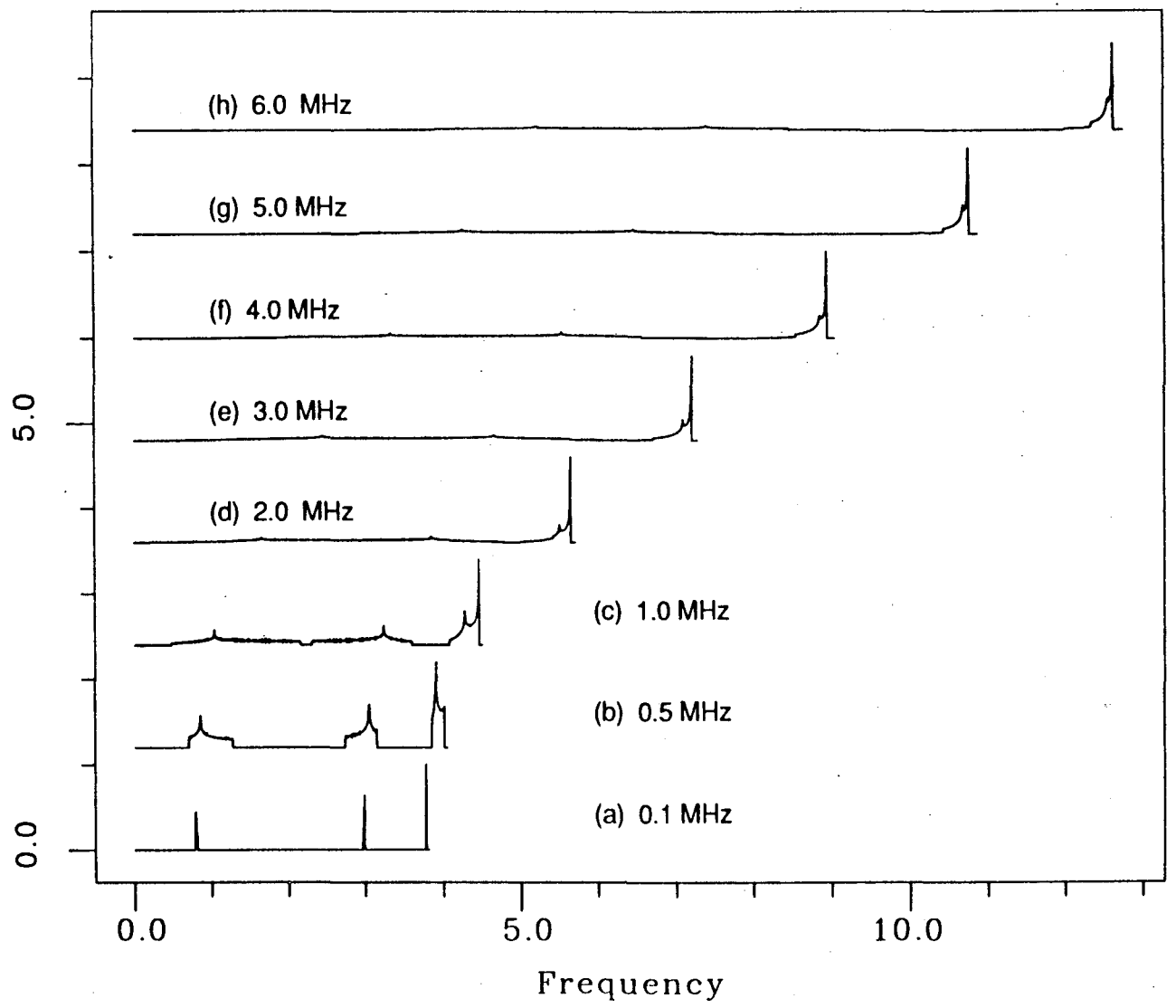
(h) 6.0 MHz
(g) 5.0 MHz
(f) 4.0 MHz
(e) 3.0 MHz
(d) 2.0 MHz
(c) 1.0 MHz
(b) 0.5 MHz
(a) 0.1 MHz
5.0
0.0
0.0
5.0
10.0
Frequency

So far in this section we have discussed only the eigenfrequencies that result from the coupled $I = 1$ nucleus. We now address the problem of calculating the amplitudes of the frequency components observed via ESEEM. We see from the complexity of equation II-57 that analytical solutions become exceedingly cumbersome for $I > 1/2$. We therefore will address the amplitude problem numerically. A straightforward procedure for numerical calculations was provided by Mims (1972a,b).

The first step is to calculate the 3×3 unitary M-matrix which describes the state mixing. We begin with the two sublevel Hamiltonians for the $m_s = +1/2$ and $m_s = -1/2$ manifolds. Following Mims, we denote these respectively as the α- and β-manifolds. The sublevel Hamiltonians $\mathcal{H}_\alpha$ and $\mathcal{H}_\beta$ can be diagonalized as described previously, revealing the two sets of eigenfrequencies $\{\omega_\alpha\}$ and $\{\omega_\beta\}$ as well as the associated eigenvectors. The three eigenvectors resulting from the diagonalization of $\mathcal{H}_\alpha$ form the columns of a 3×3 matrix, $M_\alpha^\dagger$. The matrix $M_\beta^\dagger$ is likewise assembled from the eigenvectors of $\mathcal{H}_\beta$. The matrix M describing the coupling between the two manifolds results as the product

$$M = M_\alpha^\dagger M_\beta. \qquad (II-68)$$

The amplitudes $\{\chi\}$ of the eigenfrequencies can be directly calculated from the M-matrix (Mims 1972b). For a 2-pulse experiment the modulation is given by

$$\begin{aligned} E_{mod}(\tau) = &\chi_0 + \sum_{i,j}^{i\neq j}{}' \chi_{ij}^{\alpha} cos\omega_{ij}^{\alpha}\tau + \sum_{k,n}^{k\neq n}{}' \chi_{kn}^{\beta} cos\omega_{kn}^{\beta}\tau \\ &+ \sum_{i,j}^{i\neq j}{}' \sum_{k,n}^{k\neq n}{}' \chi_{ij,kn}^{\alpha,\beta} \left[cos(\omega_{ij}^{\alpha} + \omega_{kn}^{\beta})\tau + [cos(\omega_{ij}^{\alpha} - \omega_{kn}^{\beta})\tau \right]. \end{aligned} \qquad (II-69)$$

The primed summations indicate that pairs of indices are included in only one order.

The amplitude of the zero-frequency component is denoted χ_0. The value of this dc term is given by

$$\chi_0 = \frac{1}{2I+1} \sum_{i,k} |M_{ik}|^4. \qquad (II-70)$$

The second and third terms give the amplitudes of the eigenfrequencies of the two manifolds, with

$$\chi_{ij}^{\alpha} = \frac{2}{2I+1} \sum_{k} |M_{ik}|^2 |M_{jk}|^2, \qquad (II-71)$$

$$\chi_{kn}^{\beta} = \frac{2}{2I+1} \sum_{i} |M_{ik}|^2 |M_{in}|^2. \qquad (II-72)$$

The amplitudes of the sum and difference frequencies enter in the final term, with

$$\chi_{ij,kn}^{\alpha,\beta} = \frac{2}{2I+1} Re\left[M_{ik}^* M_{in} M_{jn}^* M_{jk}\right]. \qquad (II-73)$$

The modulation amplitude for the 3-pulse ESEEM experiment is given by

$$\begin{aligned} E_{mod}(\tau,T) =& \chi_0 + \frac{1}{2}\sum_{i,j}^{i\neq j}{}' \chi_{ij}^{\alpha}\left[cos\omega_{ij}^{\alpha}\tau + \omega_{ij}^{\alpha}(T+\tau)\right] \\ &+ \frac{1}{2}\sum_{k,n}^{k\neq n}{}' \chi_{kn}^{\beta}\left[cos\omega_{kn}^{\beta}\tau + cos\omega_{kn}^{\beta}(T+\tau)\right] \\ &+ \sum_{i,j}^{i\neq j}{}' \sum_{k,n}^{k\neq n}{}' \chi_{ij,kn}^{\alpha,\beta}\Big[cos\omega_{ij}^{\alpha}(T+\tau)cos\omega_{kn}^{\beta}\tau \\ &\quad + cos\omega_{ij}^{\alpha}\tau\, cos\omega_{kn}^{\beta}(T+\tau)\Big]. \end{aligned} \qquad (II-74)$$

The coefficients $\{\chi\}$ are the same as in the 2-pulse case. In a typical 3-pulse ESEEM experiment, T is varied with τ held fixed. The ESEEM frequencies are obtained by Fourier analysis of the resulting pattern, with $(\tau + T)$ used as the conjugate time variable. The sum and difference terms do not appear in the 3-pulse ESEEM.

The value of the dc-component χ_0 is related to the sum of the ESEEM amplitudes of the α- and β-manifolds, denoted $S^{(\alpha)}$ and $S^{(\beta)}$, as well as to the sum of the combination frequency amplitudes $S^{(\alpha,\beta)}$ (Mims, 1972c). The relations

$$S^{(\alpha)} = S^{(\beta)} = -S^{(\alpha,\beta)} = 1 - \chi_0 \qquad (II-75)$$

result from the unitary form of the M-matrix and the normalization of the echo envelope for $\tau = 0$.

In the remainder of this section we show the results of some numerical ESEEM calculations with parameters relevant to ^{14}N. Such simulations are described in detail by Flanagan and Singel (1987). It is convenient to present results with the hyperfine and quadrupole variables normalized to the nuclear Zeeman term. We introduce the reduced variables $\tilde{a} = a/\nu_i$ and $\tilde{K} = K/\nu_i$.

Envelope modulation occurs as long as both the nuclear Zeeman and hyperfine terms are non-zero. It is useful to examine closely the particular subset of sublevel

parameter space where $a/2 = \nu_i$, or $\tilde{a} = 2$ in our reduced variable notation. In this case the nuclear Zeeman and isotropic hyperfine terms exactly cancel in the α-manifold, and the resulting eigenfrequencies coincide with the pure NQR frequencies. The amplitudes of these frequency components are nonisotropic. For example the ν_0 component exhibits maximal modulation amplitude when the applied magnetic field is along the z-axis of the quadrupole tensor. The ν_0 modulation vanishes when the field is oriented along the x- or y-axes. In a like fashion the ν_+ and ν_- components are maximized with the external field respectively along the x-axis and the y-axis. The dependence of the component amplitudes on the value of $\tilde{K}$ is shown in Figure II-6. These calculations are performed at the field orientation giving rise to the maximum modulation amplitude for each NQR frequency. As predicted by equation II-75, The amplitude of the pure NQR modulation component with ν_{ef} aligned along a principal axis is exactly matched in the β-manifold, where only the "double-quantum" high-frequency transition is excited. The dc-component χ_0 is simply given by $\chi_0 = (1 - \chi_\alpha)$.

We see from Figure II-6 that in the special case of exact cancellation, the ESEEM modulation is significant unless $\tilde{K} \gg 1$. The amplitude diminution for very high $\tilde{K}$ occurs because the β-eigenstates also become nearly the purely quadrupolar eigenstates, and no branching is induced. For our X band ESEEM experiments ν_i is on the order of 1 MHz, and the condition $\tilde{K} \gg$ corresponds to unreasonably high values of e^2qQ for ^{14}N. Thus in the special case of $\tilde{a} \approx 2$ we expect to see strong ^{14}N modulation.

Since we are generally studying non-crystalline samples, it is necessary to examine the powder pattern average of the ESEEM amplitudes. These powder pattern averages are obtained by averaging the calculated amplitudes $\{\chi\}$ over the unit sphere through 200 increments of $cos\,\theta$ between 0 and 1 and 200 increments of φ between 0 and $\pi/2$. The resulting 2-pulse frequency domain results are plotted in a 2000 point histogram, with the average value of the dc-term χ_0 providing the maximum of the plotted amplitude scale (see Flanagan and Singel, 1987). This FORTRAN program completes a powder pattern simulation in about 20 minutes on a VAX 11/785.

Figures II-7 through II-11 show the simulated ESEEM powder patterns for exact cancellation over a range of quadrupolar coupling parameter $\tilde{K}$. The asymmetry parameter η is held fixed with a value of 0.35. In all cases the α-manifold gives rise to sharp transitions at the three zero-field NQR frequencies. The frequencies observed

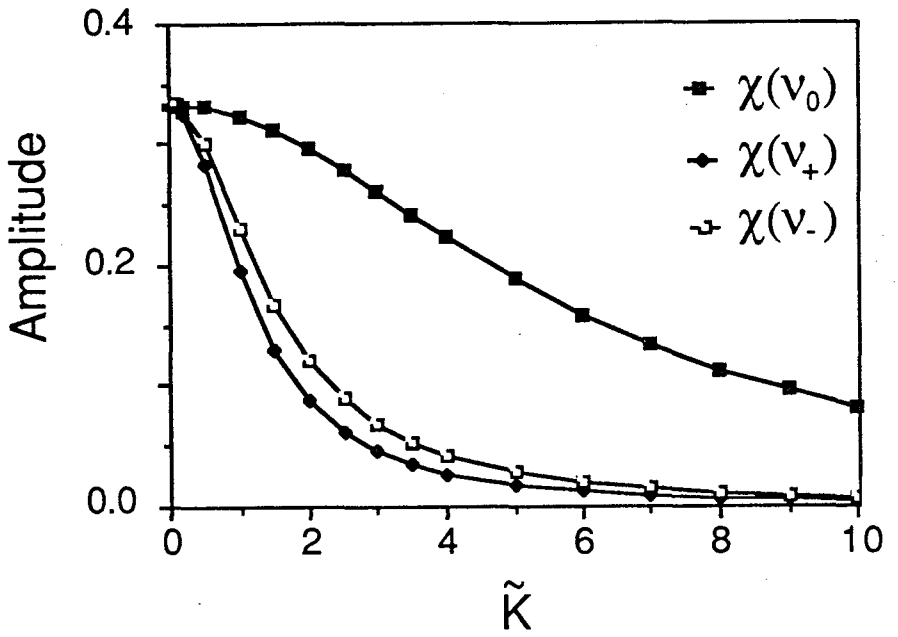

Figure II-6 ESEEM amplitudes of the pure NQR frequency components in the case of exact cancellation of Zeeman and isotropic hyperfine coupling ($\tilde{a} = 2$). The amplitudes of the three NQR frequencies ν_0, ν_+, and ν_- are shown as a function of the reduced quadrupolar coupling parameter $\tilde{K}$. The results are obtained by simulations at values of θ and φ which maximize each of the three components. The value of η is fixed at 0.35. The ν_0 component is calculated with $\theta = 0$ and $\varphi = 0$. The ν_+ and ν_- amplitudes are calculated with respectively $\theta = \pi/2$, $\varphi = 0$; and $\theta = \pi/2$, $\varphi = \pi/2$.

from the β-manifold depend dramatically on the value of $\tilde{K}$.

Figure II-7 shows the ESEEM pattern pattern for a very small quadrupolar coupling, $\tilde{K} = 0.02$. There are two major sets of transitions due to the β-manifold. The very sharp transition near the frequency of 4. is due to the "double-quantum" interval which corresponds to $(m_i = -1) \leftrightarrow (m_i = +1)$ in the Zeeman dominated limit. The frequency ν_{dq} of this narrow peak is given by (Astashkin et al., 1984)

$$\nu_{dq} = 2\left[\nu_{ef}^2 + K^2(3+\eta^2)\right]^{1/2}. \qquad (II-76)$$

This peak is flanked by sharp, negative features arising from sums and differences of the α-manifold frequencies with the "double-quantum" frequency.

The broader feature near the frequency of 2 is due to the two "single-quantum" intervals described by $(m_i = -1) \leftrightarrow (m_i = 0)$ and $(m_i = 0) \leftrightarrow (m_i = +1)$ in the Zeeman dominated limit. The center frequency ν_{sq} of this peak is given by

$$\nu_{sq} = \left[\nu_{ef}^2 + K^2(3+\eta^2)\right]^{1/2} \qquad (II-77)$$

This feature is relatively broad compared to the "double-quantum" feature due to the strong anisotropic effects of the quadrupole interaction as described earlier in the section. The feature is somewhat smoothed relative to the powder pattern in Figure II-4 obtained without calculating the exact ESEEM amplitudes (Flanagan and Singel, 1987). The "single-quantum" feature is also flanked by negative sum and difference terms.

Figure II-8 shows the powder pattern for $\tilde{K} = 0.1$. The "single-quantum" feature is very broad while the "double-quantum" feature remains narrow. With the value of $\tilde{K}$ increased to 0.2 (Figure II-9), the "single-quantum" feature is broadened to the limits of perceptibility. This trend continues to higher values of $\tilde{K}$ ($\tilde{K} = 0.4$ in Figure II-10 and $\tilde{K} = 1.0$ in Figure II-11), with the "double-quantum" transition remaining relatively sharp. Details of the structure of this peak at intermediate values of $\tilde{K}$ are provided by Flanagan and Singel (1987). Of particular interest is the small splitting of the peak for small values of the asymmetry parameter η, such as observed in Figures II-10 and II-11.

The simulations shown above were all performed with the special constraint of $\tilde{a} = 2$. This is a useful limit, because the pure quadrupole frequencies are clearly revealed, but it arises only by good fortune or through the construction of a spectrometer which can be operated over a very large frequency range so that one may

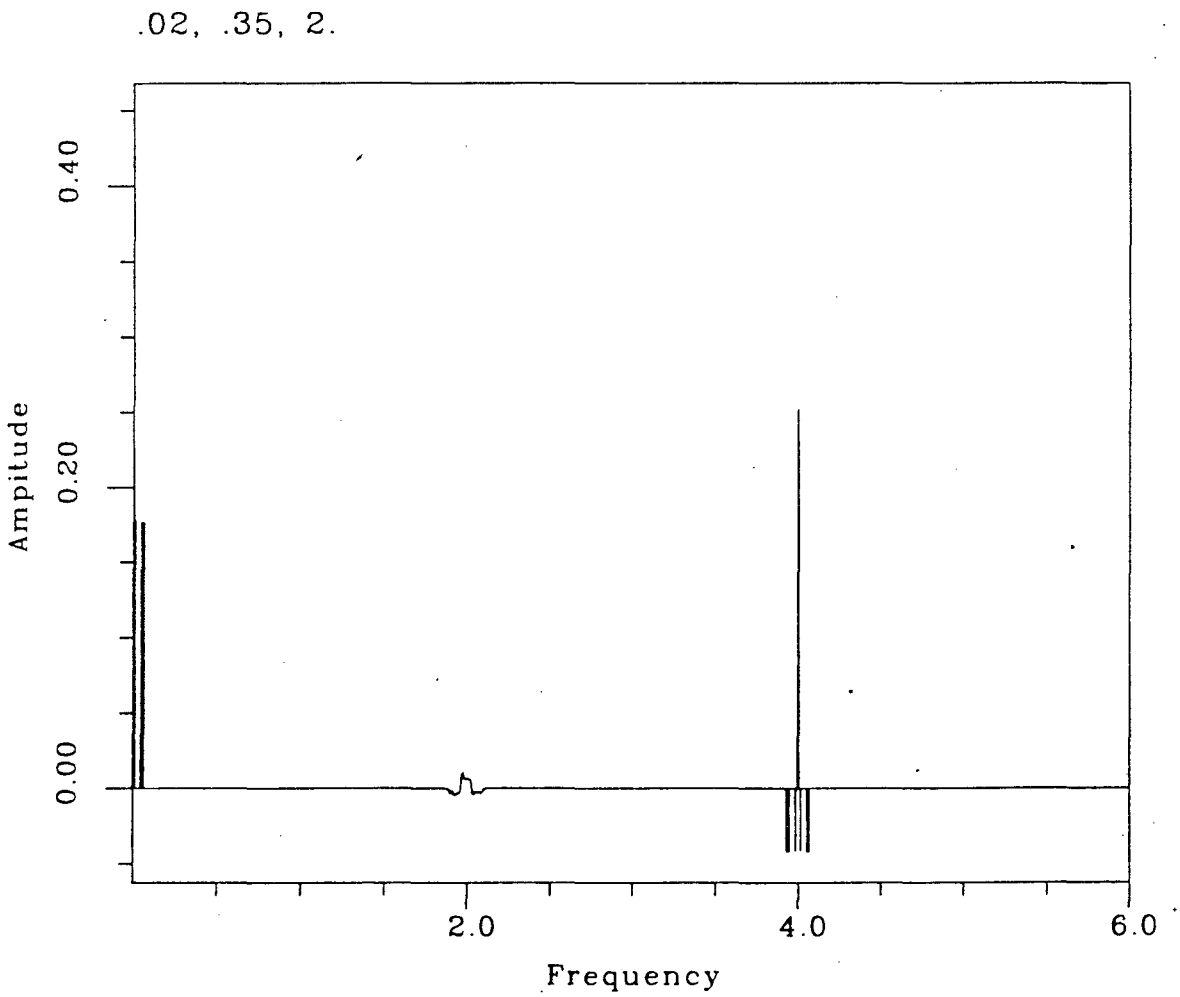

Figure II-7 ESEEM powder pattern in the exact cancellation limit ($\tilde{a} = 2$) with $\tilde{K} = 0.02$ and $\eta = 0.35$. The amplitude axis maximum is set to the dc-term amplitude χ_0.

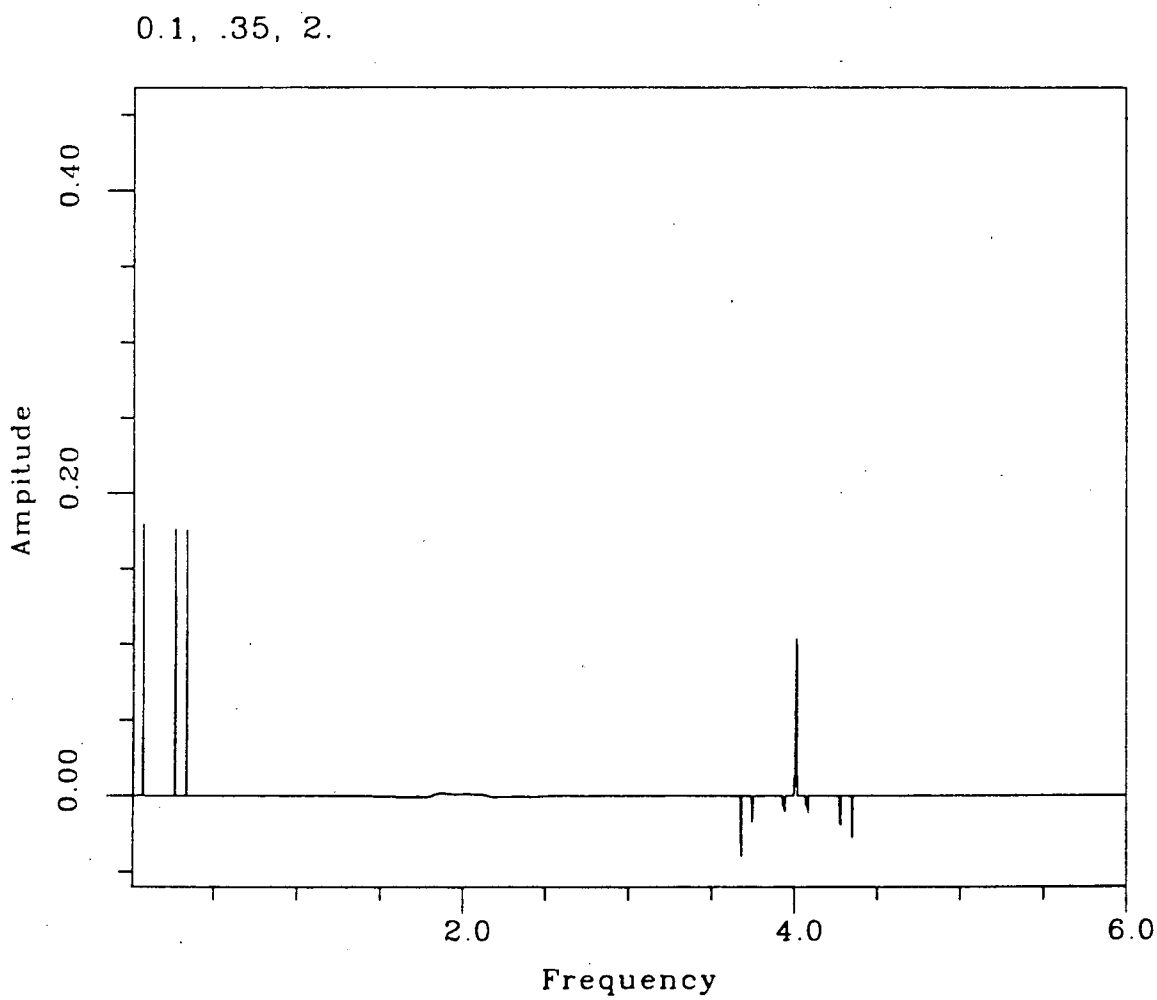

Figure II-8 ESEEM powder pattern in the exact cancellation limit ($\tilde{a} = 2$) with $\tilde{K} = 0.1$ and $\eta = 0.35$. The amplitude axis maximum is set to the dc-term amplitude χ_0.

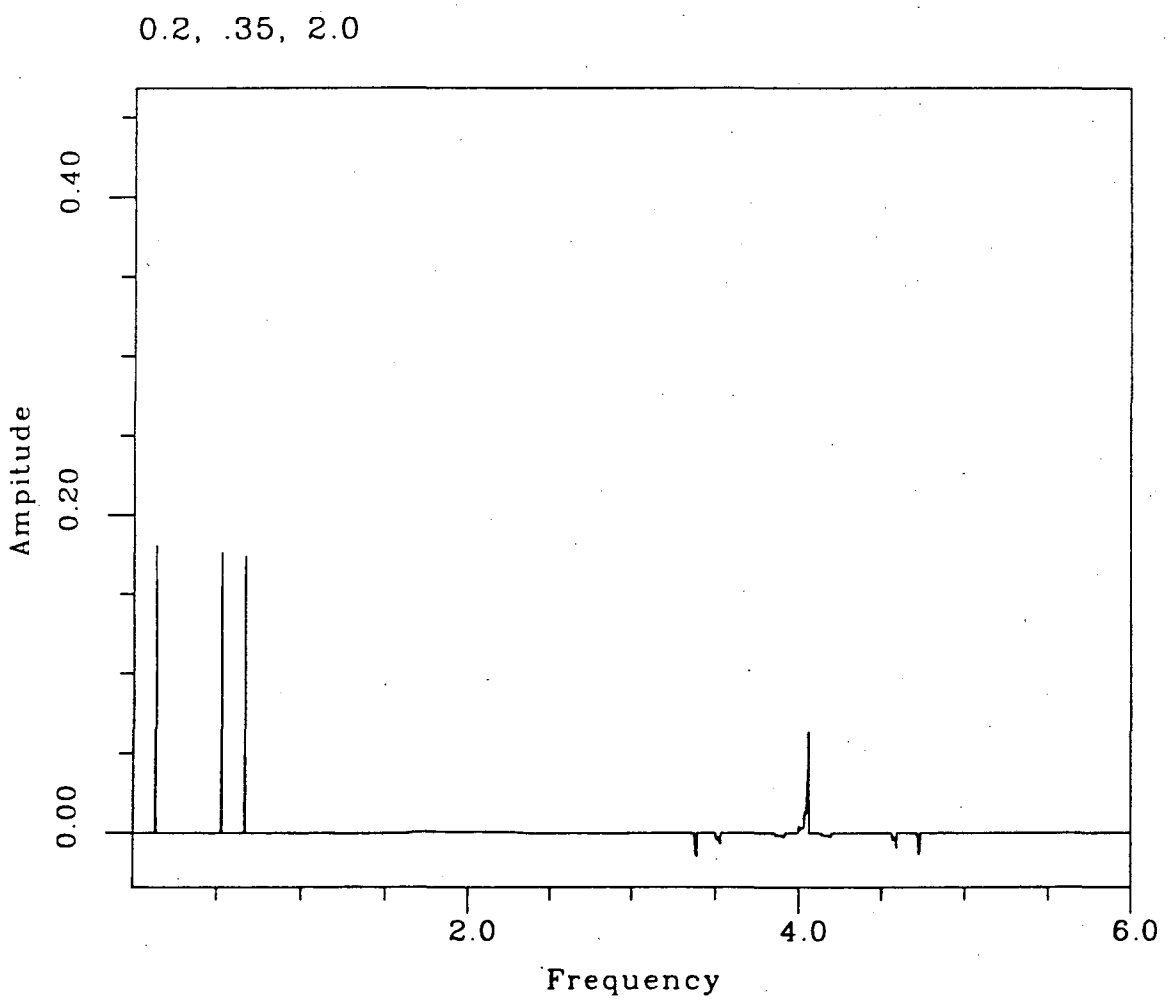

Figure II-9 ESEEM powder pattern in the exact cancellation limit ($\tilde{a} = 2$) with $\tilde{K} = 0.2$ and $\eta = 0.35$. The amplitude axis maximum is set to the dc-term amplitude χ_0.

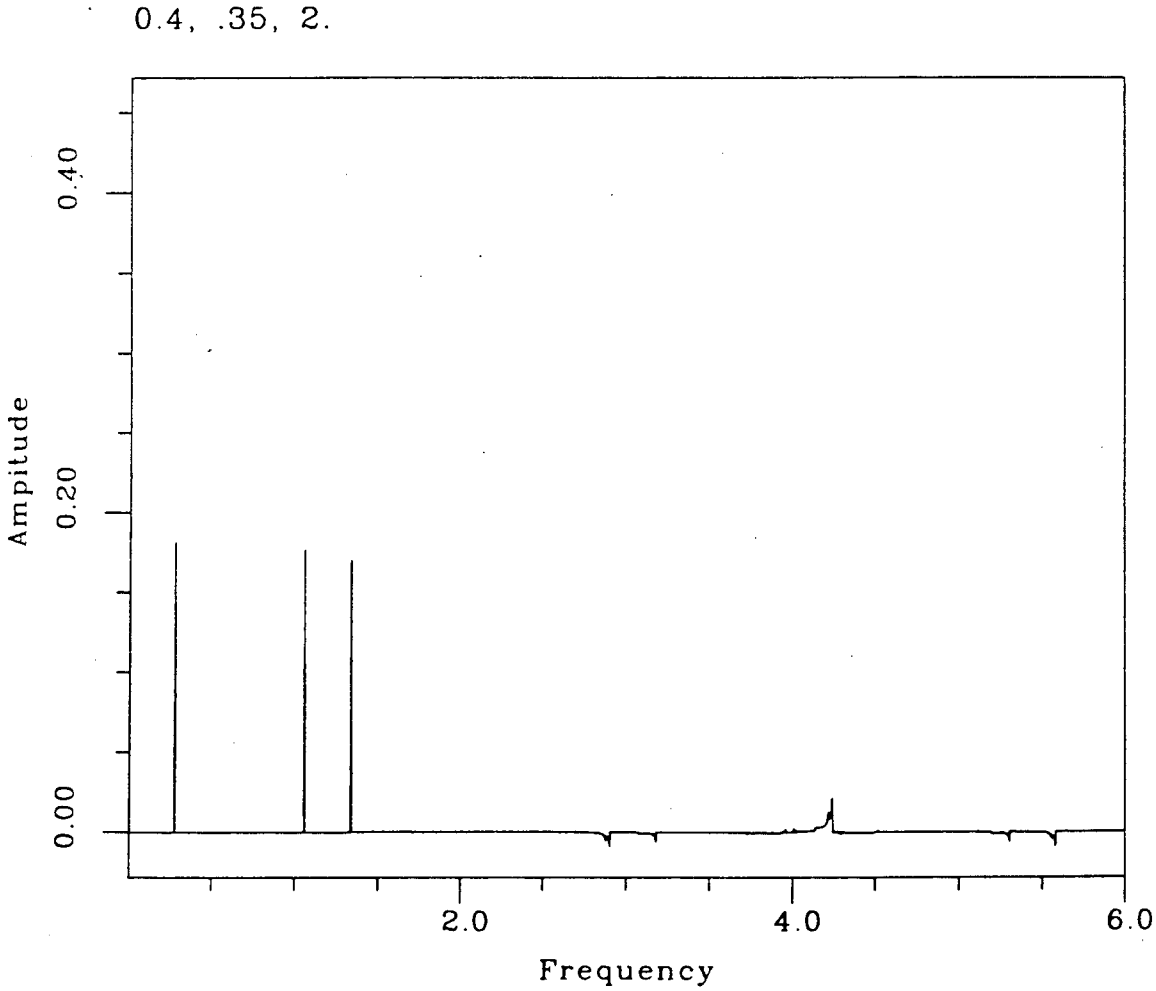

Figure II-10 ESEEM powder pattern in the exact cancellation limit ($\tilde{a} = 2$) with $\tilde{K} = 0.4$ and $\eta = 0.35$. The amplitude axis maximum is set to the dc-term amplitude χ_0.

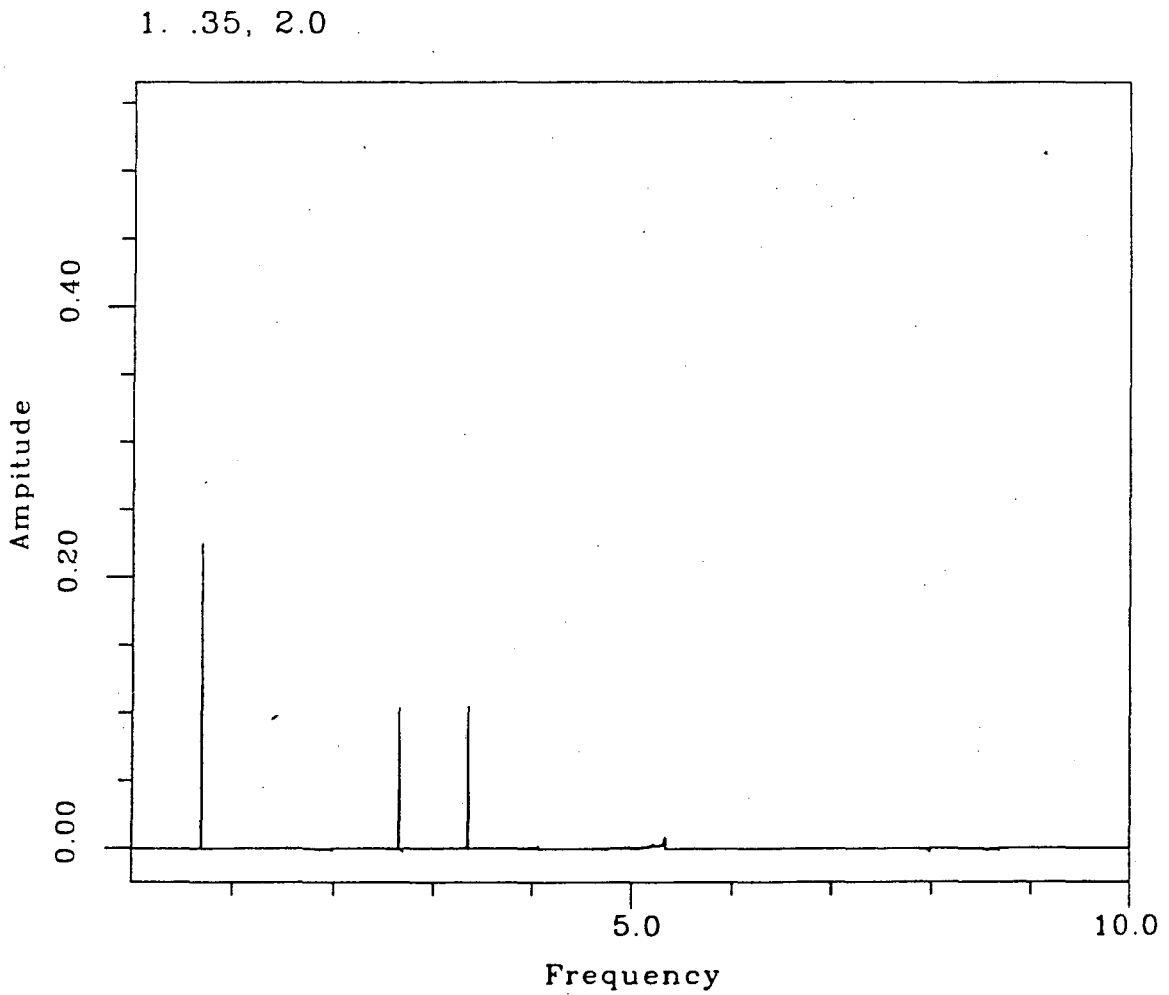

Figure II-11 ESEEM powder pattern in the exact cancellation limit ($\tilde{a} = 2$) with $\tilde{K} = 1.0$ and $\eta = 0.35$. The amplitude axis maximum is set to the dc-term amplitude χ_0.

observe the ESEEM pattern over a large range of nuclear Zeeman frequency while maintaining a constant g-value (Flanagan et al., 1987). ESEEM patterns will generally be obtained away from this limit. Figures II-12 through II-17 demonstrate the changes in the ESEEM pattern which occur for $\tilde{a} \neq 2$. These simulations are performed with $\tilde{K} = 1.0$ and $\eta = 0.35$.

Figure II-12 shows the ESEEM pattern for $\tilde{a} = 2.1$ The pattern is very similar to the ESEEM pattern for exact cancellation (Figure II-11). Figure II-13 displays the results when $\tilde{a}$ is increased to a value of 2.2. The ν_0 and ν_- peaks begin to broaden perceptibly, while the ν_+ peak remains quite sharp. This trend continues through Figure II-14, with $\tilde{a} = 2.4$. The two low frequency transitions are quite broadened in Figure II-15, with $\tilde{a}$ increased to 3.0. The high frequency feature can no longer be well described as the pure quadrupole transition ν_+. It has taken more character of the "double-quantum" transition previously described for the β-manifold. This conversion is nearly complete when $\tilde{a}$ is increased to 4.0 (Figure II-16). With such large deviation from exact cancellation both the α- and β-manifold modulations are sharp only for the "double-quantum" features. The frequencies are given by equation II-76, with ν_{ef} taking the two distinct values from equation II-59.

In addition to the two ν_{dq} peaks observed when $\tilde{a} \not\approx 2$, a sharp negative-going combination peak is observed in the 2-pulse ESEEM pattern at large deviations from exact cancellation. For $\tilde{a} > 2$, this combination peak occurs at the sum of the two "single-quantum" frequencies given by equation II-77 with the two values of ν_{ef} (Flanagan and Singel, 1987). This feature is readily visible in Figures II-15 and II-16. If $\tilde{a} < 2$, as in Figure II-17 with $\tilde{a} = 1$, this combination peak occurs at the difference of the two "single-quantum" transition frequencies.

Figure II-18 demonstrates the decrease in ESEEM modulation for large deviation from exact cancellation. The y-axis values in Figure II-18 are obtained from the function $(1 - \chi_0)$, which is the sum of ESEEM amplitudes from each manifold (equation II-75). This function is plotted vs. the reduced hyperfine coupling parameter $\tilde{a}$. The calculations are performed at a single orientation, with angles $\theta = 45°$ and $\varphi = 45°$ chosen so that all polarized frequencies will be represented. The fixed quadrupolar parameters are $\tilde{K} = 1.0$ and $\eta = 0.35$. The summed ESEEM amplitudes decrease with increased deviation from exact cancellation as both the α- and β-manifold become more purely Zeeman states.

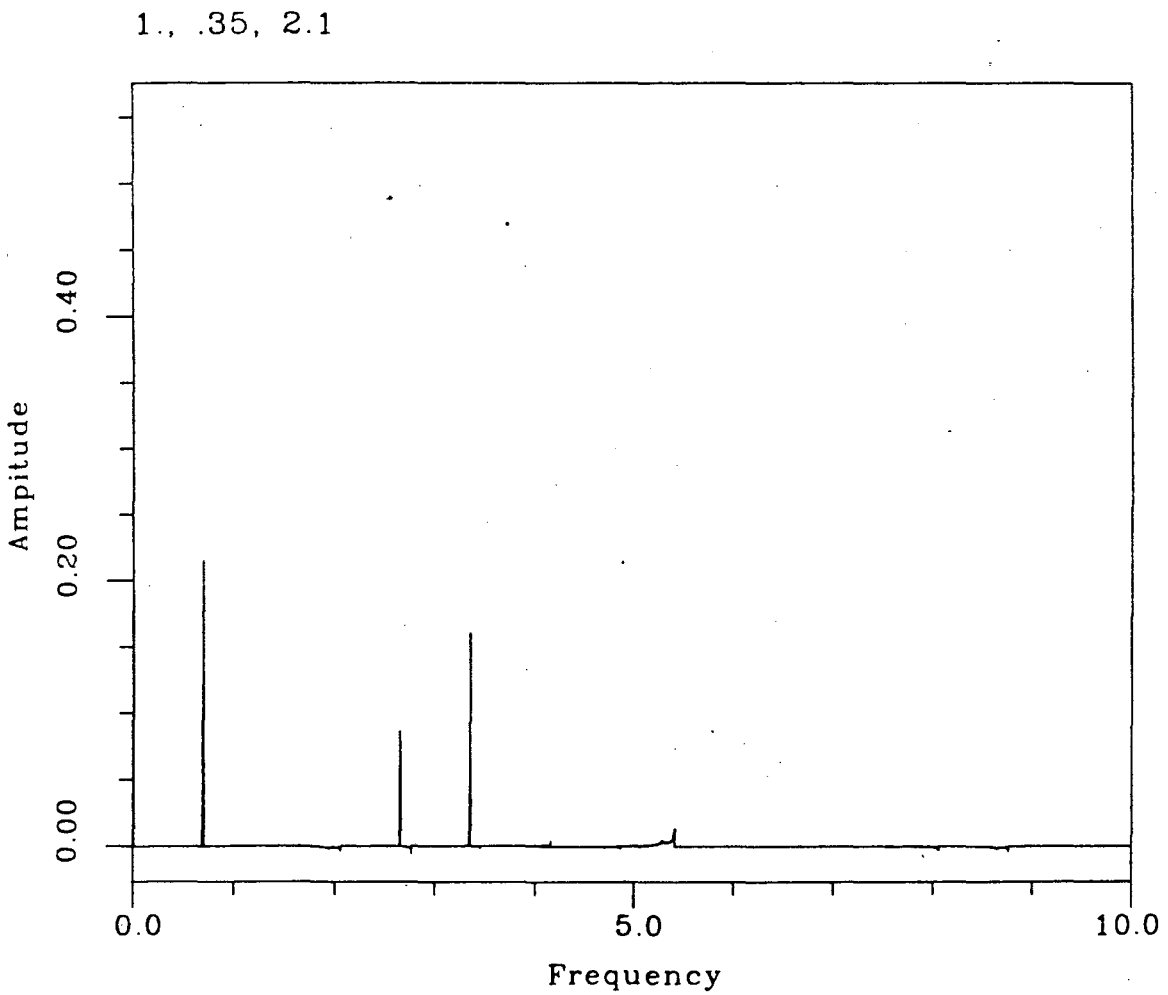

Figure II-12 ESEEM powder pattern away from the exact cancellation limit. The parameters for this simulation are $\tilde{a} = 2.1$, $\tilde{K} = 1.0$ and $\eta = 0.35$. The amplitude axis maximum is set to the dc-term amplitude χ_0.

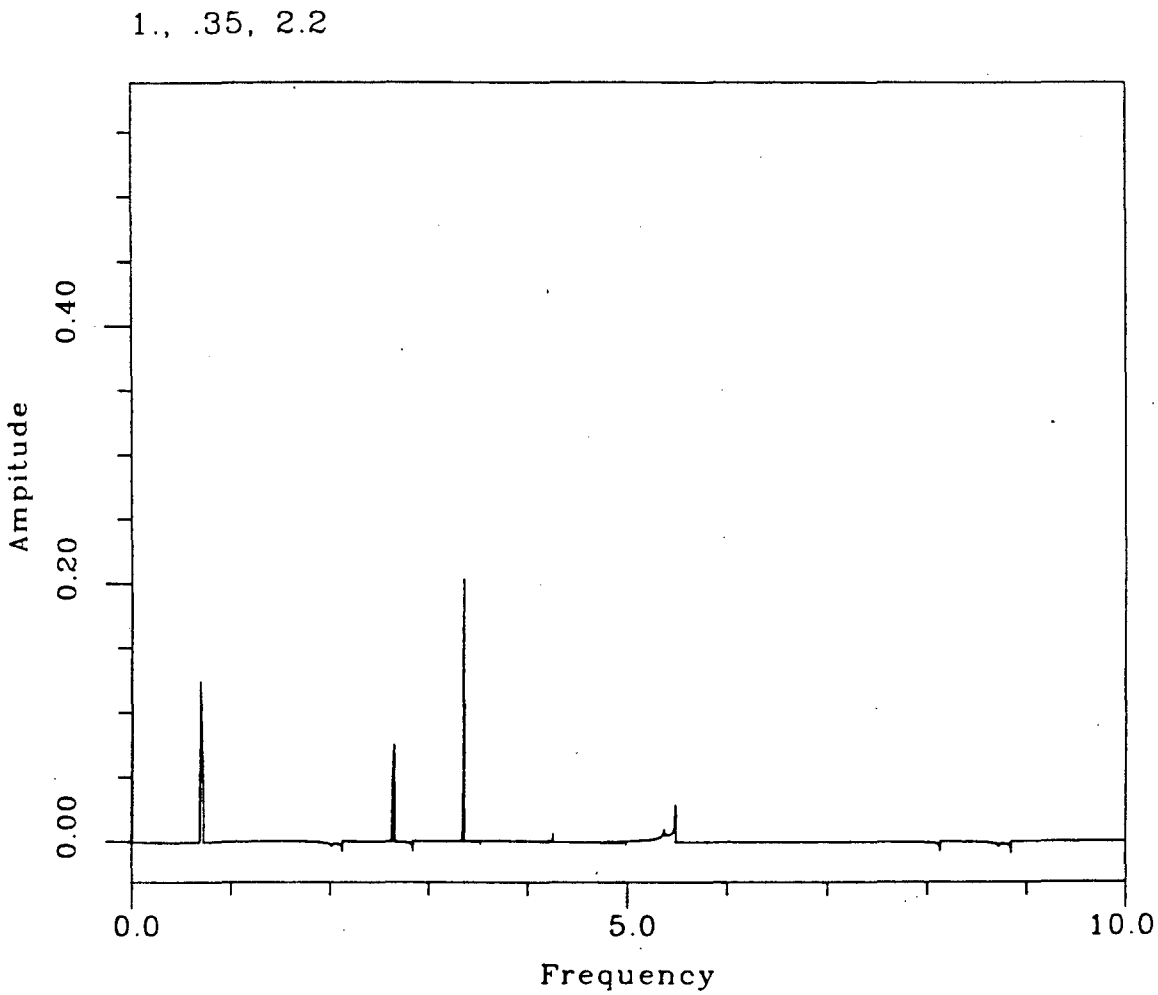

Figure II-13 ESEEM powder pattern away from the exact cancellation limit. The parameters for this simulation are $\tilde{a} = 2.2$, $\tilde{K} = 1.0$ and $\eta = 0.35$. The amplitude axis maximum is set to the dc-term amplitude χ_0.

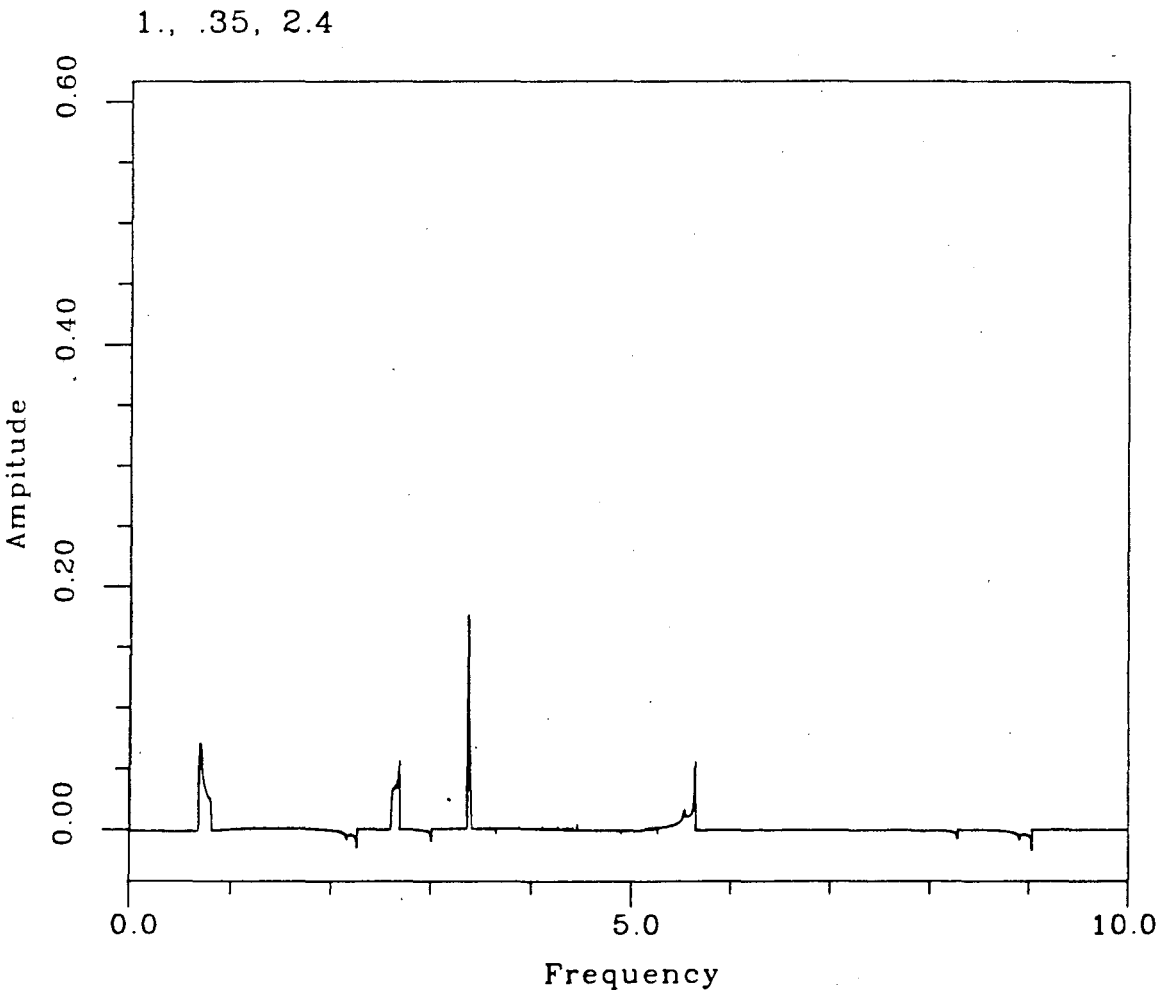

Figure II-14 ESEEM powder pattern away from the exact cancellation limit. The parameters for this simulation are $\tilde{a} = 2.4$, $\tilde{K} = 1.0$ and $\eta = 0.35$. The amplitude axis maximum is set to the dc-term amplitude χ_0.

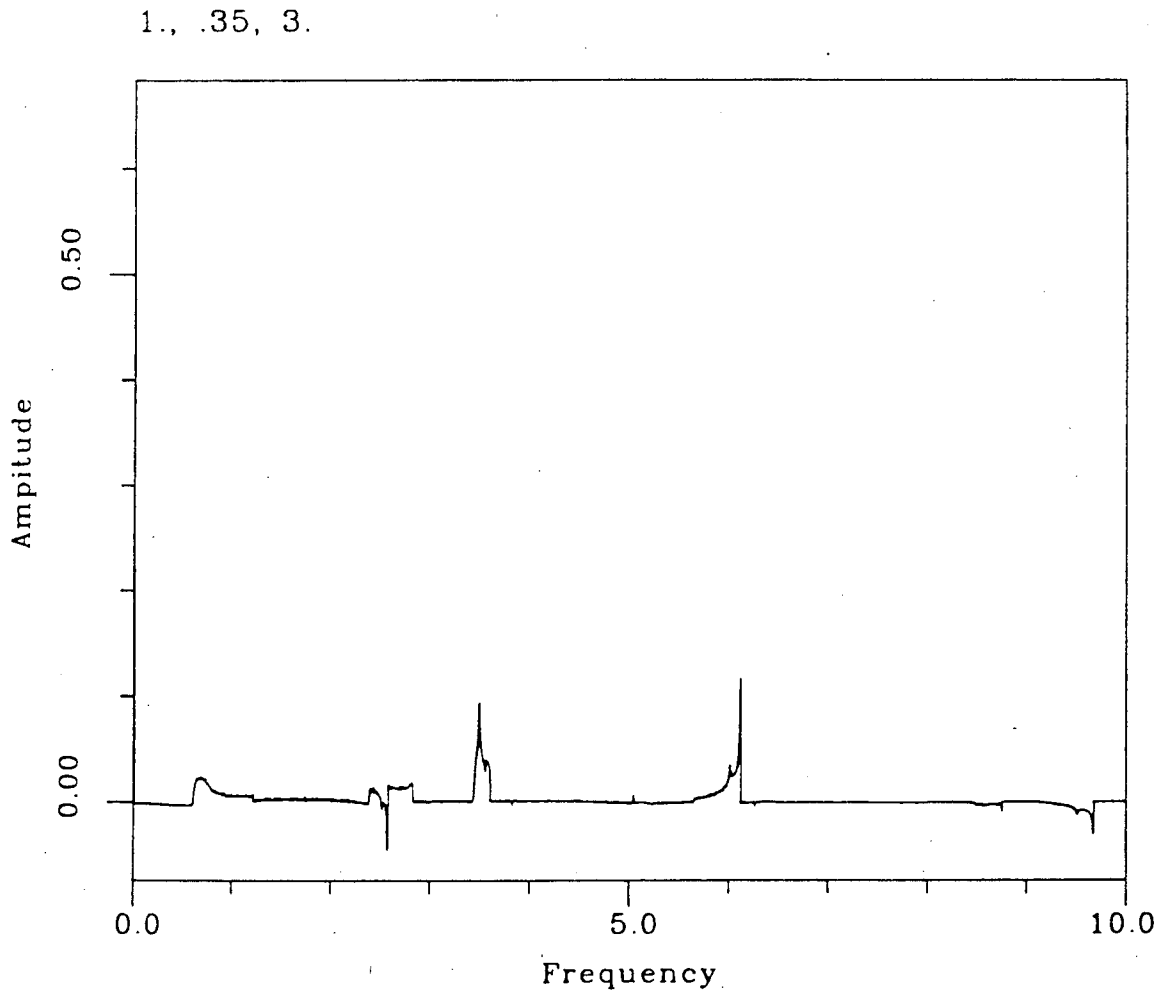

Figure II-15 ESEEM powder pattern away from the exact cancellation limit. The parameters for this simulation are $\tilde{a} = 3.0$, $\tilde{K} = 1.0$ and $\eta = 0.35$. The amplitude axis maximum is set to the dc-term amplitude χ_0.

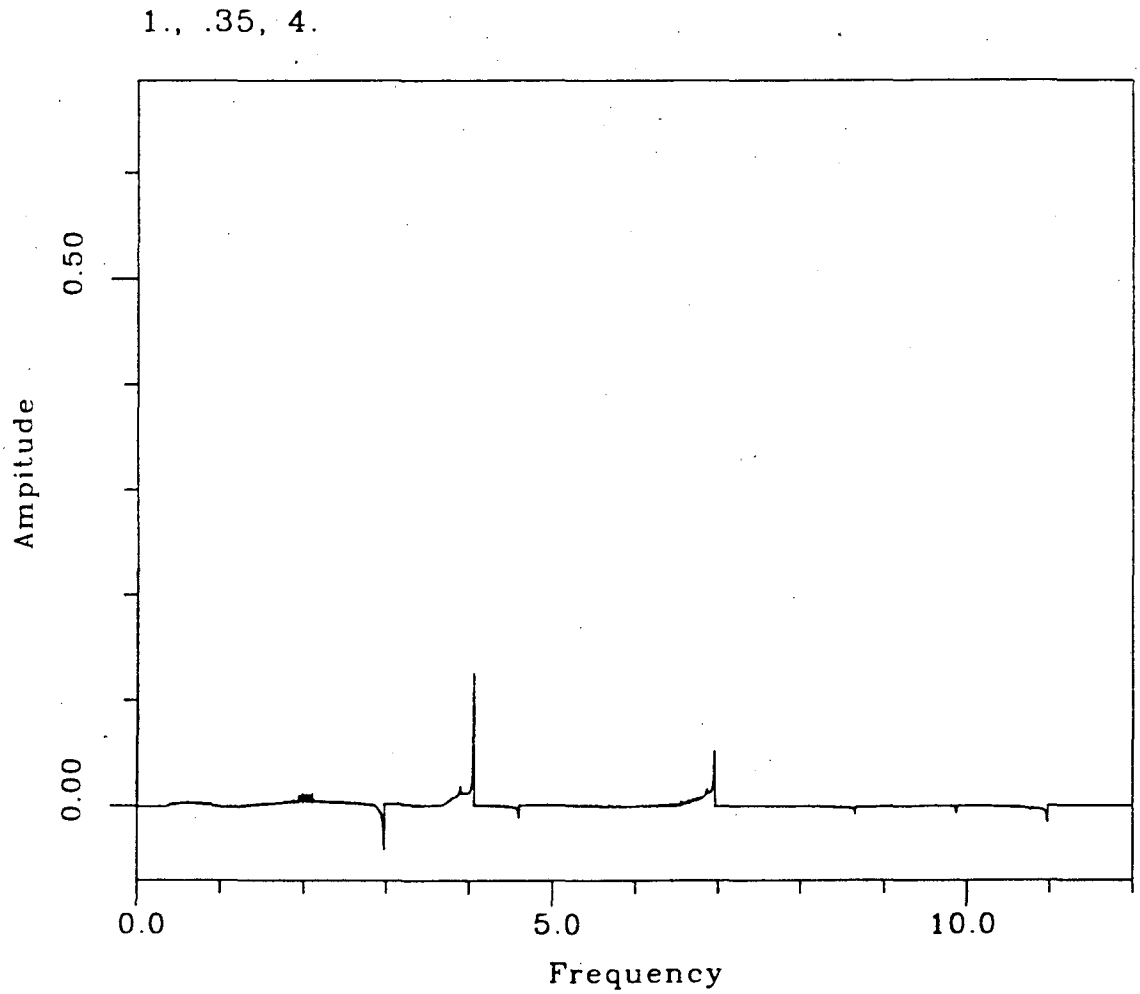

Figure II-16 ESEEM powder pattern away from the exact cancellation limit. The parameters for this simulation are $\tilde{a} = 4.0$, $\tilde{K} = 1.0$ and $\eta = 0.35$. The amplitude axis maximum is set to the dc-term amplitude χ_0.

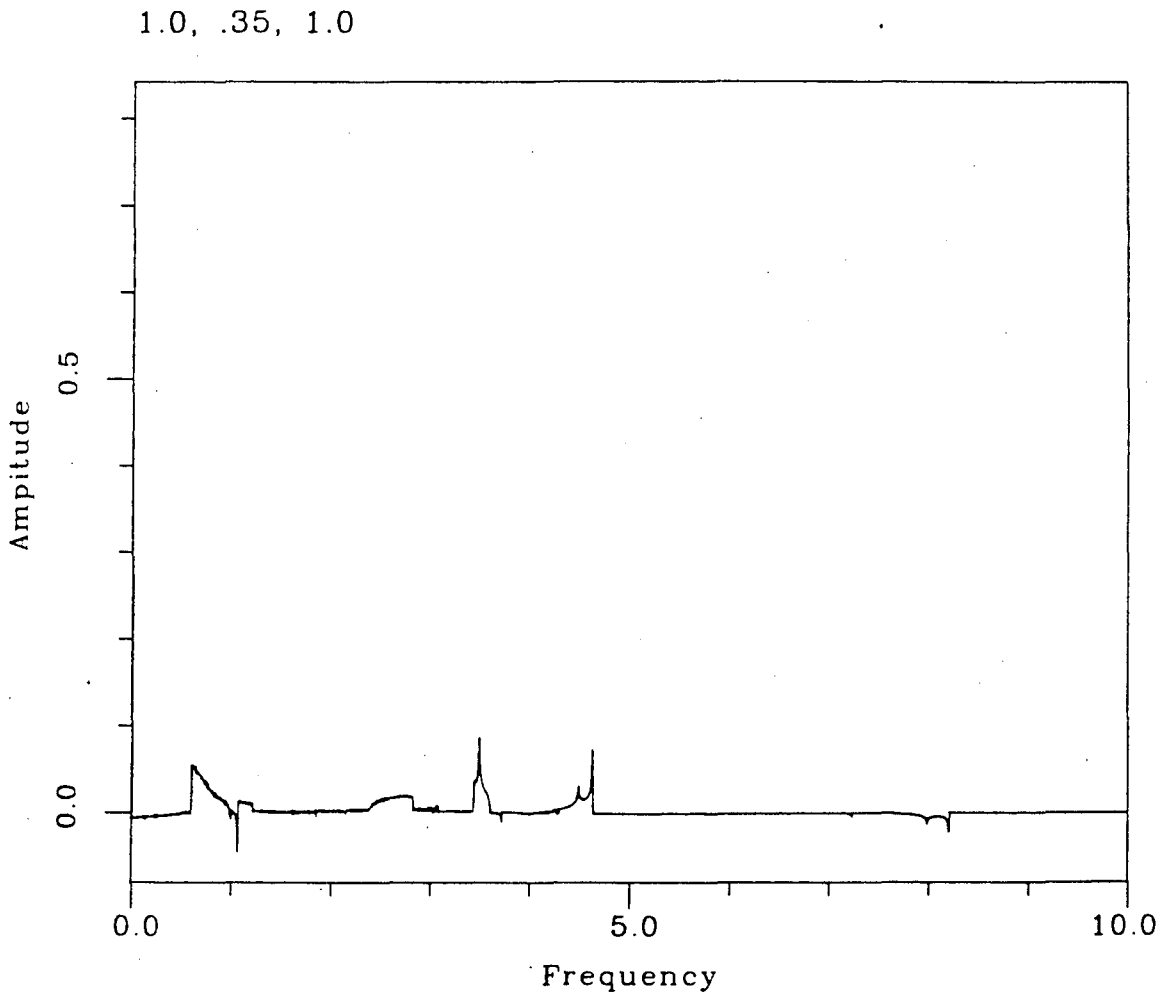

Figure II-17 ESEEM powder pattern away from the exact cancellation limit. The parameters for this simulation are $\tilde{a} = 1.0$, $\tilde{K} = 1.0$ and $\eta = 0.35$. The amplitude axis maximum is set to the dc-term amplitude χ_0.

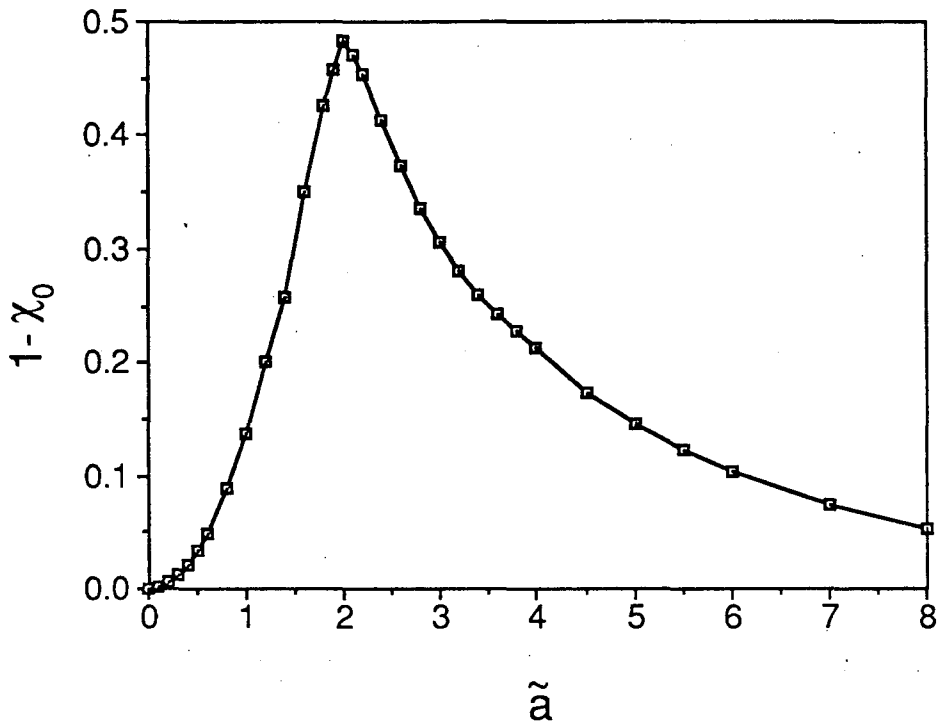

Figure II-18 ESEEM modulation vs. reduced hyperfine parameter $\tilde{a}$. The function $(1 - \chi_0)$ is plotted vs. $\tilde{a}$ for the single orientation $\theta = 45°$, $\varphi = 45°$. The quadrupolar parameters are $\tilde{K} = 1.0$ and $\eta = 0.35$.

Chapter III — Electron Spin Echo Instrumentation

This chapter details the construction and operation of the electron spin echo spectrometer. Section 1 covers the design of the microwave components and how they are integrated to form the spectrometer bridge. Details of other physical components such as the magnet and power supply are also included in this section. Section 2 details the design and construction of the loop-gap resonator probe device that we use for the pulsed EPR studies. Pulse electronics and computer interfaces are described in Section 3.

Section 1 — Spectrometer Design

A schematic layout of the Electron Spin Echo Spectrometer is shown in Figure III-1. *X* band microwave power is produced by a Gunn oscillator. The spectrometer operates in homodyne receiver mode (Poole, 1983, ch. 7) with power supplied to the reference arm by a -10 dB directional coupler. An additional -30 dB of power is tapped from the main spectrometer arm for power level and frequency measurement. Low power pulses are formed by a PIN diode switch and amplified to kilowatt levels with a pulsed travelling wave tube amplifier. The high power pulses are applied to the sample resonator through a circulator. The resultant signals are amplified via a limiter-protected GaAs FET microwave amplifier and mixed with the reference power to achieve a video frequency output signal. This output signal is further amplified to desired levels and integrated and averaged with a boxcar integrator. This final signal is digitized and stored in a PDP11/34A minicomputer. The magnetic field is produced within a high impedance Varian electromagnet with 12 in. diameter pole faces and a 3 in. gap. This magnet is powered by a Varian V2100-1 high voltage power supply modified for magnetic field regulation with a Varian Fieldial Mark I.

The remainder of this section describes the components and their integration in greater detail. The spectrometer is designed to perform both pulsed and cw EPR and ENDOR. To minimize microphonics and long-term drift, the spectrometer is constructed on an optical breadboard table with all components rigidly mounted to the table. Microwave isolators are included at many points to minimize standing waves throughout the system. DC blocks are also incorporated at strategic points to prevent ground loops. Hewlett-Packard X382A rotary-vane variable attenuators are used throughout. These waveguide attenuators are very accurate and offer minimal phase

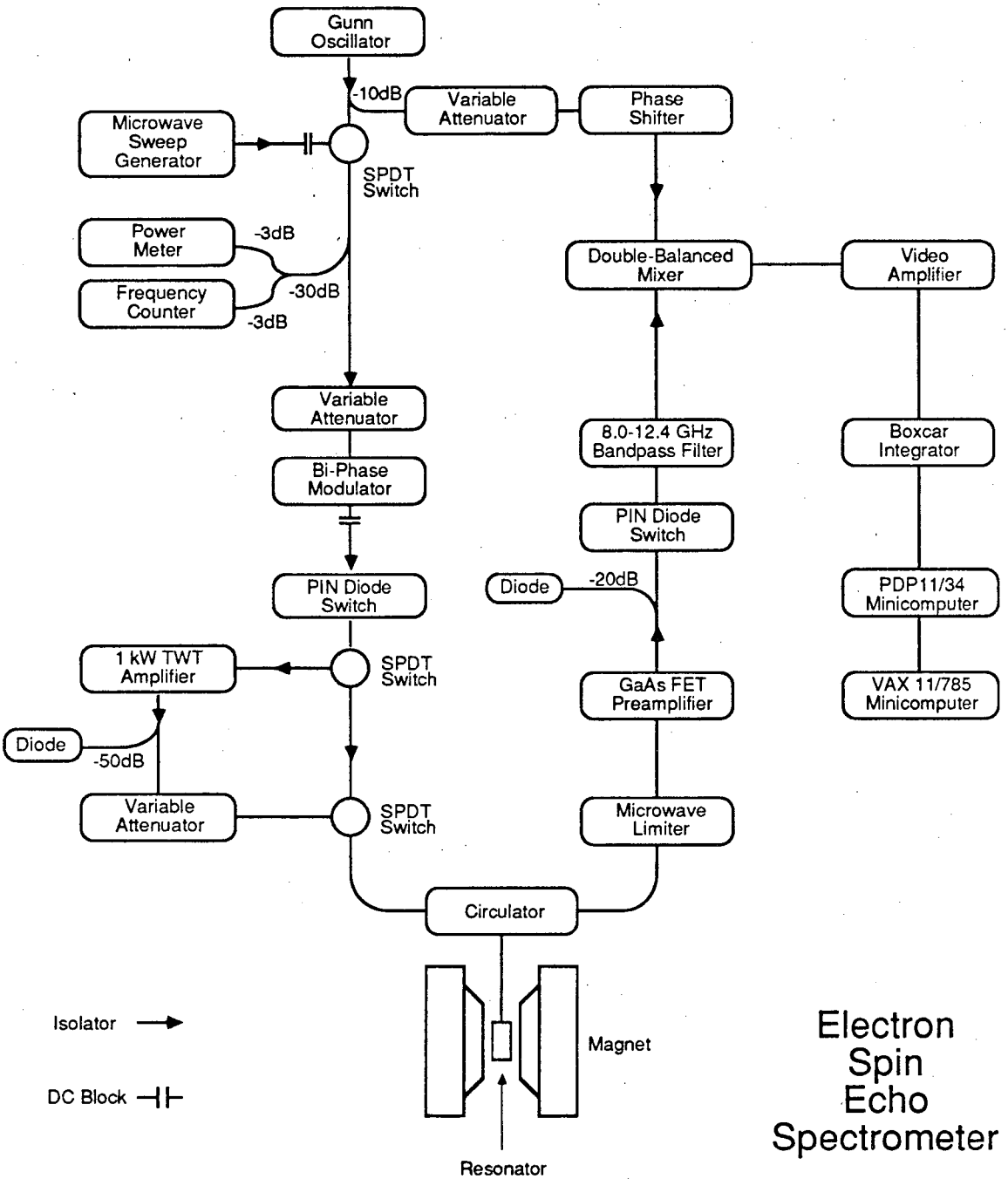

Figure III-1 Design of electron spin echo spectrometer.

shifts. A high-precision HP X885A waveguide phase shifter is employed in the reference arm. The Gunn oscillator has a waveguide output, and one waveguide isolator is used in the TWT bypass arm to prevent kilowatt pulses from propagating back through the bridge in case of a switch failure. All other components have coaxial connectors. The extensive use of coaxial components saves a great deal of space. The coaxial components are connected with 0.141 or 0.250 in. diameter semi-rigid coaxial lines with SMA connectors.

As shown in Figure III-1, the primary microwave source for the spectrometer is a Gunn-effect oscillator. This Central Microwave Company CMF422AA oscillator provides 200 mW output power from 8.8 to 9.6 GHz. The oscillator is powered by a homebuilt 12 V power supply with feedback circuitry for an AFC circuit or a phase-lock input (LBL 26X1153). The original microwave source for the spectrometer was a Varian VA 297V klystron with a 1 W output level. The higher power klystron was employed because the specified gain of the kilowatt TWT was 30 dB. We anticipated using a full watt to drive the amplifier. However the actual gain of the TWT is closer to 40 dB, and with the loop-gap resonator probe we do not need a kilowatt output power, so the output power of the solid-state source is sufficient for our current needs. The Gunn oscillator is trivial to phase lock, has less AM noise, and requires no flowing water coolant. A -10 dB directional coupler routes 10% of the power through the reference arm to bias the mixer. The remaining 90% is applied to the main spectrometer arm.

An HP 7690B microwave sweeper is used as a secondary source. With the *X* band plug-in, the sweeper covers a frequency range of 8.0 to 12.0 GHz. This device is used primarily to tune the spectrometer when a new microwave resonator is introduced. Its wide bandwidth and fast sweep time make it useful for finding resonances and measuring frequencies and quality factors precisely. A solenoid activated HP 8761A single-pole, double throw (SPDT) microwave switch is used to select between the microwave sweeper and the Gunn oscillator.

An additional -30 dB of power is tapped for frequency and power measurement. One half of this power is routed to an HP 431C analog power meter. The other half is input to an EIP 575 source locking microwave counter. This counter is used to phase lock the Gunn oscillator for noise suppression and long term stability. The phase lock uses an internal 10 MHz crystal oscillator for its time base. The frequency lock resolution is 10 KHz. The EIP counter also provides for digital power level

measurement with 0.1 dB resolution.

The variable waveguide attenuator on the main arm is used to set power levels for cw EPR or for resonator tuning. For pulsed applications this attenuator is set to 0 dB attenuation.

A Triangle Microwave MP-62-1 bi-phase modulator is used to shift the microwave phase in 180° increments. This device contains a pair of PIN SPDT switches which select between a reference path and a path with 180° phase delay. The switching time of this device is 10 ns. The bi-phase modulator is used to alternate the phase of selected microwave pulses in ESE experiments.

The actual microwave pulses for ESE experiments are formed by a M/A-COM 2660-123-31 single-pole single-throw (SPST) PIN diode switch. This switch provides transition times of 2 ns with total pulse widths as short as 10 ns.

A pair of HP 8761A SPDT switches are used to select between the high-power pulsed TWT arm and the cw arm. The cw arm consists of only a heavy duty waveguide isolator installed to assure that no high power pulses can propagate back through the bridge. The high power TWT arm is used for ESE studies. The travelling wave tube amplifier is manufactured by Space Microwave Laboratories. The TWT amplifier consists of a model 61213 amplifier mainframe with a model 66310-H70J11 rf plug-in. The amplifier is specified for 30 dB gain from 7.0 to 11.0 GHz with a minimum output power of 1 KW. The specified maximum duty cycle is 1%, and the specified maximum pulse rise and fall times are 35 ns. The actual measured maximum saturated output of the TWT is 1.9 KW with a 1 W input. The measured gain in the linear regime is over 40 dB from 8.0 to 10.0 GHz. With the Gunn oscillator source we achieve a maximum output power of about 650 W. This is sufficient power for our purposes. We measure a pulse rise time of 25 ns and a fall time of 22 ns. The minimum pulse width which can be formed with the TWT alone is 50 ns. We create shorter pulses with the PIN switch and amplify them to high power levels by simultaneously gating on the TWT. Output pulse shapes are monitored by an HP 8472A point contact crystal detector fed by a -50 dB directional coupler. The actual power applied to the sample resonator is set with the variable attenuator in the output arm of the TWT.

Microwave power is routed to the sample resonator through a ferrite circulator. The sample resonator is described in detail in Section 2. Reflected pulse power and signals are directed through the circulator into the receiver arm.

A M/A-COM 2690-0111 solid state limiter protects the receiver amplifier from

high power pulses. This passive limiter is rated to 500 W. The low power insertion loss is measured at 1.0 dB, and we see little or no distortion from incomplete recovery down to our minimum deadtime of 70 ns. The receiver amplifier is a Narda N6244S-237 GaAs FET amplifier with 8.5 to 9.6 GHz bandwidth and a gain of 27 dB. The measured noise figure is 3.4 dB. The resulting noise figure for the limiter/amplifier combination is thus approximately 4.4 dB. When we first built the spectrometer we employed a Watkins-Johnson WJ-276 low noise TWT amplifier rather than the solid state limiter/amplifier. This device had an noise figure of 8.0 dB and was destroyed by a few hundred hours of high power pulsed operation. We are much satisfied by the improved noise figure and reliability of the solid state limiter/amplifier combination.

The overall noise figure for a receiver of multiple components is determined by

$$NF_{total} = NF_1 + \frac{NF_2}{G_1} + \frac{NF_3}{G_1 G_2} \cdots \qquad (III-1)$$

where NF_i and G_i are the noise figure and gain of the ith component. With the 27 dB gain of the GaAs FET amplifier we greatly reduce the noise contribution of subsequent components. The first component after the amplifier is a -20 dB directional coupler with an HP 8473B low barrier Schottky diode detector. This diode detector monitors pulse shapes through this stage of the receiver. We also use this detector as the output source when using the spectrometer bridge for measuring resonator characteristics.

Also installed in the receiver before the mixer is another fast SPST PIN switch. This HP 33144A switch with HP 33190B TTL driver is used to blank out the remaining microwave pulse energy that passes the limiter and is amplified by the GaAs FET. The primary reason to do this is to eliminate any offsets from the pulses which will cause the signal to reside on a sloping baseline due to AC coupling in the video amplifiers. The switch is followed by a coaxial 8.0 to 12.4 GHz bandpass filter which is used to eliminate video burst artifacts originating in switching transients.

The resulting signal is mixed with the reference arm power with a RHG DM8-12B double balanced mixer. The variable attenuator in the reference arm is used to set the desired mixer LO power of 7 mW. The reference arm phase shifter is used to select between absorptive and dispersive components of the signal. The double balanced mixer uses a ring quad diode structure to cancel source noise. The mixer has a conversion loss of 5.4 dB and a 0 to 300 MHz IF bandwidth.

Video amplification is performed with a pair of EE&G 574 timing amplifiers. Each amplifier consists of four sections with 50Ω impedance, voltage gain of 4.5, and

0 to 300 MHz bandwidth. We typically use the number of stages required to produce a final spin echo signal between 20 and 100 mV. A 10 KHz high-pass filter is inserted after the first section to remove any DC component from the mixer output.

The final spin echo signal is processed with a Stanford Research Systems SR250 boxcar integrator. The spin echo signal is integrated over a sampling gate window set to the width of the echo. This is typically about 30 ns. The signal is averaged over the desired number of repetitions and the resulting average value is converted to digital form in the PDP11/34. The SR250 boxcar integrator features an active baseline subtraction mode. In this mode odd-number acquisitions are added and even number acquisitions subtracted from the running average. This is very useful in conjunction with cycling the phase of ESE excitation pulses. The simplest example is in a 2-pulse experiment where we alternate the phase of the first pulse by 180° from one repetition to the next. This alternates the phase of the spin echo without altering the DC baseline level or the ringdown from the second pulse. By alternately subtracting the signal while averaging we discriminate against baseline drift and pulse ringdown. The effect of canceling baseline drift is similar to using phase sensitive detection in a field modulated experiment.

The phase cycling serves an additional purpose in 3-pulse experiments. Figure III-2a shows the spin echoes which result in a 3-pulse experiment. For ESEEM studies we are interested in the stimulated echo (SE). There are other "unwanted" echoes which form. Two-pulse Hahn echoes occur corresponding to pulse pairs I and II (echo 1), II and III (echo 2), and I and III (echo 3). The refocused echo (RE) results as microwave pulse III refocuses the 2-pulse echo 1. While performing a 3-pulse ESEEM experiment the time position of the stimulated echo may coincide with the positions of one or more of these "unwanted echoes", giving rise to glitches in the ESEEM pattern (Fauth et al., 1986). If we cycle the phase of the third pulse by 180° only the stimulated echo has its phase cycled as shown in Figure III-2b. We thus readily subtract the unwanted echoes along with the baseline.

Figure III-2 Echoes observed with a 3-Pulse ESE sequence. Figure III-2a shows the various echoes which occur in a typical 3-pulse ESE experiment. The experiment is performed to observe the stimulated echo (SE). Incidental 2-pulse echoes (1,2,3) are formed as well as the refocussed echo (RE). Figure III-2b shows the simple phase cycling which allows us to average only the stimulated echo.

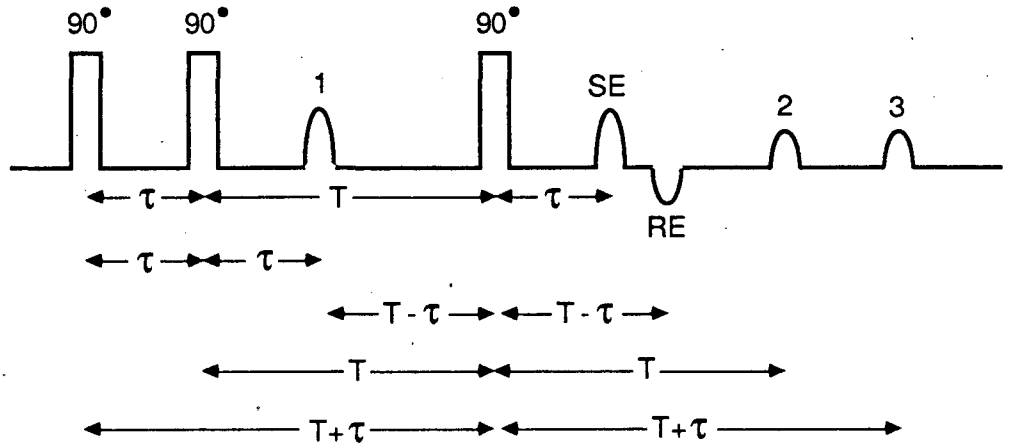

Figure III - 2a . Three-Pulse Spin Echoes

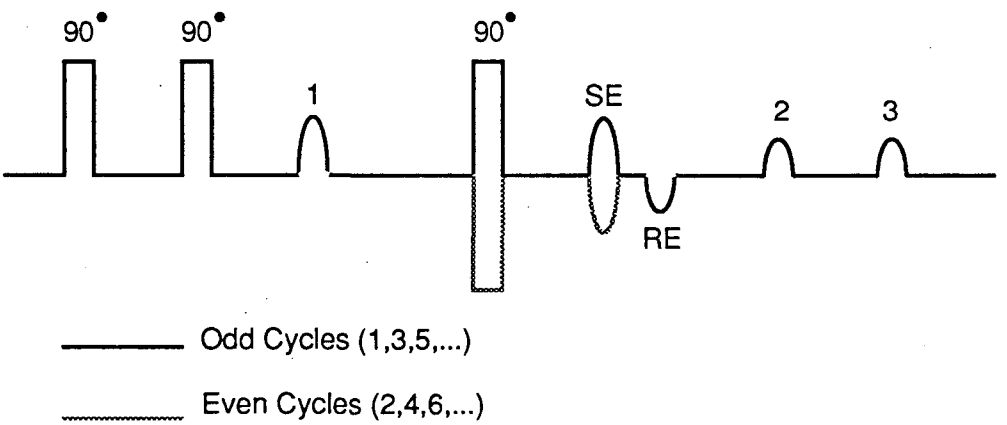

Figure III - 2b . Three-Pulse Phase Cycling

Section 2 — Resonator Assembly

This section describes the construction of the loop-gap based cryogenic probe which we have used in our ESE studies. This section is similar to a paper we have published on this assembly (Britt & Klein, 1987). However, the microwave pulse lengths that we now achieve are much shorter than when the paper was written, so this section contains updated and improved specifications.

The spectrometer produces 12 ns microwave pulses with power levels up to one kilowatt. The bandwidth requirement for admitting such narrow pulses limits the quality factor, Q, for the EPR sample cavity or resonator to a value of a few hundred. A conventional microwave cavity, such as the TE_{102} cavity often used in EPR, has a critically coupled Q of several thousand. Thus the Q must be greatly reduced to meet the bandwidth requirements for pulsed EPR. Without the asset of very high Q, the large volume and resultant poor filling factor of such a cavity limit sensitivity and increase the microwave power necessary to create a given microwave magnetic field amplitude. The stripline transmission cavity of Mims provides a well-tested alternative for pulsed EPR (Mims, 1974). This device has a high filling factor and appropriately low Q, but is inconvenient to use because samples are placed directly into the cavity rather than into conventional EPR tubes, precluding measurements of pulsed and conventional EPR with identical samples. In recent years, other reduced volume resonators have been introduced to EPR (Froncisz & Hyde, 1982, Mehring & Freysoldt, 1980; Lin et al., 1985). We have constructed a low temperature pulsed EPR probe built around the loop-gap resonator of Froncisz and Hyde (1982), taking advantage of its moderate Q and high filling factor. This loop-gap probe mounts in a liquid He immersion dewar. The immersion dewar provides economical operation and excellent stability at temperatures as low as 1.5 K. The first loop-gap probe we constructed used a movable inductive loop to variably couple microwave power to the resonator. This system suffered from excessive microphonics, because the coupling loop vibrated in the bubbling liquid He. This led us to consider a system in which microwave power is coupled to the loop-gap resonator directly through a waveguide or cavity. In designing such a system we were constrained by the relatively small i.d. of the liquid helium dewar (3.2 cm). Many of our samples are poised in an EPR-active state at cryogenic temperatures, and are unstable at room temperature. Thus an additional constraint was provided by the necessity of introducing these samples directly into the resonator while the probe system was immersed in liquid He. This

capability would additionally allow us to change samples without removing the entire probe structure from the liquid He, conserving both liquid He and experimental time. We also planned to use the design for conventional EPR and for ENDOR experiments. In this note we present details of the construction and performance of a loop-gap probe which meets all of these requirements. We have used this system exclusively in our ESE studies of paramagnetic species involved in photosynthetic oxygen evolution (Britt et al., 1987).

The construction of the waveguide-mounted loop-gap resonator is illustrated in Figure III-3. The resonator is assembled within a 1.02 cm wide square teflon body block. This block fits tightly into standard *X* band waveguide with interior dimensions of 1.02 cm by 2.29 cm. The two gold-plated copper arcs which form the "loop" of the resonator fit tightly into a 5.5 mm hole in the teflon block. Small strips of 0.51 mm teflon sheet are placed in a crosswise slit in the block and extend into the resonator gap, holding the two metal arcs firmly in place. The interior diameter of the resonator is 4.0 mm. The resonator length is 5.0 mm. The resulting assembly is quite rigid, requires no adhesives, and is readily cycled between room and cryogenic temperatures. The teflon spacers in the gap affect the capacitance of the resonator and therefore the resonator frequency, which can be varied over several hundred MHz by changing the extent to which the teflon fills the resonator gaps. With the spacer edges aligned with the interior surface of the metal arcs, the assembly resonates at approximately 9.2 GHz.

Figure III-4 displays how the waveguide microwave magnetic field couples into the loop-gap resonator. The resonator resides inside a structure that is effectively a TE_{102} cavity oriented with its long axis vertically in order to fit inside the liquid He dewar. The standing wave magnetic field lines of the cavity couple to the desired axial magnetic field mode of the loop-gap resonator. The resulting coupled system is similar to that observed by placing a loop-gap resonator in a standard TE_{102} cavity at the usual sample position (Anderson et al., 1985). However in this geometry, the loop-gap couples to the field lines running tangentially along the narrow walls of the cavity rather than to the field lines at the cavity center.

A cutaway side view of the actual probe structure is shown in Figure III-5. The loop-gap resonator assembly is mounted adjacent to one of the narrow walls of the TE_{102} cavity. These narrow walls are made of gold-plated brass. The wide side walls are constructed of Macor ceramic (Corning Glass). The interior surfaces support a

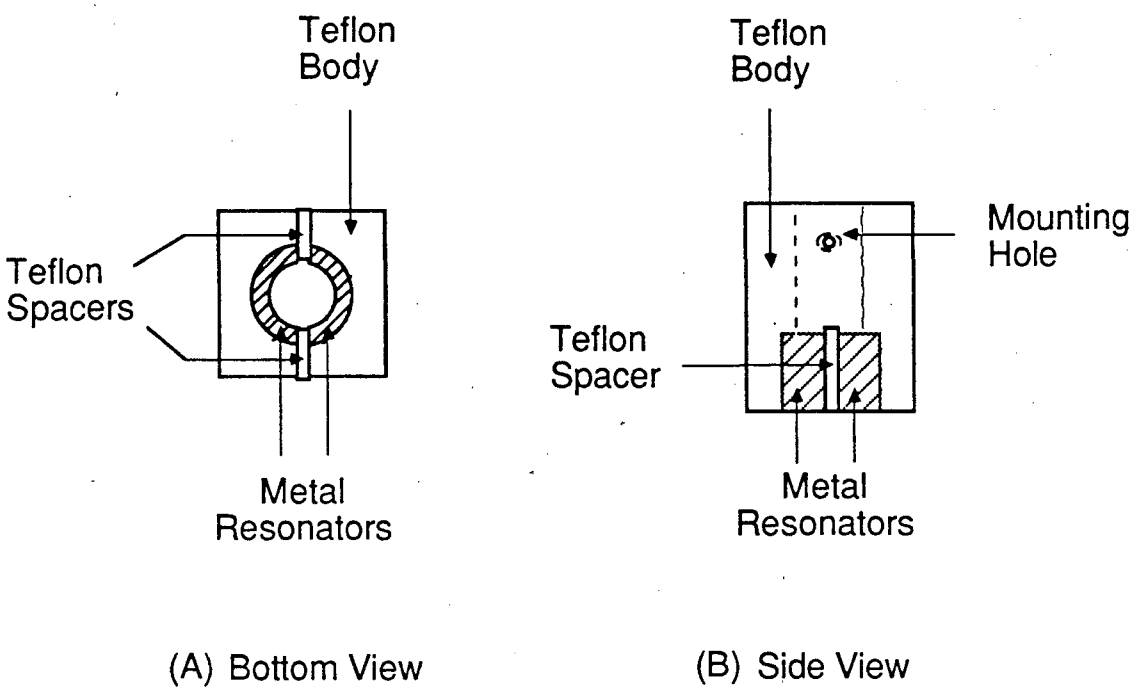

Figure III-3 Design of waveguide-mounted loop-gap resonator. Figure III-3a provides a view from the bottom of the assembly, and Figure III-3b shows a cutaway side view. The resonator is composed of two metal arcs which fit tightly into a hole drilled into a teflon body block. Teflon spacers fit into slots in the body block and extend into the two gaps between the arcs. EPR tubes are introduced from above through a hole in the teflon body block.

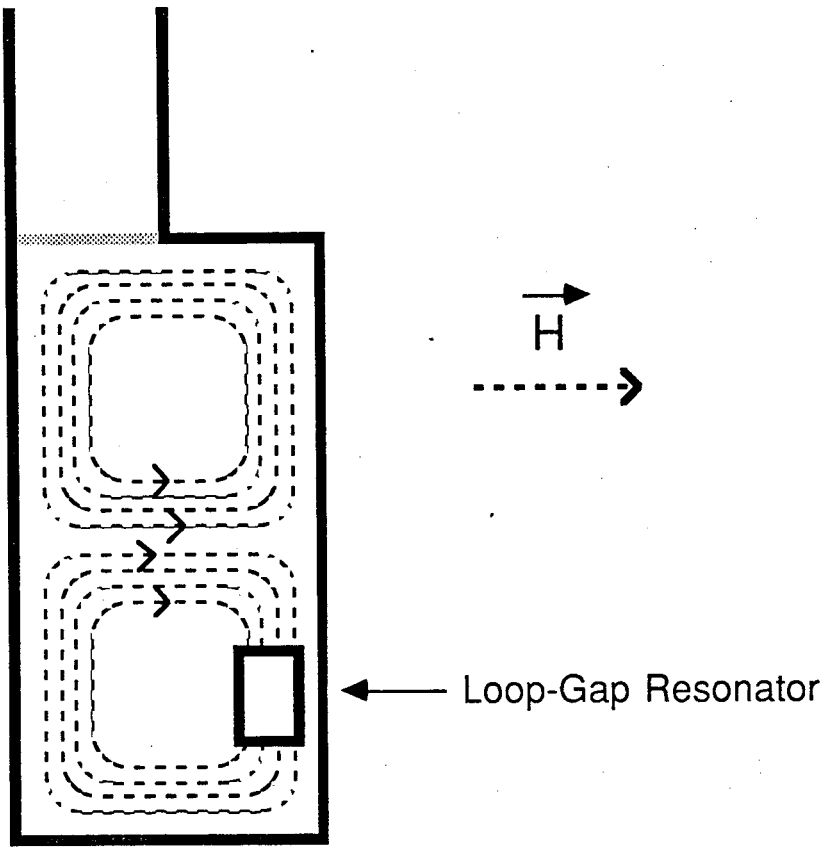

Figure III-4 Mode diagram for coupling microwave power into the loop-gap resonator. The resonator assembly illustrated in Figure III-3 is mounted along the narrow side of a TE_{102} cavity. The microwave magnetic field $\vec{H}$ running along this narrow wall couples into the desired axial mode of the loop-gap resonator.

silver base formed by baking Dupont 7713 conductor composition paint following airbrush application. Approximately 5 μm of gold are electroplated over this base. These ceramic sidewalls are then screwed onto the metal walls. The loop-gap resonator of Fig. 1 fits tightly into this assembly. This construction minimizes rf loss in the cavity walls during field modulation or ENDOR experiments. If only pulsed EPR applications are planned, this section of the assembly could easily be replaced by a short piece of X band waveguide.

Microwave power is coupled into the cavity via a Gordon coupler (Gordon, 1961). A teflon insert fits tightly inside an 8 cm long section of K_u band waveguide (i.d. = 1.58 cm by .79 cm). The position of this insert can be adjusted with a teflon control rod that runs through the waveguide and exits through an H-plane bend above the probe header plate. The teflon insert tapers as a wedge within a K_u band to X band waveguide transition. Thin wall stainless steel X band waveguide extends upward from this adapter to the header plate. The Gordon coupler allows us to widely vary the loaded Q of the resonator while the probe is immersed in liquid He. In addition, the use of the smaller K_u band waveguide provides free space on the resonator side of the cavity, allowing direct access to the sample region from above. Samples in quartz EPR tubes are introduced through a stainless steel guide tube mounted along the axis of the resonator. The upper ends of the EPR tubes are slipped into teflon sleeves which are, in turn, affixed to a stainless steel sample support tube that is inserted in the guide tube.

A screw-operated sliding short forms the bottom of the cavity. The position of the short is initially adjusted to provide maximal coupling to the resonator. In normal operation this is left fixed and further coupling adjustments are made with the Gordon coupler. The sliding short also serves as a bottom stop for the EPR tubes. We operate the probe with the short approximately 1 mm from the bottom of the resonator.

The loop-gap probe assembly is inserted into a liquid He / liquid N_2 dewar pair. The liquid He dewar has a volume of 2.2 liters. Both dewars have narrow tailpieces which fit within the 7.6 cm magnet gap. The i.d. of the inner liquid He dewar tailpiece is 3.18 cm. The top of the liquid He dewar is sealed to a vacuum manifold with an O-ring joint. The header plate of the probe assembly seals to the top of this manifold. Experiments are performed at temperatures as low as 1.5 K by pumping through this manifold. One liquid He fill provides for approximately 15 hours of operation at 4.2 K. This corresponds to about 0.25 liters per hour of operation, including liquid He used

Figure III-5 Cutaway side view of the cryogenic loop-gap probe structure. The resonator assembly is shown mounted in the TE_{102} cavity. The cavity is made with ceramic side walls with a thin metal coating. The EPR sample is introduced from above via a sample guide tube. A Gordon coupler is used to adjust the microwave matching conditions.

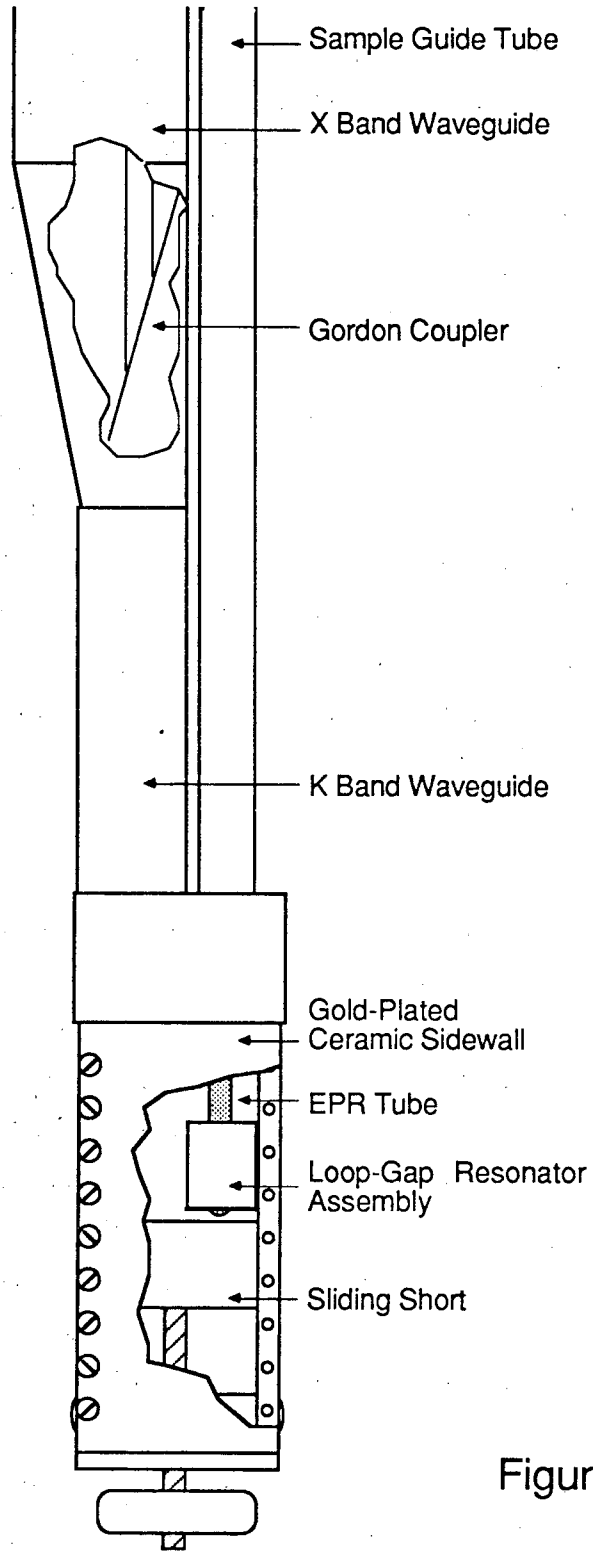

Pulsed EPR Probe

Figure III - 5

in the initial cooldown of the dewar and probe. Experiments can also be performed at temperatures above 4.2 K by flowing cold He gas through the inner dewar and regulating the probe and sample temperature with a manganin wire heating element (Flournoy et al., 1960). Precise temperature measurements are obtained with a carbon glass resistance thermometer epoxied to the cavity.

In typical spin echo experiments, we form microwave pulses of 12 ns length with a PIN diode switch. As previously described, these pulses are amplified to kilowatt levels with the high-power TWT, and the actual pulse power applied to the probe is set by a variable attenuator on the TWT output arm. At a temperature of 4.2 K, the critically coupled Q of the loop-gap resonator is approximately 1300, significantly higher than the corresponding room temperature value of approximately 900. The Gordon coupler is used to overcouple the resonator to achieve the desired Q for pulse applications. Mims has estimated the proper Q for such experiments by matching the resonator bandwidth with the Fourier transform of a Gaussian microwave pulse of width t_p and frequency f_0 (Mims, 1965). The resulting condition is

$$Q \simeq 2\pi f_0 t_p/4 \qquad (III-2)$$

This predicts an optimal Q of approximately 200 for 12 ns X band pulses. With this Q we observe maximal two pulse spin echo amplitudes with a input pulse power of about 100 W. The Q also determines the "dead time" after a pulse during which echoes are obscured by the ringdown of the resonator. With a Q of approximately 200 we observe a "dead time" of about 100 ns. It is often useful to reduce this dead time by further overcoupling the resonator. With a Q of 100 we obtain dead times of about 70 ns. We then require about 160 W input power for maximal echo amplitude.

The frequency of the resonator is essentially independent of the temperature of the surrounding liquid He bath. This allows us to maintain a constant spectrometer frequency in experiments where the sample temperature is varied, even through the 2.17 K λ-point transition of liquid He.

The loop-gap resonator is not unique in providing the high filling factor and moderate Q useful for pulsed EPR. Lin, Bowman, and Norris have introduced the folded half-wave resonator for use in pulsed EPR (1985). This resonator works simply as a half-wave stripline bent about the EPR sample. Such a device can be used in place of the loop-gap resonator in our probe. Mehring and Freysoldt have adapted the slotted tube resonator for pulsed EPR use (1980). In this device a pair of striplines

produce a microwave magnetic field perpendicular to the resonator axis. The slotted tube resonator can also be used in our probe structure by mounting the device halfway up the TE_{102} cavity where it couples to the microwave magnetic field traversing the cavity. The folded half-wave resonator and the slotted tube resonator offer high microwave magnetic field densities comparable with the loop-gap resonator, because they all provide improvement over traditional cavities through reduced volumes and high filling factors. However, the loop-gap resonator provides superior microwave magnetic field homogeneity.

For constant Q and filling factor the power needed for equivalent pulses varies inversely with resonator volume. With a loop-gap resonator of 1.2 mm i.d., Hornak and Freed (1985) observed maximal 2-pulse spin echoes from irradiated quartz at room temperature with only 0.5 W power. However, the small sample volume available with such a resonator limits its utility for studying dilute biological samples.

Section 3 — Computer Interface and Pulse Timing

The electron spin echo spectrometer is controlled by a Digital Equipment Corporation PDP11/34A minicomputer. The PDP11/34A is a 16-bit UNIBUS computer. The computer has 256KB of memory and two RL02 10 MB removable cartridge disk drives, and runs with the RSX-11M multi-user, multi-tasking operating system. Three terminals are connected to the system. A Teletype Model 43 hard-copy terminal is used as an operating console. A DEC VT100 video terminal is used for programming the computer and operating the spectrometer. Data are displayed on a Tektronics 4006 graphics terminal. The PDP11 communicates with the laboratory VAX11/785 via a DEUNA Ethernet controller. Data files are sent over the Ethernet to the VAX for final analysis.

I/O operations are performed with K-series UNIBUS boards. RSX-11 supports a package of K-series drivers which are called as subroutines from FORTRAN programs. The UNIBUS modules installed for I/O applications are listed below:

KW11-K Dual Programmable Real-Time Clock – This device contains two independently programmable crystal oscillator clocks. This is the time base which determines the repetition rate at which experiments are performed. A pulse from the chosen clock output starts a synchronous series of pulses in a homebuilt timing interface which creates the microwave pulses, sets the boxcar, and performs phase cycling. The KW11-K simply determines the number of repetitions to be averaged and the time delay between each repetition.

AD11-K A/D Converter – This is a 16 channel 12-bit successive approximation A/D converter. This device is used to measure the output of the boxcar integrator. It is also used to digitize the magnetic field value in field-swept experiments.

DR11-K Digital I/O Interface – The is a 16-bit digital input/output interface. Digital output from this device is used to control the homebuilt timing interface. The digital delay generators which form the pulse sequences are programmed with BCD code transmitted from the DR11-K. The Programmed Test Sources PTS 500 synthesizer which we have installed for ENDOR experiments is controlled in similar fashion. The first 4 bits of an output word are used to determine the destination for the remaining 12 bits to control. There are thus 16 separate addresses, each of which control 3 BCD decades. The digital delay generators each have a 5 decade dynamic range and thus require 2 addresses each. The PTS

synthesizer has a 10 decade range and requires 4 separate addresses. Strobing an address applies the new data to a set of 74174 D-type flip-flops connected in parallel to the BCD input of the desired device.

AA11-K – This device supplies 4 independent 12-bit D/A outputs. This device is not currently used in ESE experiments.

The rest of this section describes the formation of pulses in the homebuilt timing interface in more detail. All timing programming information is transmitted by the DR11K digital interface. This gives much faster control than can be obtained with a general purpose interface bus such as the IEEE Standard 488. The obvious disadvantage of this approach is that it takes more knowledge and work to design and construct, but we are here for an education.

The key timing elements of the spectrometer are Evans Associates 4145-2 digital delay generators (DDG's). These BCD programmed delay generators provide delays from 0 to 99999 ns in 10 ns increments, with a maximum pulse jitter of less than $\pm$ 2 ns. The timing interface includes 4 of these DDG modules which are all triggered simultaneously in normal use. In an ESE experiment, pulse I is triggered by the DDG #1 reference pulse and pulse II is triggered by the DDG #1 variable delay pulse. If a third microwave pulse is needed it is triggered by the delay of DDG #2. The boxcar gate trigger is provided by the delay from DDG #3. A fourth DDG is included for future expansion. The DDG pulses are routed through front-panel LEMO jacks. A variety of TTL logic devices are also accessible through front-panel ports, so that flexible pulse sequences can be quickly "patched" together with short LEMO cables.

Figure III-6 shows the outputs of different stages of the timing interface for a typical 3-pulse experiment, in this case with τ = 100 ns and T = 500 ns. The first event performed by a computer program designed to create this pulse sequence is to download the desired delay times to the three required DDG's through the DR11K. The KW11-K is given a repetition rate and the pulse sequence is started and repeated at this rate until the program commands a stop. The averaged output of the boxcar is sampled and the program continues to the next step. The figure shows the train of events within a single repetition. Parenthetical numbers in the text reference relevant lines in the figure.

The pulse train begins with output of a 200 ns TTL pulse (1). This negative-going TTL pulse triggers each of the DDG's simultaneously. The DDG reference pulses are

Figure III-6 Primary electron spin echo pulse timing diagram. This diagram shows the principal electronic pulse sequences used in performing a 3-pulse ESE experiment. A pulse from the computer clock B starts the sequence train. Digital delay generators are used to set the microwave switch and boxcar integrator delays. A 4-input NAND gate is used to sum the microwave pulse triggers onto one logic line. These summed pulses are sent to the fast PIN diode switch and the TWT gate with appropriate delays. See text for details of each line.

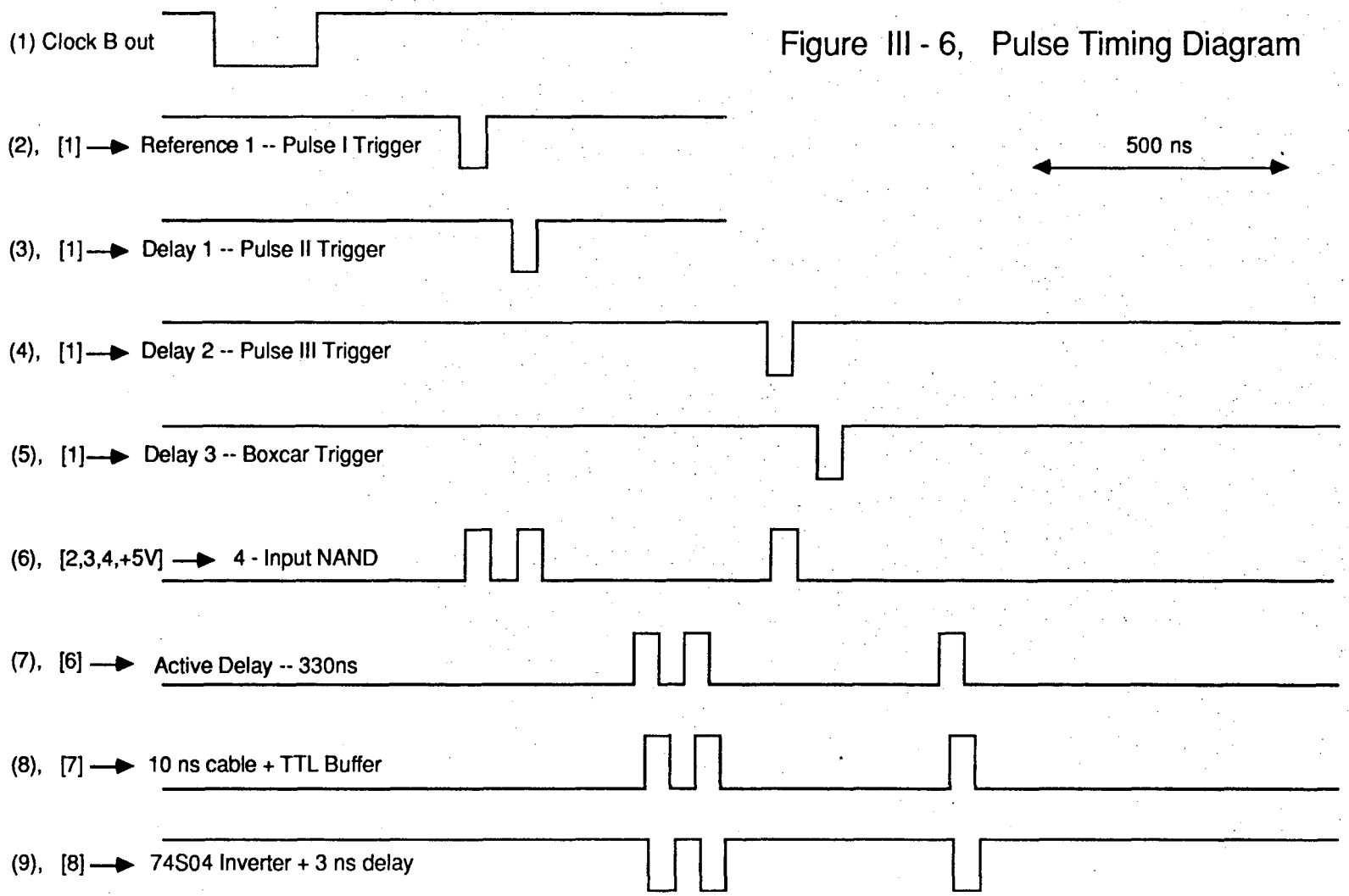

Figure III - 6, Pulse Timing Diagram

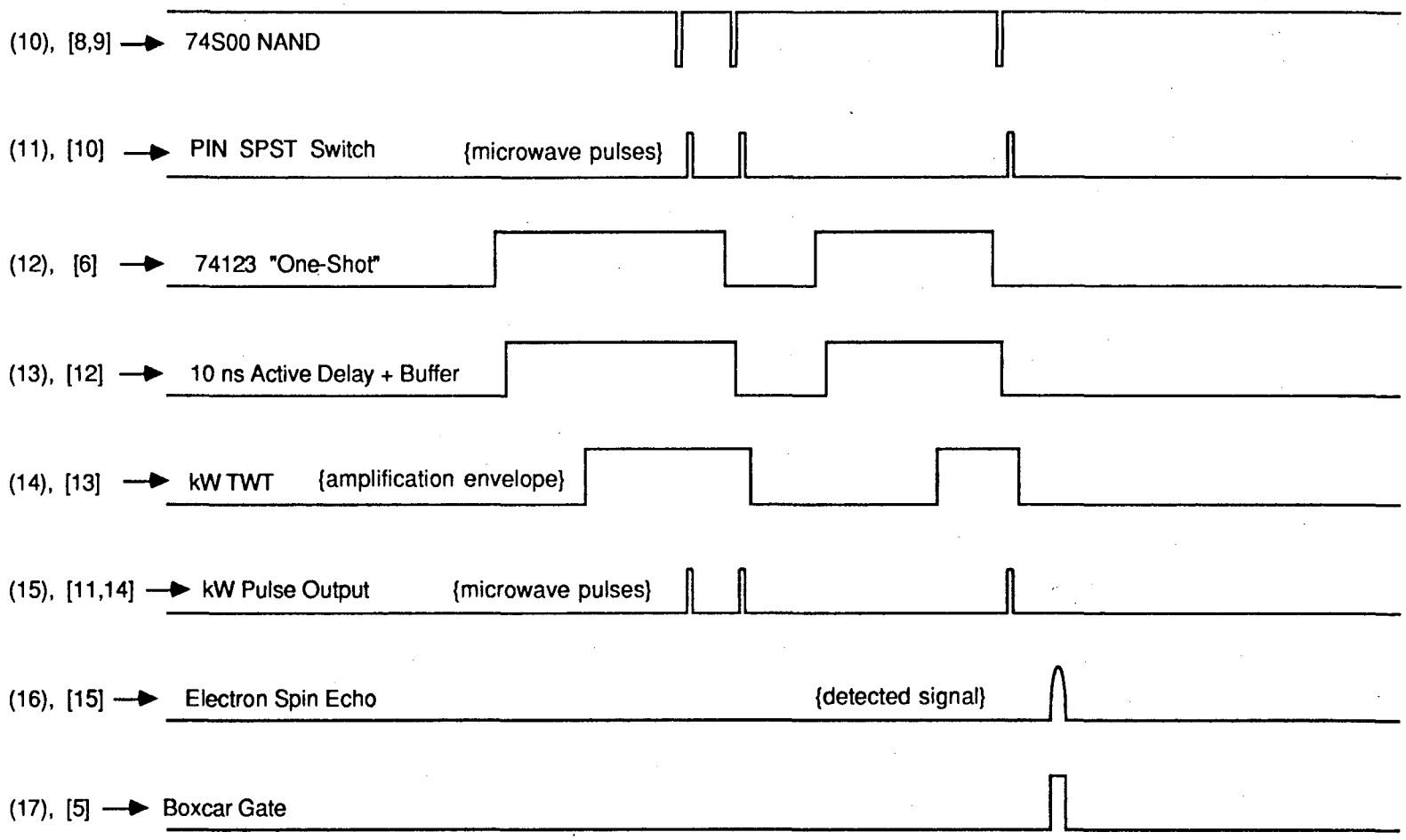

Figure III - 6 continued

generated 480 ns later. As described before, the reference pulse of DDG #1 is used to trigger microwave pulse I (2). The delay pulse from DDG #1 is generated 100 ns later to trigger pulse II (3). The delay output of DDG #2 is formed with a delay from reference of 600 ns to trigger a third microwave pulse for $T = 500$ ns (4). DDG #3 provides a delay of 700 ns to trigger the boxcar gate to coincide with the echo (5). These output pulses are all 50 ns long.

The three microwave pulse triggers are fed into a 74S20 4-input NAND to combine the three pulse triggers onto one logic line (6). The 74Sxx family of Schottky-clamped TTL chips is used wherever possible because of its fast ($\approx$3 ns) switching speed. The NAND output is used to trigger both the fast PIN SPDT switch and the TWT amplifier. Since the TWT has a longer turn-on time than the PIN switch, it is necessary to delay the PIN input pulses so that the input microwave pulse to the TWT will arrive at the proper point in time for high power amplification. The pulse delays are inserted with DDU-7-100 active delay lines manufactured by Data Delay Devices. Each of the DDU-7-100 units provides 9 output lines with 10 ns delay differential between taps. The total delay for each unit is 100 ns. The NAND output is delayed 330 ns with a series of these units (7). The resulting pulse train is sent through a 10 ns cable into a TTL buffer formed by two 74S04 inverters in series (8). The TTL buffer provides nice square pulses to trigger the formation of the actual pulses which drive the PIN switch. These pulses are formed by a 74S00 NAND gate with one input directly from the buffer, and the other input from the buffer, but also inverted and delayed (9). The NAND output forms very clean 10 ns wide pulses (10). These pulses are fed into the PIN switch. The resulting low-power microwave pulses have a 12 ns duration.

The kilowatt TWT has a minimum pulse output of 50 ns. The output pulse is not perfectly square. There is a some of an overshoot as the pulse comes on followed by an undershoot. The pulse level reaches a steady value after about 100 ns. We obtain good ESE pulses if we set the TWT gate for a pulse of 150 ns duration and feed in the low power pulses so that they are amplified in the last portion of the gain envelope before the TWT is shut off. We set the pulses as close as possible to the shut-off transition to minimize the final deadtime. The TWT switching delay is longer for turn-on than for turn-off. Therefore we use a 330 ns input pulse to create a 150 ns amplification pulse. Since we may use pulse intervals shorter than the 330 ns TWT trigger width, we use a 74123 retriggerable monostable multivibrator to form the TWT input pulses.

The initial NAND output containing the pulse delays is fed into the 74123 (12). The 74123 "one-shot" is triggered by the first pulse, and retriggered by the second pulse before its output has returned to logical 0. One long (430 ns) pulse is formed. The third input pulse arrives after the 74123 has reset to 0. This pulse simply triggers a new 330 ns output pulse. The 74123 output is sent into another DDU-7-100 delay for a 10 ns delay and through another TTL buffer (13). This buffered pulse train actives the TWT gain (14), amplifying the low-power pulses to kW levels (15). This gives rise to an electron spin echo (16). The demodulated spin echo signal is integrated by the boxcar gate which follows the boxcar trigger by a suitable internal delay (17).

The necessity for phase cycling has been previously described. The circuitry to implement this is shown in Figure III-7. The Clock B output is used to trigger a type T flip-flop (18). The output of this flip-flop alternates between pulse repetitions. The DDG output representing the pulse to be phase shifted is tapped and fed into a 74123 "one-shot" (19). The length of this pulse is set to provide a final phase shift pulse that is well-centered about the microwave pulse. The 74123 output is inverted (20) and used to trigger a second 74123 with a 50 ns output pulse (21). This 50 ns pulse is applied to a NAND gate along with the alternating flip-flop output (22). The NAND output is applied to the bi-phase modulator, which shifts the phase of the desired pulse by 180° between each repetition (23).

Figure III-8 shows the simple circuitry for "blanking" the applied high power pulses in the receiver. The same "one-shot" output used to drive the TWT is delayed an appropriate amount (24) and used to gate the PIN switch in the receiver (25). The amount of delay is chosen to blank the pulses without affecting the spin echo (26,27). We typically achieve a deadtime of about 70 ns.

Figure III-7 Phase timing diagram. This figure shows the electronic timing sequences used to flip the phase of a given microwave pulse on alternate repetitions. The computer clock B triggers a type T flip-flop. The alternating logic output of the flip-flop is entered into a NAND gate along with the appropriately delayed pulse trigger. The resultant output toggles the biphase modulator, which alternates the phase of the desired microwave pulse (Pulse III in the figure).

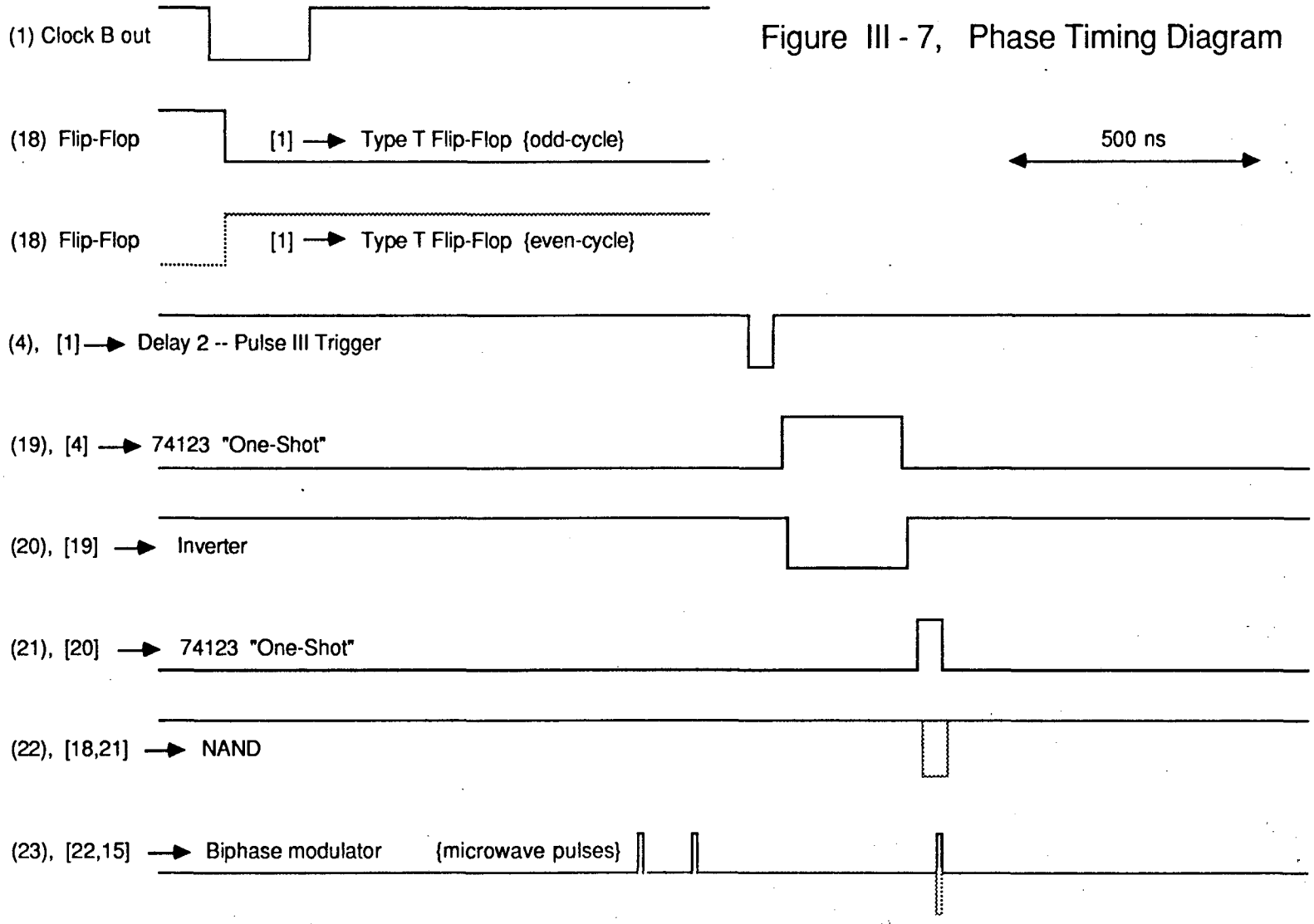

Figure III - 7, Phase Timing Diagram

Figure III-8 Receiver blanking diagram. This figure shows the electronic pulse sequences used to shut off the receiver during the high power microwave pulses. The same 74123 monostable multivibrator output used to trigger the TWT gate is fed into the receiver PIN switch with appropriate delay. The PIN switch shuts off during the time that the TWT gate is on.

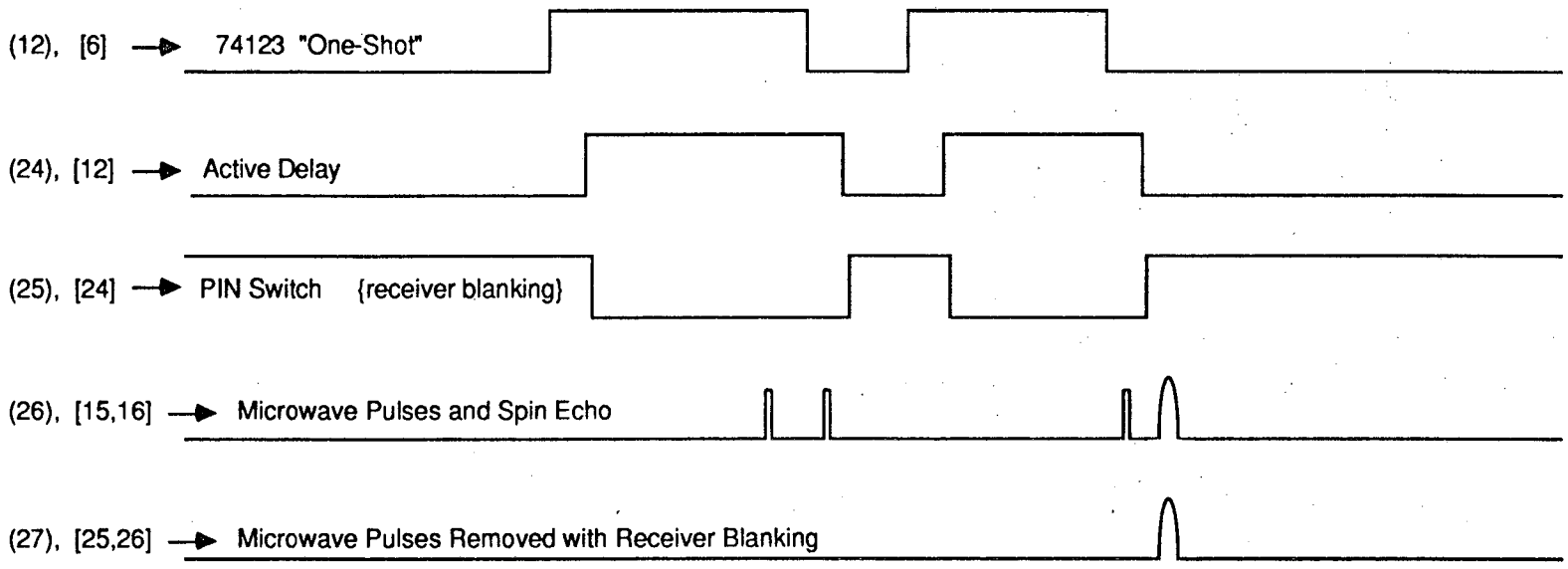

Figure III - 8, Receiver Blanking Diagram

Chapter IV – ESEEM of Mixed Valence Mn Compounds

In this chapter we discuss the results of ESEEM studies on mixed valence Mn compounds, in particular di-μ-oxo bridged Mn(III)Mn(IV) dimers with 2,2'-bipyridine or 1,10-phenanthroline ligands. These mixed valence Mn compounds give rise to sixteen line EPR spectra similar to the Mn multiline EPR spectrum associated with photosynthetic oxygen evolution. ESEEM results obtained from these compounds can be used as a basis for interpreting the results from the PSII signal. In particular, we focus our efforts on examining the ^{14}N ESEEM observed with these compounds.

More generally, mixed valence transition metal centers are interesting for their electron transport and storage properties, both in inorganic model systems and in the large number of biological centers which employ two or more interacting metal centers for such functions. Section 1 of this chapter provides some general background material on mixed valence transition metal systems. Section 2 discusses specifics of the mixed valence Mn systems. Sections 3 and 4 present our ESEEM results and interpretations.

Section 1 – Mixed Valence Classes

Mixed valence materials contain an element in more than one oxidation state. In this chapter, we focus on transition metal mixed valence compounds. This has been an active area of study for the past two decades, with much interest generated by systematic reviews in 1967 by Robin and Day, Hush, and Allen and Hush. In particular, the Hush article provides a theoretical link between mixed valence physical parameters and rates of electron transport. Much work has progressed in this area with model systems, particularly with coupled $d^5 - d^6$ metal ions (see for example the review by C. Creutz, 1983). An excellent example of such extensive research activity can be seen by examining the literature on the Creutz-Taube complex, $[Ru(NH_3)_5]_2L\text{–}L^{5+}$, L–L=pyrazine (Cruetz and Taube, 1969). Over one hundred compounds of similar structure have been synthesized and physically characterized (Cruetz, 1983).

We start by reviewing the mixed valence classification scheme of Robin and Day (1967). Class I systems represent the limit of weak coupling between the metal ions. All physical properties of the system result as the simple sum of the properties of the individual ions. Such weak coupling may result from greatly different symmetries or ligand field environments for the ions. The opposite coupling limit is represented by

class III systems, where the coupling between ions is sufficiently large that physical properties of the system can no longer be treated as arising from the sum of the discrete components. Physical properties must be considered to arise from the complex as a whole. The intermediate regime is represented by class II systems, where the basic properties reflect the sum of the individual ions, but a weak to moderate interaction introduces added effects as perturbations.

These three classes are represented schematically by the potential energy surfaces shown in Figure IV-1. Each curve represents the energy of a state of the system along a particular configuration coordinate. For simplicity the figures are drawn for the special case of symmetric mixed valence dimers. The configuration coordinate is a one-dimensional representation of nuclear position. The zeroth-order potential energy surface reflects a harmonic potential energy curve.

We begin with the class I situation which results in the limit of extremely weak interaction between the two individual ions. In the class I limit, the potential energy surfaces for the two ions are are minimally perturbed. Each energy surface may be represented in the configuration coordinate diagram as a harmonic potential well with little distortion at the intersection of the two curves. The rate of thermal electron transfer tends to zero in the class I limit. The intervalence band energy is denoted λ. However the intensity of this intervalence band also approaches zero in the class I limit. The energy where the two surfaces intersect is denoted ΔG. For a symmetric harmonic system we can simply relate the two energy values by

$$\Delta G = \lambda/4. \qquad (IV-1)$$

A class II system results if the coupling between the two ions is not negligible. The interaction energy J between the two ions creates an energy splitting of $2J$ at the point of intersection. We may view the resulting states as two distinct molecular orbitals. The excited state molecular orbital presents a single minimum. However, the resulting ground state orbital presents two separate minima, representing the two oxidation state isomers. An electron can pass adiabatically from one well to the other, so thermal electron transfer is allowed in the class II system. The class III situation arises in the limit where the coupling becomes very strong, $J \geq \lambda/2$, and the two separate minima disappear. In this case the electronic system is completely delocalized.

Figure IV-1 Classification of mixed valence systems in the scheme of Robin and Day (1967). The three figures represent the energy surface for each class of symmetric mixed valence transition metal centers. The class I system represents the limit of very weak coupling between the two ions. The harmonic potential wells are only slightly perturbed in this limit where the interaction energy J approaches zero. In this limit thermal electron transfer is nonadiabatic. Thermal electron transfer tends not to occur at the intersection of the two energy surfaces. The energy difference denoted λ represents the intervalence transfer band energy. However, the intensity of this intervalence band is weak in the class I limit. The energy ΔG is the energy surface value where the two surfaces intersect. The interaction energy J in the class II system is sufficient to distort the individual energy surfaces. The result is a ground state surface with two distinct minima and an excited state surface with a single minimum. Thermal electron transfer is allowed in these systems. The intervalence transfer band may be moderately intense for class II systems. For class III systems the interaction is sufficiently strong to completely remove the two local energy minima. This occurs when $J \geq \lambda/2$. The resulting system is completely delocalized.

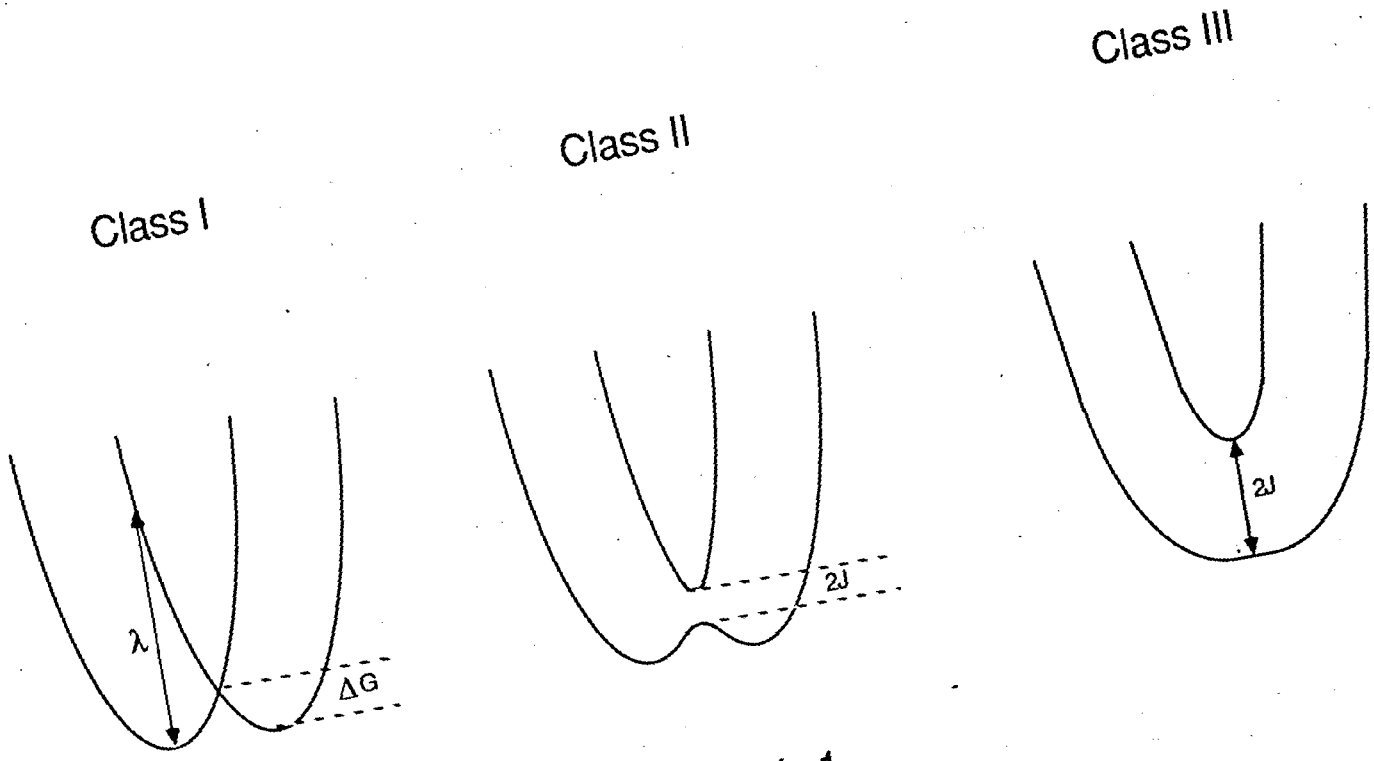

Figure IV - 1

The class II case is of particular interest for both optical and electron transfer properties. Figure IV-2 shows the class II energy surface for a symmetric Mn(III)Mn(IV) dimer. For expository purposes we assume that we can distinguish the two Mn ions as Mn_a and Mn_b. The ground state potential energy minimum on the left side of the figure then represents the Mn_a(III)Mn_b(IV) configuration, and the right side energy minimum represents the Mn_a(IV)Mn_b(III) configuration. The two potential minima are connected as previously described, and thermal electron transfer may occur between the two configurations. The configuration coordinate labeled A represents the set of nuclear positions which minimizes the system energy for the Mn_a(III)Mn_b(IV) configuration. The system may absorb a photon of energy E_{op} with the promotion of an electron to the excited state molecular orbital. The system may relax from this excited state to either isomerization minimum in the ground state. Thus the optical absorption may promote electron transfer between the two isomerization states. The presence of such an optical electron transfer feature is a indication of a class II system. We note that the analogous class I transition, denoted by λ in Figure IV-1, becomes formally forbidden in the limit of zero interaction.

In addition to optical electron transfer, class II systems can also undergo thermal electron transfer. We again refer to Figure IV-2, and assume that we begin in the Mn_a(III)Mn_b(IV) configuration. At nonzero temperature the coupled system may achieve the energy E_{th} required to reach the configuration coordinate denoted B. From this position a labile electron may be transferred to the other Mn ion, resulting in the Mn_a(IV)Mn_b(III) configuration. This transfer occurs with unit probability if the adiabaticity factor κ is unity. In the limit of small coupling we can write in analogy to equation IV-1,

$$E_{th} \approx E_{op}/4. \qquad (IV-2)$$

For this symmetric system, $E_{th} = \Delta G_{th}$, and the reaction rate for thermal electron transfer can be written as

$$k_{th} \approx \kappa \nu_n exp(-E_{op}/4kT), \qquad (IV-3)$$

where $\nu_n \approx 5 \times 10^{12} sec^{-1}$ is the nuclear frequency factor. This simple theory of Hush (1967) gives an approximate estimate of thermal electron transfer rates from measured optical band properties.

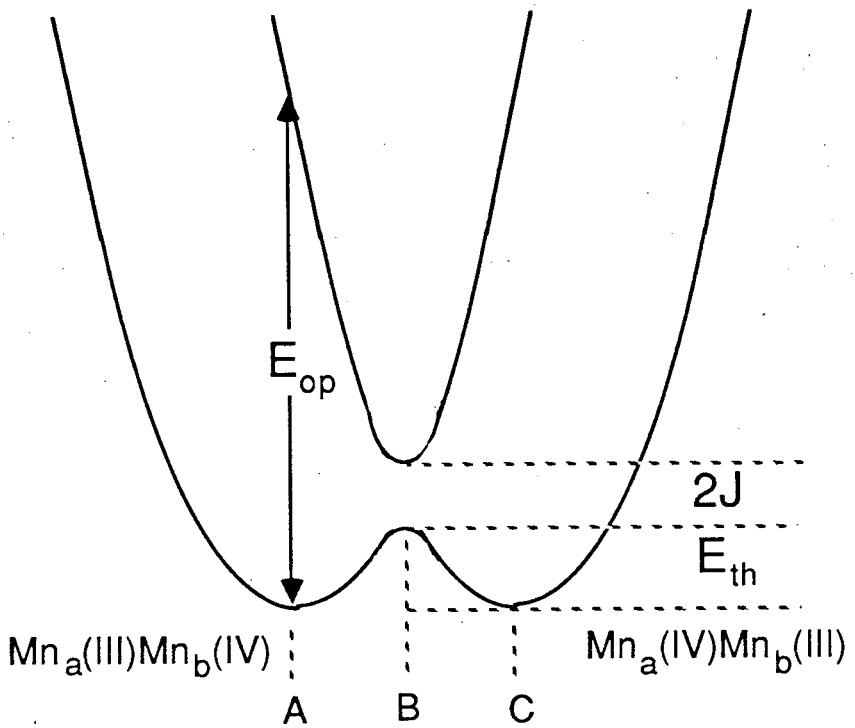

Figure IV-2 Details of the energy surface for a symmetric class II Mn(III)Mn(IV) system. The theory of Hush (1967) relates the energy E_{op} of the partially allowed optically induced transition to the thermal barrier energy E_{th}, which in turn can be used to calculate rates of thermal electron transfer.

Section 2 – Mixed Valence Mn Dimers

In this section we discuss in detail the structure of the mixed valence Mn dimer systems which we have studied via ESEEM. Figure IV-3 shows the central structure of the di-μ-oxo bridged Mn(III)Mn(IV) dimers and both the 2,2'-bipyridine (bipy) and 1,10- phenanthroline (phen) ligands. The bipyridyl and phenanthroline ligands are both bidentate aromatic heterocycles, and are often used by inorganic chemists to stabilize a wide range of transition metal oxidation states. In the di-μ-oxo bridged Mn(III)Mn(IV) dimers, these bidentate compounds provide four terminal N ligands to each of the two Mn ions. The goal of our ESEEM studies is to measure the ^{14}N superhyperfine frequencies and examine the physical origins of these frequencies. The majority of our studies have been with the Mn(III)Mn(IV) bipyridyl dimer. The results with the Mn(III)Mn(IV) phenanthroline dimer are almost identical. For the rest of the chapter we will mainly concentrate on the bipyridyl system, though we will introduce remarks of comparison with the phenanthroline system where appropriate.

The X-ray crystal structure of the bipyridyl Mn(III)Mn(IV) compound was solved by Plaksin et al. (1972). The local structure about the Mn ions is shown in Figure IV-4. The structure shows a marked asymmetry of bond lengths about the two different Mn centers. The bonds about the ion denoted MN2 are all appreciably shorter than for the ion denoted MN1. For example, the MN2-O bond lengths are 1.784 Å and the MN1-O bond lengths average 1.854 Å. This suggests that we can identify MN2 with the Mn(IV) and MN1 with the Mn(III). Therefore the dimer has deeply trapped valences, and the dimer cannot belong to the mixed valence class III. On the MN2 side, there is a slight difference in the bond lengths to the equatorial and axial N ligands. The equatorial MN2-N bonds have a length 2.075 Å, compared with 2.016 Å and 2.028 Å for the axial MN2-N bonds. This small difference arises from the trans influence of the more electronegative bridging oxygens on the equatorial nitrogen bonds. These sets of distances are very similar to those found in the crystal structure of the phenanthroline Mn(IV)Mn(IV) dimer (Stebler et al., 1986). For this compound, with both Mn ions in the (IV) oxidation state, the average equatorial Mn-N distance is 2.076 Å, and the average axial Mn-N distance is 2.010 Å. This is further indication that the MN2 $\equiv$ Mn(IV) assignment is correct.

The difference between axial and equatorial Mn-N distances is much greater for the ion denoted MN1. The average axial MN1-N bond length is 2.217 Å, vs. only 2.131 Å for the equatorial MN1-N bond lengths. Plaskin et al. (1972) considered this

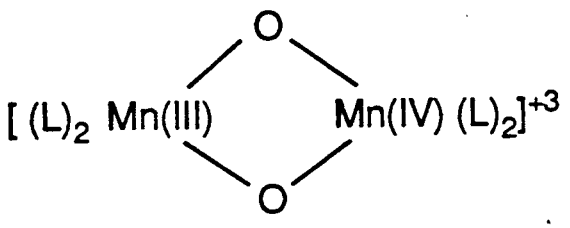

with L = 2,2'-bipyridine (bipy)

or L = 1,10-phenanthroline (phen)

bipy =

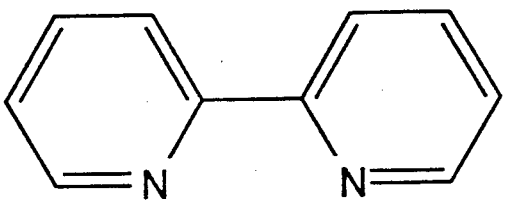

phen =

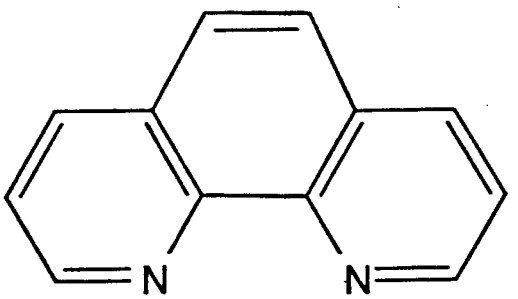

Figure IV-3 Chemical structure of the Mn(III)Mn(IV) models examined in this chapter. The upper figure shows the core structure with the di-μ-oxo bridged Mn ions. Each of the Mn ions is terminally capped by two bidentate ligands, either 2,2'-bipyridine (bipy) or 1,10-phenanthroline (phen). The structures of these ligands are shown in the lower portion of the figure.

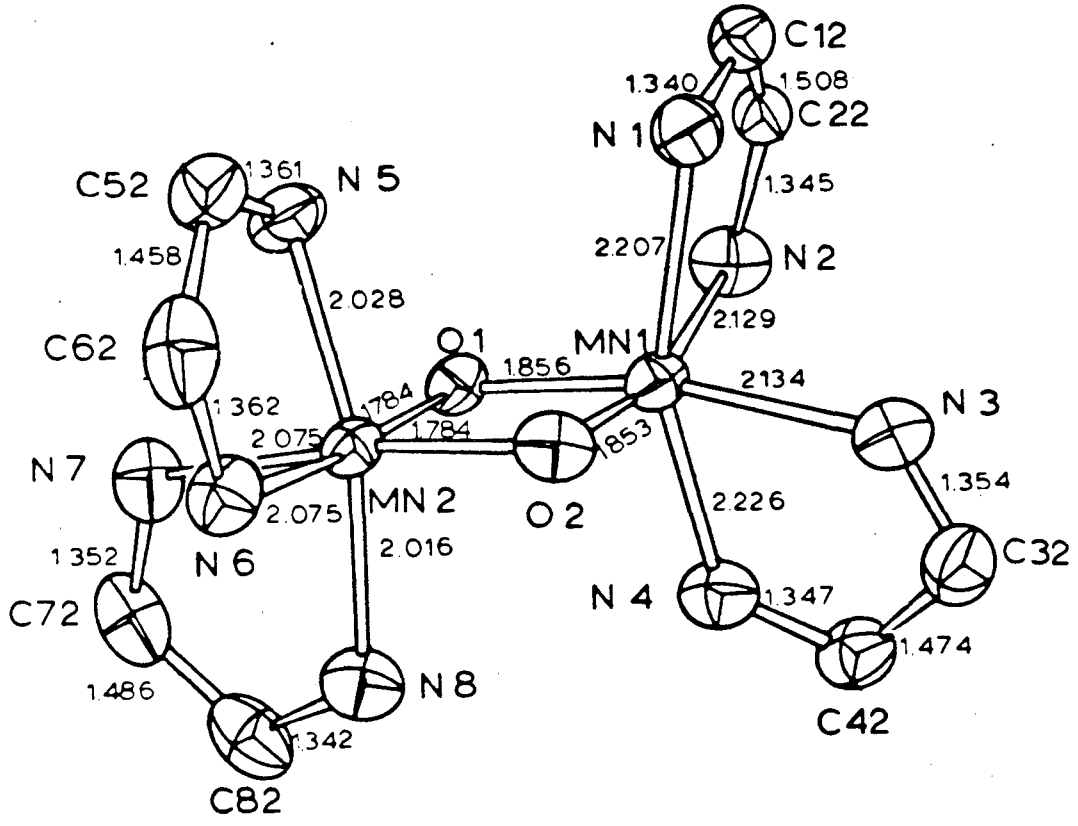

XBL 7511-9090

Figure IV-4 Structure of the core of the Mn(III)Mn(IV) bipyridyl dimer as determined by X-ray crystallography (Plaksin et al., 1972).

to be further evidence that MN1 can be assigned to the Mn(III) ion, because such a large difference likely originates in the Jahn-Teller effect for the d^4 Mn(III) ion. If we assume an equatorial elongation of 0.053 Å due to the trans oxo bridges, the resultant Jahn-Teller distortion is about 0.138 Å. This is very similar to the reported distortion of 0.141 Å for isolated Mn(III) complexes (Nyholm and Turco, 1960).

Figure IV-5 shows how Jahn-Teller distortion arises for a high-spin d^4 ion such as Mn(III). The left side of the figure shows the energy levels for an octahedral complex. The octahedral crystal field splits the d-orbital energies into two groups. The low energy group is the triply degenerate t_{2g} group composed of the d_{xy}, d_{xz}, and d_{yz} orbitals. The doubly degenerate e_g group contains the d_{z^2} and $d_{x^2-y^2}$ orbitals, and is at an energy Δ_0 higher than the t_{2g} group. The origin of this level splitting is easily understood. The d_{z^2} and $d_{x^2-y^2}$ orbitals project directly toward the octahedrally coordinating ligands. The electrostatic repulsion is greater for these two orbitals than for the d_{xy}, d_{xz}, and d_{yz} orbitals which are directed between the ligands. In almost all octahedral Mn(III) complexes the energy required to pair electrons within an orbital is greater than the crystal field splitting Δ_0. The ion thus assumes the ${}^5E_g(t_{2g}^3 e_g)$ high-spin configuration shown in the figure. For perfect octahedral symmetry this state is doubly degenerate. The e_g electron can occupy either the d_{z^2} or $d_{x^2-y^2}$ orbital with identical total system energy. A lower energy system can be obtained if the complex undergoes tetragonal elongation, as shown in the right half of the figure. The d_{z^2} orbital will have a lower energy than the $d_{x^2-y^2}$ orbital. This energy splitting is designated δ_1. The single e_g electron can reside in the low energy d_{z^2} orbital. The t_{2g} group also splits as a result of tetragonal elongation, but the sum energy of the three levels is constant. By undergoing the Jahn-Teller distortion, the total energy of the complex is reduced by $\delta_1/2$.

The observed inequivalence of Mn(III) and Mn(IV) in the X-ray crystal structure is actually rather interesting. The fact that the crystal structure shows this inequivalence means that that the crystal lattice forces are great enough to prevent end-to-end substitution during growth, and that there is no oxidation state isomerization within the crystal. We will demonstrate below that optical measurements in solution predict a thermal electron transfer rate at room temperature on the order of $10^6 s^{-1}$. It seems that the extremely deep trapping in the crystal is largely a lattice energy effect. In fact for the very similar Mn(III)Mn(IV) phenanthroline dimer, the crystal structure results are symmetric (Stebler et al., 1986). In this case either the crystal is formed with

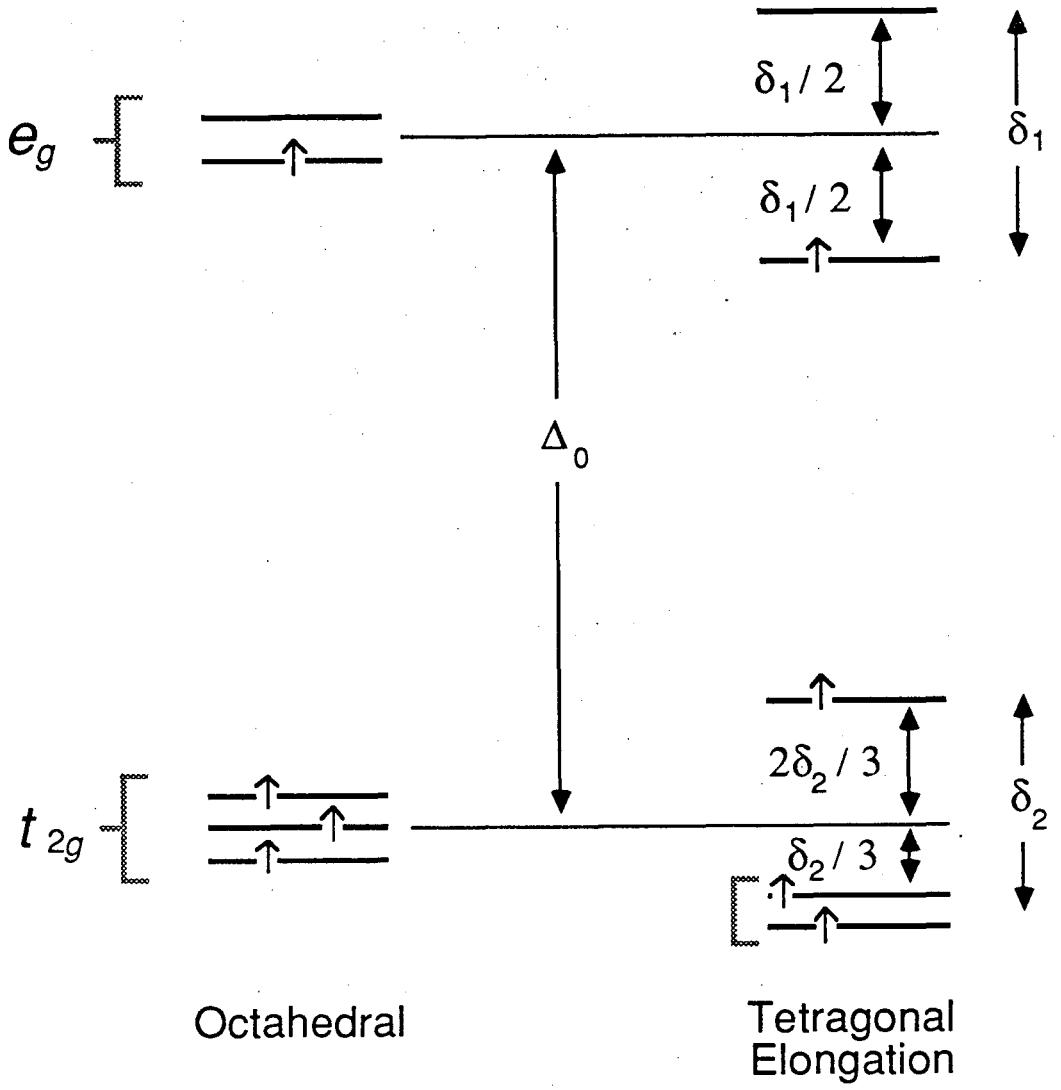

Figure IV-5 Illustration of Jahn-Teller distortion for a high-spin d^4 ion. The left side of the figure shows the energy levels for a perfect octahedral complex. The right side of the figures shows the energy levels with the addition of a tetragonal elongation, resulting in a lowered total system energy.

end-to-end disorder, or intervalence thermal electron transfer occurs on a time scale short compared to the duration of the crystal growth and X-ray data acquisition.

We now turn to solution studies. In the same paper which displayed the bipyridyl Mn(III)Mn(IV) dimer crystal structure, Plaksin et al. (1972) reported magnetic susceptibility studies which showed an antiferromagnetic coupling between the two Mn ions. They interpreted this as arising by a superexchange mechanism through the di-μ-oxy bridge, with the zeroth order states arising from d^3 and high-spin d^4 ions. No intervalence optical bands were reported in this study.

Thorough optical studies of the Mn(III)Mn(IV) dimers were performed by Cooper and Calvin (1977). The optical spectra show absorption bands at 525, 555, and 684 nm which are similar to bands in the isolated Mn(III) compound bis-(malonato)diaquo Mn(III) (Dingle, 1966). The Mn(IV) $d \rightarrow d^*$ transitions are thought to be in the ultraviolet region of the spectrum, and are likely obscured by strong ligand $\pi \rightarrow \pi^*$ transitions. The existence of optical transitions comparable to those in isolated Mn(III) systems shows that the exchanged coupled dimers are not class III systems, even in solution.

The most interesting aspect of the reported optical spectra is a broad near-infrared band not present in the Mn(III) monomer or in the Mn(IV)Mn(IV) phenanthroline dimer. The maximum of this band is at about 830 nm. The band was thought to originate from a class II mixed valence transition. This assignment was confirmed by pH dependence studies which demonstrated a reversible disappearance of the band correlated with a change in the magnetic susceptibility reflecting the acidic cleaving of the di-μ-oxy bridge.

From a molecular orbital theory point of view, it is not surprising that these compounds are class II rather than class III. The intervalence electron transfer involves removing an electron from one e_g^* orbital and placing it in another. These e_g^* orbitals are antibonding in these systems, and therefor there is a large reorganization energy associated with the removal or addition of an electron to these orbitals. Class III systems often involve electron transfer among non-bonding orbitals. A good example of this principle can be found in class III Fe-S clusters, where electronic rearrangement involves t_{2g} orbitals which are non-bonding for tetrahedral Fe (Holm et al., 1974).

Cooper and Calvin (1977) applied the previously described theory of Hush to calculate the thermal electron transfer rate. The assignment of E_{op} = 830 nm gives a thermal energy barrier of 8.6 kcal mol^{-1}. Assuming an adiabaticity factor of unity

and no activation entropy, they arrived at a maximum thermal electron transfer rate of $10^{-6}s^{-1}$ at 298 K.

The rate of electron transfer is important in determining the result of physical measurements. If the electron transfer is fast in comparison to the timescale of a physical phenomenon, an averaged result will be observed. If the electron transfer is slow compared to the timescale of interest, physical measurements will reveal results attributable to the individual ion states. Cooper (1976) looked for the Mn-ligand stretching frequencies to test if the bipyridyl dimer was averaged on the far-infrared timescale ($\approx 10^{13}s^{-1}$) and was able to tentatively assign Mn(III)-N and Mn(IV)-N stretching frequencies for both the bipyridyl and phenanthroline mixed valence dimers. To explore a longer timescale, Cooper et al. (1978) performed EPR experiments on the mixed valence species. The temperature dependences of the magnetic susceptibilities were also reported over a range from 4 to 250 K. The complexes were seen to have strong antiferromagnetic coupling, with J = -150 cm^{-1} for the bipyridyl Mn(III)Mn(IV) dimer and J = -134 cm^{-1} for the phenanthroline Mn(III)Mn(IV) dimer. Similar values of the exchange coupling J for the phenanthroline dimer were later reported by Stebler et al. (1986).

The bipyridyl and phenanthroline Mn(III)Mn(IV) dimers show identical EPR spectra. The spectra present 16 well-resolved Mn hyperfine lines (see Figure IV-7 for the Mn(III)Mn(IV) bipyridyl spectrum as obtained by ESE). Cooper et al. (1978) analyzed the EPR features using the spin Hamiltonian

$$\mathcal{H}_S = g_{||}\beta H_z S_z + g_\perp \beta (H_x S_x + H_y S_y) + (A_1 I_1 + A_2 I_2) S - 2J S_1 S_2. \quad (IV-4)$$

Axial symmetry is assumed, with $g_{||}$ and $g_\perp$ representing the parallel and perpendicular components of the g-tensor. J is the isotropic spin exchange energy between the Mn(III) and Mn(IV) ions. S is the total spin ($S = S_1 + S_2$). A_1 and A_2 are the respective hyperfine coupling tensors for the Mn(III) and Mn(IV) ions. The allowed transition energies are obtained through second order as

$$E_M - E_{M-1} = g\beta H + (A_1 m_1 + A_2 m_2) + (2g\beta H)^{-1}(A_1^2(I_1(I+1) - m_1^2) + A_2^2(I_2(I_2+1) - m_2^2)). \quad (IV-5)$$

where m_1 and m_2 are the two Mn nuclear quantum numbers, and g is defined by

$$g^2 = g_{||}^2 cos^2\theta + g_\perp^2 sin^2\theta, \quad (IV-6)$$

with θ the angle between the magnetic field and the axial g-tensor symmetry axis. This equation gives a good fit to the experimental data with A_1 = 167 G and A_2= 79 G. The approximate 2:1 ratio of these hyperfine values results from projecting the nearly identical hyperfine values for the individual Mn ions upon the effective S=1/2 state resulting from the strong antiferromagnetic coupling between the ions (Valentine et al., 1977). Many of the EPR transitions are thus degenerate, and 16 EPR lines are observed rather than the full set of 36 lines predicted by equation I-3. The perturbation calculation is taken to second order because of the large value of the Mn hyperfine couplings which cause a non-negligible mixing between the electronic states. The fact that two distinct hyperfine constants are resolved demonstrates that electron transfer is slow on the EPR timescale. Otherwise, an 11 line EPR spectrum would be observed. Such inequivalence in hyperfine values was reported up to the maximum observation temperature of 298 K.

The linewidths of the EPR spectral features provide a measure of the maximum electron transfer rate. In solution studies at 298 K, the individual transitions show a linewidth of 30 G. The maximum electron transfer rate is thus about $10^8 s^{-1}$. Below 120 K in a glassy medium the linewidths are about 10 G. The electron transfer rate is therefore slower than about $3 \times 10^7 s^{-1}$ at these temperatures. We stress that these are the maximum possible electron transfer rates. The linewidths are most probably first limited by more ordinary T_2 processes. We again note that the Hush theory predicts a maximal rate of about $10^6 s^{-1}$ at room temperature.

The Mn(III)Mn(IV) bipyridyl dimer shows no resolved ^{14}N coupling in its EPR spectrum. However, the individual EPR linewidths are decreased in the analogous complex $(bipyO)_2Mn(III)Mn(IV)(bipyO)_2$ [bipyO≡ 2,2'-bipyridine-N,N'-dioxide], which has no directly coordinating nitrogen (Dismukes et al. 1982). This result provides evidence for a small amount of ^{14}N superhyperfine coupling to the electron spin.

Section 3 – Electron Spin Echo Results

The remainder of this chapter discusses electron spin echo results obtained for the mixed valence Mn dimers. It is particularly important for low temperature ESE studies to obtain a good glass in order to prevent solute aggregation. We obtained good results for the Mn dimer systems by preparing sample concentrations of about 2 mM in a 50% acetonitrile (CH_3CN) /50% methylene chloride (CH_2Cl_2) solution. A good glass is formed by slowly freezing the resulting solution. ESEEM results were repeated with ^{15}N substituted acetonitrile to check for any possible modulation from solvent nitrogen. The ESEEM results with ^{15}N-acetonitrile are identical to those obtained with ^{14}N-acetonitrile, showing no modulation contribution from the solvent. All reported experiments were performed at a temperature of 4.2 K. The spin echo microwave pulses were of 12 ns duration.

Figure IV-7 shows the field swept 2-pulse ESE spectrum for the di-μ-oxo bridged Mn(III)Mn(IV) bipyridyl dimer. This spectrum was obtained by measuring the amplitude of the spin echo during a 2500 Gauss wide field sweep. The value of τ for the 2-pulse echo is 380 ns. The spectrum reveals 16 clearly resolved hyperfine lines which result from the two nonequivalent ^{55}Mn nuclei. Some of the resulting 16 lines show a very small amount of axial g-anisotropy.

Our approach in the following ESEEM studies is to measure the ^{14}N sublevel frequencies at a number of magnetic field positions across this broad spectrum. By following the field dependence of the ESEEM transitions we can check the consistency of our projected ^{14}N parameters. To this end, ESEEM experiments were performed at several of the largely resolved hyperfine lines within the spectrum. Each resulting ESEEM pattern is analyzed as resulting from a powder pattern average from an isotropic line at the given field position. The small degree of g-anisotropy is for the moment ignored. We note that the large ^{55}Mn hyperfine couplings are well out of range for observing via the ESEEM technique.

The 2-pulse ESEEM data for the di-μ-oxo bridged Mn(III)Mn(IV) bipyridyl dimer is shown in Figure IV-8a. These data are obtained with τ varied from 120 to 3000 ns in 10 ns increments. The magnetic field is 3465 Gauss. The ^{14}N envelope modulation is seen to be very deep. The Fourier cosine transform of this data is shown in Figure IV-8b. The short dead time in the time domain data is filled by a Fourier dead time reconstruction technique described by Mims (1984). The ESE modulation has components presumably due to ^{14}N at 1.96, 3.66, 5.29, 7.14, and 10.44 MHz. A

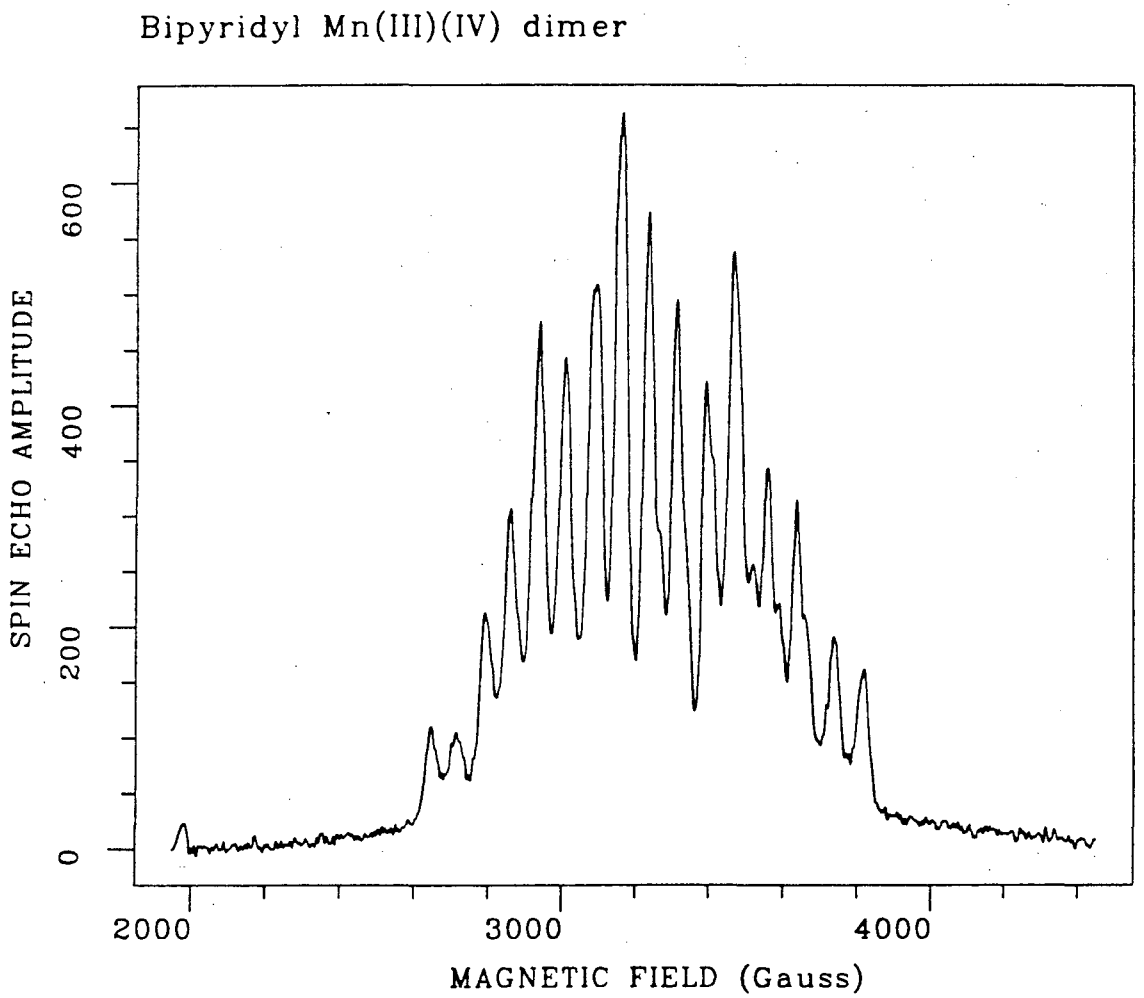

Figure IV-7 Electron spin echo spectrum for the di-μ-oxo bridged Mn(III)Mn(IV) bipyridyl dimer. Measurements were obtained with a 2-pulse ESE sequence with τ=380 ns. The sample temperature is 4.2 K and the microwave frequency is 8.9774 GHz.

weak proton component is also observed near the free-proton Larmour frequency of 14.7 MHz.

Figure IV-9a shows the 2-pulse ESEEM results obtained at 3080 Gauss. The time domain results are shown in Figure IV-9a. The ESEEM pattern is visibly different from the corresponding pattern at 3465 Gauss. The Fourier cosine transform data is displayed in Figure IV-9b. The ESEEM peaks all shift somewhat from their values at higher field. The ^{14}N peaks are now at 2.14, 5.04, 7.04, and 10.05 MHz. The 5.04 MHz component has a broad shoulder on the low frequency side. The weakly coupled proton feature is shifted to 13.08 MHz.

Improved spectral resolution can be obtained by examining 3-pulse ESEEM data. Figure IV-10a displays a 3-pulse ESEEM pattern for the bipyridyl dimer at 3465 Gauss. The value of τ is fixed at 140 ns, and T is incremented from 80 to 4000 ns. Modulation clearly persists to longer values of the time variable than in the corresponding 2-pulse experiment shown in Figure IV-8a. This is reflected in the narrower lineshapes seen in the Fourier cosine transform of Figure IV-10b. The positions of the ^{14}N peaks are similar to those obtained with the 2-pulse experiment. We measure 3-pulse ESEEM peaks at 1.84, 3.69, 5.34, 7.31, and 10.67 MHz. The proton peak is absent due to the 3-pulse suppression effect discussed in Chapter II.

Improved resolution of the 3-pulse experiment is also seen at the 3080 Gauss peak. The time domain ESEEM pattern is shown in Figure IV-11a, and the Fourier cosine transform is displayed in Figure IV-11b. The shoulder observed below the 5 MHz peak in the 2-pulse data becomes resolved with the 3-pulse data. Also the large 2.14 MHz peak is seen to split into a doublet. The ESEEM peaks are at 1.94, 2.18, 4.16, 5.12 7.51, and 10.32 MHz.

It is instructive to analyze the ESEEM data as a function of magnetic field. Varying the magnetic field allows us to sample the ESEEM patterns for different values of the ^{14}N Zeeman frequency ν_i. For all field positions we expect to observe the "double-quantum" peak from the β-manifold with a frequency given by equation II-76. This expression may be rewritten as

$$\nu_{dq} = 2[|\nu_i + A/2|^2 + \varsigma]^{1/2} \qquad (IV-7)$$

with the quadrupolar parameters contained in the term $\varsigma = K^2(3+\eta^2)$. As described fully in Chapter II, for the special case of exact cancellation the α-manifold reveals the pure NQR frequencies. For significant deviation from exact cancellation an expression

Figure IV-8 2-pulse ESEEM for the di-μ-oxo bridged Mn(III)Mn(IV) bipyridyl dimer at 3465 Gauss. The 2-pulse time domain modulation is shown in (a). Data are obtained in 10 ns increments between 120 and 3000 ns. The sample temperature is 4.2 K, and the microwave frequency is 8.9774 GHz. The Fourier cosine transform of the ESEEM pattern is displayed in (b). Modulation components at 1.96, 3.66, 5.29, 7.14, and 10.44 MHz presumably arise from ^{14}N sublevel transitions. The small feature near 14.7 MHz is due to weakly coupled protons.

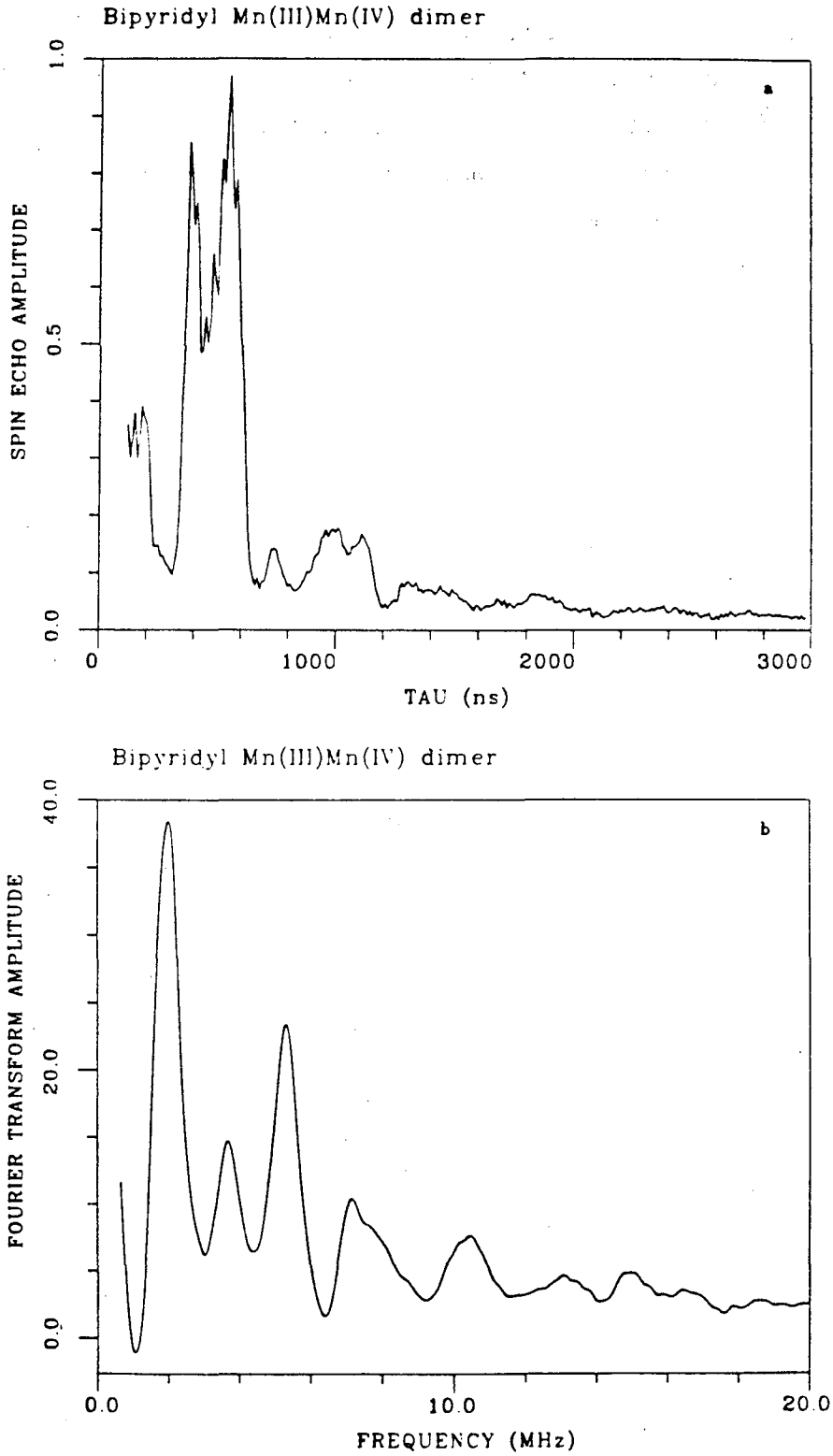
Bipyridyl Mn(III)Mn(IV) dimer
a
SPIN ECHO AMPLITUDE
1.0
0.5
0.0
0
1000
2000
3000
TAU (ns)
Bipyridyl Mn(III)Mn(IV) dimer
b
FOURIER TRANSFORM AMPLITUDE
40.0
20.0
0.0
0.0
10.0
20.0
FREQUENCY (MHz)

Figure IV-9 2-pulse ESEEM for the di-μ-oxo bridged Mn(III)Mn(IV) bipyridyl dimer at 3080 Gauss. The 2-pulse time domain modulation is shown in (a). Data are obtained in 10 ns increments between 120 and 3000 ns. The sample temperature is 4.2 K, and the microwave frequency is 8.9774 GHz. The Fourier cosine transform of the ESEEM pattern is displayed in (b). Modulation components at 2.14, 5.04, 7.04, and 10.05 MHz presumably arise from ^{14}N sublevel transitions. The small feature near 13.08 MHz is due to weakly coupled protons.

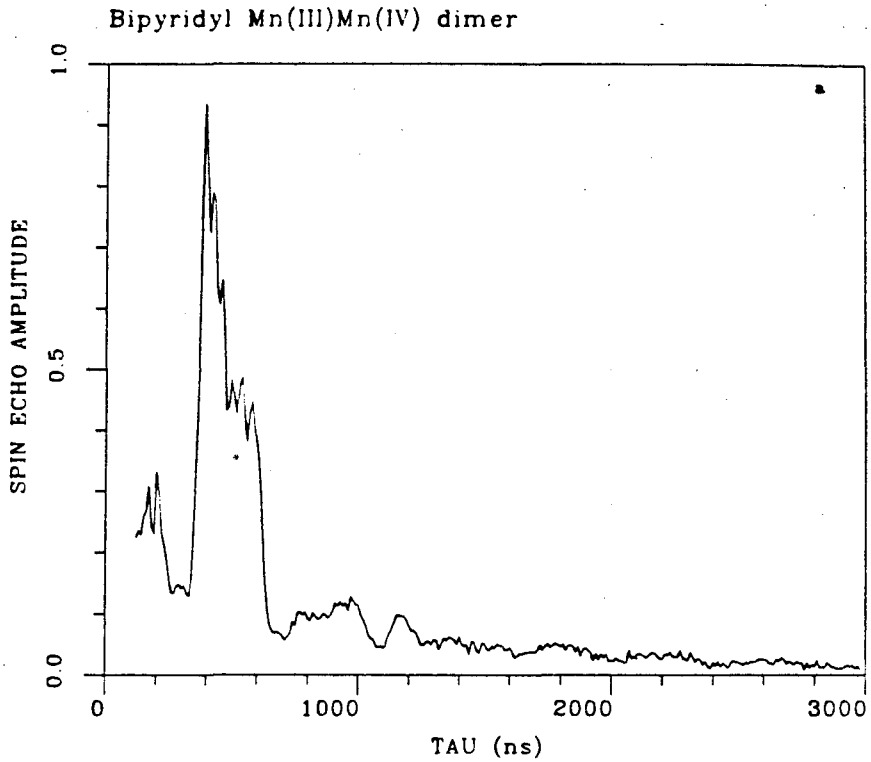
Bipyridyl Mn(III)Mn(IV) dimer
a
SPIN ECHO AMPLITUDE
1.0
0.5
0.0
0
1000
2000
3000
TAU (ns)

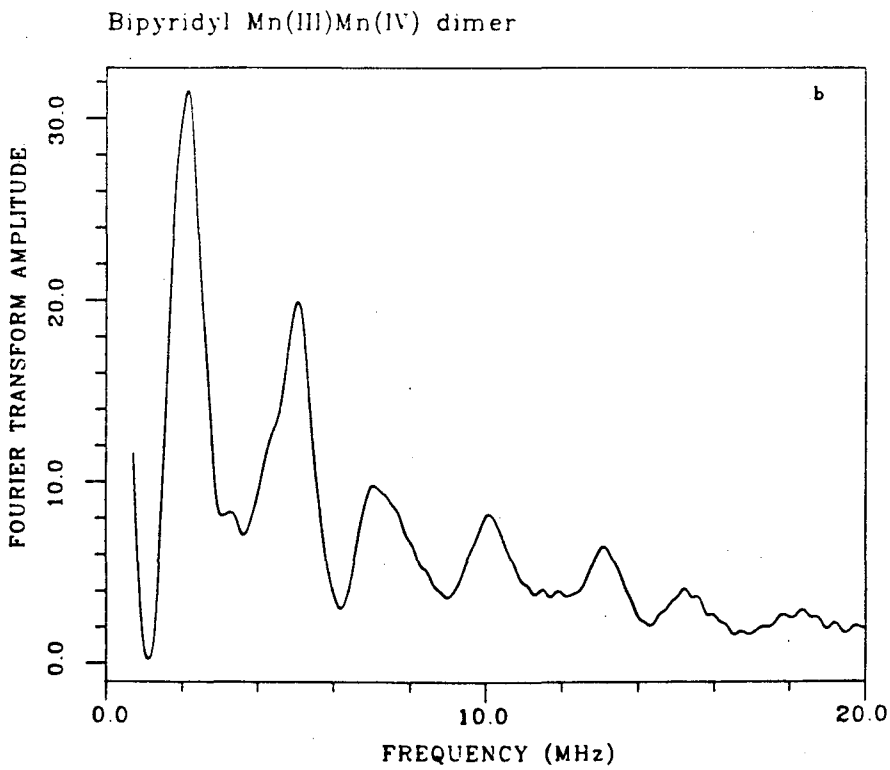
Bipyridyl Mn(III)Mn(IV) dimer
b
FOURIER TRANSFORM AMPLITUDE
30.0
20.0
10.0
0.0
0.0
10.0
20.0
FREQUENCY (MHz)

Figure IV-10 3-pulse ESEEM for the di-μ-oxo bridged Mn(III)Mn(IV) bipyridyl dimer at 3465 Gauss. The 3-pulse time domain modulation is shown in (a). Data are obtained in 10 ns increments of T between 80 and 4000 ns, with τ held constant at 140 ns. The sample temperature is 4.2 K, and the microwave frequency is 8.9774 GHz. The Fourier cosine transform is displayed in (b). Modulation components at 1.84, 3.69, 5.34, 7.31, and 10.67 MHz presumably arise from ^{14}N sublevel transitions.

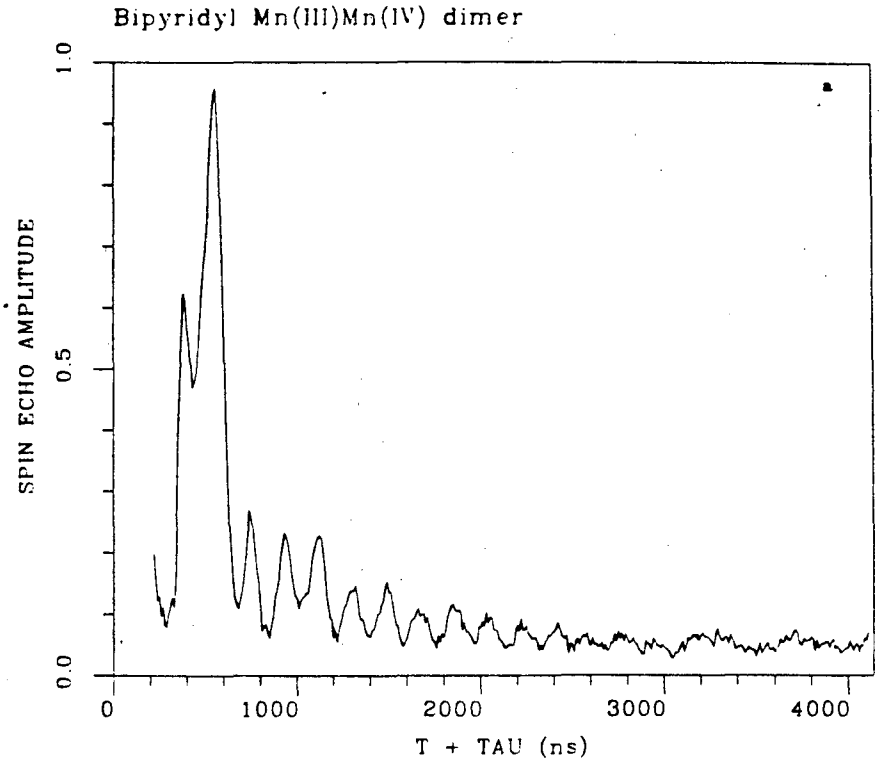
Bipyridyl Mn(III)Mn(IV) dimer
a
SPIN ECHO AMPLITUDE
1.0
0.5
0.0
0
1000
2000
3000
4000
T + TAU (ns)

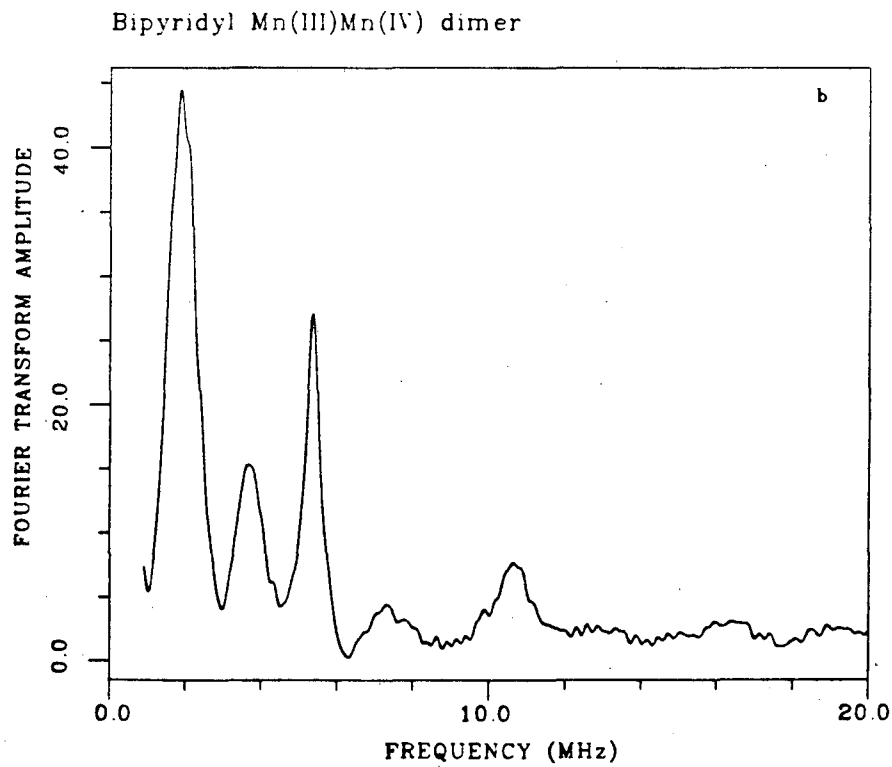
Bipyridyl Mn(III)Mn(IV) dimer
b
FOURIER TRANSFORM AMPLITUDE
40.0
20.0
0.0
0.0
10.0
20.0
FREQUENCY (MHz)

Figure IV-11 3-pulse ESEEM for the di-μ-oxo bridged Mn(III)Mn(IV) bipyridyl dimer at 3080 Gauss. The 3-pulse time domain modulation is shown in (a). Data are obtained in 10 ns increments of T between 80 and 4000 ns, with τ held constant at 140 ns. The sample temperature is 4.2 K, and the microwave frequency is 8.9774 GHz. The Fourier cosine transform is displayed in (b). Modulation components at 1.94, 2.18, 4.16, 5.12, 7.51, and 10.32 presumably arise from ^{14}N sublevel transitions.

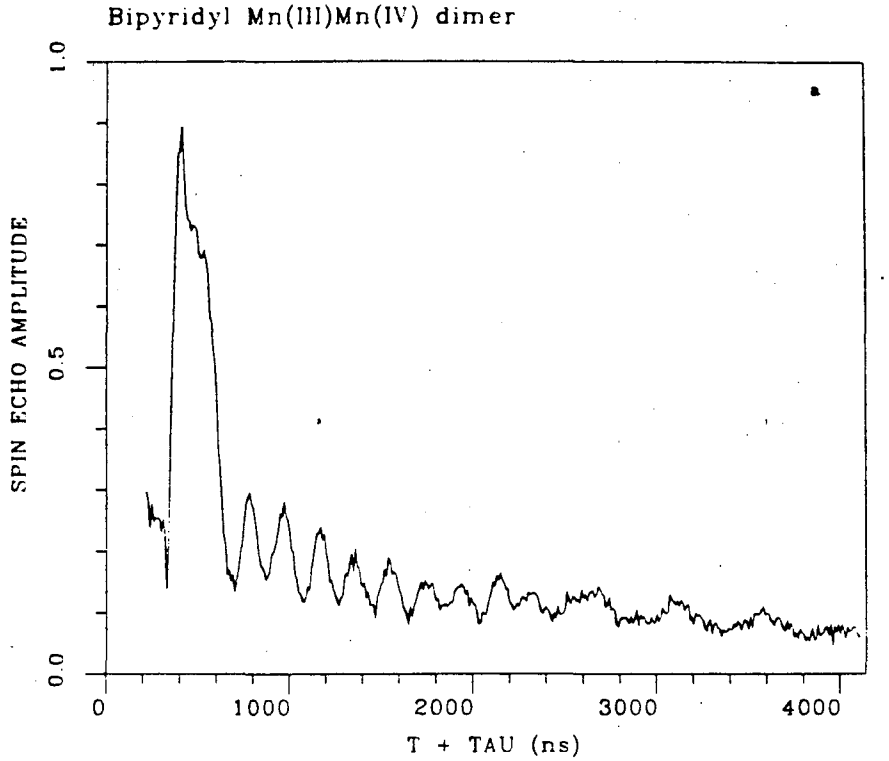
Bipyridyl Mn(III)Mn(IV) dimer
a
SPIN ECHO AMPLITUDE
1.0
0.5
0.0
0
1000
2000
3000
4000
T + TAU (ns)

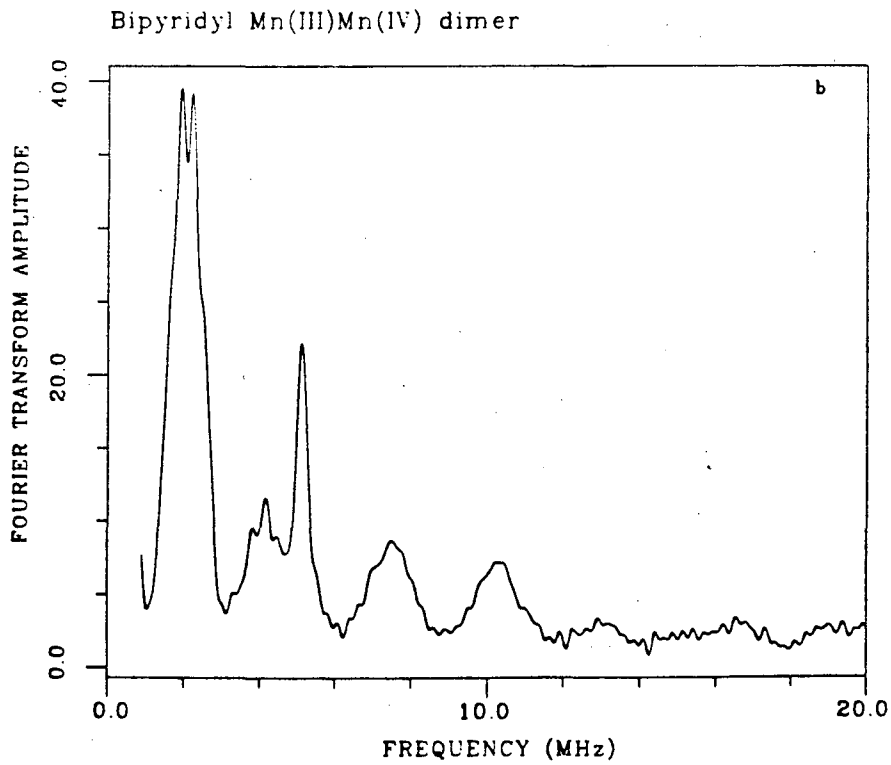
Bipyridyl Mn(III)Mn(IV) dimer
b
FOURIER TRANSFORM AMPLITUDE
40.0
20.0
0.0
0.0
10.0
20.0
FREQUENCY (MHz)

similar to equation IV-7 may be written for the α-manifold:

$$\nu_{dq} = 2[|\nu_i - A/2|^2 + \varsigma]^{1/2}. \qquad (IV-8)$$

We note that close to exact cancellation, this expression fails for the α-manifold. This can be seen by examining the limit of $\nu_i = A/2$, where equation IV-8 predicts a frequency of $2K(3+\eta^2)^{1/2}$ rather than the pure NQR frequency $\nu_+ = (3+\eta)K$.

Figure IV-12 displays the magnetic field dependence of the two largest ESEEM features for the di-μ-oxo bridged Mn(III)Mn(IV) bipyridyl dimer. The open squares denote the frequency component near 5 MHz measured with a 3-pulse sequence with τ=140 ns. The solid line represents a nonlinear least squares fit to these data using equation IV-7, with both A and ς allowed to vary. The results of this fit are A=2.79 MHz and ς=1.07. Results of additional 3-pulse measurements with τ=210 ns overplot these data well and result in fit parameters of A=2.79 MHz and ς=1.00. The ESEEM component near 2 MHz is also plotted as a function of magnetic field in Figure IV-12. The open squares again denote 3-pulse data with τ=140 ns. The black diamonds show the 3-pulse results with τ=210 ns. It is apparent from the fact that this frequency diminishes with increasing field that this component results from the α-manifold with $A/2 > \nu_i$. We have found it impossible to achieve a good fit to this entire data set using the α-manifold expression given by equation IV-8. The solid line associated with this data set results from applying the β-manifold fit results of A=2.79 MHz and ς=1.07 to the α-manifold expression given by equation IV-8. The resulting line fits the data well only at the lowest field points. At higher field values the data are of lower frequency than predicted by equation IV-8 and approach an asymptotic value of approximately 1.75 MHz. The highest field point measured is 3932 G with ν_i=1.207 MHz. This is approaching the limit of exact cancellation, with the projected value $A/2 \approx 1.4$. However the deviation from exact cancellation is sufficiently great that the pure quadrupolar transitions ν_0 and ν_- are not resolved in the ESEEM data at this high field.

The poor fit of the high-field α-manifold data to equation IV-8 is expected because this α-manifold double-quantum expression is not valid close to exact cancellation of hyperfine and Zeeman fields where the frequency approaches ν_+. It does however provide good results at lowest field positions. We can solve equations IV-7 and IV-8 simultaneously at the lowest field value to get an additional check on the values of A and ς. The results are A=2.84 and ς=0.97. These values are very close to those

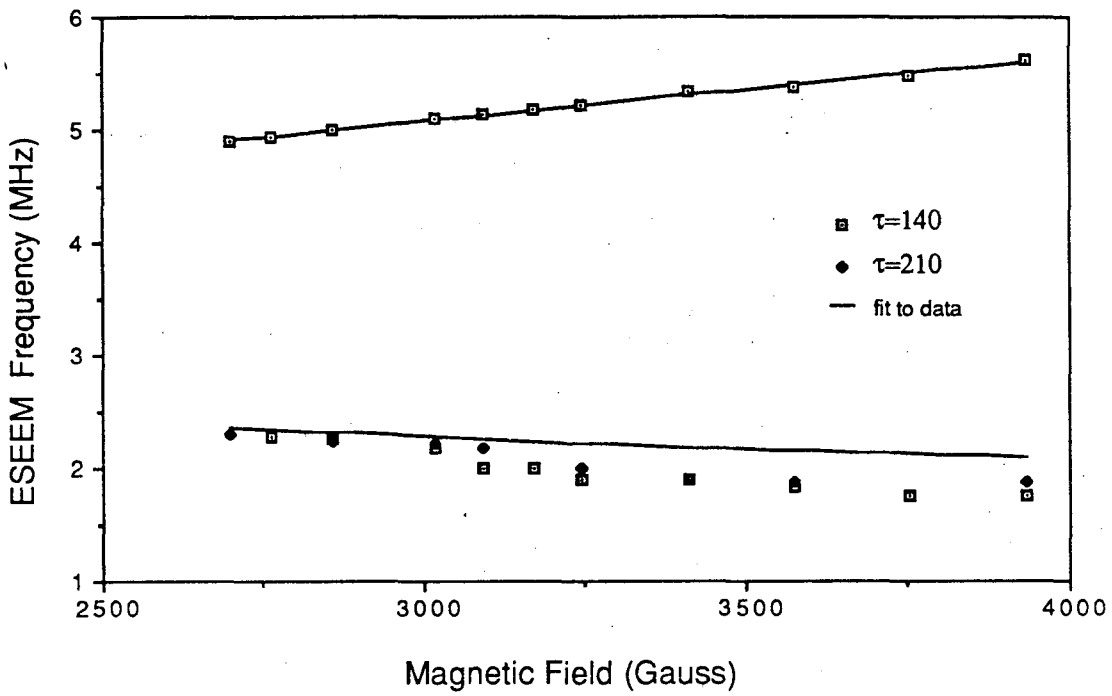

Figure IV-12 ESEEM data for the di-μ-oxo bridged Mn(III)Mn(IV) bipyridyl dimer as a function of magnetic field. The open squares represent data obtained via 3-pulse ESEEM with τ=140 ns. The black diamonds represent 3-pulse ESEEM data with τ=210 ns. The line associated with the $\approx$ 5 MHz data set results from a non-linear least squares fit of the data to equation IV-7, with resultant parameters A=2.79 MHz and ζ=1.07. The line associated with the lower frequency data set results from applying these same parameters to equation IV-8.

obtained by fitting the β-manifold transition frequencies to equation IV-7 as a function of field.

It is instructive to examine the change in quality of fit if either A or ς is fixed to values away from the optimal fit result. The quadrupolar parameter ς has an influence on the derivative of the double quantum frequency with respect to the ^{14}N Zeeman frequency ν_i:

$$\frac{d\nu_{dq}}{d\nu_i} = \frac{2(\nu_i + A/2)}{[(\nu_i + A/2)^2 + \varsigma]^{1/2}}. \qquad (IV-9)$$

The derivative value maximum of 2 (normalized units) is obtained in the pure Zeeman limit where $(\nu_i + A/2) \gg \varsigma$.

Figure IV-13 shows the effect of constraining ς on the nonlinear least squares fits of the β-manifold double-quantum frequency data. In each of the three displayed fits the value of ς is fixed to the denoted value. The value of the isotropic coupling constant A is optimized by the fitting routine to provide the best fit to the data that can be obtained for the fixed value of ς. We observe systematic deviations in slope resulting from the forced deviations of ς away from the optimal value of 1.07.

Figure IV-14 shows the complementary process of constraining A in the β-manifold double-quantum fits while optimizing ς for the best possible fit to the data. The optimal fit results from fixing A=2.79 MHz. If A is constrained to a smaller value, the nonlinear least squares optimization forces a larger fit value for ς, resulting in too small a slope. If A is constrained to a value larger than 2.79 MHz, the best overall fit is obtained with a small value of ς. However the slope is then too great. The best-fit value of ς reaches zero for A=3.22 MHz. The fit value of ς cannot decrease past zero for larger input values of A. Thus for a large fixed value of A such as A=3.5 MHz, the line obtained by the nonlinear least squares fit is forced to frequency values well above the actual data.

Unfortunately we are not able to perform experiments at high enough magnetic field to achieve exact cancellation of the Zeeman and hyperfine components. We are unable to resolve the ν_0 and ν_- NQR frequencies, which would provide a direct measure of e^2qQ and η. Fortunately we can achieve a good estimate of these parameters from the data at hand. From the asymptotic value of the low frequency transition we can write $\nu^+ = K(3+\eta) \approx 1.75$. We have also determined $\varsigma = K^2(3+\eta^2) \approx 1.0$. The values of K and η that satisfy both conditions require $e^2qQ \approx 2.28$ MHz and $\eta \approx 0.07$.

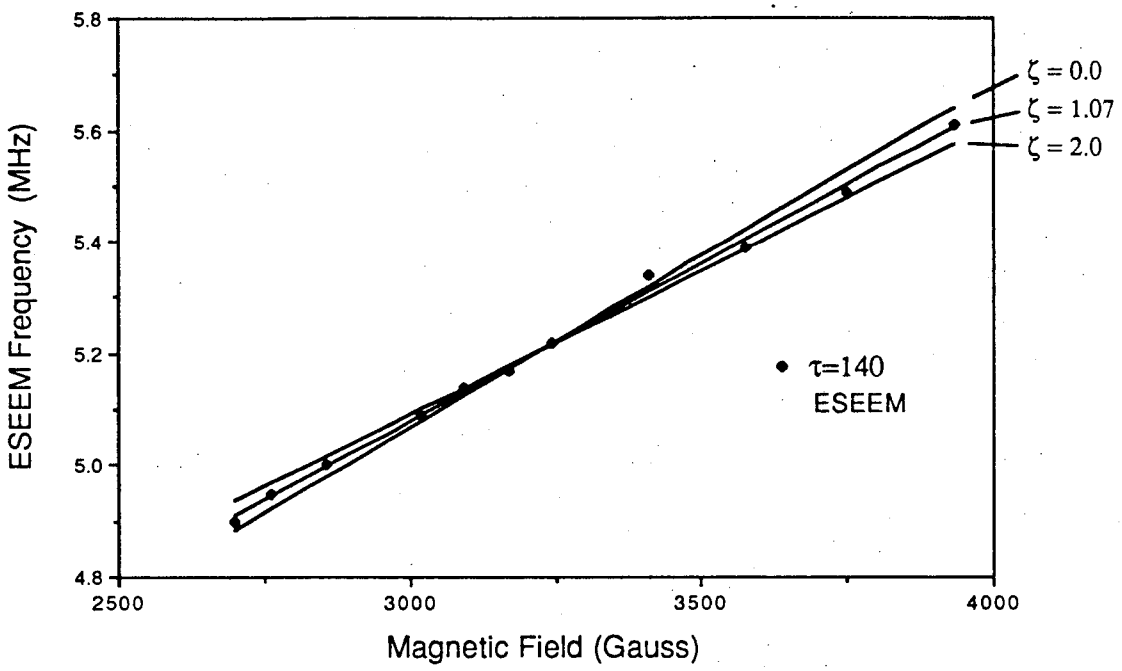

Figure IV-13 Effect of constraining the quadrupolar parameter ς in fitting the β-manifold double-quantum ESEEM feature. The double-quantum ^{14}N transition is fit to equation IV-7, with ς fixed and A optimised to provide the best fit to the data. Deviations from the optimal value of $\varsigma = 1.07$ result in poor fits to the slope of the data, though the center position can always be matched by adding more or less isotropic coupling. The slope is increased for decreasing values of ς. The fixed ς and matching A results are

ς=0.0, A=3.22 MHz

ς=1.07, A=2.79 MHz

ς=2.0 A=2.39 MHz.

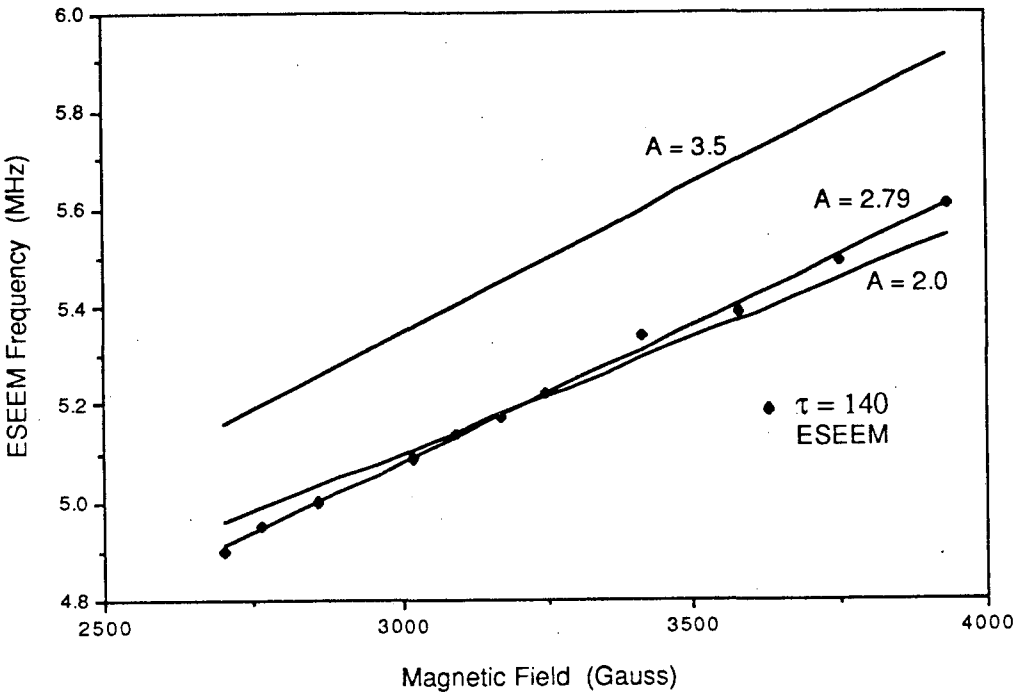

Figure IV-14 Effect of constraining the isotropic coupling parameter A in fitting the β-manifold double-quantum ESEEM feature. The double-quantum ^{14}N transition is fit to equation IV-7, with A fixed and ς optimised to provide the best fit to the data. Deviations from the optimal value of A=2.79 MHz result in poor fits to the slope of the data, although the center position can be matched by increasing or decreasing the quadrupolar parameter ς. For the input value A= 3.22 MHz, the quadrupolar parameter $\varsigma = 0$, and increased values of A beyond this point can no longer be mitigated by further decrease in ς, as illustrated in the terrible fit for A=3.5 MHz. The fixed A values and matching ς results are

A=2.00 MHz, ς=2.81

A=2.79 MHz, ς=1.07

A=3.5 MHz, ς=0.0.

There is evidence in the ESEEM spectra to suggest such a low value of the asymmetry parameter as η=0.07. For small values of η, the double-quantum peaks are split into doublets. Such a doublet structure is evident in the low frequency peak in Figure IV-11. Figure IV-15 displays a 2-pulse ESEEM powder pattern simulation with conditions similar to those resulting in the Figure IV-11 ESEEM pattern. The simulation parameters are ν_i=1.0 MHz, A=2.80 MHz, e^2qQ=2.28 MHz, and η=0.10. The presentation format is identical to that for the corresponding plots in Chapter II. In the simulation, the peak near 2 MHz is clearly split into a doublet structure. The 5 MHz peak is also split; however the splitting is asymmetric and narrow. Such a splitting would probably be missed with the limited resolution of the experimental data. For larger values of the asymmetry parameter η the doublet structure disappears (see Flanagan and Singel (1987) for details). Also, for higher field values closer to exact calculation, the splitting of the ν_+ peak is greatly diminished. The doublet structure appears primarily in the nearly pure NQR ν_0 and ν_- peaks which are unresolved in our experimental data.

So far we have examined only the two major ESEEM peaks. Figure IV-16 shows the field dependence of the ESEEM component near 10 MHz. The solid line is the best possible nonlinear least squares fit to the data which can be obtained for physically meaningful values of A and ς. The extracted parameters are A=8.35 MHz and ς=0.0. With ς=0.0, the slope of the fit line represents the maximum slope which can be obtained for a ^{14}N β-manifold double-quantum transition. The system is then in the pure Zeeman limit, with a normalized slope of 2. The actual ESEEM data present a slope almost twice as large. Also, we note that the frequency of this component at a given field value is almost exactly twice the frequency of the large ESEEM component near 5 MHz. The explanation of this data is evident if we examine equation II-54, which states that the ESEEM pattern resulting from more than one coupled nucleus can be treated as the product of the individual envelope modulations. The familiar trigonometric function-product relations show that the multiplication of two *cos* components results in terms with sum and difference frequencies. The $\approx$10 MHz component is thus seen to arise as an intermodulation product from a set of at least two ^{14}N nuclei with significant 5 MHz modulation amplitude over a non-negligible fraction of the angular phase space averaged in the powder pattern.

Figure IV-17 shows the field dependence of the ESEEM component near 4 MHz. The 3-pulse ESEEM data for τ=140 ns are displayed as open squares. The best

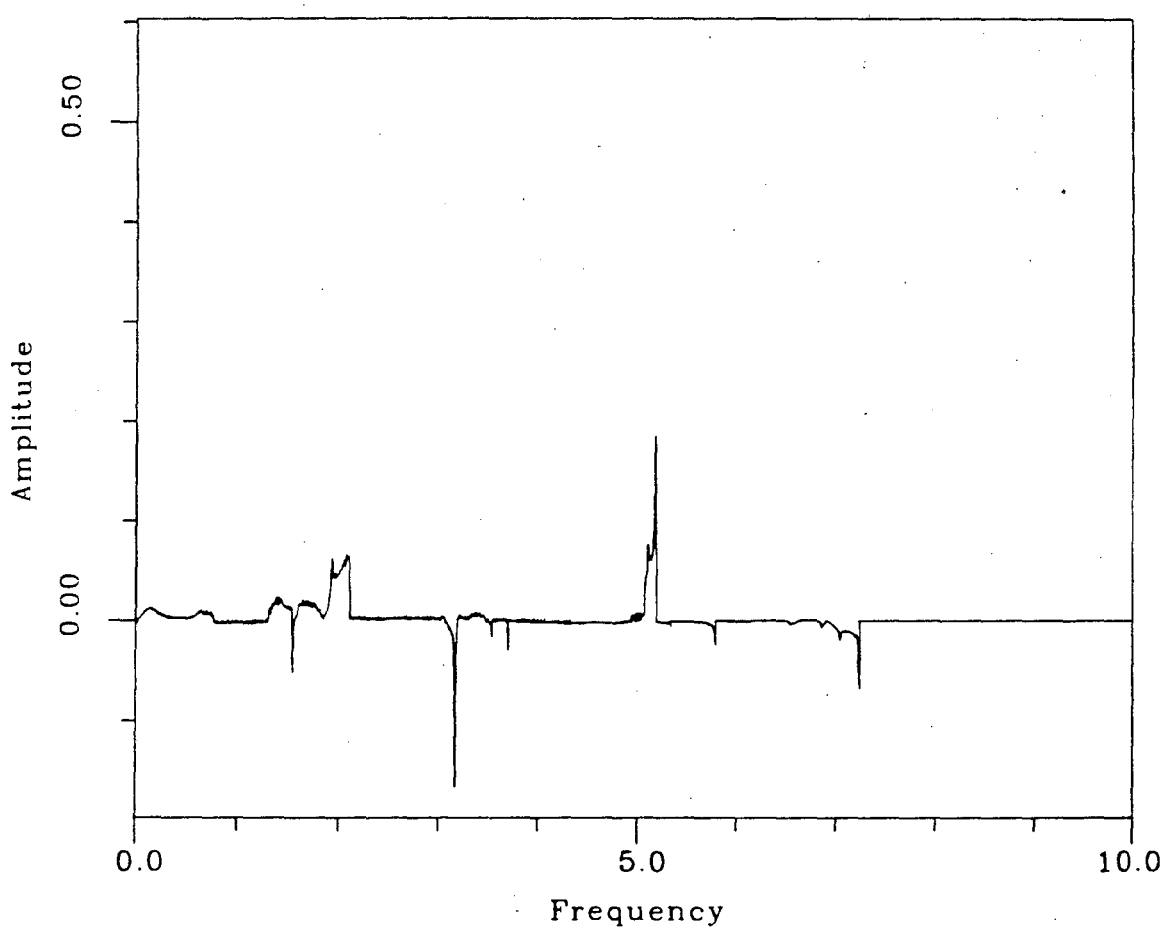

Figure IV-15 ESEEM powder pattern simulation for a low value of the ^{14}N asymmetry parameter η. Simulation parameters are ν_i=1.0 MHz, A=2.80 MHz, e^2qQ=2.28 MHz, and η=0.10. The 2-pulse simulation shows out-of-phase sum and difference frequencies not present in the 3-pulse experimental data. For low values of η the double-quantum peaks are split into doublets as can be observed in this simulation.

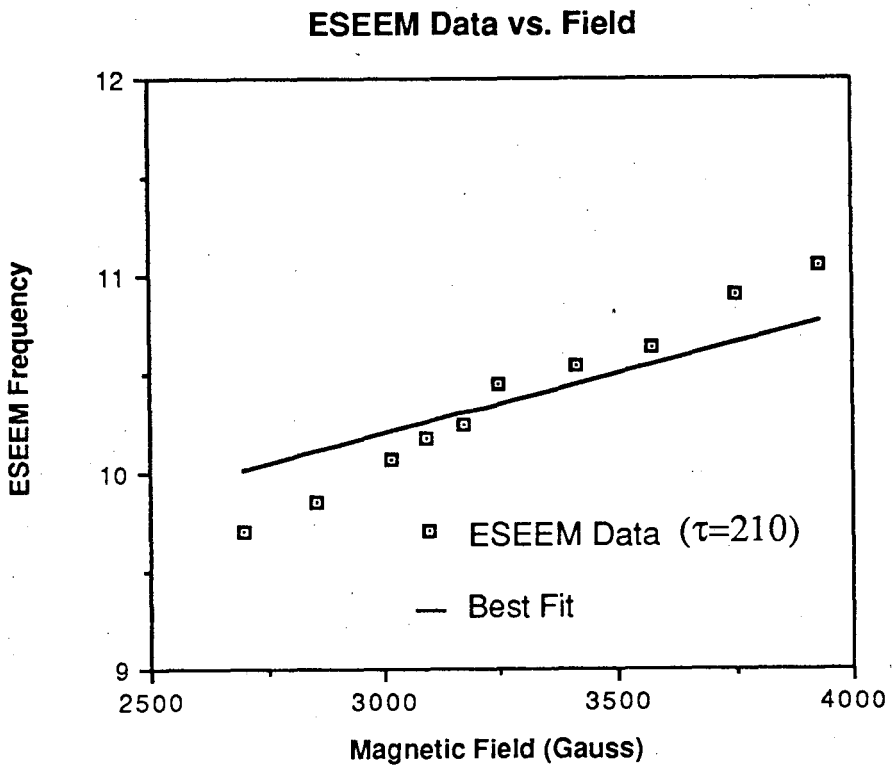

Figure IV-16 Magnetic field dependence of the ESEEM component near 10 MHz. The solid line shows the best fit to the data which can be obtained with physically meaningful parameters. The fit results are A=8.35 MHz and ς =0.0. The slope of the ESEEM data is approximately twice the largest value possible for an actual ^{14}N double-quantum transition. This component is seen to arise as an intermodulation product term from multiple ^{14}N nuclei.

nonlinear least squares fit results from equation IV-8 with A=5.97 MHz and ς=0. The predicted deviation from exact cancellation with A=5.97 MHz is sufficient that equation IV-8 should accurately predict the field dependence of this component. We see that the fit is actually terrible. The open diamonds show the frequencies obtained by multiplying the large ≈2 MHz frequency components by a factor of 2 at each field position. The resulting sum frequencies follow the general trends of the ≈4 MHz component frequencies. We therefore attribute the ≈4 MHz ESEEM features to intermodulation products resulting from multiple ^{14}N nuclei with large ≈2 MHz modulation. In a similar fashion the ESEEM components near 7 MHz appears to result as a sum of ≈5 and ≈2 MHz components.

In summary, the results of the ESEEM studies of the di-μ-oxo bridged Mn(III)Mn(IV) bipyridyl dimer reveal a class of ^{14}N ligands with similar hyperfine and quadrupolar parameters. The measured isotropic hyperfine coupling constant for this class is A ≈2.80 MHz. We also obtain a ^{14}N quadrupolar coupling value of e^2qQ≈2.28 MHz and an asymmetry parameter value η ≈0.07. All of the measured ESEEM frequencies not resulting from weakly coupled protons can be attributed to this one ^{14}N nuclear class. The two largest components result from the α- and β-manifold double-quantum transitions. The α-manifold double-quantum transition takes on increased NQR ν_+ character at the highest field positions. We do not resolve the ν_- and ν_0 features. The remaining ESEEM features result as intermodulation products of these two strong components. Virtually identical results are obtained with the analogous di-μ-oxo bridged Mn(III)Mn(IV) phenanthroline dimer.

The survey at the beginning of this chapter suggested three possible classes of inequivalent ^{14}N nuclei. The bipyridyl ^{14}N nuclei ligated to Mn(IV) form one such class. The largely Jahn-Teller distorted Mn(III) ligand environment could provide two additional classes of ^{14}N nuclei. Thermal electron transfer is unlikely to average the ^{14}N sublevel frequencies produced by these three classes at the low experimental temperature of 4.2 K. The ^{14}N modulation observed from the one evident class is extremely deep. The modulation reaches the baseline at several early points in the time-domain pattern. The two double-quantum features and their associated sum and different terms provide large features in the frequency domain spectrum out to past 10 MHz. It is likely that ESEEM contributions from other classes of ^{14}N nuclei are totally obscured by the modulation from this ^{14}N class with near exact cancellation of hyperfine and Zeeman fields. We recall Figure II-18 which illustrates the rapid

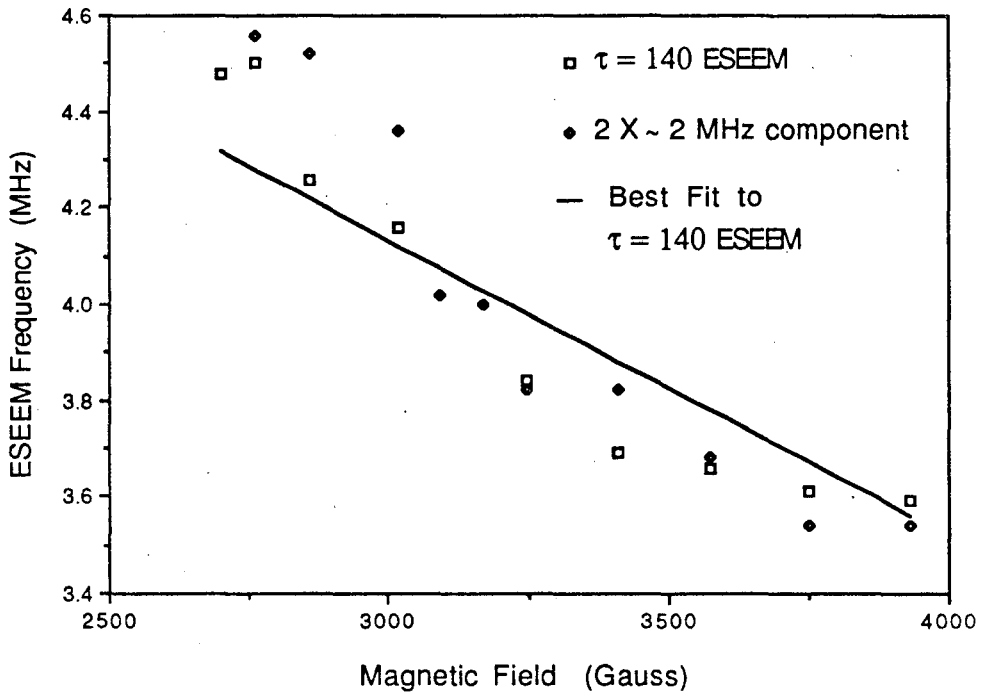

Figure IV-17 Magnetic field dependence of the ESEEM component near 4 MHz. The 3-pulse ESEEM data for τ=140 ns are denoted by open squares. The solid line shows the best allowed fit of equation IV-8 to the data, with A=5.97 MHz and ζ =0.0. The fit of this line to the ESEEM data is very poor. The open diamonds denote the ≈2 MHz ESEEM components multiplied by a factor of 2. These sum frequencies follow the general trend of the ≈4 MHz data.

falloff of ^{14}N ESEEM modulation amplitude for large deviation from the special case of exact cancellation.

We are currently preparing the di-μ-oxo bridged Mn(III)Mn(IV) bipyridyl dimer with ^{15}N-substituted 2,2'-bipyridine. The $I = 1/2$ ^{15}N nucleus has no quadrupole moment. The resultant ESEEM patterns should be less complex. We plan to search for any other classes of nitrogen ligands through ESEEM experiments with these preparations. These experiments should also provide a measure of anisotropic contributions to the hyperfine coupling.

Section 4 – Analysis of Hyperfine and Quadrupolar Parameters

Results of ESEEM studies on the di-μ-oxo bridged Mn(III)Mn(IV) bipyridyl dimer reveal a class of directly coordinated ^{14}N nuclei with an isotropic coupling constant A=2.80 MHz. Isotropic couplings in this range provide deep ^{14}N modulation for the high valence Mn ions. This can be contrasted with ^{14}N coordination studies with the relatively "soft" Cu(II) ion, which projects a large amount of unpaired spin density onto nitrogen bearing ligands, causing very large isotropic hyperfine couplings (A >30 MHz) (Maki and McGarvey, 1958; Kivelson and Neiman, 1961). The d^9 Cu(II) ion is considered soft (Pearson, 1968a,b) because its d-orbital electrons are rather loosely held and form π-bonds with ligands. The large degree of covalency gives rise to large isotropic couplings which render ^{14}N directly coordinated to Cu(II) invisible in ESEEM experiments (Mims and Peisach, 1978). Imidazole and histidine ligation to Cu(II) has been extensively studied via ESEEM (Mims and Peisach, 1976; Mondoví et al., 1977; Mims and Peisach, 1978, 1979b; Zweier et al., 1979; Mims et al., 1980; Avigliano et al., 1981; Burger et al., 1981; Fee et al., 1981; Zweier et al., 1982; McCracken et al., 1987, 1988). In these studies the observed ^{14}N echo modulation originates in the remote nitrogen of the imidazole ring. However many other metal centers show ESEEM features attributable to directly coordinated ^{14}N. ESEEM studies on heme proteins and iron metalloporphyrins typically reveal modulation from directly coordinated ^{14}N, either from the pyrrole nitrogens or from axially coordinated nitrogen ligands (Magliozzo et al., 1987). Directly coordinated nitrogen gives rise to ^{14}N ESEEM in the FeMo center of nitrogenase (Thomann et al., 1987) and the Rieske 2Fe-2S center (Telser et al., 1987; Britt et al., manuscript in preparation)

We are of course concerned with superhyperfine couplings to Mn ions. Even Mn(II) is classified as a hard acid. It is not very polarizable and its interactions with ligands are more ionic in character. Since Mn(II) ions do not donate much electron density to coordinated bases, the corresponding isotropic hyperfine couplings are small. As a result, ^{14}N superhyperfine couplings are typically unresolved in EPR spectra of Mn(II) complexes (Reed and Markham, 1984). The isotropic couplings for directly coordinated ^{14}N are in the regime which gives rise to observable ESEEM effects (LoBrutto et al., 1986).

The Mn(III) and Mn(IV) ions are more charged than Mn(II) and therefore smaller. The ionic radii for high-spin octahedrally coordinated Mn(II), Mn(III), and Mn(IV) ions are respectively 0.830, 0.645, and 0.530 Å (Jolly, 1984). Mn(III) and Mn(IV)

ions act as very hard Lewis acids, and thus the high valence Mn ions in our model compounds and in PSII are unlikely to donate a greater unpaired spin density onto ligands than Mn(II). We consider it unlikely that any directly coordinated nitrogens would present A values so large as to be unobservable by ESEEM techniques.

We now turn to the interpretation of the ^{14}N quadrupole parameters of $e^2qQ \approx$ 2.28 MHz and $\eta \approx 0.07$ as determined by analysis of our ESEEM data for the di-μ-oxo bridged Mn(III)Mn(IV) bipyridyl dimer. A starting point for the analysis of these parameters is provided by Nuclear Quadrupole Resonance (NQR) spectroscopy. A great deal of NQR spectroscopy was performed on ^{14}N containing compounds in the 1960's and 1970's. NQR frequencies for ^{14}N are relatively low compared to those of halogen nuclei and are much more difficult to obtain by direct resonance methods. However, over this time period a number of very sensitive double-resonance techniques were developed which allowed ^{14}N NQR experiments on many previously inaccessible compounds. The review by Edmonds (1977) discusses several of these double resonance techniques in detail and provides a comprehensive survey of the ^{14}N NQR literature.

We start the discussion of the NQR parameters by reviewing studies of free-base pyridine and derivatives thereof. Such free-base nitrogen compounds have rather large electric field gradients due to the presence of the lone electron pair. Our discussion continues in analyzing the effects of coordination to a Lewis acid center (electron acceptor) such as a metal, the principal result of which is to reduce the density in the lone pair orbital and therefore the electric field gradient and corresponding NQR frequencies.

The NQR frequencies for crystalline pyridine were first reported by Guibé (1960). They provide a starting point for the analysis of our bipyridyl quadrupole data. Guibé observed four sets of transitions due to four distinct crystalline environments for pyridine. The calculated values for e^2qQ and η are shown in Table IV-1. Lucken (1961) interpreted these data within the context of the classic Townes and Dailey (1949) model relating NQR frequencies to atomic orbital densities.

The theory of Townes and Dailey (1949) relates NQR values to molecular orbitals as a linear summation of atomic orbitals. Complete inner electron shells possess spherical symmetry and produce no net electric field gradient at the nucleus. The electric field gradients determining the NQR frequencies therefor are produced by valence electrons. The contribution from the spherically symmetric s shells is zero.

Thus the major contribution arises from valence p orbitals.

A molecular orbital description of pyridine is shown in Figure IV-18. The maximum electric field gradient is along the axis of C_{2v} symmetry which passes through the nitrogen lone electron pair. This axis is labelled the z-axis in Figure IV-18. We choose the x-axis to lie in the plane of the ring and the y-axis perpendicular to this plane. The molecular orbitals used to describe the nitrogen bonding in pyridine arise from sp^2-hybridization. Two of the resulting sp^2 orbitals are used in σ-bonding to the pyridine ring carbons. The third sp^2 orbital is occupied by the lone electron pair. The atomic p_y orbital remains relatively unmixed and is involved in π-bonding in the ring. The wavefunctions of these four orbitals are presented in Table IV-2 as a linear summation of the relevant nitrogen atomic orbitals. The occupation number for these orbitals is also displayed. The lone pair orbital Ψ_{σ_1} is assigned an occupancy of 2. The orbital Ψ_π involved in π-bonding is assigned an occupancy of a. The value of a is to be determined through the Townes and Dailey theory. In a like fashion, the two orbitals Ψ_{σ_2} and Ψ_{σ_3}involved in σ-bonding to carbons are each assigned an occupancy factor b.

The three principal components of the field gradient tensor can be written as a function of the occupation factors in Table IV-2 (Lucken, 1961)

$$\begin{aligned} q \equiv q_{zz} &= -\left(\frac{a}{2}+\frac{b}{6}-\frac{4}{3}\right) q_p \\ q_{yy} &= \left(a-\frac{2b}{3}-\frac{2}{3}\right) q_p \\ q_{xx} &= -\left(\frac{a}{2}-\frac{5b}{6}+\frac{2}{3}\right) q_p. \end{aligned} \qquad (IV-10)$$

The resulting value for the asymmetry parameter given by

$$\eta = \frac{\pm 3(a-b)}{a+\frac{b}{3}-\frac{8}{3}}. \qquad (IV-11)$$

The term q_p is the calculated field gradient from a single $2p$ valence electron, with $e^2 q_p Q \approx 10$ MHz. The π-bond occupancy parameter a and the σ-bond occupancy parameter b can in turn be written (Guibé and Lucken, 1966)

$$\begin{aligned} 2-b &= \frac{3}{2}\left(1 \pm \frac{\eta}{3}\right)\frac{e^2 Q q_p}{e^2 Q q} \\ a-b &= \pm\frac{2\eta}{3}\frac{e^2 Q q}{e^2 Q q_p} \end{aligned} \qquad (IV-12)$$

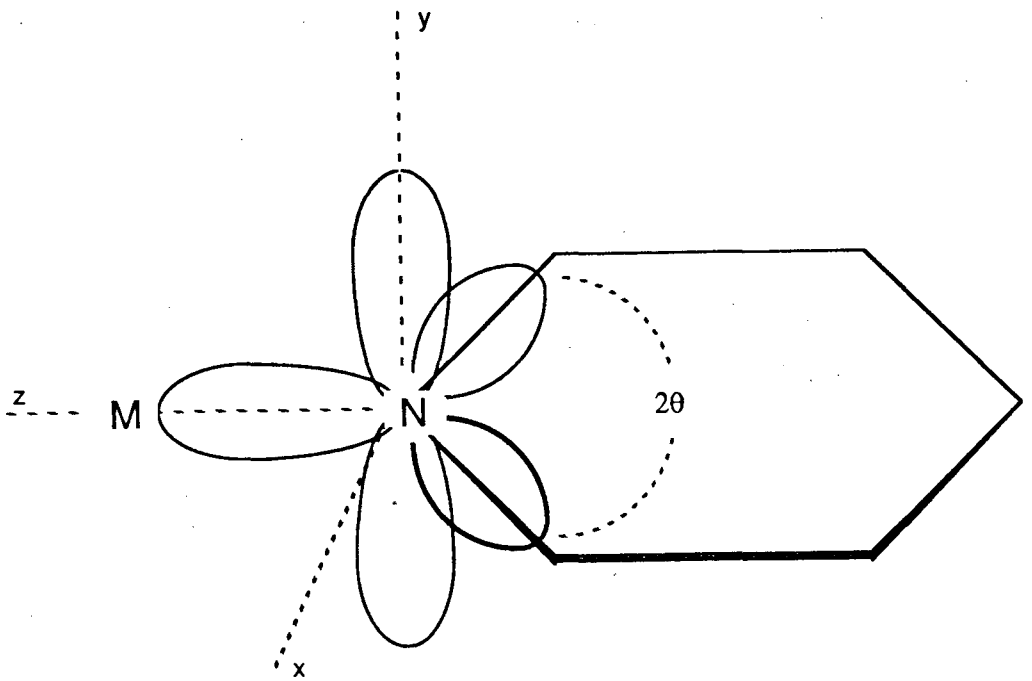

Figure IV-18 Molecular orbital structure about the nitrogen atom in pyridine. The molecular orbitals used to describe the nitrogen bonding in pyridine arise from sp^2-hybridization. Two of the three sp^2 orbitals are used in σ-bonding to adjacent pyridine ring carbons. The third sp^2 orbital is occupied by the lone electron pair. The atomic p_y orbital remains relatively unmixed and is involved in ring π-bonding.

Table IV-1 NQR frequencies for crystalline pyridine (Guibé, 1960)

e^2qQ (MHz)	η
4.572	0.374
4.591	0.393
4.574	0.415
4.601	0.403

Table IV-2 Molecular orbital composition for nitrogen in pyridine

molecular orbital	atomic orbitals	occupation number
Ψ_π	p_y	a
Ψ_{σ_1}	$\frac{1}{\sqrt{3}}s + \frac{2}{\sqrt{3}}p_z$	2
Ψ_{σ_2}	$\frac{1}{\sqrt{3}}s - \frac{1}{\sqrt{6}}p_z + \frac{1}{\sqrt{2}}p_x$	b
Ψ_{σ_3}	$\frac{1}{\sqrt{3}}s - \frac{1}{\sqrt{6}}p_z - \frac{1}{\sqrt{2}}p_x$	b

Lucken (1961) used the average of the four pyridine resonance parameters (e^2qQ=4.6 MHz and η=0.40) and a graphical solution to equations IV-10 and IV-11 to calculate the occupancy factor for the σ and π-bond orbitals. NQR data for hexamethylenetetramine and γ-picoline were simultaneously analyzed to check for consistency in the sign ($\pm$) of results. With e^2q_pQ set to 10 MHz, Lucken arrived at a π-bond occupation a=1.29 and a σ-bond occupation b=1.40. These values are close to those predicted by molecular orbital calculations. For example Orgel et al. (1951) had calculated a value of a=1.29 with a simple l.c.a.o. calculation.

An extension of this analysis was performed with additional NQR data for pyrazine, tetramethyl pyrazine, phenazine, and *s*-triazine (Guibé and Lucken, 1966). These heterocyclic compounds all contain symmetric $\widehat{CNC}$ bonds similar to that of pyridine. The molecular orbital composition of Table IV-2 assumes a $\widehat{CNC}$ angle of exactly 120°. Guibé and Lucken included deviation from this ideal sp^2 hybridization angle in calculating the form of the molecular orbitals and in the resulting expression for a and b analogous to equation IV-12. The actual $\widehat{CNC}$ angles in these azabenzenes range from 113° to 117.5°. Guibé and Lucken also considered deviations in the lone pair occupancy from the limiting value of 2, possible contributions from excited MO states, and the small field gradient contribution from the carbon neighbors. The resulting values for the π and σ populations compared favorably to the theoretical MO calculations. Later papers extended the method to compounds with asymmetic azabenzenes such as pyrimidine and pyridazine ((Guibé and Lucken, 1968; Guibé et al., 1970). For such compounds the NQR data predict the average occupancy of the inequivalent σ-bonds. Trends in the σ and π orbital populations for a variety of substituted pyridine derivatives were analyzed. The results were quite consistent with expected trends from varied substituent electronegativity and position. Similar work was reported by Schempp and Bray (1968) for a wide variety of substituted pyridines, including cyano, acetyl, and chloro derivatives, as well as methyl esters of pyridine monocarboxylic acids. Schempp and Bray also noted very good agreement between trends in the charge density as determined from the NQR data and those trends predicted by chemical intuition.

Our ESEEM studies involve two bidentate ligands, 2,2'-bipyridine and 1,10-phenanthroline. The chemical structure about the nitrogen atoms in these compounds is similar to that in pyridine. Negita et. al (1970) published NQR data for 2,2'-bipyridine. The published values for the two high frequency transitions are ν_-=3.074 MHz and

ν_+=3.902 MHz. We note that the associated published value of $e^2qQ = 4.152$ MHz is incorrect. We calculate e^2qQ = 4.65 MHz with η = 0.35. Cheng et al. (1977) reported NQR results for 1,10-phenanthroline, with averaged crystal parameters of e^2qQ = 4.75 MHz with η = 0.35. These values are comparable to the average values for the simple pyridine molecule, e^2qQ = 4.58 MHz with η = 0.396.

As previously described, the coordination of nitrogen to Lewis acids reduces the NQR frequency by drawing electron density from the lone pair orbital. This suggests that the NQR values for coordinated ^{14}N can be interpreted as a measure of Lewis acidity. Such studies have been performed in the laboratory of T. L. Brown (Rubenacker and Brown, 1980; Hsieh et al., 1976; Hsieh et al., 1977; Cheng et al.,1977; Ashby et al., 1978). Metals used in such NQR coordination experiments are limited to diamagnetic species. The major change in the Townes-Dailey theory for treating these systems is the addition of a new parameter to characterize the occupancy of the new acid-base σ-bond. This parameter value approaches 2 in the limit of zero interaction with the Lewis acid.

Hsieh et al. (1977) used the Townes-Dailey model for free-base pyridine as a starting point in their analysis of the NQR frequencies for coordinated pyridine complexes. The $\widehat{CNC}$ half-angle θ is included explicitly in their expression for the principal axis field gradients

$$\begin{aligned} q \equiv q_{zz} &= [2(1-cot^2\theta) - a_0/2 + b_0(cot^2\theta - 1/2)]q_p \\ q_{yy} &= [-(1-cot^2\theta) + a_0 - b_0(1+cot^2\theta)/2)]q_p \\ q_{xx} &= [-(1-cot^2\theta) - a_0/2 + b_0(2-cot^2\theta)]q_p \end{aligned} \qquad (IV-13)$$

where the occupancy for the lone pair orbital is set to 2, and a_0 and b_0 represent the π and σ-bonding occupancy for pyridine. The coordination of the base to the Lewis acid results in a decrease in the occupation of the lone pair orbital as electron density is transferred to the acid center. We denote as λ the occupancy of the lone pair orbital. An inductive effect also occurs as σ and π electron density from the N-C bonds increase to replace lost lone pair density. Hsieh et al. (1977) treated this inductive effect with a simple linear model

$$\begin{aligned} a &= a_0 + A(2-\lambda) \\ b &= b_0 + B(2-\lambda) \end{aligned} \qquad (IV-14)$$

such that the N-C σ and π-bond population increase in proportion to the electron withdrawal from the N lone pair. Chemical intuition requires that A and B should be

positive, and that $2B + A < 1$; i.e. the increase in N-C bonding orbitals should be not quite as large as the decrease in the lone pair orbital. If the values of A and B can be reliably determined, this model predicts e^2qQ and η as function of only λ, the donor orbital occupancy.

The z-field gradient expression can be written for this generalized coordination model (Hsieh et al., 1977) as

$$q \equiv q_{zz} = \left[\lambda(1 - cot^2\theta) - \frac{1}{2}\left[a_0 + A(2-\lambda)\right] + \left[b_0 + B(2-\lambda)\right](cot^2\theta - 1/2)\right] q_p \qquad (IV-15)$$

or by regrouping terms

$$e^2qQ = \alpha e^2 q_p Q \qquad (IV-16)$$

with

$$\alpha \equiv \left[\lambda(1 - cot^2\theta) - \frac{1}{2}\left[a_0 + A(2-\lambda)\right] + \left[b_0 + B(2-\lambda)\right](cot^2\theta - 1/2)\right] \qquad (IV-17)$$

The value of the asymmetry parameter $\eta = (q_{xx} - q_{yy})/q_{zz}$ may also be written for this new model as

$$\eta = \frac{3}{2\alpha}\left\{\left[b_0 + B(2-\lambda)\right] - \left[a_0 + A(2-\lambda)\right]\right\} \qquad (IV-18)$$

These equations predict a linear relationship between $1/\alpha$ and η, which was tested by examining the NQR parameters for a number of Zn(II) and Cd(II) pyridine complexes. A plot of $1/(e^2qQ)$ vs η for these compounds shows such a linear dependence, and the slope and intercept of the plot provide an additional constraint to the values of parameters A and B. The authors were able to provide maximum ranges for the two induction parameters, with $0.0 < B < 0.17$ and $0.42 < A < 0.66$. The authors chose midrange values (A=0.50 and B=0.06) and calculated donor orbital occupancy values for the coordinated pyridine complexes. The Townes and Dailey theory modified by the orbital induction correction was found to provide an adequate model.

Rubenacker and Brown (1980) provided a more extensive test of this theory by applying it to a group of 58 distinct ^{14}N NQR resonance sets from 42 different coordinated pyridine compounds. Coordinated metals included Li, Ag, Cd, Mo, Cr, Zn, Hg, and Fe. Several pyridinium salt complexes were also studied. With this large number of experimental points, the authors found it possible to tightly constrain the model parameters. Each pyridine adduct contributes two items of data, e^2qQ and η.

The three field gradients q_{zz}, q_{yy}, and q_{xx} can be calculated from these experimental parameters. For each adduct there is one unknown parameter, λ, the donor orbital occupancy. The σ and π orbital densities are given by equation IV-14, which states that these populations deviate linearly from the free pyridine value as the population λ decreases from its free-base value of 2. The inductive parameters A and B are the two remaining unknowns. The total system provides a well constrained problem, with $2k$ fixed data and only $k+2$ unknowns for the series of $k = 58$ data sets. Rubenacker and Brown assigned each complex a value λ_i to fit the experimental field gradient results for the complex to that predicted by equations IV-15 and IV-18. The rms deviation $\delta_i = (\delta_{xx}^2 + \delta_{yy}^2 + \delta_{zz}^2)^{1/2}$ was obtained for each complex, where δ_{kk} represents the deviation of the experimental field gradient along quadrupolar axis k from that predicted by the model. Finally, the sum of all deviations δ was minimized to obtain best-fit values for the inductive parameters A and B. The optimal inductive parameters are $A = 0.446$ and $B = 0.087$. The graphic result of this assignment procedure is displayed in Figure IV-19. In this figure the three calculated field gradients for each adduct are displayed as a function of the donor occupation λ_i resulting in the mimimum δ_i. The solid lines represent the three field gradients as a function of λ, and are calculated using equations IV-15 and IV-18 with $A = 0.446$ and $B = 0.087$. The systematic fit to the data is excellent, and the linear induction model apparently provides a useful interpretation for the NQR results for such coordination series. It is interesting to note that the π-bond inductive parameter A=0.445 has a much larger value than the σ-bond parameter B=0.08. This reflects the fact that the π orbital system is much more polarizable than is the σ N-C bond. Also the sum $2B + A = 0.66$ shows that about 0.66 additional electronic equivalents are drawn into the N σ and π bonding orbitals for each electronic equivalent donated to the Lewis acid.

Figures IV-20 and IV-21 present the results of Figure IV-19 in a different format. Figure IV-20 shows the experimental values of e^2qQ plotted along with the matching theoretical curve predicted by equation IV-15. The NQR results of Rubenacker and Brown are shown as black squares. The fit to the theoretical curve (with the same parameters used for Figure IV-19) is very good. The open box denotes our di-μ-oxo bridged Mn(III)Mn(IV) bipyridyl dimer ESEEM result. The calculated value e^2qQ= 2.28 MHz is placed along the theoretical fit line. The projected donor orbital density $\lambda = 1.703$ is obtained by examining the horizontal position of the ESEEM-derived data point. Figure IV-21 shows the corresponding experimental and theoretical

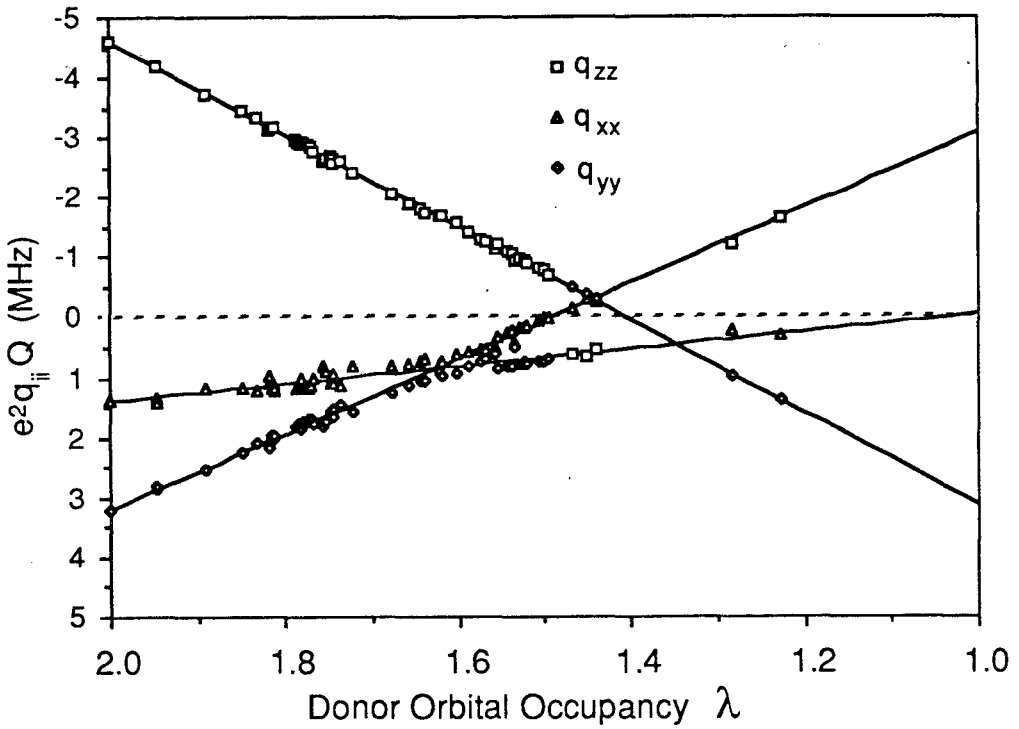

Figure IV-19 Experimental and calculated ^{14}N electric field gradients for a series of pyridine coordination complexes (from Rubenacker and Brown, 1980). Experimental data for the e^2qQ and η are used to calculate the three ^{14}N quadrupole tensor components q_{zz}, q_{yy}, and q_{xx}. The horizontal axis represents the donor orbital density λ. Each set of experimental data are placed horizonally to minimize deviation from the theoretical predictions derived from equations IV-15 and IV-18. The solid lines correspond to predicted values of the electric field gradients vs. λ, with inductive parameters A=0.446 and B=0.087. The free-base pyridine values employed are a_0=1.156 and b_0=1.290, and the value of e^2q_pQ is set to 9.0 MHz.

values for the asymmetry parameter η. We note that the apparent scatter in these data is greater than for the e^2qQ data. This is due to the definition of the asymmetry parameter, $\eta = (q_{xx} - q_{yy})/q_{zz}$, because scatter from each of the three quadrupolar field components contributes to the value of η. Rubenacker and Brown performed the initial fit optimization in the principal axis format shown in Figure IV-19 just to avoid this amplification of scatter which is evident in this presentation format. However, we see in Figure IV-21 that the experimental NQR data for η follow the theoretical curve. The asymmetry parameter obtained from our di-μ-oxo bridged Mn(III)Mn(IV) bipyridyl dimer ESEEM experiments is displayed as the open square. This data point is positioned at the horizontal value $\lambda = 1.703$ obtained from the e^2qQ value in the previous figure. We see that the relatively low value of $\eta \approx 0.07$ is consistent with the modified Townes-Dailey theory prediction.

The donor orbital density of 1.703 indicates that the high valence Mn acts as a relatively strong Lewis acid for the bipyridyl ligand. The value of λ=1.703 is lower than those for any of the coordinated metals in the NQR study (Li^+, Ag^+, Cd^{2+}, Mo(0), Cr(0), Zn^{2+}, Hg^{2+}, and Fe(0)). Lower donor densities were only achieved in pyridinium salts in which the base is formally protonated or in largely covalent complexes such as pyridine-sulfur trioxide.

So far we have used pyridine as a starting point for analyzing the 2,2'-bipyridine quadrupolar data from our ESEEM experiment. Cheng et al. (1977) examined ^{14}N NQR frequencies for 1,10-phenanthroline coordinated to a series of palladium(II) complexes. We recall that the ESEEM results obtained with the di-μ-oxo bridged Mn(III)Mn(IV) phenanthroline dimer are virtually identical to the ESEEM results obtained with the di-μ-oxo bridged Mn(III)Mn(IV) bipyridyl dimer. Pd-coordinated phenanthroline provides a better geometrical and chemical match to our 2,2'-bipyridine ligand than coordinated pyridine, although the range of complexes studied by NQR is more limited. The complexes studied by Cheng et al, are of the form (phen)PdX_2 and (phen)PdY, where X and Y respectively represent monodentate and bidentate ligands. The complexes all have nearly square-planar geometry. Although the central ion remains formally Pd(II) through the series, changes in Lewis acidity from one complex to the next represent effects of the ligands trans to the phenanthroline on the effective metal charge. Pd(II) is considered a "soft" acid, and therefore its effective charge is strongly influenced by these trans ligands.

Figure IV-22 shows the NQR e^2qQ data for the phenanthroline ^{14}N in the coor-

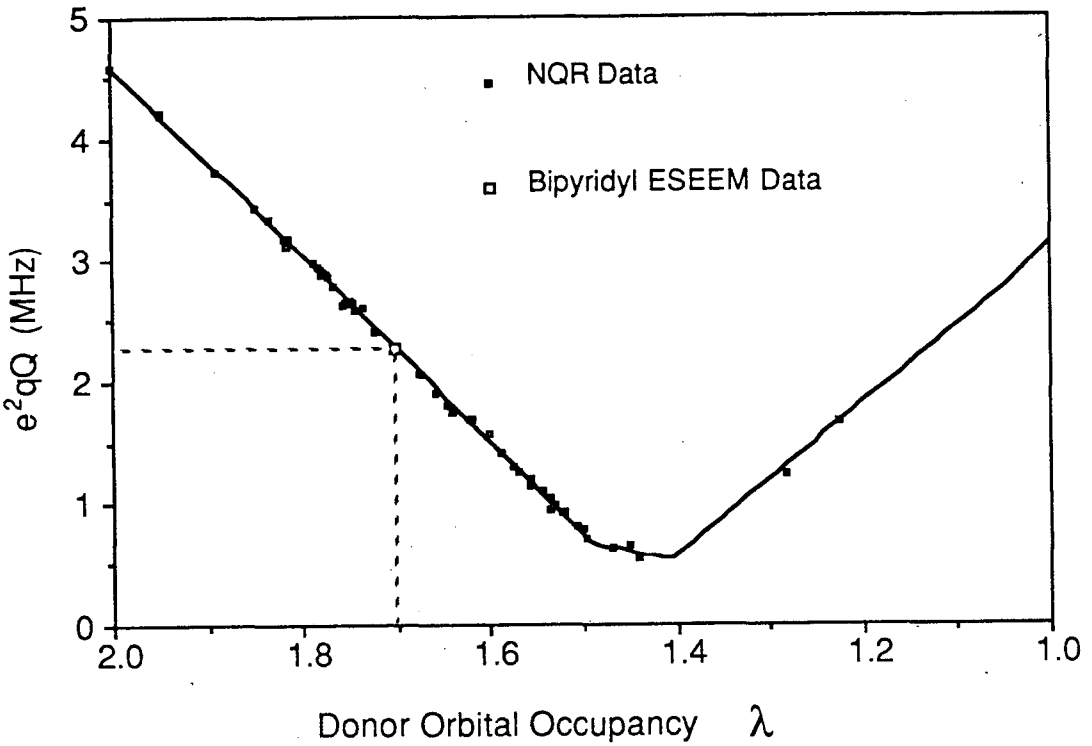

Figure IV-20 Experimental and calculated values of the quadrupolar coupling constant e^2qQ for ^{14}N in a series of pyridine coordination complexes (adapted from Rubenacker and Brown, 1980). The value of e^2qQ is plotted vs. the donor orbital density λ. The theoretical line corresponds to inductive parameters A=0.446 and B=0.087. The free-base pyridine values employed are a_0=1.156 and b_0=1.290, and the value of e^2q_pQ is set to 9.0 MHz. The black squares represent NQR data from a series of pyridine adducts. The open white square represents our di-μ-oxo bridged Mn(III)Mn(IV) bipyridyl dimer result of e^2qQ=2.28 MHz, with a projected donor density λ=1.703.

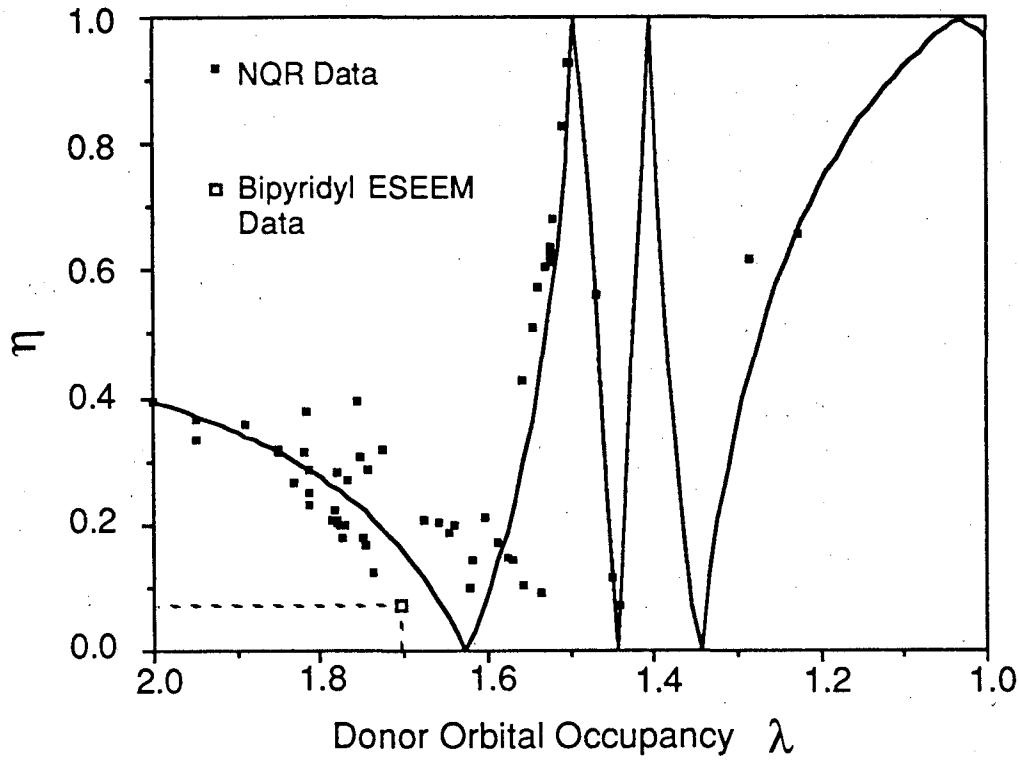

Figure IV-21 Experimental and calculated values of the asymmetry parameter η for ^{14}N in a series of pyridine coordination complexes (adapted from Rubenacker and Brown, 1980). The value of η is plotted vs. the donor orbital density λ. The theoretical line correspond to inductive parameters A=0.446 and B=0.087. The free-base pyridine values employed are a_0=1.156 and b_0=1.290, and the value of e^2q_pQ is set to 9.0 MHz. The black squares represent NQR data from a series of pyridine adducts. The open white square represents our di-μ-oxo bridged Mn(III)Mn(IV) bipyridyl dimer result of $\eta \approx 0.07$. The donor density value λ=1.703 is obtained from the more accurate e^2qQ fit from Figure IV-20.

dinated Pd(II) series. The solid line again represents the theoretical results from the modified Townes-Dailey model. Fit parameters are the same as for pyridine except for the inductive terms A=0.50 and B=0.06. Figure IV-23 displays the corresponding data for the asymmetry parameter η. We see the ESEEM data for the di-μ-oxo bridged Mn(III)Mn(IV) bipyridyl dimer (open boxes) fit both e^2qQ and η very well. The projected orbital occupancy parameter λ=1.713 is very close to the value λ= 1.703 obtained from comparison with the more extensive pyridine data set.

We see from these results that we can readily analyze the ^{14}N NQR parameters obtained by ESEEM experiments with a theory that relates these parameters to molecular orbital densities. Having applied these techniques with great success to mixed valence Mn complexes of known structure gives us confidence in our ability to extract meaningful results from similar ESEEM data obtained on the Mn signal of Photosystem II. We have also shown that the magnitude of superhyperfine coupling between high-valence Mn and directly coordinating ^{14}N ligands is in a range which produces large ESEEM effects. We therefore proceed to Chapter V, which presents our ESEEM results on the multiline Mn signal associated with the Kok S_2 state of photosynthetic water oxidation.

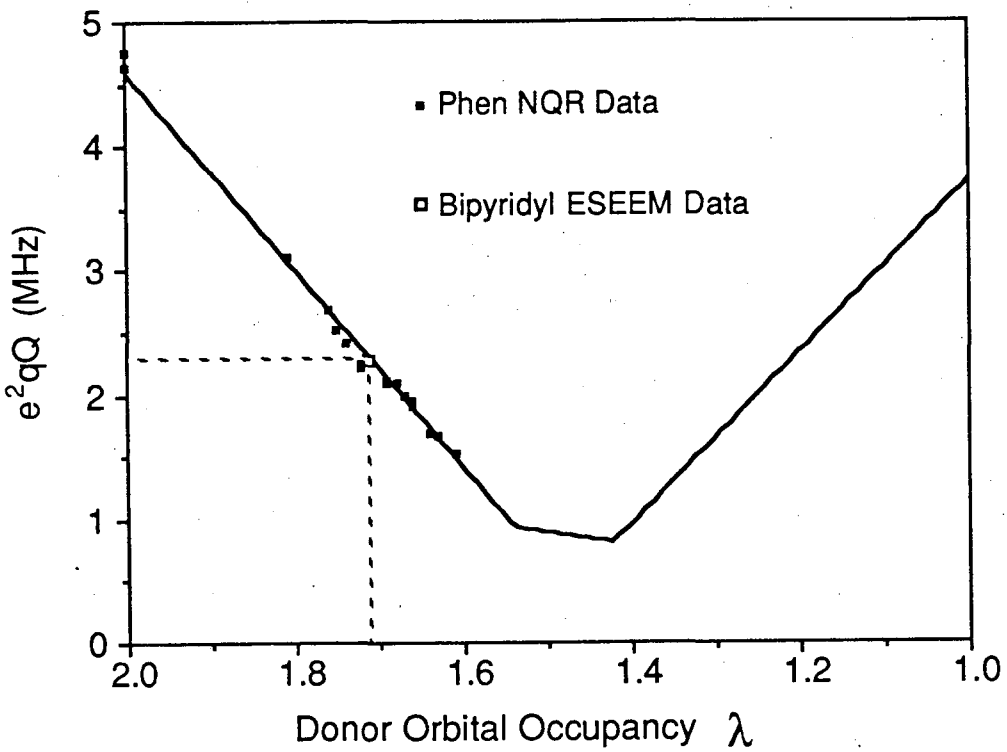

Figure IV-22 Experimental and calculated values of the quadrupolar coupling constant e^2qQ for ^{14}N in a series of 1,10-phenanthroline Pd(II) coordination complexes (adapted from Cheng et al., 1977) The value of e^2qQ is plotted vs. the donor orbital density λ. The theoretical line correspond to inductive parameters A=0.500 and B=0.060. The free-base phenanthroline values employed are a_0=1.156 and b_0=1.290, and the value of e^2q_pQ is set to 9.0 MHz. The black squares represent NQR data from the series of phenanthroline adducts. The open white square represents our di-μ-oxo bridged Mn(III)Mn(IV) bipyridyl dimer result of e^2qQ=2.28 MHz, with a projected donor density λ=1.713.

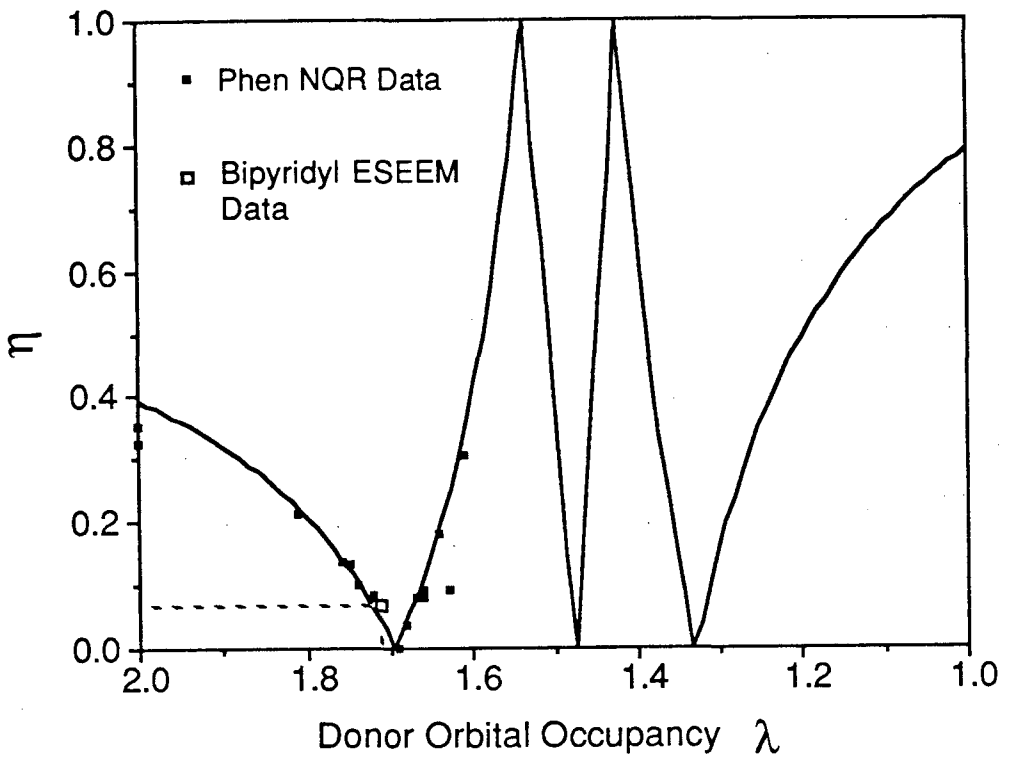

Figure IV-23 Experimental and calculated values of the asymmetry parameter η for ^{14}N in a series of 1,10-phenanthroline Pd(II) coordination complexes (adapted from Cheng et al., 1977) The value of η is plotted vs. the donor orbital density λ. The theoretical line correspond to inductive parameters A=0.500 and B=0.060. The free-base phenanthroline values employed are a_0=1.156 and b_0=1.290, and the value of e^2q_pQ is set to 9.0 MHz. The black squares represent NQR data from the series of phenanthroline adducts. The open white square represents our di-μ-oxo bridged Mn(III)Mn(IV) bipyridyl dimer result of $\eta \approx 0.07$, with a projected donor density value λ=1.713 as determined from the more accurate e^2qQ fit of Figure IV-22.

Chapter V–Electron Spin Echo Studies of Mn in Photosystem II.

This chapter discusses the results of electron spin echo experiments on the light-induced Mn EPR signal associated with photosynthetic water oxidation. The first section reviews the results of previous cw EPR experiments and current thought as to the structure and function of the Mn complex. Section 2 presents our ESEEM data on the Mn multiline EPR signal and addresses the question of protein ligation to the PSII Mn. Section 3 reports the results of ESEEM studies of ammonia binding at or near the Mn site. Section 4 examines the interaction of the Mn with water by comparing results obtained with ^1H_2O and ^2H_2O buffers

Section 1–Structure of the Photosystem II Mn Cluster as Determined by EPR

Dismukes and Siderer (1980, 1981) published the first observation of an EPR signal attributable to a multinuclear Mn center in Photosystem II. These first experiments were performed on dark-adapted broken spinach chloroplasts. The chloroplast samples were subjected to a series of light flashes and quickly frozen. The first flash was seen to produce a broad low-temperature EPR signal with at least sixteen partially resolved hyperfine lines with a regular separation of about 80 Gauss (see Figure V-1b). The EPR signal amplitude was diminished by a second flash, remained small until increasing on the fifth flash, and diminished again on the sixth flash. The amplitude vs. flash dependence was thus seen to follow the period-four dependence of the Kok S-state cycle. The dark-adapted chloroplasts were poised primarily in the S_1 state. The Mn EPR signal exhibited maximal amplitude after the first and fifth flashes, and thus Dismukes and Siderer assigned the signal to the S_2 state of the Kok water oxidation cycle. Various inhibitors of photosynthetic oxygen evolution were observed also to inhibit the formation of this multiline Mn EPR signal.

The Mn hyperfine pattern observed for this "multiline" EPR signal is similar to that observed from the synthetic Mn(III)Mn(IV) dimers discussed in Chapter IV. Based on this similarity, Dismukes and Siderer proposed that the PSII signal arises from a dimer or tetramer of magnetically coupled high-valence Mn ions. The spectrum is very different from the simple six-line spectra observed for isolated Mn(II) complexes (Reed and Markham, 1984). We will discuss models for the origin of the Mn multiline signal later in this section.

Hansson and Andréasson (1982) succeeded in reproducing the S_2 Mn EPR signal of Dismukes and Siderer. They were able to produce a significant population of the

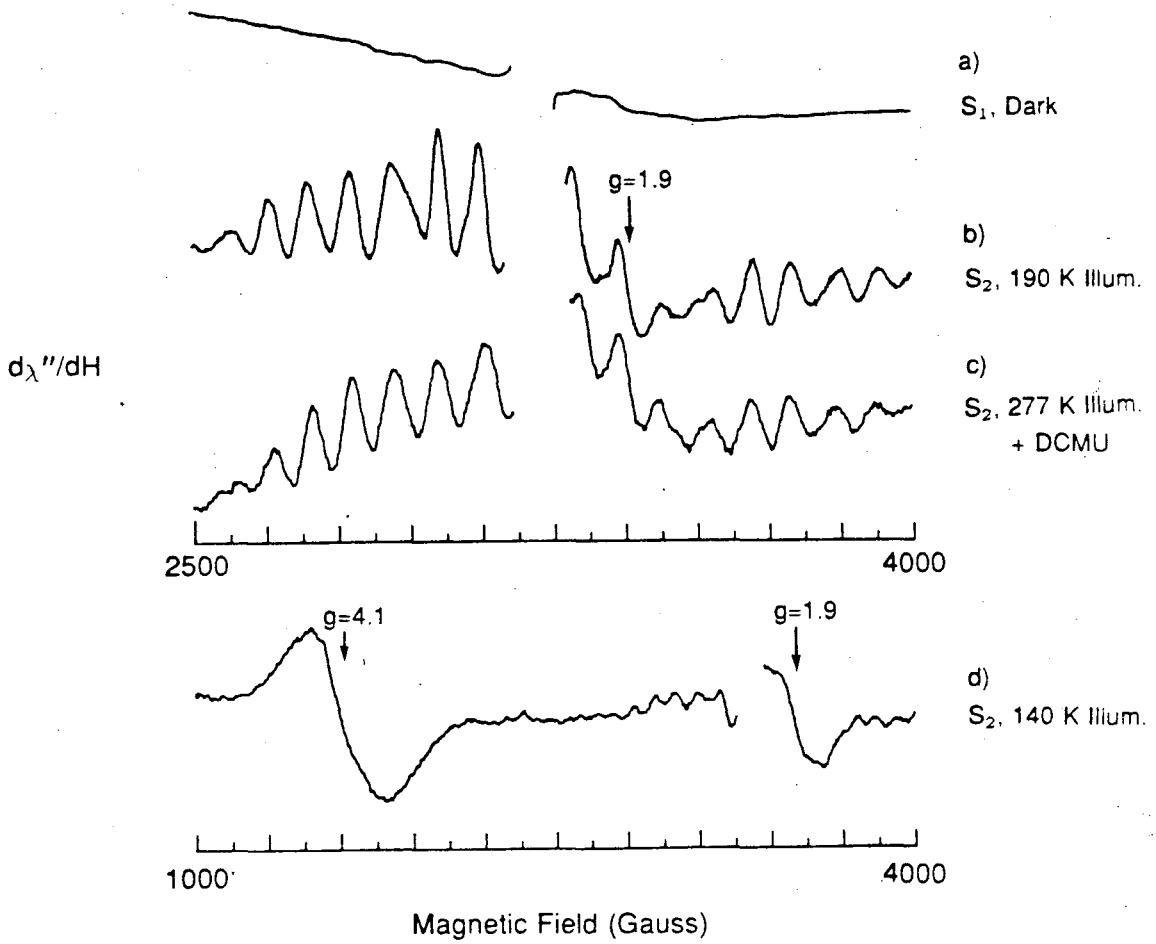

Figure V-1 Light-induced Photosystem II EPR signals (Yachandra et al., 1987). These cw EPR spectra were obtained with PSII membrane preparations from spinach chloroplasts. The narrow free-radical signal from the tyrosine radical denoted D^+ is excised in all spectra. The EPR spectrum of the dark-adapted S_1 state is shown as (a). This background spectrum is subtracted from light-induced spectra to give the results (b), (c), and (d). The light-induced S_2 Mn multiline EPR signal in (b) is produced by illumination at a temperature of 190 K. The S_2 Mn multiline signal can also be produced by 277 K illumination in the presence of DCMU (c), which blocks S-state transfer past S_2 by replacing the acceptor quinone Q_b. Illumination at the low temperature of 140 K produces a light-induced g=4.1 signal (d). A quinone signal is also observed when Q_a is reduced (d).

S_2 state by simply freezing chloroplasts during illumination. Brudvig et al. (1983) explored the effect of illumination temperature on the formation of the Mn multiline S_2 signal. They demonstrated a maximal generation of this signal under continuous illumination at a temperature of about 190 K. The kinetics of the formation and decay of the signal were shown to correspond to the S_2 state.

Casey and Sauer (1984) demonstrated the formation of another light-induced EPR signal by continuous illumination of PSII membranes at 140 K. This signal (see Figure V-1d) has a width of about 320 Gauss and is centered at a magnetic field corresponding to g=4.1. There is no resolved Mn hyperfine structure on this light-induced g=4.1 signal. Warming of 140 K illuminated samples to 190 K causes a disappearance of the g=4.1 signal and an appearance of the multiline Mn signal. Thus Casey and Sauer proposed that this signal results from a state intermediate between S_1 and S_2 that is trapped at the lower illumination temperature of 140 K. From the g-value and the linewidth they also proposed that this new signal arises from a high-spin Fe(III) in a rhombic enviroment. Zimmermann and Rutherford (1984) also observed this g=4.1 signal in PSII membrane preparations illuminated at 200 K. They interpreted their results to indicate that the g=4.1 signal arises from an intermediate state between S_2 and S_3. In a later paper Zimmermann and Rutherford (1986) showed the results of examining the light-induced EPR spectra as a function of flash number in a fashion similar to the original Dismuke and Siderer experiment. They were able to demonstrate that the g=4.1 signal actually arises from the S_2 state. The differences in their early results and the results of the experiments of Casey and Sauer were shown to result from using different "cryoprotectants" to protect the samples during freezing. Casey and Sauer had used glycerol as a cryoprotectant, and Zimmermann and Rutherford had used sucrose. The new model of Zimmermann and Rutherford (1986) describes both the multiline EPR signal and the g=4.1 EPR signal as arising from the S_2 state, with a subtle heterogeneity among PSII centers determining which EPR signal is presented by a given center. de Paula and Brudvig (1985) had previously presented a model with the g=4.1 EPR signal arising from an $S = 3/2$ electronic state of the Mn cluster. Cole et al. (1987) demonstrated a shift of the Mn X-ray K-edge to higher energies for PSII membranes illuminated at 140 K and exhibiting large light-induced g=4.1 EPR signals. The Mn X-ray edge shift for these samples is comparable to that observed with 190 K illumination and the production of the Mn multiline EPR signal. These data were considered as evidence that the g=4.1 EPR signal results from oxidation of

Mn on the $S_1 \rightarrow S_2$ transition.

The PSII Mn multiline EPR signal typically shows 18 or 19 resolved Mn hyperfine lines. Dismukes and coworkers first suggested that the presence of more than 16 lines in the PSII Mn multiline spectrum indicates the contribution of more than two Mn ions (Dismukes and Siderer, 1981; Dismukes et al. 1982). Dismukes et al. proposed that the multiline EPR signal arises from a Mn tetramer with the spins of the individual ions correlated by a combination of ferromagnetic and antiferromagnetic couplings. They proposed a cluster of three Mn(III) and one Mn(IV) as a likely candidate. A tetrameric model is consistent with the observed stoichiometry of 4 Mn ions per PSII reaction center.

The EPR properties of the Mn multiline EPR signal have been examined in detail in the laboratory of Gary Brudvig (de Paula and Brudvig, 1985; de Paula et al. 1986; Beck and Brudvig, 1986; de Paula et al. 1987). This group reports observing forms of the Mn multiline EPR signals with unusual dependence of amplitude vs. observation temperature. For such samples the multiline EPR signal amplitude diminishes at temperatures below $\approx$7.0 K. Their interpretation for these results is that the S=1/2 state producing the multiline signal in these samples is an excited state rather than a ground state. Thus at low temperatures this excited state is thermally depopulated, and the multiline signal amplitude is diminished. Their models favor a Mn ground state S=3/2 origin for the light-induced g=4.1 signal. A antiferromagnetically coupled Mn dimer could not yield an S=1/2 excited state. Brudvig and coworkers consider this as important evidence for a Mn tetramer complex with the four Mn atoms linked by both ferromagnetic and antiferromagnetic couplings. Their proposed structure for the S_2 state cluster consists of a Mn_4O_4 complex arranged in a "cubane-like" structure analogous to that observed in Fe_4S_4 centers (de Paula et al. 1986). Brudvig and Crabtree (1986) have proposed a model for oxygen evolution that posits a conversion of this "cubane-like" structure to a Mn_4O_6 "adamantane-like" structure during the $S_2 \rightarrow S_3$ transition.

The model of a Mn tetrameric excited state origin for the Mn multiline signal was challenged by Hansson et al. (1987). These authors studied the temperature dependence of both the Mn multiline and g=4.1 signals and concluded that they both arise from separate ground state doublets. The g=4.1 signal is proposed to originate from an isolated Mn(IV) species. They suggest that the Mn multiline signal arises from a Mn(III)Mn(IV) dimer. In the model of Hansson et al., these two signals result from

two types of distinct centers in redox equilibrium. In the same paper these authors show using X and Q band experiments that the Mn multiline signal is isotropic, with g=1.98. EPR simulations by de Paula et al. (1986) had previously argued for an anisotropic g-tensor ($g_x = 1.810$, $g_y = 1.960$, $g_z = 2.274$).

Recently de Paula et al. (1987) have suggested that the difference in observed properties of the Mn multiline signal results from using different "cryoprotectants" in the PSII suspension buffers. They report a ground-state origin for the multiline signal observed in buffer containing sucrose and an excited-state origin in buffer containing ethylene glycol. We have studied the S_2 multiline signal prepared in buffer with ethylene glycol with no exposure to sucrose at any stage of the preparation. We have examined the integrated area of the light-induced Mn multiline ESE signal at temperatures down to 1.5 K with no indication of an excited-state origin of the signal (Britt, Sauer, and Klein; manuscript in preparation). The assignment of the multiline signal to an excited state origin remains controversial. It is possible that the differences in observed behavior may result from subtle differences in preparative techniques.

We also note that J.-L. Zimmermann (personal communication) has suggested that the observed Mn multiline spectrum originates from the superposition of spectra from two dimer forms with slightly different Mn hyperfine couplings. The coupled tetramer spectral simulations require g-anisotropy to explain the regular spacing of lines, yet such g-anisotropy seems to be ruled out by the results of Hansson et al. (1987).

We see that there is still a great deal of controversy regarding the exact configuration of the Mn ions involved in photosynthetic water oxidation. Future research should resolve many of these controversies and provide a more consistent picture of the Mn site structure.

The following sections present the results of our electron spin echo envelope modulation studies of the Mn multiline signal. These ESEEM experiments have allowed us to measure superhyperfine couplings (<1 Gauss) that are too weak to be resolved with conventional EPR techniques. The ESEEM experiments also provides a direct measure of nuclear quadrupolar couplings for ^{14}N nuclei. The following section describes our measurements to determine the ligation environment of Mn in Photosystem II.

Section 2–Photosystem II Mn Ligands as Determined by ESEEM

This section describes our ESEEM studies of the Mn multiline signal. The goal of these studies is to determine the ligand environment of the PSII Mn ions which produce the EPR signal. All studies are performed with spinach PSII membrane fragments. The preparation of these PSII membranes is performed by a Triton X-100 fractionation procedure (Berthold et al. 1981; Kuwabara and Murata, 1982).

The preparative procedure begins with destemmed fresh market spinach. The buffered solutions employed are described in Table V-1. All buffered solutions are kept at 4°C, and all steps following leaf destemming are performed in darkness or low-level green light. The destemmed leaves are immersed in the grinding medium and ground in a Waring blender for approximately 10-15 sec. The resulting homogenate is filtered through 8 layers of cheesecloth and centrifuged at 6000×g for 10 min. The resulting centrifuge pellet is resuspended in washing media. The resulting suspension is centrifuged at 6000×g for 10 min. The centrifuge pellet is then resuspended in the SHN buffer. This suspension is subjected to a short 2800×g centrifugation to remove heavy debris. The loose pellet is discarded, and the supernatant is centrifuged at 6000×g for 10 min. The final pellet consists of broken chloroplasts.

The chloroplast pellet is resuspended in TSB to a *Chl* concentration of 2 mg/ml. A solution of 25% Triton X-100 in TSB is added to the suspension with vigorous stirring to give a Triton X-100/*Chl* ratio of 25:1. The resulting solution is incubated for 1 min. and then centrifuged at 6000×g for 2 min. The pellet is discarded, and the supernatant is centrifuged at 35000×g for 10 min. This pellet is resuspended in TSB and centifuged at 6000×g for 2 min. The resulting pellet is discarded and the supernatant is centrifuged at 35000×g for 10 min. The resulting pellet consists of Photosystem II enriched membrane fragments. Measured O_2 evolution rates are in the range of 300-400 μmol O_2 per mg *Chl* per hour. The pellet is resuspended in TSB with either 0.4 M sucrose or 30% (v/v) ethylene glycol. A final 35000×g centrifugation is performed for 20 min. The resulting firm pellet is resuspended in TSB with the same cryoprotectant to a *Chl* concentration of ≈6.0 mg/ml and placed in 3.8 mm O.D. quartz EPR tubes. The samples are further dark-adapted for 1 h. at 4°C and then frozen in liquid N_2. S_2 samples are prepared by 2 min. illumination at a temperature of 195 K with a 400 W tungsten lamp equipped with a 5 cm water filter. The S_2 samples are immediately returned to liquid N_2 storage.

Figure V-2a shows the light-induced ESE signal obtained by illuminating PSII

Grinding Media

0.4 M NaCl
2.0 mM $MgCl_2$
1.0 mM EDTA
20.0 mM HEPES (to pH 7.5)

Washing Media

150.0 mM NaCl
4.0 mM $MgCl_2$
20.0 mM HEPES (to pH 7.5)

SHN Media

0.4 M Sucrose
10.0 mM NaCl
10.0 mM $MgCl_2$
50.0 mM HEPES (to pH 7.6)

Triton Suspension Buffer (TSB)

15.0 mM NaCl
5.0 mM $MgCl_2$
50.0 mM MES (to pH 6.0)

Table V-1 Buffers used in the preparation of Photosystem II membrane fragments.

membrane preparations at 195 K. The spectrum results from measuring the 2-pulse electron spin echo amplitude as a function of magnetic field over a 2500 Gauss range centered about 3300 Gauss. The ESE spectrum from a matching dark-adapted S_1 sample is subtracted from the illuminated S_2 spectrum to achieve this difference spectrum. Thus all features of this spectrum are induced by illumination. The S_1 background spectrum shows some Cu(II) contamination. Sibbald and Green (1987) have shown that Cu(II) is associated with the PSII antenna complex LHCII. All of the ESEEM data presented in this chapter are obtained by subtracting the background signal ESEEM from the S_2-state data.

The light-induced ESE spectrum shown in Figure V-2 corresponds to the cw EPR Mn multiline spectrum. Conventional cw EPR data are obtained with magnetic field modulation and phase-sensitive detection. The resulting spectra show the derivative of the absorbed microwave power with respect to field. We do not employ field modulation in the spin echo experiments. Equivalent noise suppression is obtained with gated integration techniques as described in Chapter III. Thus the ESE technique does not present field-derivative spectra. However we may numerically differentiate our ESE spectra for comparison with conventional EPR spectra. The derivative spectrum presented in FIgure V-2b results from numerical differentiation of the spectrum of V-2a. Although the results are somewhat noisy, we can clearly see the Mn hyperfine features that characterize the Mn multiline spectrum. The peak spacings and amplitude patterns across the spectrum are the same as observed by conventional EPR.

The multiline ESE spectrum presents a broad isotropic set of transitions covering more than 1200 Gauss. The center of the spectrum is at slightly higher field than g=2.0. The Mn hyperfine features are only partially resolved. They appear as regularly spaced shoulders on the sides of the spectrum. The ESE spectrum closely resembles the results of a single integration of the cw Mn multiline spectrum (Hansson et al. 1987). The great breadth of the signal allows us to perform ESEEM experiments over a wide range of magnetic field. An integration over field of the light-induced spectrum allows us to calculate the effective electron spin concentration. The results show $\approx$0.5 electron spins per PSII center. We thus are not observing a tiny minority component.

We have performed several control experiments to further confirm that this signal is the ESE analogue of the cw multiline EPR signal. The signal is not generated in PSII membranes where oxygen evolution is inactivated by *Tris* or high-concentration NH_2OH treatments. The signal is not produced by illumination of active PSII mem-

Figure V-2 The light-induced Mn EPR signal as observed by electron spin echo spectroscopy. The spectrum displayed in (a) results from subtraction of dark-adapted S_1 spectrum from the illuminated S_2 spectrum. The displayed features are thus all light-induced. The spectra are obtained by measuring the amplitude of a 2-pulse electron spin echo as a function of magnetic field over a 2500 Gauss range centered about 3300 Gauss. The interpulse time τ is 140 ns and the time interval between successive spin echo pulse sets is 5.0 ms. The observation temperature is 4.2 K. The microwave frequency is 9.2984 GHz. The derivative of this spectrum with respect to magnetic field is shown in (b) for comparison with conventional field-modulated spectra. The D^+ radical signal is excised from the center of both spectra.

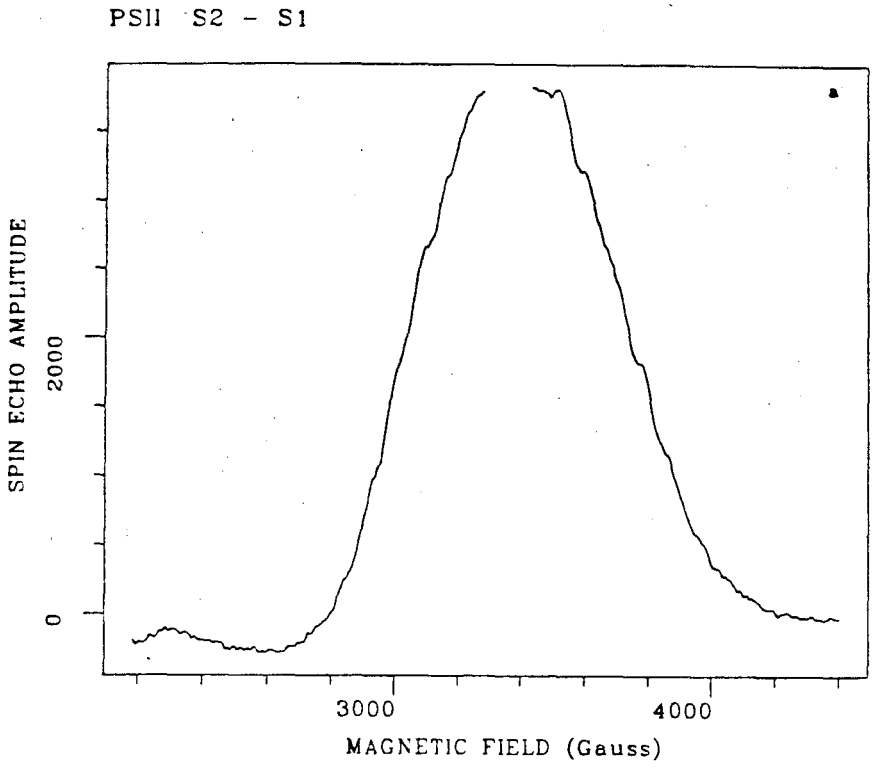
PSII S2 - S1
a
SPIN ECHO AMPLITUDE
2000
0
3000
4000
MAGNETIC FIELD (Gauss)

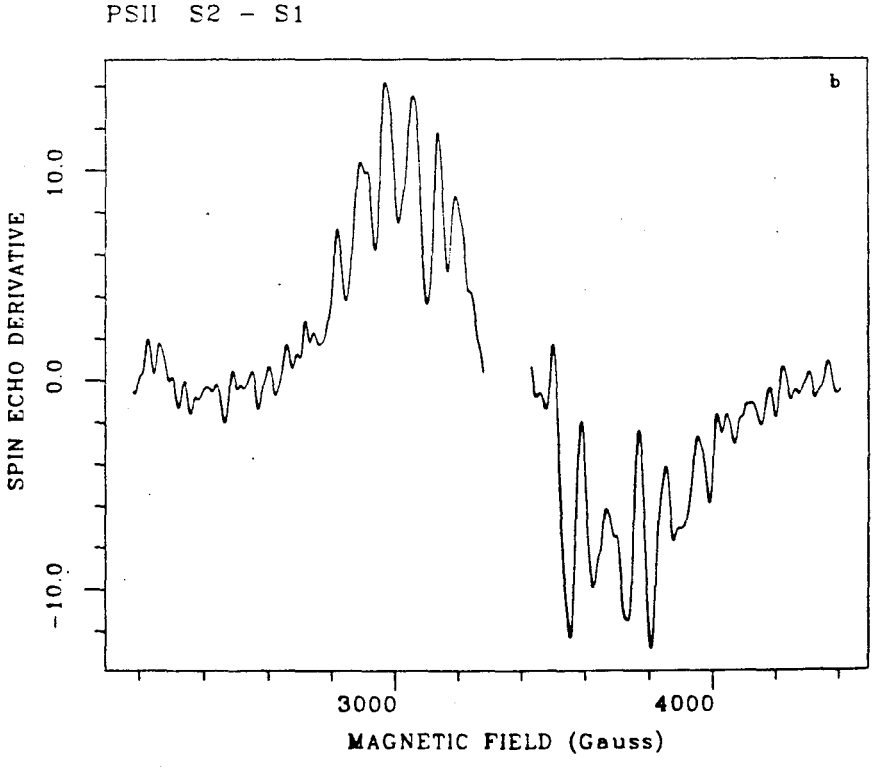
PSII S2 - S1
b
SPIN ECHO DERIVATIVE
10.0
0.0
-10.0
3000
4000
MAGNETIC FIELD (Gauss)

branes at a temperature of 77 K. The signal is produced by 0°C illumination in the presence of DCMU [3-(3,4-dichlorophenyl)-1,1-dimethylurea] to block S-state transfer past S_2. Incubation in F^- containing buffer results in a decrease in the signal to ≈30% of its magnitude in Cl^- containing buffer. We also note that we do not see the acceptor quinone or cytochrome b_{559} signals produced by 77 K illumination when the spin echo experiments are performed at 4.2 K. We thus do not have ESEEM contamination from these signals if measurements are performed at 4.2 K.

Figures V-3 and V-4 display 2-pulse ESEEM data for the light-induced Mn EPR signal obtained at 3400 and 3200 Gauss. The 2 pulse time-domain ESEEM patterns obtained at the two field positions are displayed in Figures V-3a and V-4a. These patterns are obtained by varying the interpulse time τ in 10 ns increments between 80 and 3000 ns. The Fourier cosine transforms of these data are displayed in Figures V-3b and V-4b. In each case the short 80 ns deadtime is backfilled by the method described by Mims (1984). In addition to discrete ESEEM effects, the ESE intensity is observed to decrease rapidly with increased τ. This reflects a phase memory for the light-induced Mn signal of about 800 ns. This short phase memory may limit the resolution of the ESEEM Fourier components.

The largest components in the ESEEM-derived spectra originate from weakly coupled protons. These "matrix" proton lines occur near the proton Larmor frequency for the applied magnetic field. The matrix line at 3400 Gauss occurs at 14.44 MHz, and the corresponding peak in the 3200 Gauss ESEEM is at 13.59 MHz. We have examined the 2-pulse ESEEM patterns at several field positions between 3000 and 3600 Gauss, and we always observe a large and sharp feature at precisely the weakly coupled proton limit. We see no evidence of any strongly coupled protons with frequencies shifted appreciably from the Larmor frequency. We will address the question of proton and deuteron coupling in some detail in Section 4 of this chapter.

A second large feature occurs in the ESEEM data at frequencies between 4.0 and 4.8 MHz. Several cycles of this low-frequency component are apparent in the time-domain data sets displayed in Figures V-3a and V-4a. However, this frequency component damps out very quickly, and the corresponding peak in the Fourier transform is quite broad. We have examined the frequency of this peak as a function of magnetic field across the spectrum of the Mn signal. The results of these field dependence studies demonstrate that the feature originates in the β-manifold double-quantum transition for a directly coordinated ^{14}N nucleus. Unfortunately this ^{14}N feature is

Figure V-3 2-pulse ESEEM at 3400 Gauss for the light-induced Mn EPR signal in PSII membrane preparations. The time-domain ESEEM pattern in (a) is obtained by varying τ in 10 ns increments from 80 to 3000 ns. The Fourier cosine transform of this ESEEM pattern is displayed in (b). The results are obtained at a temperature of 4.2 K, a microwave frequency of 9.3322 GHz, and a time interval between spin echo pulse sets of 3.0 ms. The displayed ESEEM pattern results from a subtraction of S_1 background from the 195 K illuminated S_2 data.

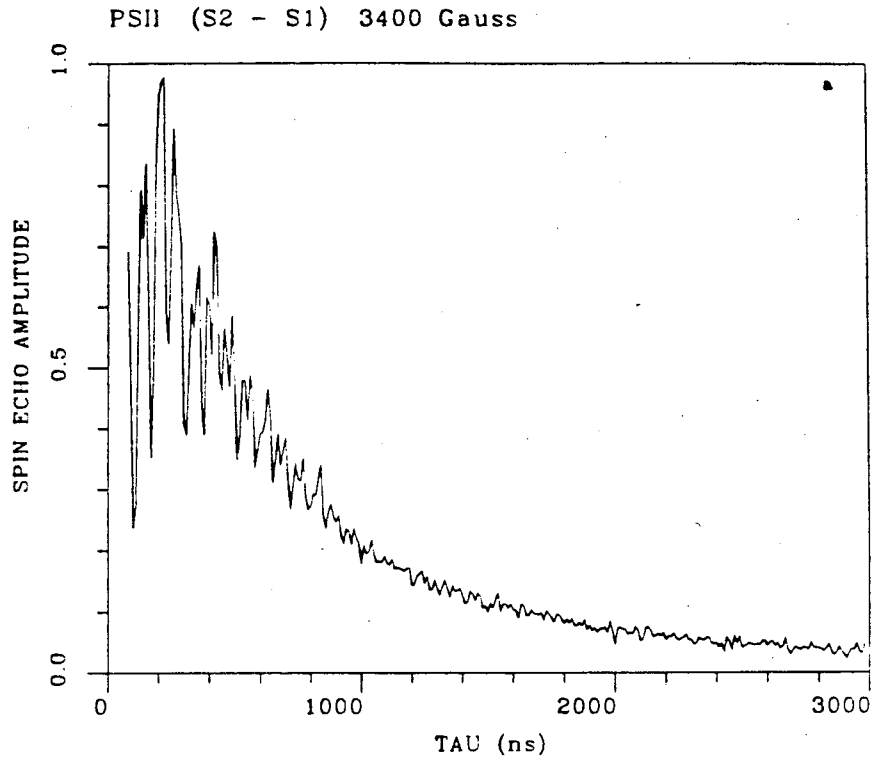
PSII (S2 - S1) 3400 Gauss
a
SPIN ECHO AMPLITUDE
1.0
0.5
0.0
0
1000
2000
3000
TAU (ns)

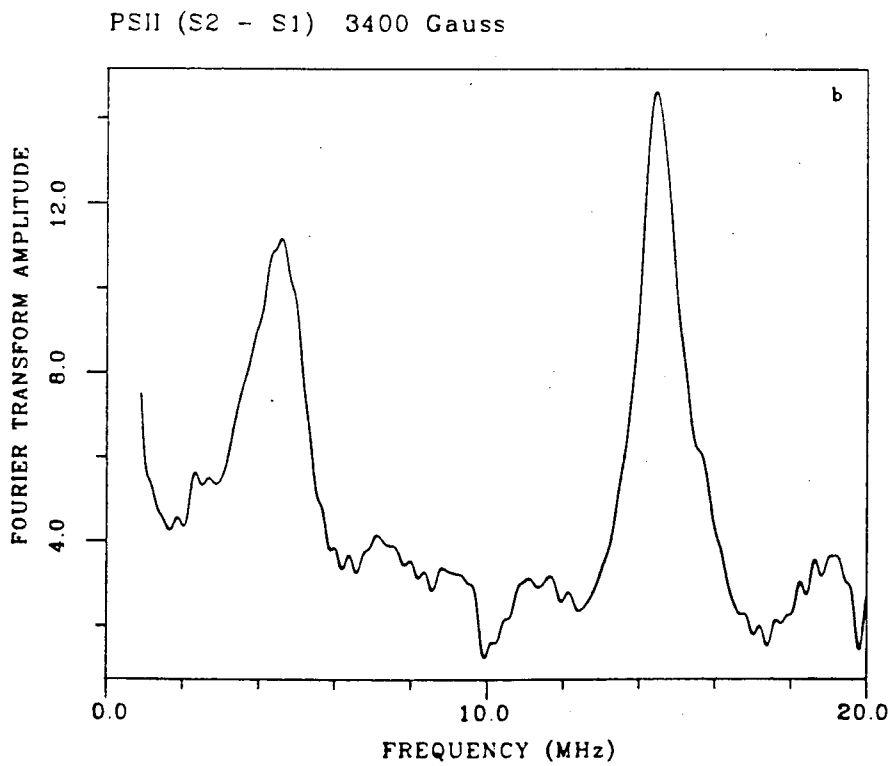
PSII (S2 - S1) 3400 Gauss
b
FOURIER TRANSFORM AMPLITUDE
12.0
8.0
4.0
0.0
10.0
20.0
FREQUENCY (MHz)

Figure V-4 2-pulse ESEEM at 3200 Gauss for the light-induced Mn EPR signal in PSII membrane preparations. The time-domain ESEEM pattern in (a) is obtained by varying τ in 10 ns increments from 80 to 3000 ns. The Fourier cosine transform of this ESEEM pattern is displayed in (b). The results are obtained at a temperature of 4.2 K, a microwave frequency of 9.3322 GHz, and a time interval between spin echo pulse sets of 3.0 ms. The displayed ESEEM pattern results from a subtraction of S_1 background from the 195 K illuminated S_2 data.

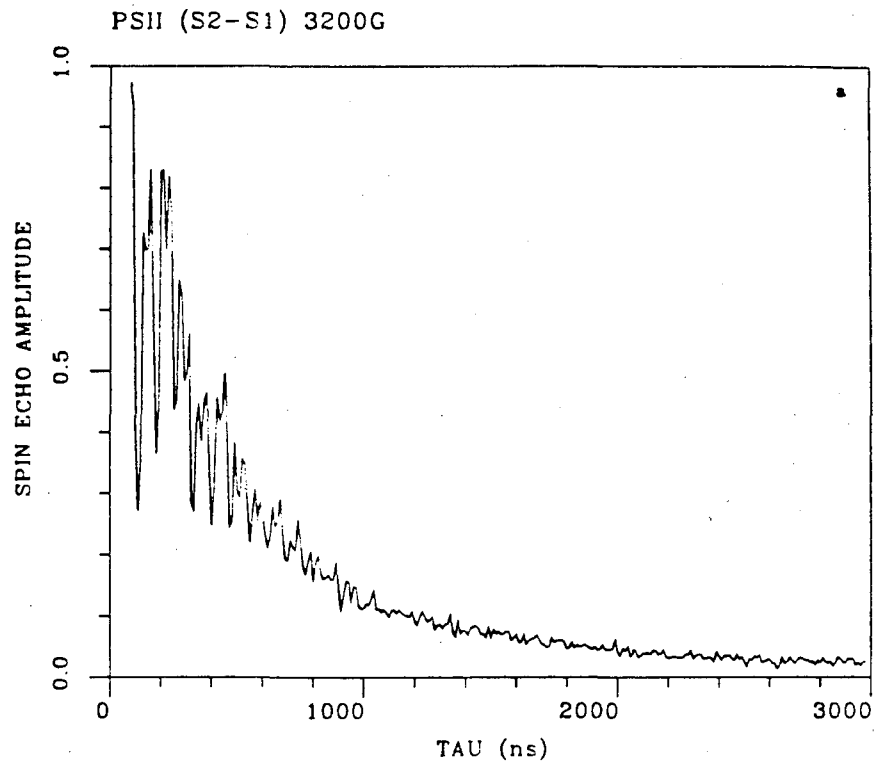
PSII (S2-S1) 3200G
a
SPIN ECHO AMPLITUDE
1.0
0.5
0.0
0
1000
2000
3000
TAU (ns)

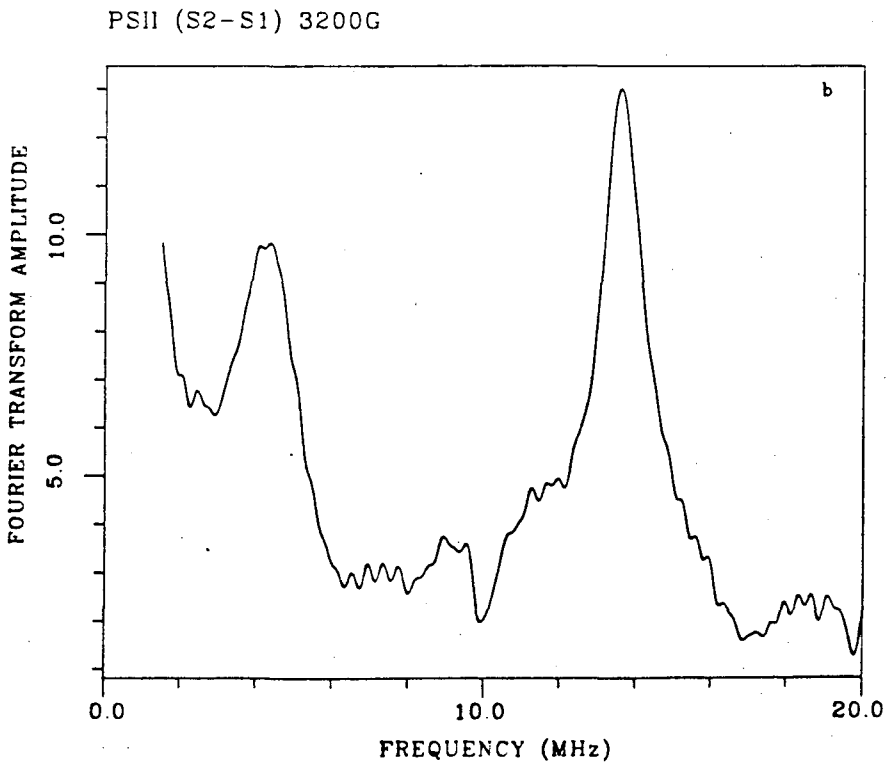
PSII (S2-S1) 3200G
b
FOURIER TRANSFORM AMPLITUDE
10.0
5.0
0.0
10.0
20.0
FREQUENCY (MHz)

quite broad and superimposed on the $\approx 1/f$ tail due to the short phase memory, and the resultant imprecision in frequency determination does not support the precise 3-pulse ESEEM frequency vs. field data fits employed for the model compounds in the last chapter. Also there is no clear evidence for the low-frequency α-manifold transitions in the 2-pulse data. Therefore it is important to analyse the 3-pulse stimulated ESEEM data for more precise information.

The principal disadvantage of the 3-pulse ESEEM technique is the increased deadtime interval. This increased deadtime is particularly disadvantageous for broad ESEEM lines, because the modulations damp out very quickly. There is also the complication of suppression effects as discussed in Chapter II. We find very shallow ^{14}N modulation in the 3-pulse ESEEM for short values of τ. Figure V-5a shows the 3-pulse ESEEM obtained at 3500 Gauss with the relatively long value τ=270 ns. We observe shallow modulation in this case, but the deadtime is long and much of the ^{14}N modulation has died out before our time-domain data begins. Nevertheless we can obtain useful frequency data from the Fourier cosine transform of this 3-pulse ESEEM pattern as seen in Figure V-5b. The high frequency feature at 14.8 MHz is again due to weakly coupled protons. The amplitude of this proton feature is relatively small due to 3-pulse suppression. The ^{14}N β-manifold double quantum frequency is at 4.75 MHz. The highest frequency component of the α-manifold is at 2.50 MHz. We see lower frequency features at about 1.05 and 1.42 MHz. These components appear to be the ν_0 and ν_- frequencies for the ^{14}N nucleus near exact cancellation of the Zeeman and hyperfine fields. These four frequency values form a consistent set of ^{14}N frequencies from a single ^{14}N nucleus, with $e^2qQ \approx 2.6$ MHz, $\eta \approx 0.8$, and $A \approx 1.90$ MHz. We see from this value of A that we are indeed close to the case of exact cancellation of hyperfine and Zeeman fields, which is why we resolve the three separate α-manifold components.

The Mn multiline ESEEM has been measured for a number of PSII samples. The ESEEM pattern is the same with sucrose or ethylene glycol as the cryoprotectant. The pattern is also identical for samples poised in the S_2 state by 0°C illumination in the presence of DCMU. The amplitude of the ^{14}N modulation damps out quickly, as can been seen in 2-pulse patterns shown in Figures V-3a and V-4a. The Fourier linewidths are thus broad. We are interested in determining the sources of this ^{14}N line-broadening. Certainly a component comes from hyperfine anisotropy. In the analysis of the ^{14}N frequencies we have assumed the hyperfine coupling to

Figure V-5 3-pulse ESEEM for the light-induced Mn EPR signal in PSII membrane preparations. The time-domain ESEEM pattern in (a) was obtained by varying T in 10 ns increments from 120 to 3000 ns. The value of τ was held fixed at 270 ns. The Fourier cosine transform of this ESEEM pattern is displayed in (b). The results are obtained at a temperature of 4.2 K, a microwave frequency of 9.3322 GHz, and a time interval between spin echo pulse sets of 2.0 ms. The displayed ESEEM pattern results from a subtraction of S_1 background from the 195 K illuminated S_2 data.

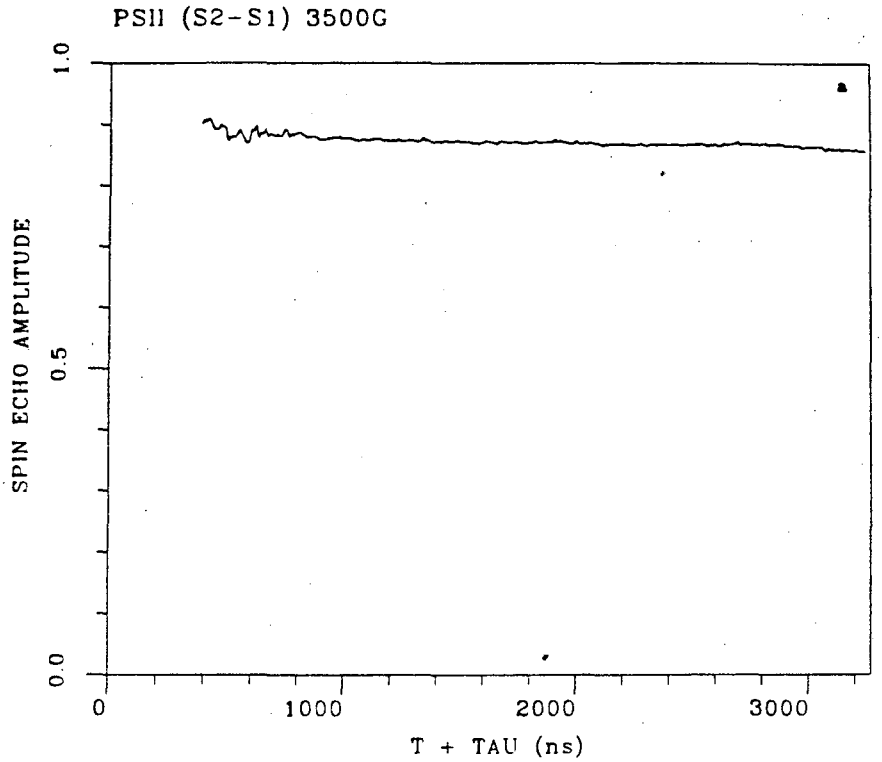
PSII (S2-S1) 3500G
a
SPIN ECHO AMPLITUDE
1.0
0.5
0.0
0
1000
2000
3000
T + TAU (ns)

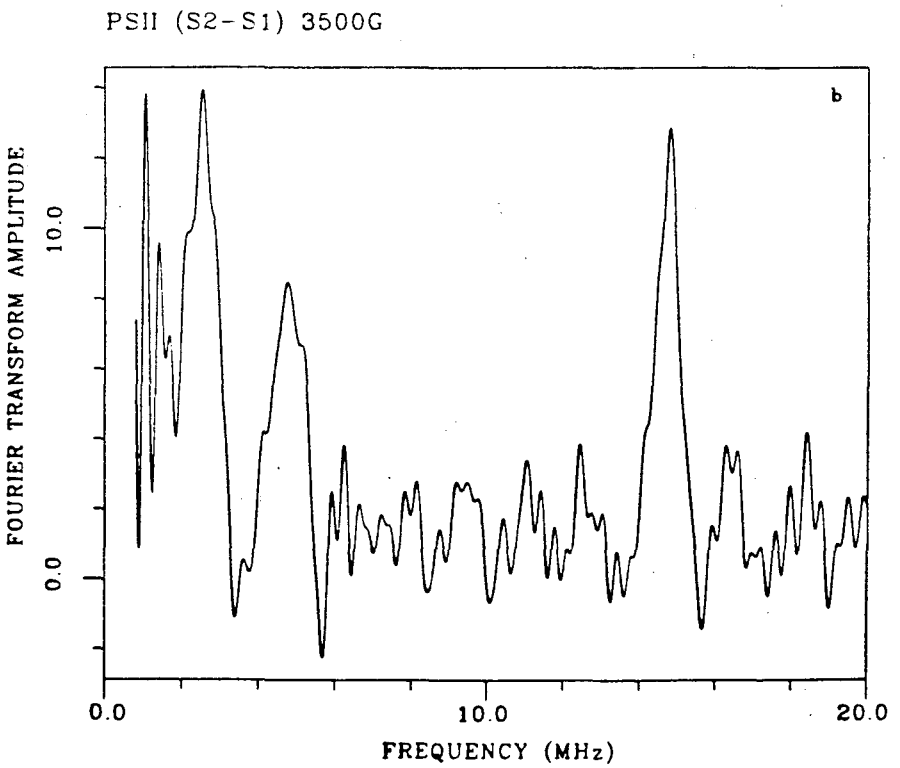
PSII (S2-S1) 3500G
b
FOURIER TRANSFORM AMPLITUDE
10.0
0.0
0.0
10.0
20.0
FREQUENCY (MHz)

be isotropic. However the linewidths are much greater than in the di-μ-oxo bridge Mn(III)Mn(IV) bipyridyl dimer, which should have comparable anisotropic components. We hope to address the linewidth question further by examining the multiline ESEEM obtained from PSII preparations from a thermophilic strain of the cyanobacterium *Synechococcus* grown on ^{15}N sources. The ^{15}N ESEEM patterns should be less complex, because the I=1/2 ^{15}N nucleus has no quadrupole moment. These experiments will help determine whether electric quadrupolar or magnetic dipolar effects dominate the ^{14}N linebroadening. The ^{15}N results will also provide a rigorous test of our assignment of the observed ^{14}N frequencies. These experiments are in progress.

The most likely nitrogen ligand for Mn is the imidazole side chain of the amino acid histidine. Histidines account for the majority of non-porphyrin nitrogen ligands to metals in biological systems. Ashby et al. (1978a) have studied the NQR spectra of metal-coordinated imidazole. The imidazole binding of metals occurs through the imino nitrogen (see Figure V-6). The NQR parameters for the imino nitrogen in free base imidazole (e^2qQ=3.270 MHz and η=0.135) are very similar to those for side chain imidazole in histidine (e^2qQ=3.362 MHz and η=0.131). Coordination to a metal Lewis acid center reduces the magnitude of e^2qQ while increasing the asymmetry parameter η. In Cd and Zn coordination complexes Ashby et al. observed values of e^2qQ between 2.0 and 2.8 MHz with η ranging between 0.25 and 0.70. The NQR values are analysed well by the modified Townes-Dailey theory described in detail in Chapter IV. In the model complexes studied in this paper the metal-nitrogen bonds lie close to the $\widehat{CNC}$ bisector. Studies by Ashby et al. (1978b) on imidazole-Zn complexes where this geometrical constraint fails to hold show increased asymmetry parameter values as large as 0.90. For biological coordination of a metal by histidine this high symmetry is unlikely to be precisely followed, and we expect a fairly large range of possible values for the asymmetry parameter η. The ESEEM results are thus consistent with histidine ligation to the Mn ions which give rise to the multiline EPR signal.

As noted earlier, histidine is the most common amino acid for nitrogen-based ligation to metals in biology. The imidazole group acts as a good base, and the imino nitrogen is easily deprotonated ($pK_a \approx$ 6.4-7.0) at physiological pH. Thus the metal Lewis acids do not have to compete with strongly bound protons. We have also seen that our measured NQR parameters are consistent with what is expected for direct Mn ligation to the imino nitrogen. However, there are several other amino

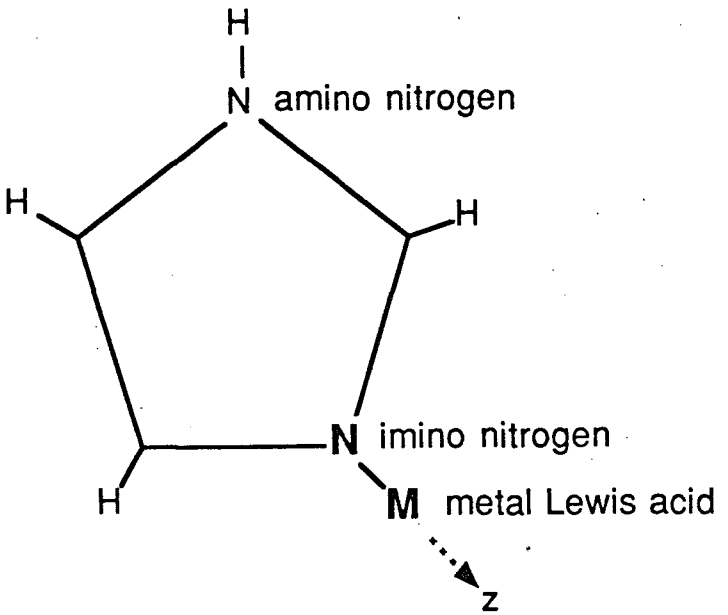

Figure V-6 Metal binding to imidazole. This diagram shows a metal **M** coordinated to the imino nitrogen of imidazole. The metal acts as a Lewis acid and accepts electron charge density from the lone-pair orbital of the imino nitrogen. In this diagram, the **M-N** bond axis is directed along the $\widehat{CNC}$ bisector. This may not be the case for biological metal ions bound to imidazole groups of histidines, and the deviation from this highly symmetric geometry will have large effects on the measured asymmetry parameter η.

acids with nitrogen groups which could serve to bind Mn. The amide groups of asparagine and glutamine may act as bases. However the value of e^2qQ of the amide nitrogen of asparagine is only 2.5 MHz (Hunt and Mackay, 1974) and would be considerably reduced upon losing lone-pair density to a Mn ion. The NQR parameters obtained from the ESEEM data would rule out such a amide coordination. Lysine presents a terminal amino group with a high proton affinity ($pK_a > 10.0$). Lysine is thus positively charged at physiological pH. In order for metal ligation to occur the strongly held proton must be displaced. The amino nitrogen environment for lysine resembles the ethyl ammonium ion, which has a e^2qQ value of only 0.8 MHz and a similarly low asymmetry value of 0.1 (Hunt and Mackay, 1974). These quadrupolar parameters would probably increase somewhat upon replacement of the proton by a metal, but not so high as to be consistent with our ESEEM data. The quanidino group of arginine is yet another candidate. However, the proton affinity of this group is very high ($pK_a > 12.0$), so this group is almost always positively charged at physiological pH. The guanidino group is greatly stabilized by resonance between the symmetric protonation forms. We know of no NQR studies of arginine. However the local structure about the basic NH_2 would be similar to that in amides, and the resultant value of e^2qQ would probably be too low for a good match with our ESEEM results. The net result is that our ESEEM results suggest coordination of Mn to histidine, although other nitrogen bearing ligands cannot be completely ruled out.

The 2-pulse ESEEM of the multiline signal shows no evidence of am intermodulation product at twice the $\approx$4.5 MHz frequency attributed to ^{14}N ligation. We would expect to see such a feature if multiple ^{14}N ligands were present. Also this modulation component is rather small, particularly when compared to the extremely deep modulation observed for the Mn dimers with all ^{14}N ligands described in Chapter IV. We estimate that only 1 or 2 ^{14}N ligands to the Mn pool giving rise to the multiline EPR signal would result in the observed modulation. However, until we have a more definitive assignment as to the origin of the multiline signal itself it is not possible to accurately assert that this represents the full sum of ^{14}N ligation to all of the PSII Mn.

In focusing on the ^{14}N ligation it is easy to forget that the vast majority of ligands to the PSII Mn are ^{16}O-presenting groups and therefore completely unobserved by ESEEM. Most of these oxygen ligands probably are provided by the carboxyl groups of aspartic and glutamic acids. The number of protein ligands required to coordinate four Mn atoms into the protein complex depends on the Mn structural model chosen.

Each Mn will almost certainly be octahedrally coordinated, but some of the ligands will come from oxy, hydroxy, or water bridges. A cubane structure would require only 12 protein ligands to stabilize 4 Mn atoms. A structure with two separate Mn dimers would require 16 protein ligands. A single Mn dimer with two flanking Mn monomers would require 20 protein ligands.

We have learned a great deal in recent years about the structure of Photosystem II. In the next few paragraphs we attempt to integrate what we have learned about the Mn ligand environment into the current body of knowledge of PSII structure and function. The structure of the Photosystem II reaction center is portrayed in Figure V-7. The membrane-bound proteins $D1$ and $D2$ form the core on the PSII reaction center. They extend through the thylakoid membrane and are exposed to both the stromal and lumenal regions (Rao et al. 1983). Small complexes composed of $D1$, $D2$, and *cyt* b_{559} have been isolated which perform photo-induced electron transfer (Nanba and Satoh, 1987; Satoh et al., 1987; and Barber et al., 1987). $D1$ and $D2$ show strong sequence homology to the L and M proteins of the purple photosynthetic bacteria (Hearst, 1986; sequences from Zurawski et al., 1982; Alt et al., 1984; Holschuh et al., 1984; Michel et al., 1986a; Youvan et al; 1984). The most recent data assign parallel roles of $D1$ to L and $D2$ to M (Michel and Deisenhofer, 1988). Sayre et al. (1986) generated antibodies against synthetic peptides based on hydrophilic regions of the $D1$ protein. These antibodies were allowed to interact with PSII membranes on the lumenal or stromal sides of the thylakoid. These studies constrain the $D1$ folding pattern to a model with five membrane-spanning sections. This construction is in perfect analogy to the membrane-spanning α-helices of L and M. Such a five α-helix arrangement for $D1$ and $D2$ was supported by Trebst (1986, 1987). These secondary structures are illustrated in Figures V-8 and V-9, which show the structures for $D1$ and $D2$ respectively. Michel and Deisenhofer (1988) have carefully examined the set of amino acids conserved between $D1$, $D2$, L, and M. Most of the residues which are seen to bind cofactors in the *R.viridis* structure are conserved in $D1$ and $D2$. The only major exception is the set of residues which bind the accessory *Bchl* molecules in *R.viridis*. This set is lacking in the $D1$ and $D2$ sequences. In addition to the pigment and quinone binding residues, a number of other residues of likely structural significance are conserved throughout $D1$, $D2$, L, and M.

Metz et al. (1987) demonstrated that the non-oxygen evolving LF-1 mutant of *Scenedesmus* results from improper processing of the $D1$ protein. Debus et al. (1988)

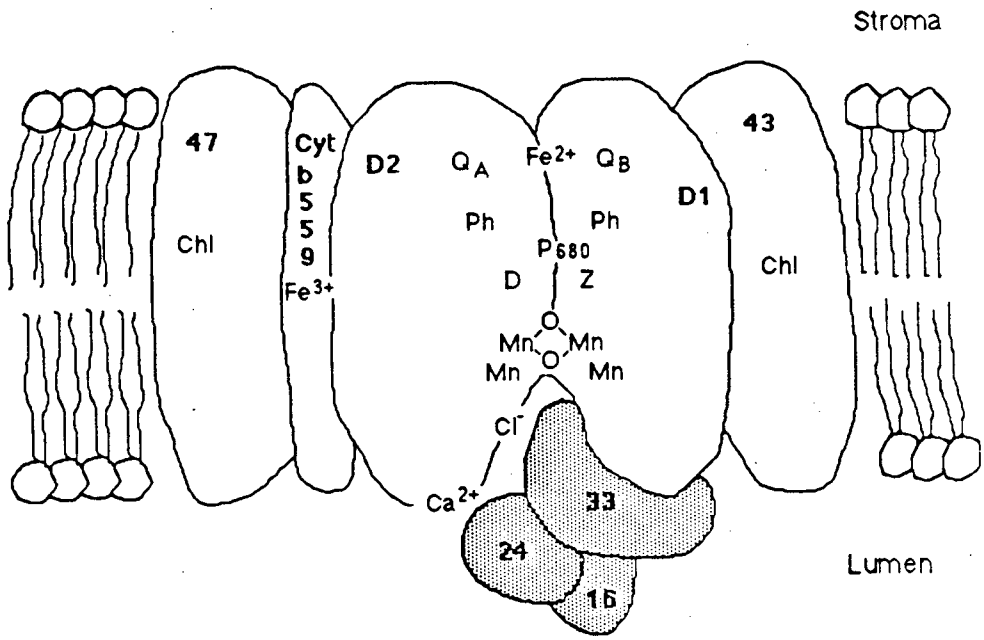

Figure V-7 Composition of Photosystem II reaction center. This cartoon illustrates the likely organization of PSII reaction center polypeptides.

Figure V-8 The secondary structure of the $D1$ polypeptide of Photosystem II (after Trebst (1986, 1987)). The $D1$ polypeptide has 5 α-helices which span the membranes. The amino-terminus is on the stromal side of the membrane. The carboxy-terminus is on the lumenal side. The Mn binding sites are thought to be on the lumenal segments of the $D1$ and $D2$ polypeptides. Amino acid residues which may bind metals are designated with outlined letter codes. These include:

D–Aspartic acid

E–Glutamic acid

H–Histidine

K–Lysine

N–Asparagine

Q–Glutamine

R–Arginine

Y–Tyrosine

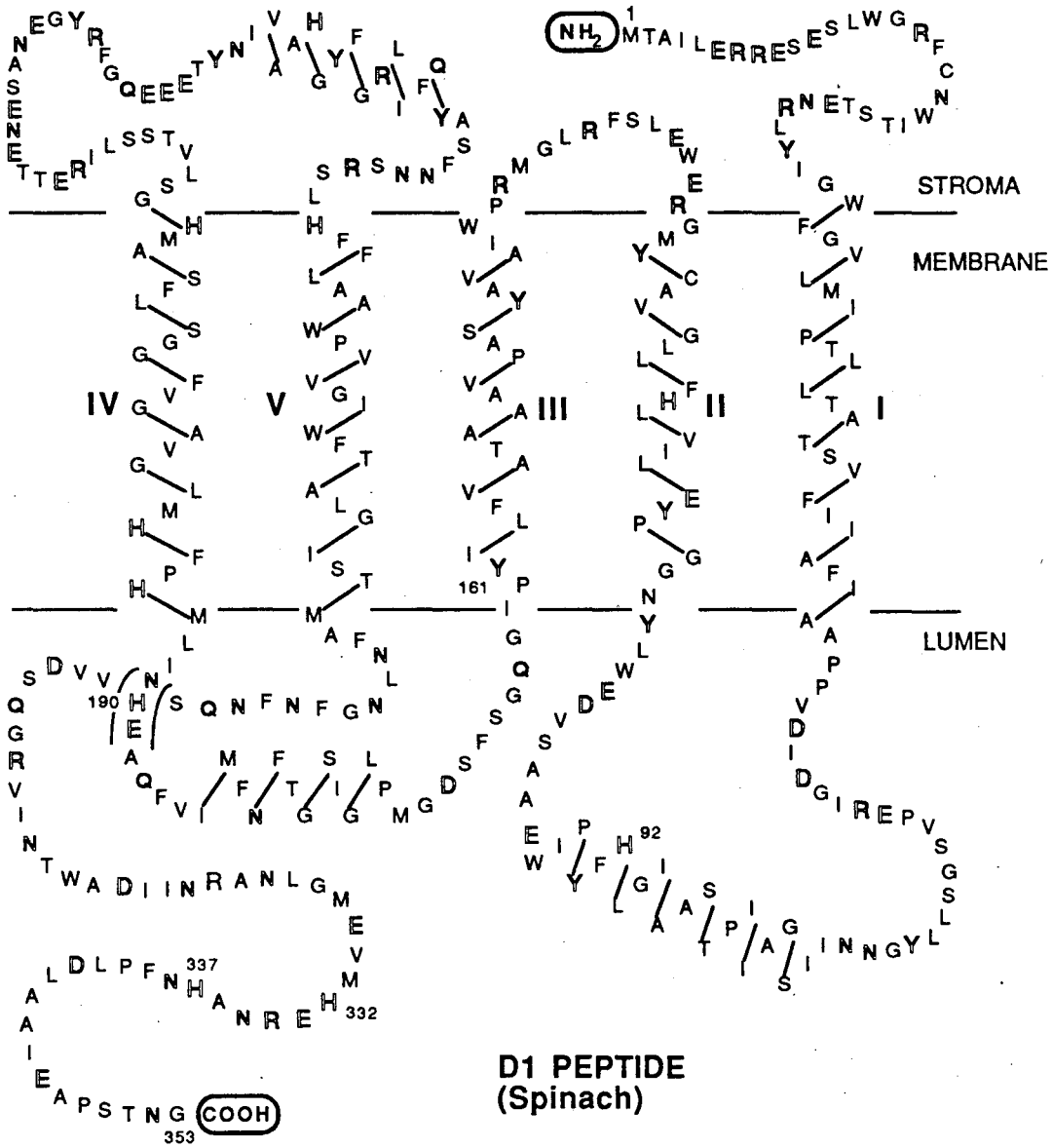

D1 PEPTIDE
(Spinach)

Figure V-8 The secondary structure of the *D2* polypeptide of Photosystem II (after Trebst (1986, 1987)). The *D2* polypeptide has 5 α-helices which span the membranes. The amino-terminus is on the stromal side of the membrane. The carboxy-terminus is on the lumenal side. The Mn binding sites are thought to be on the lumenal segments of the *D1* and *D2* polypeptides. Amino acid residues which may bind metals are designated with outlined letter codes. These include:

D–Aspartic acid

E–Glutamic acid

H–Histidine

K–Lysine

N–Asparagine

Q–Glutamine

R–Arginine

Y–Tyrosine

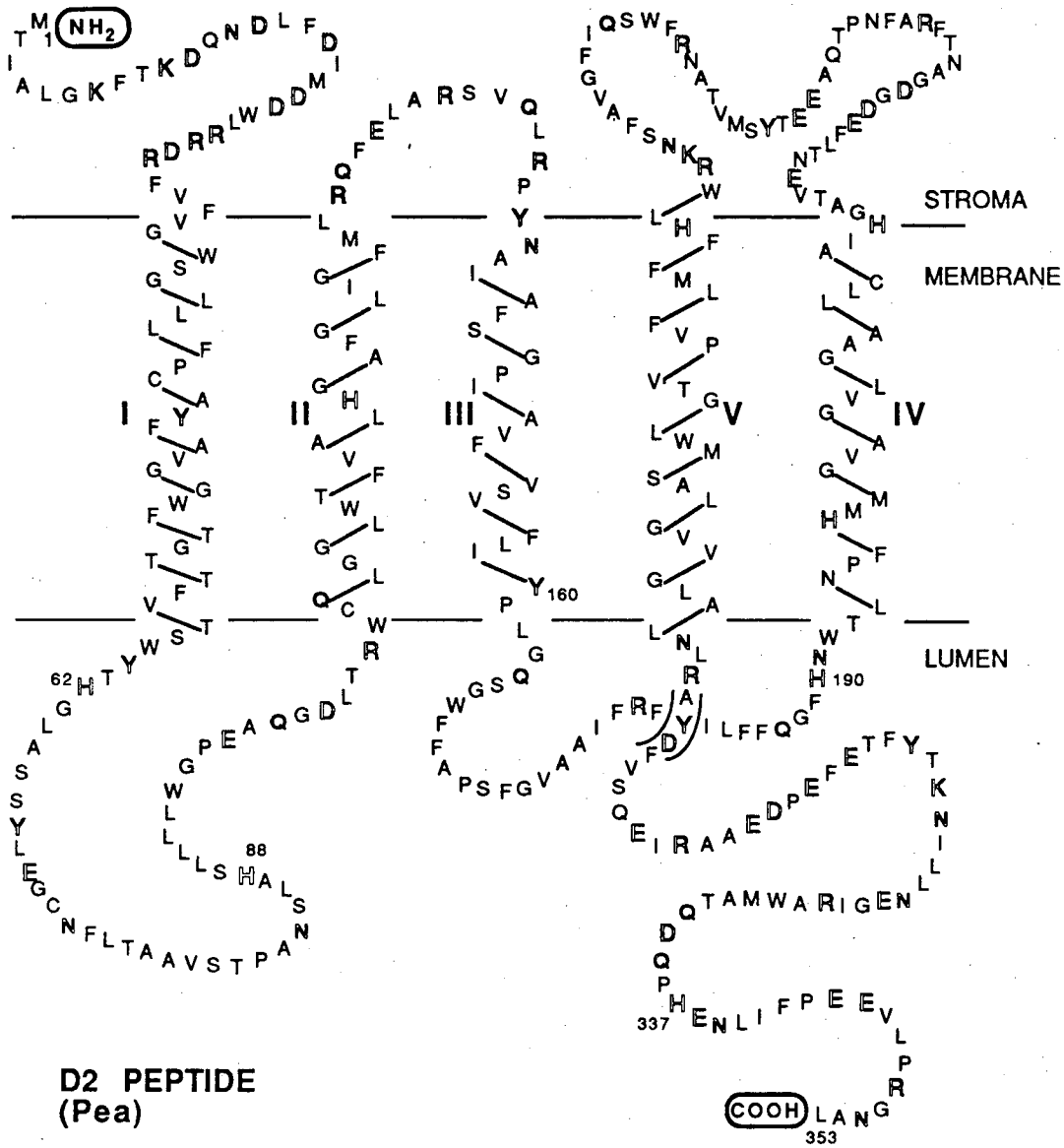

D2 PEPTIDE
(Pea)

have demonstrated through site-directed mutagenesis techniques that the PSII tyrosine radical denoted D^+ is the tyrosine-160 of the $D2$ polypeptide. Analogy to the 2-fold symmetry of the purple bacterial reaction centers suggest that the species Z which transfers electrons from the WOC to P_{680}^+ is the $D1$ polypeptide tyrosine-161. This suggests that $D1$ and $D2$ may also be involved in the binding of the active Mn pool.

Three extrinsic proteins are also linked to oxygen evolution. These hydrophilic proteins have molecular weights of ≈16, 24, and 33 kDa (Murata and Miyao, 1985; Andersson, 1986; Ghanotakis and Yocum, 1985). They all are associated with the lumenal side of the thylakoid membrane. The three extrinsic proteins seem to be involved in oxygen evolution in a peripheral manner. The 16 kDa protein is necessary for efficient oxygen evolution under conditions of low Cl^- concentration. However for Cl^- concentrations ≥3mM, oxygen evolution readily proceeds with the 16 kDa protein removed (Akabori et al., 1984) The 16 kDa protein thus seems to act as a Cl^-gathering protein. If the 24 kDa protein is also removed, oxygen evolution occurs only with ≥ 5mM Ca^{2+} (Ghanotakis et al., 1984a) as well as ≥30 mM Cl^- (Murata and Miyao, 1985). The 24 kDa protein thus appears to have a Ca^{2+}concentrating function. The 16 and 24 kDa extrinsic proteins do not bind Mn, because all 4 Mn atoms remain in the membrane complex when these two proteins are removed (Kuwabara and Murata, 1983; Ghanotakis et al., 1984b).

The 33 kDa protein seems to be more closely associated with the Mn site of water oxidation than the 16 and 24 kDa proteins. If the 33 kDa protein is removed under low Cl^- conditions, slow release of ≈2 of the PSII Mn atoms occurs (Ono and Inoue, 1984; Miyao and Murata, 1984). Removal under more moderate Cl^- concentration retains the full complement of Mn, but with no oxygen evolution activity (Blough and Sauer, 1984). With higher concentrations of Cl^- (≥100mM) and sufficient Ca^{2+}, PSII membranes are able to evolve oxygen with the 33 kDa protein removed, although the rates are not as high as obtained with the 33 kDa protein present (Ono and Inoue, 1984; Miyao and Murata, 1984). The light-induced Mn multiline EPR signal can be induced under such conditions (Miller et al., 1987; Styring et al., 1987). The 33 kDa protein is thus seen to serve additional Cl^- and Ca^{2+} gathering and stabilizes the Mn binding. However the 33 kDa extrinsic protein does not apparently bind the PSII Mn directly.

The best analysis of current data thus suggests that the four Mn atoms associated with PSII are all bound to the $D1$ and $D2$ membrane-intrinsic proteins. Such an

arrangement is suggested in the PSII reaction center cartoon displayed as Figure V-7. The three extrinsic proteins are shown bound to the luminal side, with Cl^- and Ca^{2+} ions also displayed to suggest their possible sequestering by the extrinsic proteins. The *cyt* b_{559} protein is intimately associated with $D1$ and $D2$, though its function is still unknown. The 47 and 43 kDa proteins shown in the figure are *Chl*-binding proteins.

With indication that the PSII Mn is bound to $D1$ and $D2$ we can search the secondary structure diagrams of Figures V-8 and V-9 for likely sites for Mn coordination. We restrict our search for binding sites to the lumenal side of the membrane. $D1$ and $D2$ each present three hydrophilic sections to the lumenal side. Two of these sections are loops which bridge pairs of tranmembrane helices. One of these loops links helices I and II. The other links helices III and IV. The carboxy-terminal end of the protein forms the third lumenal section. This section is of particular interest, because both $D1$ and $D2$ extend some twenty residues past the homologous carboxy-terminal in L and M. This region is thus missing in the core proteins of the non-oxygen evolving organisms.

These lumenal sections are rich in possible ligands to Mn. The most likely oxygen-bearing ligands are aspartic acid (D) and glutamic acid (E). The lumenal sections of $D1$ contain seven aspartic acids and seven glutamic acids. The corresponding sections of $D2$ contain four aspartic acids and ten glutamic acids. There are thus 28 residues which could coordinate Mn via carboxyl groups. There are a total of 8 histidines present in these regions. The $D2$ histidine residues are in the sequence sites 62, 88, 190, and 337. The corresponding $D1$ histidine residues are in positions 92, 190, 332, and 337. A number of these potential ligands are conserved across a variety of oxygen-evolving organisms (Coleman and Govindjee, 1987). There are many more of these potential ligands than are required to bind 4 Mn atoms. Some of the additional ligands are probably employed for Ca^{2+} and Cl^- binding (Coleman and Govindjee, 1987). Charged groups in this region may also be involved in the binding of the 33 and 24 kDa extrinsic proteins to the lumenal interface of $D1$ and $D2$. Much of the progress in understanding the function of specific residues will probably come from site-directed mutagenesis studies.

We may broadly divide proposed mechanisms for photosynthetic water oxidation into two schools. One approach to a hypothetical mechanisms allows successive oxidation of only Mn ions in the four WOC oxidations between S_0 and S_4. No ligand oxidation occurs for such mechanisms, and water binding is favored to occur late in the

Kok cycle. Such mechanisms are favored by optical difference measurements which suggest Mn oxidation during each of the four S-state oxidations (Dekker et al. 1984a, 1984b). However the interpretation of such optical results is still quite controversial. This type of mechanism requires generally "hard" ligands to be presented from the protein, such as the carboxyl side chains of aspartic and glutamic acid. The point is to concentrate the oxidative potential in the metal ions and not dilute it by oxidizing ligands other than the desired substrate, water. In such models the metal cluster performs the water oxidation chemistry, and the surrounding protein mainly "fine-tunes" the process. Our observation of one or two nitrogen ligands may be incorporated into such a "fine-tuning" process. For example, an imidazole ligand is appreciably softer than a carboxyl ligand. Placement of one or two imidazoles in the coordination environment of the cluster would break oxidation-state isomerization symmetry. As the simplest example we could imagine a mixed valence Mn(III)Mn(IV) dimer with all carboxyl ligands to one Mn ion and with one or two imidazole ligands replacing carboxyls on the other ion. This arrangement would tend to stablize the Mn oxidation isomer with Mn(IV) on the all-carboxyl side and Mn(III) on the "softer" side with the imidazole ligands. Such a asymmetric coordination might focus the oxidative potential onto the site of the cluster where water oxidation occurs.

A second school places equivalent emphasis on the role of selected protein ligands to the Mn atoms. The Mn pool still serves the major function in the oxidation of water, and most of the protein ligands are hard. However select ligands serve critical functions in the water oxidation cycle. The imidazole side chains of histidine residues are good candidates for such "special" ligands. In particular, there is the possibility of histidine oxidation at the high potential presented by the photo-oxidized Z^+ (Padhye et al. 1986). We therefore discuss a few of the possible roles for histidine.

The amino nitrogen of imidazole in histidine has a very strong proton affinity (pK_a=14.5). However on coordination of the imino nitrogen to a metal center, this amino pK_a value is lowered. For example, Appleton and Sarkar (1974) found amino nitrogen pK_a values in the range of 7.0 to 7.3 for imidazole coordinated to Zn(II). The pK_a of Zn(II)-bound H_2O in such systems was observed to be around 9.1. Thus in systems with both water and imidazole bound to Zn(II) the amino nitrogen of the imidazole presents the most easily removed proton. Such an activation of imidazole amino proton transfer was proposed to play a key role in the action of the Zn(II) enzyme carbonic anhydrase (Appleton and Sarkar, 1974). Such a mechanism could

also be involved in photosynthetic water oxidation.

We note that Kambara and Govindjee (1985) have proposed a model of photosynthetic water oxidation based on the presence of redox-active ligands to Mn. In their model the redox-active ligand mediates electron transfer between Mn and Z. Building on this model, Padhye et al. (1986) suggested the imidazole of histidine as the identity of this redox-active ligand. In the most recent analysis of this model, Coleman and Govindjee (1987) propose that $D1$ histidine-190 and $D2$ histidine-190 act as such redox active ligands. However in this most recent model these are not directly bound to Mn. They favor $D1$ histidine-92 and $D2$ histidines-62 and -88 for direct coordination of Mn.

A model for water-oxidation involving histidine ligands to Mn has also been proposed by Guiles (1988). In this model the ligated histidine is oxidized in the S_2 to S_3 transition. This model is supported by the lack of a Mn X-ray absorption edge shift in this S-state transition (Guiles et al., 1986; Guiles, 1988). This resullt is interpreted as a lack of oxidation of the Mn pool in the S_2 to S_3 transition. A ligated histidine is thus proposed as the oxidized species in this transition. Guiles also proposes a parallel histidine oxidation on the S_3 to S_4 transition, though there is no spectroscopic evidence for this at this time.

A role involving evanescent oxidation of a ligand such as histidine is suggested in the discussion by Dismukes et al. (1982) concerning the differences between electron transport and electron storage by metal centers. Dismukes et al. point out that the majority of metalloproteins which serve electron transport roles have oxidation-reduction reactions occurring in non-bonding orbitals. Little energy is required to transfer electrons. Examples include Fe-S proteins, blue Cu proteins, and low-spin cytochromes. In contrast, the mixed valence Mn complexes have deeply trapped valences, and electron transfer requires a large reorganization energy to transfer electrons between antibonding orbitals. This provides for more stable charge storage, but poses a barrier to the oxidation at each S-state transition. Dismukes et al. suggest that a coordinated ligand may be initially oxidized, with inner sphere electron transfer then occurring between the oxidized ligand and the coordinated Mn ion.

Photosynthetic oxygen evolution requires Cl^- to function. Sandusky and Yocum (1984) have proposed that Cl^- binds directly to Mn as a bridging ligand. Our ESEEM experiments are not expected to contribute any information about Cl^- ligation. The natural isotopes of chlorine and bromine all possess nuclear spin I=3/2. These iso-

topes are ^{35}Cl, ^{37}Cl, ^{79}Br, and ^{81}Br. These halogen nuclei typically have very large values for e^2qQ. For example, ^{35}Cl and ^{37}Cl NQR resonances for the 1/2↔3/2 and -1/2↔-3/2 transitions are typically from 30 to 40 MHz. The corresponding ^{79}Br and ^{81}Br frequencies are even higher. Such large sublevel intervals will not be spanned by the relatively small microwave H_1 fields, and these frequencies will not be observed by ESEEM techniques. However one must also consider the -1/2↔1/2 transition. The $\Psi_{+1/2}$ and $\Psi_{-1/2}$ states are degenerate in the absence of an applied magnetic field. Application of a magnetic field removes this degeneracy and mixes the zeroth-order states. We can arrive at an expression for the eigenvalues in the simple case of an axial quadrupolar tensor (Das and Hahn, 1958). The interval between the states is given by

$$\Delta\nu = \left[1 + 8\,tan^2\theta\right]^{1/2} cos\theta\,\hbar\gamma B, \qquad (V-1)$$

where θ is the angle between the applied field $\vec{B}$ and the axial quadrupole axis. We see that the frequency is extremely dependent of the angle θ. The transitions will be too broad to observe via ESEEM in a powder pattern sample.

The abundant fluorine nucleus ^{19}F has a nuclear spin I=1/2. Unfortunately fluoride treatment inhibits the formation of the Mn multiline signal. However the light-induced g=4.1 signal is stablized by fluoride treatment (Casey and Sauer, 1984). This suggests the importance of future ESEEM experiments on the g=4.1 signal as produced in the presence of fluoride.

The most obvious feature of the light-induced Mn multiline EPR spectrum is the set of partially resolved Mn hyperfine lines. As reported in the introduction to this chapter, approximately 19 of these Mn hyperfine lines are observed in cw EPR experiments. EPR studies with small (≈4 Gauss) field modulation show reproducible fine structure superimposed on the large hyperfine peaks (Yachandra et al., 1986b). This fine structure shows splittings on the order of 10 to 15 Gauss. We do not attribute any of this structure to ligand superhyperfine coupling. Our ESEEM results on the PSII Mn signal and on the di-μ-oxo bridged Mn(III)Mn(IV) dimers show isotropic superhyperfine couplings to directly coordinated ^{14}N of 1 Gauss or less. Superhyperfine couplings for ^{14}N of 10 to 15 Gauss are observed only for soft, polarizable ions such as Cu(II), not for small, hard ions such as Mn(III) or Mn(IV). Even in model compounds such as the di-μ-oxo bridged Mn(III)Mn(IV) dimers we see no resolved ^{14}N superhyperfine coupling. Since there are eight coordinating nitrogens, ^{14}N couplings of 10 Gauss each would result in very broad lines indeed.

We can address the question of Cl superhyperfine coupling by examining the EPR spectrum of the tetranuclear oxide bridged Mn complex recently described by Bashkin et al. (1987). The core structure of this complex is $[Mn_4(\mu_3 - O)_3(\mu_3 - Cl)]^{6+}$, i.e. a distorted Mn_4O_3Cl cubane structure. The Mn valences of the complex can be assigned as $Mn(III)_3Mn(IV)$. In addition to the bridging Cl, there are five terminal Cl atoms as well as a terminal imidazole. The EPR spectrum of the complex shows two broad low-field features and a 16 line component near g=2. These 16 lines are quite sharp, and show no evidence of such large superhyperfine couplings to either chloride or nitrogen.

It is important to remember how many EPR lines can be associated with a multinuclear complex (see equation I-3). A mixed valence Mn dimer has 36 hyperfine lines. Systems such as the di-μ-oxo bridged Mn(III)Mn(IV) dimers show only 16 resolved lines due to overlapping of many of the transitions. A Mn tetramer with four inequivalent Mn ions would present 1296 hyperfine lines. Clearly such Mn hyperfine structure could give rise to closely spaced features such as observed in the PSII Mn EPR spectrum.

Section 3–ESEEM Studies of Ammonia Binding to the PSII Mn Site

This section provides discussion of some preliminary ESEEM experiments addressing the topic of ammonia binding to Mn of PSII. High concentrations of NH_2OH or $Tris$ [tris(hydroxymethyl)aminomethane)] release PSII Mn and cause irreversible inhibition of oxygen evolution. However low concentration treatments of certain amines, including NH_3, NH_2CH_3, and Tris, provide for reversible oxygen evolution inhibition. Amines may act as Lewis bases and interact with the Lewis acid Mn, thereby competing with the primary substrate, water. Sandusky and Yocum (1984) described two independent sites for NH_3 inhibition of oxygen evolution. The type I binding site binds both anions such as Cl^- and Br^- and inhibitory amines. The type II site shows no competitive relationship with Cl^-. The larger amine $Tris$ also was not observed to bind at this type II site. These data led Sandusky and Yocum to postulate that the type II site permits NH_3 binding to Mn as a Lewis base, with the binding site too physically restrictive to accomidate the bulker $Tris$ molecule. A later paper (Sandusky and Yocum, 1986) showed that 2-amino-2-ethylpropanediol, methylamine, and *t*-butylamine are all unable to bind at the type II site. This added additional support to the postulate that this site represents a physically restrictive site, with only ammonia being small enough to enter.

Beck et al. (1986) reported low-temperature EPR studies of the Mn multiline signal under conditions of ammonia inhibition of oxygen evolution. They treated PSII membranes with 100 mM NH_4Cl at pH=7.5 and illuminated the samples at 0°C in the presence of DCMU to block transfer beyond S_2. Under these conditions a Mn multiline spectrum was observed, but with an altered value of the Mn hyperfine coupling. The Mn line spacing were reduced from a value of ≈87 Gauss for untreated samples to ≈67 Gauss for ammonia treated samples. Ammonia treated samples illuminated at low temperature (210 K) showed the same Mn hyperfine values observed for untreated samples. This observation was explained by assuming a lack of facile ligand exchange at this low temperature. A later paper of Beck and Brudvig (1986) described parallel experiments with $Tris$, 2-amino-2-ethylpropanediol, or methylamine treatments. These larger amines have no effect on the Mn hyperfine coupling. Thus the ammonia binding site affecting the Mn hyperfine coupling may be identified with the type II ammonia binding site of Sandusky and Yocum.

Beck et al. (1986) examined the "fine-structure" on the altered Mn signal with both $^{14}NH_3$ and $^{15}NH_3$ treatments. The resultant EPR spectra were observed to

be identical within the resolution of the experiment. This places an upper limit of a few Gauss on the possible magnitude of the superhyperfine coupling to ^{14}N or ^{15}N ammonia. Beck et al. attributed the change in the observed Mn hyperfine coupling to alteration of the exchange coupling between Mn ions and argued that this indicates direct binding of ammonia to the Mn giving rise to the multiline signal. However recent results by Boussac and Rutherford (1988) place doubt on this last conclusion. They have shown that replacement of Ca^{2+} by Sr^{2+} results in an altered Mn multiline spectrum very similar to the ammonia-altered signal of Beck et al. Certainly Sr^{2+} is not binding to Mn as a Lewis base. These findings do not prove that ammonia does not bind directly to Mn. However they show that the ammonia-induced alteration of the Mn signal is not conclusive proof for direct binding. For example both ammonia and Sr^{2+} replacement of Ca^{2+} may induce a similar conformation of the Mn site which results in the altered form of the Mn EPR signal.

We have prepared ammonia-treated PSII membranes following the protocol of Beck et al. (1986). PSII membranes were treated with 100 mM NH_4Cl at pH=7.5 and illuminated at 0°C in the presence of DCMU to block transfer beyond S_2. Figure V-10 displays the 2-pulse ESEEM of the light-induced Mn signal for these ammonia-treated PSII membrane fragments. The time domain ESEEM pattern is displayed in Figure V-10a. The Fourier cosine transform of this ESEEM pattern is shown in Figure V-10b. The effect of ammonia addition is quite dramatic. The ^{14}N modulation component at 4.63 MHz is very large. There is a suggestion of resolved structure at lower frequencies. The apparent frequencies are at 0.98, 1.42, and 2.50 MHz. This is confirmed by analysis of the 3-pulse ESEEM results shown in Figure V-11. These low frequency peaks are all clearly present in the Fourier transform of the 3-pulse ESEEM pattern. We can identify these three frequencies with the nearly pure NQR frequencies ν_+=2.50 MHz, ν_-=1.42 MHz, and ν_0=0.98 MHz. The corresponding ^{14}N quadrupole parameters are e^2qQ=2.61 MHz and η=0.75. The 4.63 MHz component arises from the β-manifold double quantum transition, and with the application of equation II-76 and the measured quadrupole parameters we can assign a value value A=1.84 MHz to the ^{14}N isotropic hyperfine coupling. With this value of A we confirm that the Zeeman and hyperfine fields are near exact cancellation for the α-manifold, which is why we are able to resolve the pure NQR components. This analysis gives consistent fits to ESEEM data obtained at different field positions between 3150 and 3400 Gauss.

The most obvious interpretation of these data would suggest that ammonia does

Figure V-10 2-pulse ESEEM of the light-induced Mn signal in ammonia treated PSII membranes. The time-domain ESEEM pattern in (a) is obtained with τ varied from 200 to 2000 ns in 10 ns increments. The Fourier cosine transform is displayed in (b). Experiments are performed with a microwave frequency of 9.1191 GHz, observation temperature of 4.2 K, applied magnetic field of 3400 Gauss, and delay between ESE pulse sets of 1.0 ms.

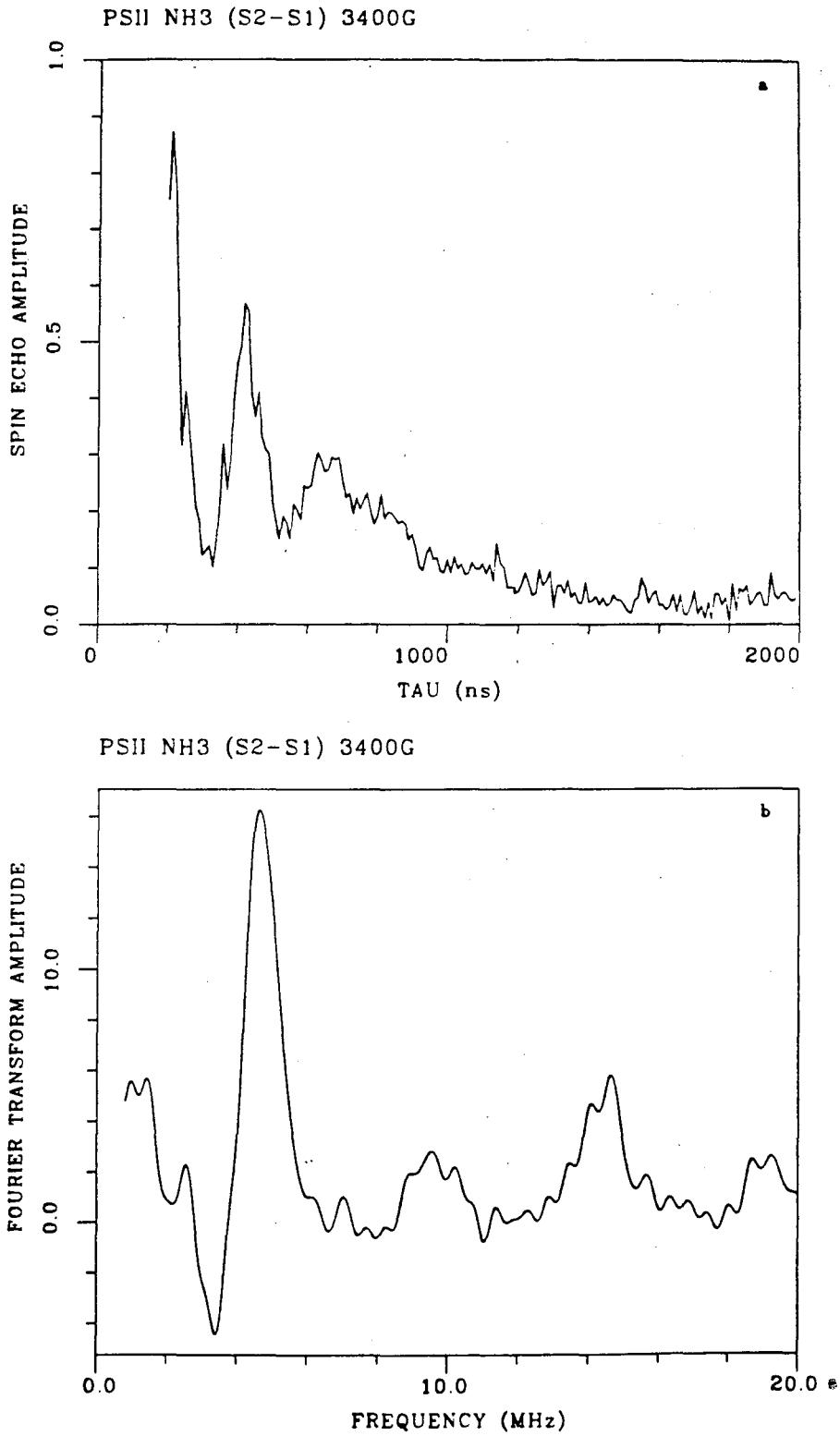
PSII NH3 (S2-S1) 3400G
a
SPIN ECHO AMPLITUDE
1.0
0.5
0.0
0
1000
2000
TAU (ns)
PSII NH3 (S2-S1) 3400G
b
FOURIER TRANSFORM AMPLITUDE
10.0
0.0
0.0
10.0
20.0
FREQUENCY (MHz)

Figure V-11 3-pulse ESEEM of the light-induced Mn signal in ammonia-treated PSII membranes. The time-domain ESEEM pattern in (a) is obtained with T varied from 200 to 3000 ns in 10 ns increments with τ held fixed at 240 ns. The Fourier cosine transform is displayed in (b). Experiments are performed with a microwave frequency of 9.1191 GHz, observation temperature of 4.2 K, applied magnetic field of 3350 Gauss, and delay between ESE pulse sets of 1.0 ms.

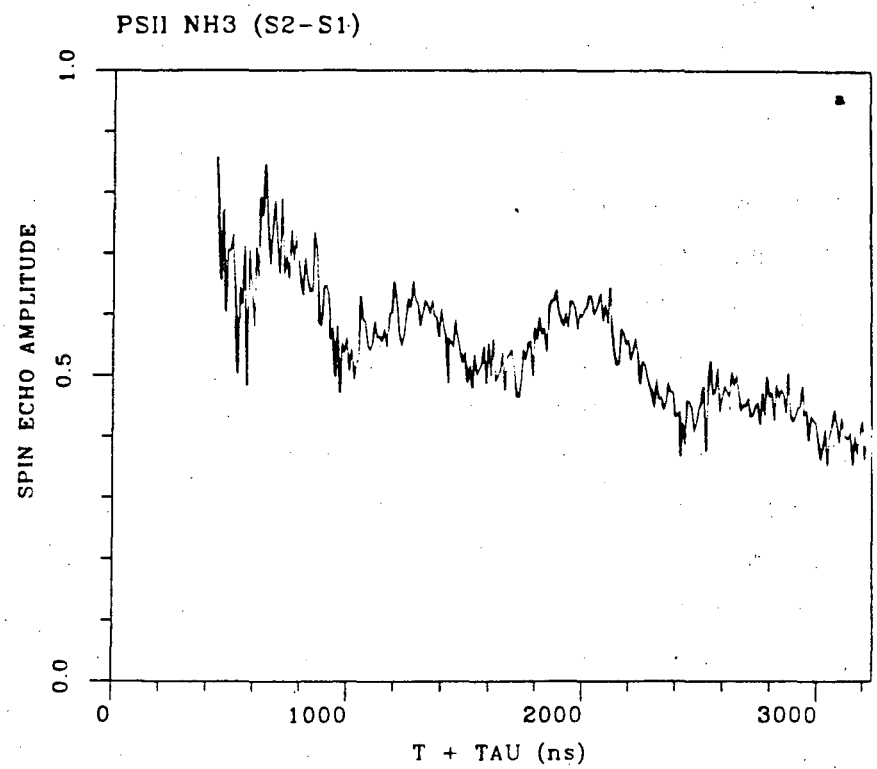
PSII NH3 (S2-S1)
a
SPIN ECHO AMPLITUDE
1.0
0.5
0.0
0
1000
2000
3000
T + TAU (ns)

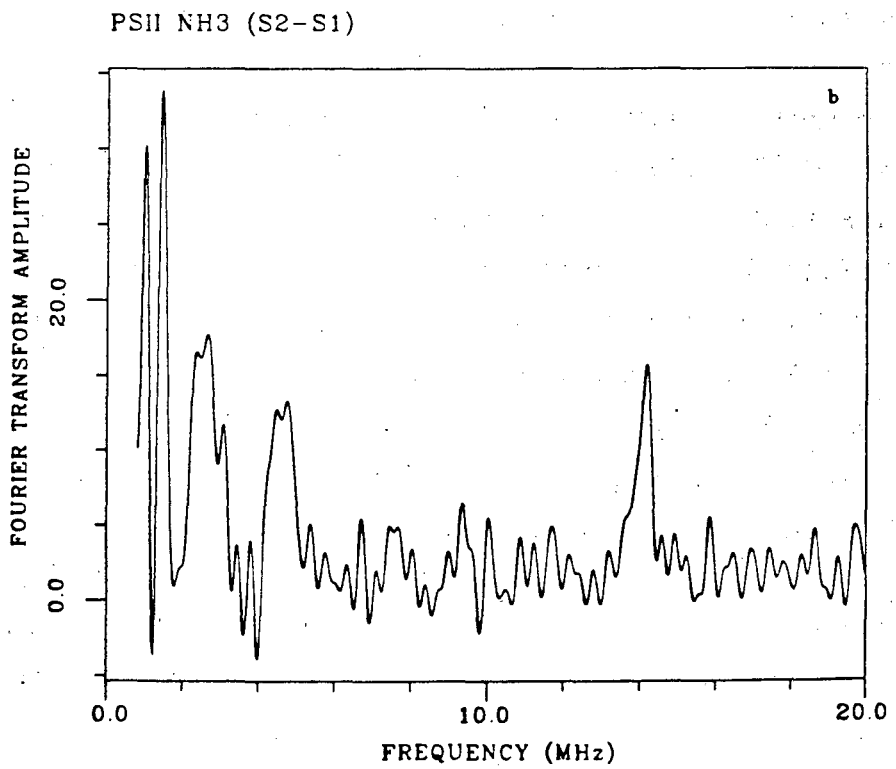
PSII NH3 (S2-S1)
b
FOURIER TRANSFORM AMPLITUDE
20.0
0.0
0.0
10.0
20.0
FREQUENCY (MHz)

indeed bind directly to Mn. The measured ^{14}N modulation depth is dramatically increased over the native PSII multiline ^{14}N modulation. The ^{14}N isotropic coupling observed in the ammonia-treated samples is in the range which we have observed for ^{14}N directly coordinated to Mn in both the model compounds and in the native PSII system. We have no ^{14}N NQR data for ammonia bridging metal ions. However, such a bridging environment could produce large electric field gradients at the nitrogen nucleus. The relatively high values of e^2qQ and η would seem consistent with possible ^{14}N NQR parameters for an ammonia-derived bridge between Mn ions. The values would probably not be consistent with a simple terminal ligation of ammonia however.

However an alternate interpretation of the ESEEM data can be offered. We note that the appearence of the ammonia treated ESEEM and the native multiline ESEEM are radically different, with much deeper and more persistent ^{14}N modulation for the ammonia-treated sample. However the ESEEM frequencies obtained in both cases are remarkably similar. The extracted NQR parameters and hyperfine couplings are almost identical. We therefore propose that the ESEEM observed in the ammonia-treated sample may originate from the same ^{14}N ligands present in the native sample. The effect of ammonia treatment may simply alter the overall structure of the complex, resulting in a more rigid form and a simultaneous decrease in the ^{14}N hyperfine or quadrupolar broadening which quickly damps the ^{14}N ESEEM in the native Mn multiline spectrum.

Fortunately we will be able to distinguish between these two alternatives. Treatment with $^{15}NH_3$ will result in a radically different ESEEM pattern if the ammonia-induced ESEEM results from coordinated ammonia. The $^{15}NH_3$ treatment will not alter the ESEEM pattern if the changes result from a conformational change induced by remote ammonia binding. Complementary experiments with Ca^{2+} replacement by Sr^{2+} will prove interesting in either case.

Another observed change in the ESEEM results for the ammonia-treated samples pertains to the weakly coupled proton modulation. This modulation at the free proton frequency is diminished in the ammonia treated samples. This may be an indication of reduced accessibility of water to the Mn site after ammonia binding. Two new features are observed displaced $\approx$4.5 MHz from the weakly-coupled proton frequency. These two features are symmetrically located about the weakly coupled proton frequency at all measured field positions One interpretation of this result would assign these peaks to protons with strong ($A \approx$9.0 MHz) isotropic couplings. However it is very unlikely

that such large proton coupling would be observed for protons resident on either a bridging or terminal nitrogen. The PSII Mn ions show deeply trapped valences and will not project such large spin density onto the ligands. The observed difference frequency between these new peaks and the free proton peak is close to the prominent ^{14}N frequency of $\approx$4.6 MHz. These features most likely arise as intermodulation products.

Section 4–ESEEM Studies of Water Binding to the PSII Mn Site

There is no definitive evidence to show at which stage water binds in the Kok S-state cycle. Different models for oxygen evolution suggest different stages of water binding. One view would have only the Mn cluster oxidized in each step of the Kok cycle. In this model the S_4 configuration initially occurs with the Mn cluster oxidized by four equivalents beyond the S_0 state. Two water molecules bind to this highly oxidized metal cluster and are themselves oxidized to molecular oxygen in a concerted reaction, with the Mn cluster resetting to the S_0 oxidation state. The opposite view posits the occurrence of "water-chemistry" at each step of the Kok cycle. In such a model water molecules bind at early stages in the cycle and are successively oxidized through intermediates such as metal-bound peroxides or bridging hydroxyl groups. The actual mechanism for water oxidation is probably intermediate between these extreme models.

It is appealing to consider the measured proton release pattern [1,0,1,2] shown in Figure I-6 as direct indication of water binding and oxidation. However this does not seem to be the case for the first two proton releases. Förster and Junge (1985) measured the kinetics of proton release into the lumen using the dye neutral red as a pH indicator. They found the following proton release stoichiometry and rates

$$\begin{aligned} S_0 \rightarrow S_1 \quad & 1H^+ \quad 250\mu s \\ S_1 \rightarrow S_2 \quad & 0H^+ \quad --- \\ S_2 \rightarrow S_3 \quad & 1H^+ \quad 200\mu s \\ S_3 \rightarrow S_4 \rightarrow S_0 \quad & 2H^+ \quad 1200\mu s \end{aligned}$$

These results were compared with the early Z^+ reduction EPR kinetics of Babcock et al. (1976) as a measure of S-state oxidation. These transient EPR results demonstrated a $S_0 \rightarrow S_1$ transition of less than 100μs and a $S_2 \rightarrow S_3$ transition of about 400μs. The release of the first proton into the lumen lags the rate of the corresponding S-state transition. More importantly, the release of the second proton occurs on a faster timescale than the oxidation of the WOC. Förster and Junge thus indicate that this proton release precedes the oxidation of the Mn cluster and may be due to redox chemistry of Z.

A number of other experiments give conflicting views of the stages of initial water coordination. A number of these experiments are discussed in the excellent review by Babcock (1987). We focus on two recent experiments using "high-resolution" cw

EPR to examine effects of EPR linebroadening due to water isotopes.

The first of these experiments was reported by Hansson et al. (1986). They examined the effect of line-broadening of the Mn multiline EPR signal in the presence of ^{17}O-enriched water. The ^{17}O nucleus has nuclear spin I=5/2. PSII particles were cycled through the S-states by illumination at 0°C and then dark adapted before illumination at 200 K to generate the S_2 Mn EPR signal. The concentration of $H_2{}^{17}O$ was estimated at 42%. The $H_2{}^{17}O$ sample showed a very slight line-broadening when compared to $H_2{}^{16}O$ control samples. This result was taken as an indication of water binding in the S_0 or S_1 states. Hansson et al. expressed the view that this experiment does not address S_2 water binding due to the low illumination temperature. They placed an upper limit of $\approx$5 Gauss on the isotropic coupling to ^{17}O.

Nugent (1987) demonstrated an increase in the resolution of the Mn EPR signal fine-structure upon preparation in ^2H_2O buffer. The resolution increase was greater for samples illuminated at 10°C than for samples illuminated at 200 K. Nugent interpreted these results as indicating water binding close to the Mn site in the $S_1 \rightarrow S_2$ state transition.

The chief difficulty with these types of experiments is obviously one of resolution. The measured effects are only slight broadening or narrowing of features. It is therefore difficult to extract reliable spectral parameters related to the superhyperfine or quadrupolar couplings for the nuclei of interest. Therefore we have started ESEEM experiments to determine such parameters more precisely, and to obtain more concrete evidence as to water binding in the lower S-state transitions.

Our approach in these experiments is to observe changes in the ESEEM patterns upon introducing ^2H_2O in place of ^1H_2O. In part this is done to give a "differential" handle on water coordination. An important additional point relates to the fact that we can obtain better ESEEM results with deuterons than with protons. The I=1 deuteron provides for deeper modulation than the I=1/2 proton, even when the small quadrupole contribution to the spin echo modulation is ignored. Also the deuteron frequencies are much lower, and therefore there are no instrumental difficulties associated with insufficient excitation of the sublevel manifolds which may occur for the higher proton frequencies.

PSII membranes were prepared as described in Section 2. A pH=6.0 ^2H_2O buffer was also prepared. PSII particles were resuspended in the ^2H_2O buffer and repelleted by centrifugation at 35000×g for 10 min. This procedure was repeated three

times to assure a high replacement of ^1H_2O by ^2H_2O. The final buffer contained the electron acceptor PPBQ (phenyl-*p*-benzoquinone) at a concentration of 1.0 mM. Rigorous dark conditions were maintained at each step. The ^2H_2O exchanged PSII membranes were placed in EPR tubes and dark adapted for 3 h. at 4°C. The total exposure time for ^1H_2O to ^2H_2O exchange was 4 h. The samples were then frozen in liquid N_2. S_2 samples were generated by 195 K illumination.

Figure V-12 shows the ESEEM results on the light-induced Mn multiline signal following this deuteration procedure. The 2-pulse time-domain ESEEM pattern displayed as Figure V-12a is obtained by incrementing τ in 10 ns increments from 140 to 3000 ns. The cosine Fourier transform is displayed in Figure V-12b. The ESEEM shows a dramatic change resulting from deuteron exchange. There is a deep modulation component at the free Larmor frequency for deuterons (2.29 MHz at 3500 Gauss). Significant proton modulation still remains in the ESEEM pattern. The amplitudes of the Fourier peaks representing free deuterons and protons are in the ratio of ≈4:1. Without considering the small quadrupole moment of the deuteron, the ESEEM modulation depth for a deuteron is a factor of 8/3 greater than for a proton in the identical environment. The quadrupole contibution to ESEEM depth may provide further increase in this ratio. An additional experimental constraint must also be considered. The microwave H_1 field more fully excites the small deuteron sublevel interval than the larger proton sublevel interval. Taking all of these factors into account, we estimate that no more than 1/2 of the proton sites are exchanged by this procedure. The exchangeable sites represent both lumenal phase water with close access to the Mn site, nearby acidic protein residues at the water interface, and possible water-binding sites to the Mn with relatively small isotropic couplings. The non-exchangeable sites represent protons from regions of the surrounding protein which are not accessible to water.

There is no clear evidence for deuterons introduced into sites with large hyperfine couplings. The linewidth of the deuteron Zeeman peak in the 2-pulse experiments is ≈0.37 MHz. This is only slightly narrowed (≈0.31 MHz) for the 3-pulse data shown in Figure V-13. The line is significantly narrower than the native proton line, which has a half-width of ≈0.70 MHz. This reduced linewidth can be interpreted as a reduction in the superhyperfine coupling strength due to the smaller gyromagnetic moment of the deuteron. To examine more closely the effects of exchanging ^2H_2O for ^1H_2O we have taken the ratio of the ESEEM obtained in ^2H_2O and ^1H_2O buffers. The ratioed

Figure V-12 2-pulse ESEEM of the Mn multiline signal of PSII membranes prepared in ^2H_2O buffer and illuminated at 195 K. The 2-pulse ESEEM results are obtained by varying τ in 10 ns increments from 140 to 3000 ns. The time domain pattern is shown in (a), and the corresponding cosine Fourier transform is displayed in (b). The applied magnetic field is 3500 Gauss. The microwave frequency is 9.29 GHz. The observation temperature is 4.2 K, and the time interval between pulse set repetitions is 1.0 ms.

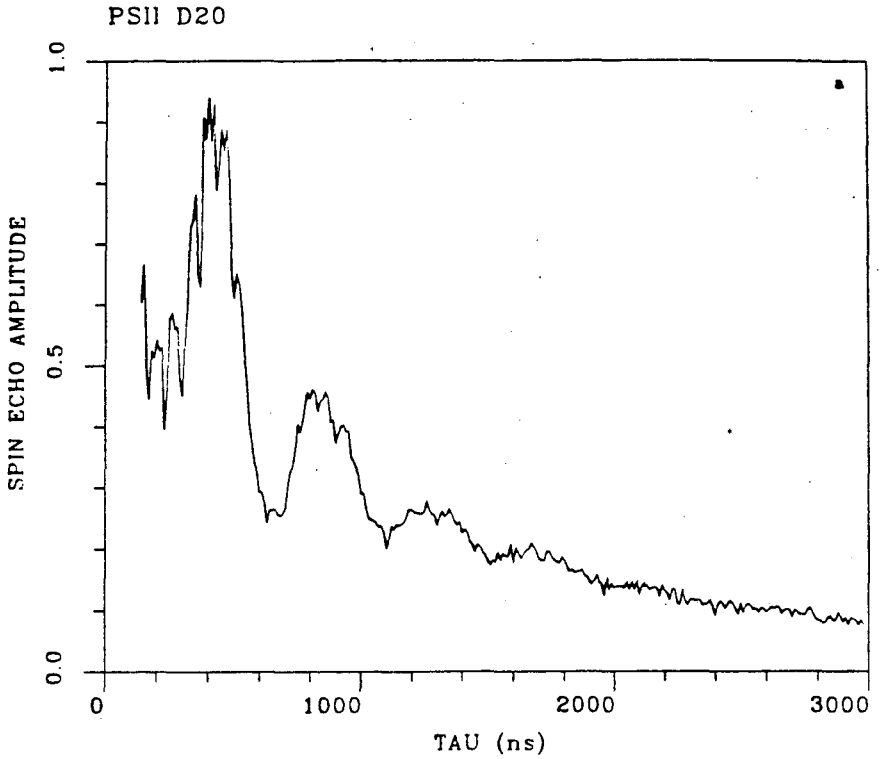
PSII D20
a
SPIN ECHO AMPLITUDE
1.0
0.5
0.0
0
1000
2000
3000
TAU (ns)

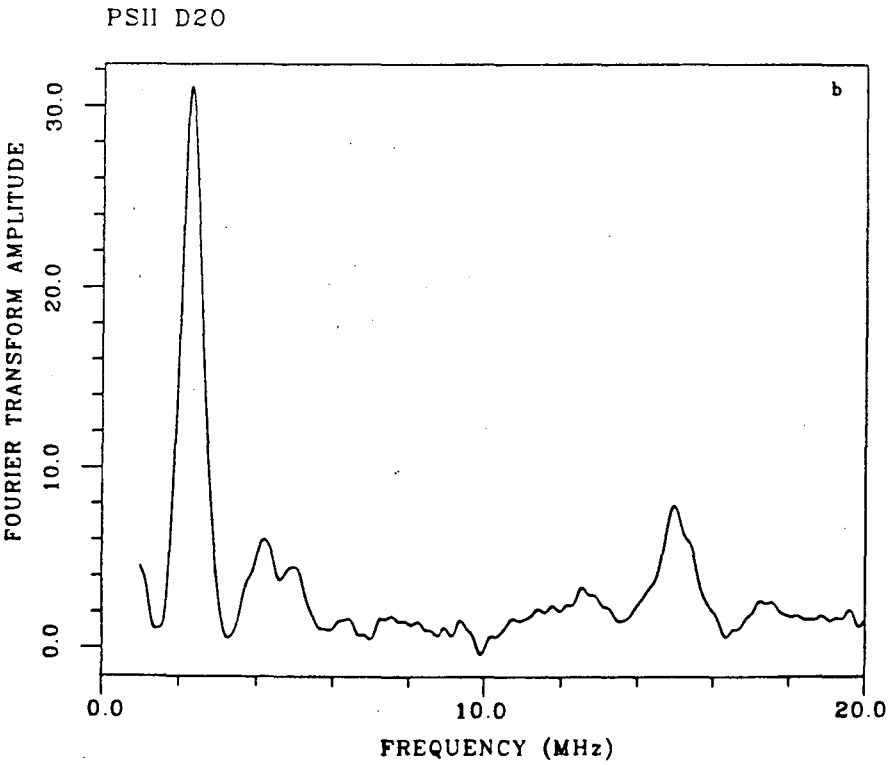
PSII D20
b
FOURIER TRANSFORM AMPLITUDE
30.0
20.0
10.0
0.0
0.0
10.0
20.0
FREQUENCY (MHz)

ESEEM pattern and the Fourier transform are displayed in Figure V-14. This ratioed ESEEM shows only the differential effects of the ^2H_2O exchange and provides a convenient removal of the non-specific phase-memory decay. The Fourier transform shows only the weakly coupled deuteron peak.

The weakly coupled deuteron feature originates in a distribution of ^{2}H nuclei with variation in both the radial distance from the Mn ions and the angle formed by the radius vector with respect to the applied field direction. The anisotropic hyperfine couplings are thus averaged over both angular powder patterns and radial distributions. The breadth of the Zeeman line is determined by the sum of these averaged anisotropic couplings, as well as from contributions from unresolved isotropic hyperfine and quadrupolar components. The 2-pulse ESEEM also shows a contribution from the ESEEM sum terms from the two electronic manifolds. The sum term peak tends to be narrow, as the hyperfine contributions cancel in the addition of contributions from the two electronic manifolds. Also, the sum component produces modulation of opposite phase to the fundamental term. The combinations of the fundamental and sum components to the envelope modulation give rise to characteristic patterns in the 2-pulse ESEEM. Kevan (1979) discusses these effects at length and presents results of simulations of proton and deuteron modulation patterns from shells of varying radial distance r. Weakly coupled deuterons ($r \geq 4$Å) give rise to small sum terms. The fundamental term is narrow due to the weakness of the anisotropic coupling which diminishes as $1/r^3$. The resulting ESEEM pattern shows a slowly decaying sine-wave with small flattening at the peaks due to the small anti-phase sum component. The ESEEM pattern is very different for more strongly coupled deuterons on a r =3Å shell. In this case the fundamental peak is broad and damps out after a few cycles. The narrow sum term produces the stronger modulation component after only a few cycles of the fundamental. We note as a useful reference that the anisotropic magnetic field generated by an electron at a radial distance of 3Å is about 340 Gauss, so the anisotopic contribution is about 1/10 the Zeeman field for X band experiments.

These 2-pulse ESEEM effects are nicely demonstrated in experiments on Cu(II) deuteron modulation as shown by McCracken et al. (1987) and reproduced as Figure V-15. The three ESEEM patterns are obtained by shielding the Cu(II) ion from solvent ^2H_2O by various degrees with the 2,2'-bipyridyl ligand. The 2,2'-bipyridyl (bipy) ligand binds tightly to the Cu(II) ion. Cu(II)-monobipyridyl, Cu(II)-bisbipyridyl, and Cu(II)-trisbipyridyl compounds were prepared by adding 2,2'-bipyridyl in ratios of 1:1,

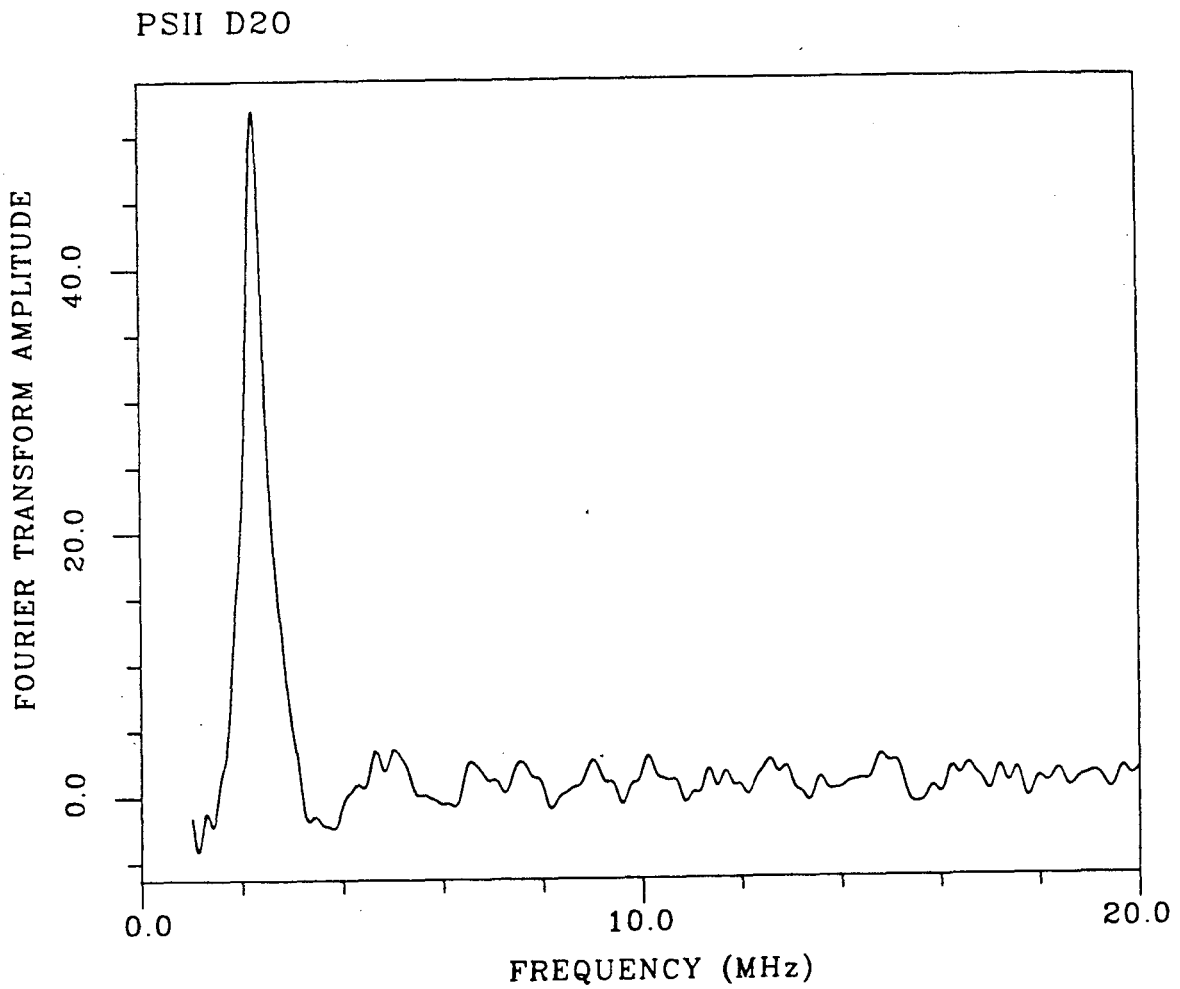

Figure V-13 3-pulse ESEEM cosine Fourier transform of the Mn multiline signal of PSII membranes prepared in ^2H_2O buffer and illuminated at 195 K. The 3-pulse ESEEM results are obtained by varying T in 10 ns increments from 100 to 3000 ns while maintaining τ fixed at 270 ns. The weakly coupled proton modulation is suppressed for this τ value. The applied magnetic field is 3500 Gauss. The microwave frequency is 9.29 GHz. The observation temperature is 4.2 K, and the time interval between pulse set repetitions is 1.0 ms.

Figure V-14 Ratio of the 2-pulse ESEEM of the Mn multiline signal of PSII membranes prepared in ^2H_2O buffer and ^1H_2O buffers and illuminated at 195 K. The 2-pulse ESEEM results are obtained by varying τ in 10 ns increments from 140 to 3000 ns. The time domain pattern is shown in (a), and the corresponding cosine Fourier transform is displayed in (b). The applied magnetic field is 3500 Gauss. The microwave frequency is 9.29 GHz. The observation temperature is 4.2 K, and the time interval between pulse set repetitions is 1.0 ms.

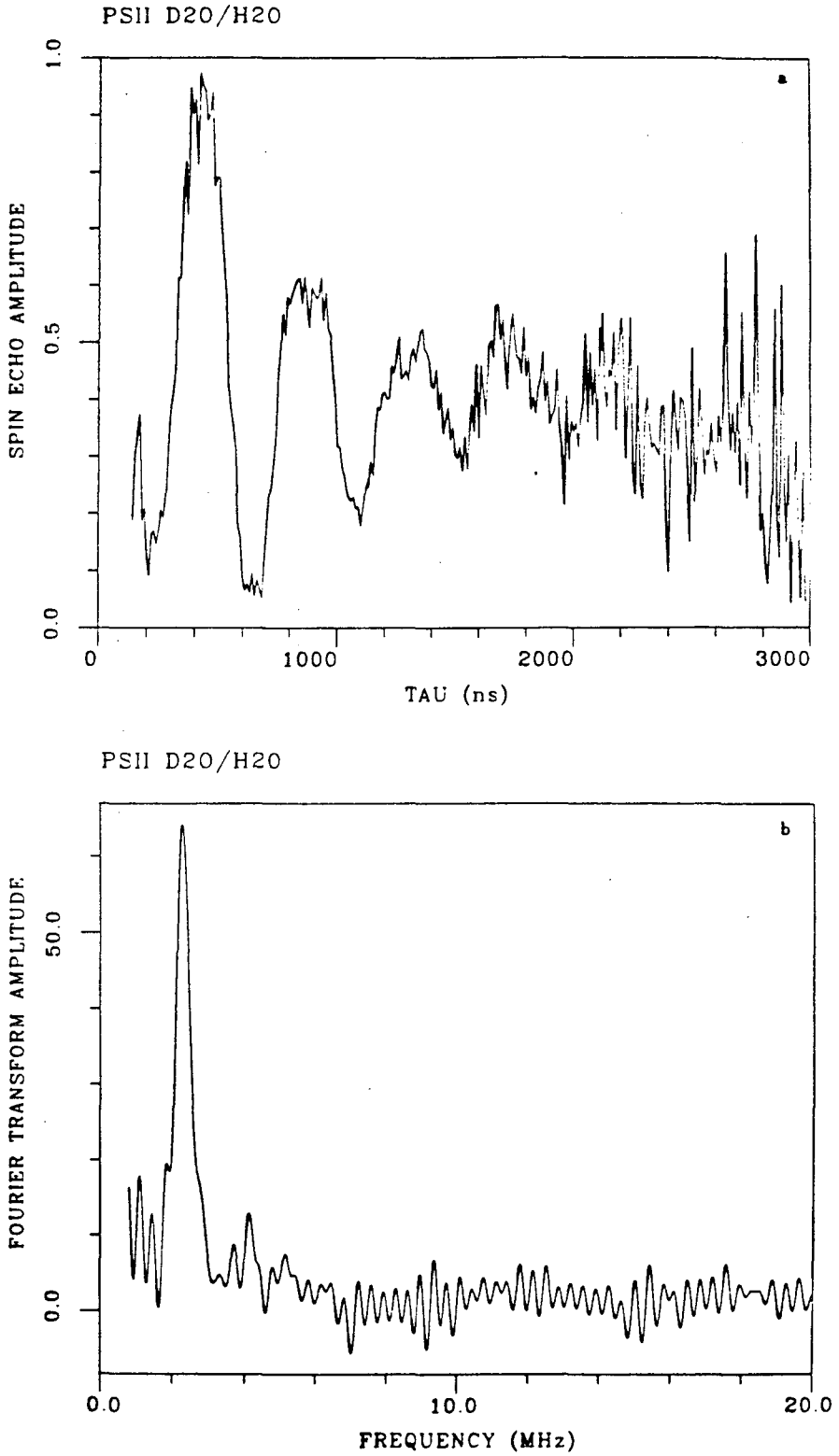
PSII D20/H20
SPIN ECHO AMPLITUDE
1.0
0.5
0.0
0
1000
2000
3000
TAU (ns)
a
PSII D20/H20
FOURIER TRANSFORM AMPLITUDE
50.0
0.0
0.0
10.0
20.0
FREQUENCY (MHz)
b

2:1, and 10:1 to the Cu(II) ion concentration in ^2H_2O and ^1H_2O solutions. The Cu(II) ion is completely shielded from bound ^2H_2O in the Cu(II)-trisbipyridyl model. Only distant ^2H_2O contributes to the modulation for this complex. The Cu(II)-bisbipyridyl offers access to ^2H_2O only along the axial sites. The Cu(II)-monobipyridyl complex has both axial and equatorial sites open for direct ^2H_2O coordination (see McCracken et al. 1987 for precise details of the coordination structures).

The contribution of equatorial bound ^2H_2O is examined in (A). This pattern is obtained by dividing the ratio of the Cu(II)(bipy) pattern in ^2H_2O and ^1H_2O by the corresponding ratio for Cu(II)$(bipy)_2$. This pattern shows the rapid dephasing of the fundamental component, with the sum component dominating after two periods. The contribution from axially bound ^2H_2O in (B) is obtained as a similar ratio of the Cu(II)$(bipy)_2$ and Cu(II)$(bipy)_3$ data. The anisotropic coupling is smaller for the axially bound water deuterons. The fundamental component is more evident throughout the time course, and the sum term is present as a flattening of the principal peaks. The contribution from unbound ^2H_2O is shown in (C), which is simply obtained as the ratio of the Cu(II)$(bipy)_3$ ESEEM data in ^2H_2O to the corresponding ESEEM data in ^1H_2O. In this case the ESEEM appears as a pure sinusoidal component at the primary frequency.

McCracken et al. simulated the observed ESEEM patterns with a matrix diagonalization treatment similar to our analysis of ^{14}N modulation in Chapter II. The major difference in these ^{2}H calculations is the inclusion of anisotropic hyperfine terms in the Hamiltonian. The ^{2}H quadrupolar parameters (e^2qQ=0.22 MHz and η=0.1) were taken from NQR studies of Ice II (Edmonds et al. 1976). The modulation for both the axially and equatorially bound ^2H_2O molecules were effectively simulated. The equatorial ^2H_2O simulation was observed to best fit the experimental data with a radial distance r=2.8Å and an isotropic hyperfine coupling A=0.2 MHz. The axial ^2H_2O modulation was best described with r=3.3Å and A=0.1 MHz.

We are limited in potential simulations of the ^{2}H modulation present in the Mn multiline ESEEM by not having a clear model for the structure of the metal cluster. A simple point-dipole treatment cannot be as well justified as for the case of an isolated Cu(II) ion. The electronic spin originates from two or more separate ions. We can however make some qualitative judgements by comparing our ratioed ESEEM pattern to those presented by McCracken et al. The ^{2}H modulation induced by ^2H_2O exchange more closely resembles the axial deuterium ESEEM shown in Figure V-15(B). The

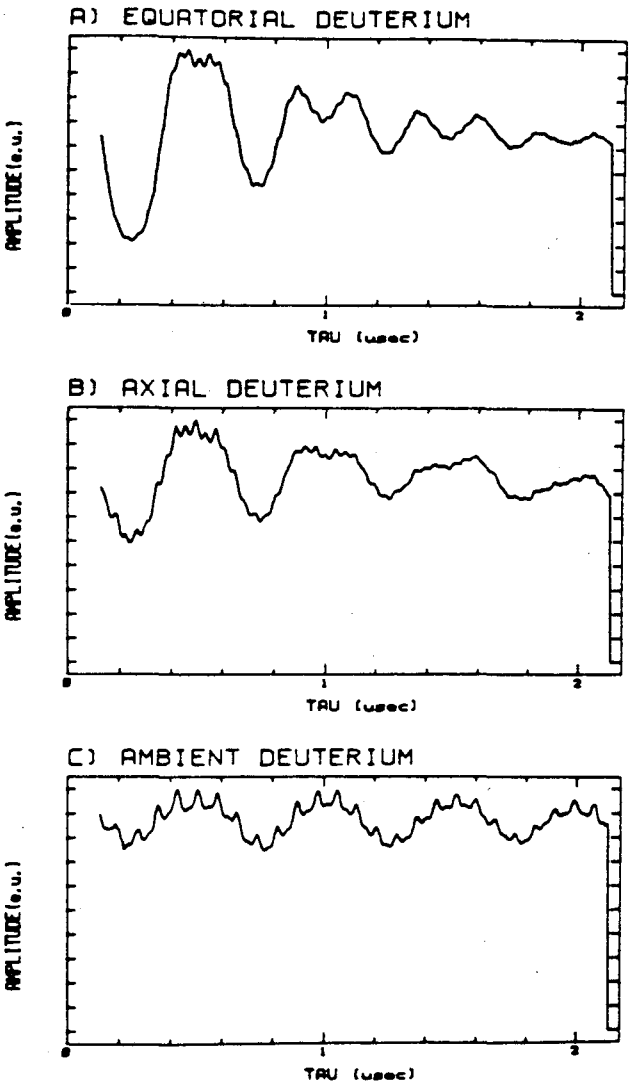

Figure V-15 2-pulse ESEEM patterns for Cu(II) interaction with deuterated water. This figure is reproduced from McCracken et al. (1987). The three ESEEM patterns are obtained by shielding the Cu(II) ion from ^2H_2O by various degrees with the 2,2'-bipyridyl ligand. Cu(II)-monobipyridyl, Cu(II)-bisbipyridyl, and Cu(II)-trisbipyridyl compounds were prepared by adding 2,2'-bipyridyl in ratios of 1:1, 2:1, and 10:1 to the Cu(II) ion concentration in ^2H_2O and ^1H_2O solutions. The contribution of equatorial bound ^2H_2O is examined in (A). This pattern is obtained by dividing the ratio of the Cu(II)(bipy) pattern in ^2H_2O and ^1H_2O by the corresponding ratio for Cu(II)$(bipy)_2$. The contribution from axially bound ^2H_2O in (B) is obtained by a similar ratio of the Cu(II)$(bipy)_2$ and Cu(II)$(bipy)_3$ data. The contribution from unbound ^2H_2O is shown in (C), which is simply obtained by ratio of the Cu(II)$(bipy)_3$ ESEEM data in ^2H_2O by that obtained in ^1H_2O.

damping of the primary frequency occurs at about the same rate, and there appears to be a flattening at the tops of the peaks. There is no domination of the sum term for larger τ values as is observed for the equatorial-bound water in Figure V-15(A). The ^{2}H modulation damps too quickly to resemble the distant ^2H_2O contribution shown in Figure V-15(C). We would not expect to observe the Cu(II)-equatorial-^2H_2O pattern for the Mn complex because the Cu(II) ion projects a large amount of unpaired spin density onto the equatorial ligands. This is another manifestation of the same Cu(II) coordination chemistry which produces such large ^{14}N superhyperfine couplings for equatorial nitrogen ligands. We propose that the Cu(II)-axial-^{2}H modulation may more precisely be compared with analogous effects for the Mn site. Comparison of the Mn multiline ESEEM of Figure V-14a with the axial ^{2}H pattern for Cu(II) shown in Figure V-15(B) suggest that water may indeed be coordinated to the Mn site.

The Mn multiline ESE signal discussed to this point in this section was generated by illumination at 195 K and kept at 77 K or below at all subsequent times. Under these conditions we may observe water coordinated in the least oxidized state S_0 as well as any water bound in the $S_0 \rightarrow S_1$ transition. The transition from S_1 to S_2 occurs at 195 K, and it is unlikely that ligand exchange readily occurs at such a low temperature. These samples were prepared with 1.0mM PPBQ. This acceptor stabilizes the S_2 state upon warming after low temperature illumination (see Styring and Rutherford, 1987). PPBQ oxidizes Q_a^- at a rate higher than $S_2 - Q_a^-$ recombination. We were thus able to warm the 195 K illuminated samples to a temperature of 4°C for 20 s. without a large loss of multiline signal amplitude. Figure V-16 shows the results of the 2-pulse ESEEM spectrum taken for this "annealed" sample divided by the ESEEM measured before the sample was warmed. There is no evidence of any change in the ESEEM pattern upon warming the sample. We consider this to be strong evidence that the $S_1 \rightarrow S_2$ transition does not promote the binding of additional water to the Mn site.

In summary, the ^2H_2O experiments thus strongly suggest that water does not bind in a protonated form during the $S_1 \rightarrow S_2$ transition. There is indication that water may be bound in the Kok S_1-state. We plan to continue these studies with ^{17}O water ESEEM experiments. This is in part motivated by the possibility that "water" may be present in an unprotonated form by the S_2-state, which is two oxidation steps up from the most reduced form in the S-state cycle. Hansson et al. place an upper limit of $\approx$5 Gauss on the isotropic coupling of ^{17}O to the Mn multiline signal. This puts the expected sublevel transitions for ^{17}O transitions within the range of

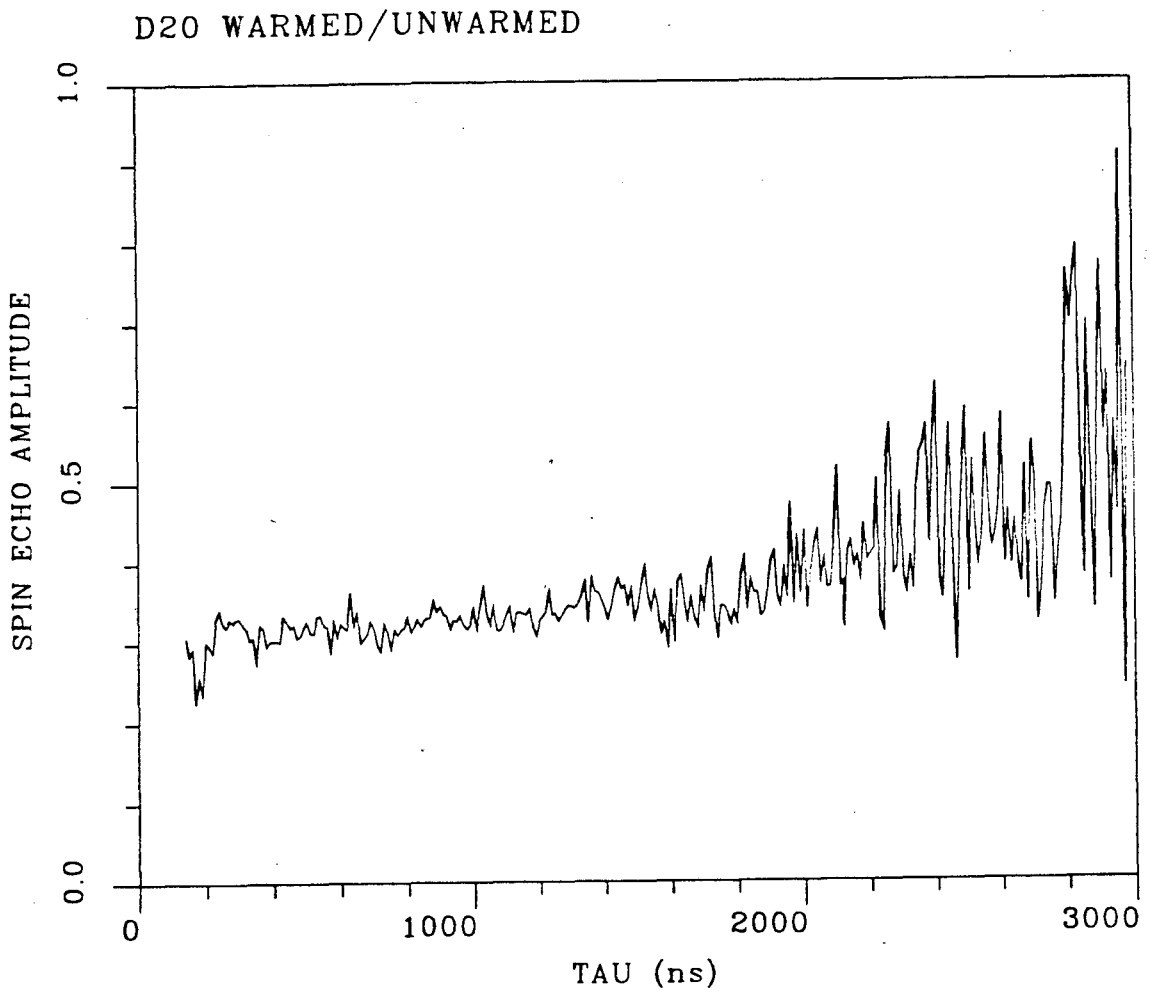

Figure V-16 Ratio of the 2-pulse ESEEM in annealed to unannealed PSII membranes samples prepared in ^2H_2O buffer and illuminated at 195 K. The annealed sample was prepared by warming to a temperature of 4°C for 20 s. The 2-pulse ESEEM results are obtained by varying τ in 10 ns increments from 140 to 3000 ns. The applied magnetic field is 3500 Gauss. The microwave frequency is 9.29 GHz. The observation temperature is 4.2 K, and the time interval between pulse set repetitions is 1.0 ms.

ESEEM techniques. The e^2qQ value for ice is about 6.9 MHz. We would expect this value to decrease upon metal coordination. Such ESEEM experiments could provide valuable information about water coordination. We note that the broadening observed by Hansson et al. was observed after long exposure to ^{17}O water, with high S-state turnover before the final dark-adaptation and illumination. It is quite possible that they were observing slow exchange of oxygen into bridging or terminal oxygen ligand rather than actual binding of water in descrete S-state transitions. ESEEM studies with ^{17}O water introduced just prior to illumination may give us a better discrimination between slow exchange and S-state water binding.

References

Akabori, K. Imaoka, A., and Toyoshima, Y. (1984) *FEBS Lett. 173*, 36.

Allen, G. C. and Hush, N. S. (1967) *Prog. Inorg. Chem. 8*, 357.

Alt, J., Morris, J., Westhoff, P., and Herrmann, R. G. (1984) *Curr. Genet. 8*, 597.

Anderson, J. R., Venters, R. A., Bowman, M. K., True, A. E., and Hoffman, B. M. (1985) *J. Magn. Reson. 65*, 165.

Andersson, B. (1986) in *Encyclopedia of Plant Physiology, New Series, Volume 19, Photosynthesis III*, ed. L. A. Staehelin and C. J. Arntzen, Springer-Verlag, Berlin, 447.

Appleton, D. W. and Sarkar, B. (1974) *Proc. Natl. Acad. Sci. U.S.A.71*, 1686.

Ashby, C. I. H., Cheng, C. P., and Brown, T. L. (1978a) *J. Am. Chem. Soc. 100*, 6057.

Ashby, C. I. H., Cheng, C. P., Duesler, E. N., and Brown, T. L. (1978b) *J. Am. Chem. Soc. 100*, 6063.

Astashkin, A. V., Dikanov, S. A., and Tsvetkov, Y., D. (1984) *J. Struct. Chem. 25*, 45.

Avigliano, L., Davis, J. L., Graziani, M. T., Marchesini, A., Mims, W. B., Mondovi, B., and Peisach, J. (1981) *FEBS Lett. 136*, 80.

Babcock, G. T. (1973) *Ph. D. thesis, Department of Chemistry, University of California, Berkeley*, Lawrence Berkeley Laboratory Report LBL-2172.

Babcock, G. T., Blankenship, R. E., and Sauer, K. (1976) *FEBS Lett. 61*, 286.

Babcock, G. T. (1987) in *New Comprehensive Biochemistry: Photosynthesis*, ed. J. Amesz, Elsevier, Amsterdam, p. 125.

Barber, J., Chapman, D. J., and Telfer, A. (1987) *FEBS Lett. 220*, 67.

Barry, B. A. and Babcock, G. T. (1987) *Proc. Natl. Acad. Sci. USA 84*, 7099.

Bashkin, J. S., Chang, H.-R., Streib, W. E., Huffman, J. C., Hendrickson, D. N., and Christou, G. (1987) *J. Am. Chem. Soc. 109*, 6502.

Beck, W. F., de Paula, J. C., and Brudvig, G. W. (1986) *J. Am. Chem. Soc. 108*, 4018.

Beck, W. F. and Brudvig, G. W. (1986) *Biochem. 25*, 6479.

Berthold, D. A., Babcock, G. T., and Yocum, C. F. (1981) *FEBS Lett. 134*, 231.

Blough, N. V. and Sauer, K. (1984) *Biochim. Biophys. Acta 767*, 377.

Boska, M. and Sauer, K. (1983) *Biochim. Biophys. Acta 765*, 84.

Boska, M., Sauer, K., Buttner, W., and Babcock, G. T. (1983) *Biochim. Biophys. Acta 722*, 327.

Boussac, A. and Rutherford, A. W. (1988) *Biochem.* in press.

Breton, J. (1986) in *Encyclopedia of Plant Physiology, New Series, Volume 19, Photosynthesis III*, ed. L. A. Staehelin and C. J. Arntzen, Springer-Verlag, Berlin, 319.

Brettel, K., Setif, P., and Mathis, P. (1987) in *Progress in Photosynthesis Research, Vol. 1*, ed. J. Biggins, Martinus Nijhoff Publishers, Dordrecht, I.233.

Britt, R. D., and Klein, M. P. (1987) *J. Magn. Reson. 74*, 535.

Britt, R. D., Sauer, K., and Klein, M. P. (1987) in *Progress in Photosynthesis Research, Vol. 1*, ed. J. Biggins, Martinus Nijhoff Publishers, Dordrecht, I.573.

Brudvig, G. W., Casey, J. L., and Sauer, K. (1983) *Biochim. Biophys. Acta 723*, 366.

Brudvig, G. W. and Crabtree, R. H. (1986) *Proc. Natl. Acad. Sci. U.S.A.83*, 4586.

Burger, R. M., Adler, A. D., Horwitz, S. B., Mims, W. B., and Peisach, J. (1981) *Biochem. 20*, 1701.

Casabella, P. A., and Bray, P. J. (1958) *J. Chem. Phys. 28*, 1182.

Casey, J. L. and Sauer, K. (1984) *Biochim. Biophys. Acta 767*, 21.

Chang, C.-H., Tiede, D., Tang, J., Smith, U., Norris, J. and Schiffer, M. (1986) *FEBS Lett. 205*, 82.

Cheng, C. P., Plankey, B., Rund, J. V., and Brown, T. (1977) *J. Am. Chem. Soc. 99*, 8413.

Cheniae, G. M. and Martin, I. F. (1966) *Brookhaven Symp. Biol., 19*, 406.

Cheniae, G. M. and Martin, I. F. (1970) *Biochim. Biophys. Acta 197*, 219.

Clayton, R. K. (1980) *Photosynthesis: Physical Mechanisms and Chemical Patterns*, Cambridge Univ. Press, Cambridge.

Cohen, M. H., and Reif, F. (1957) *Solid State Phys. 5*, 321.

Cole, J., Yachandra, V. K., Guiles, R. D., McDermott, A. E., Britt, R. D., Dexheimer, S. L., Sauer, K., and Klein, M. P. (1987) *Biochim. Biophys. Acta 890*, 395.

Coleman, W. J. and Govindjee (1987) *Photosyn. Res. 13*, 199.

Cooper, S. R. (1976) *Ph.D. thesis, Department of Chemistry, University of California, Berkeley*, Lawrence Berkeley Laboratory Report LBL-5513.

Cooper, S. R., and Calvin, M. (1977) *J. Am. Chem. Soc. 99*, 6623.

Cooper, S. R., Dismukes, G. C., Klein, M. P., and Calvin, M. (1978) *J. Amer. Chem. Soc. 100:23*, 7248.

Creutz, C. and Taube, H. (1969) *J. Am. Chem. Soc. 91*, 3988.

Creutz, C. (1983) *Prog. Inorg. Chem. 30*, 1.

Das, T. P., and Hahn, E. L. (1958) *Solid State Phys. Supplement 1*, 1.

Debus, R. J., Okamura, M. Y., and Feher, G. (1985) *Biophys. J. 47* 3a.

Debus, R. J., Barry, B. A., Babcock, G. T., and McIntosh, L. (1988) *Proc. Natl. Acad. Sci. U.S.A., 85*, 427.

Deisenhofer, J., Epp, O., Miki, K., Huber, R., and Michel, H. (1984) *J. Molec. Biol. 180* 385.

Deisenhofer, J., Epp, O., Miki, K., Huber, R., and Michel, H. (1985) *Nature 318*, 618.

Dekker, J. P., Van Gorkom, H. J., Brok, M. and Ouwehand, L. (1984a) *Biochim. Biophys. Acta 764*, 301.

Dekker, J. P., Van Gorkom, H. J., Wensink, J., and Ouwehand, L. (1984b) *Biochim. Biophys. Acta 767*, 1.

den Blanken, H. J., and Hoff, A. J. (1983) *Biochim. Biophys. Acta 724*, 52.

de Paula, J. C. and Brudvig, G. W. (1985) *J. Am. Chem. Soc. 107*, 2643.

de Paula, J. C., Beck, W. F., and Brudvig, G. W. (1986) *J. Am. Chem. Soc. 108*, 4002.

de Paula, J. C., Beck, W. F., Miller, A.-F., Wilson, R. B. and Brudvig, G. W. (1987) *J. Chem. Soc., Faraday Trans. 1, 83*, 3635.

Diner, B. A. (1986) in *Encyclopedia of Plant Physiology, New Series, Volume 19, Photosynthesis III*, ed. L. A. Staehelin and C. J. Arntzen, Springer-Verlag, Berlin, 422.

Dingle, R. (1966) *Acta Chem. Scand. 20*, 33.

Dismukes, G. C. and Siderer, Y. (1980) *FEBS Lett. 121*, 78.

Dismukes, G. C. and Siderer, Y. (1981) *Proc. Natl. Acad. Sci. USA 78*, 274.

Dismukes, G. C., Ferris, K., and Watnick, P. (1982) *Photobiochem. Photobiophys. 3*, 243.

Dutton, P. L. (1986) in *Encyclopedia of Plant Physiology, New Series, Volume 19, Photosynthesis III*, ed. L. A. Staehelin and C. J. Arntzen, Springer-Verlag, Berlin, 197.

Edmonds, D. T. (1977) *Phys. Rep. 29*, 233.

Edmonds, D. T., Goren, S. P., Mackay, A. L., White, A. A. L., and Sherman, W. F. (1976) *J. Magn. Reson. 23*, 505.

Fajer, J., Davies, M. S., Forman, A., Klimov, V. V., Dolan, E., and Ke, B. (1980) *J. Am. Chem. Soc. 102*, 7143.

Fauth, J.-M., Schweiger, A., Braunschweiler, L., Forrer, J., and Ernst, R. R. (1986) *J. Magn. Reson. 66*, 74-85.

Fee, J. A., Peisach, J., and Mims, W. B. (1981) *J. Biol. Chem. 256*, 1910.

Flanagan, H. L., and Singel, D. J. (1987) *J. Chem. Phys. 87* , 5606.

Flanagan, H. L., Gerfen, G. J., and Singel, D. J. (1988) *J. Chem. Phys.* in press.

Flournoy, J. M., Baum, L. H., and Siegel, S. (1960) *Rev. Sci. Instrum. 31*, 1133.

Förster, T. (1965) in *Action of Light and Organic Crystals, Part III. Modern Quantum Chemistry, O. Sinanoglu, ed.,* Academic, London, 93.

Froncisz, W., and Hyde, J. S. (1982) *J. Magn. Reson. 47*, 515.

Geacintov, N. E. and Breton, J. (1986) in *Encyclopedia of Plant Physiology, New Series, Volume 19, Photosynthesis III*, ed. L. A. Staehelin and C. J. Arntzen, Springer-Verlag, Berlin, 310.

George, P. (1965) in *Oxidases and Related Redox Systems*, T. King and M. Morrison, eds., Wiley, New York, p. 3.

Ghanotakis, D. F., Topper, J. N., Babcock, G. T., and Yocum, C. F. (1984a) *FEBS Lett. 170*, 169.

Ghanotakis, D. F., Babcock, G. T., and Yocum, C. F. (1984b) *Biochim. Biophys. Acta 765*, 388.

Ghanotakis, D. F. and Yocum, C. F. (1985) *Photosyn. Res. 7*, 97.

Goodin, D. B., Yachandra, V. K., Britt, R. D., Sauer, K., and Klein, M. P. (1984) *Biochim. Biophys. Acta 767*, 209.

Gordon, J. P. (1961) *Rev. Sci. Instrum. 32*, 658.

Govindjee, Kambara, T., and Coleman, W. (1985) *Photochem. Photobiol. 42*, 187.

Guibé, L. (1960) *Compt. rend. 250*, 3014.

Guibé, L., and Lucken, E. A. C., (1966) *Molec. Phys. 10*, 273.

Guibé, L., and Lucken, E. A. C., (1968) *Molec. Phys. 14*, 79.

Guibé, L., Linscheid, P., and Lucken, E. A. C., (1970) *Molec. Phys. 19*, 317.

Guiles, R. D., Yachandra, V. K., McDermott, A. E., Britt, R. D., Dexheimer, S. L., Sauer, K., and Klein, M. P. (1987) in *Progress in Photosynthesis Research, Vol. 1*, ed. J. Biggins, Martinus Nijhoff Publishers, Dordrecht, I.561.

Guiles, R. D. (1988) *Ph.D. thesis, Department of Chemistry, University of California, Berkeley.*

Haehnel, W. (1986) in *Encyclopedia of Plant Physiology, New Series, Volume 19, Photosynthesis III*, ed. L. A. Staehelin and C. J. Arntzen, Springer-Verlag, Berlin, 547.

Hahn, E. L. (1950) *Phys. Rev. 80*, 580.

Hansson, Ö. and Andréasson, L.-E. (1982) *Biochim. Biophys. Acta 679*, 261.

Hansson, Ö., Andréasson, L.-E., and Vänngård, T. (1986) *FEBS Lett. 195*, 151.

Hansson, Ö. Aasa, R. and Vänngård, T. (1987) *Biophys. J. 51*, 825.

Hauska, G. (1986) in *Encyclopedia of Plant Physiology, New Series, Volume 19, Photosynthesis III*, ed. L. A. Staehelin and C. J. Arntzen, Springer-Verlag, Berlin, 496.

Hearst, J. E. (1986) in *Encyclopedia of Plant Physiology, New Series, Volume 19, Photosynthesis III*, ed. L. A. Staehelin and C. J. Arntzen, Springer-Verlag, Berlin, 382.

Hegita, H, Masataka, H., Hirakawa, T., and Kuwata, H. (1970) *Bull. Chem. Soc. Jap. 43*, 2262.

Hill, R. and Bendall, F. (1960) *Nature 186*, 136.

Holschuh, K., Bottomley, W., and Whitfield, P. R. (1984) *Nucleic Acids Res. 12*, 8819.

Hsieh, Y.-N., Ireland, P. S., and Brown, T. L. (1976) *J. Magn. Reson. 21*, 445.

Hsieh, Y.-N., Rubenacker, G. V., Cheng, C. P., and Brown, T. L. (1977) *J. Am. Chem. Soc. 99*, 1384.

Hoff, A. J. (1982) in *Molecular Biology, Biochemistry, and Biophysics, v. 35*, ed., Fong, F. K. Springer, Berlin, 80.

Holm, R. H., Averill, B. A., Herskovitz, T., Frankel, R. B., Gray, H. B., Siiman, O., Grunthaler, F. J. (1974) *J. Amer. Chem. Soc. 96*, 2644.

Holzwarth, A. R. (1986) in *Encyclopedia of Plant Physiology, New Series, Volume 19, Photosynthesis III*, ed. L. A. Staehelin and C. J. Arntzen, Springer-Verlag, Berlin, 299.

Hornak, J. P., and Freed, J. H. (1985) *J. Magn. Reson. 62*, 311.

Hunt, M. J. and Mackay, A. L. (1974) *J. Magn. Reson. 15*, 402.

Hush, N. S. (1967) *Prog. Inorg. Chem. 8*, 391.

Joliot, P., Barbieri, G., and Chabaud, R. (1969) *Photochem. Photobiol. 10*, 309.

Jolly, W. L. (1984) *Modern Inorganic Chemistry*, McGraw-Hill, New York.

Kambara, T. and Govindjee (1985) *Proc. Natl. Acad. Sci. U.S.A.82*, 6119.

Kessler, E., Arthur, W., and Brugger, J. E. (1957) *Arch. Biochem. Biophys., 71*, 326.

Kevan, L. (1979) in *Time Domain Electron Spin Resonance*, L. Kevan and R. N. Schwartz, ed., Wiley, New York, p. 279.

Kirby, J. A., Robertson, A. S., Smith, J. P., Thompson, A. C., Cooper, S. R., and Klein, M. P. (1981) *J. Am. Chem. Soc. 103*, 5529.

Kivelson, D., and Neiman, R. (1961) *J. Chem. Phys. 35*, 149

Knox, R. S. (1986) in *Encyclopedia of Plant Physiology, New Series, Volume 19, Photosynthesis III*, ed. L. A. Staehelin and C. J. Arntzen, Springer-Verlag, Berlin, 286.

Kok, B., Forbush, B., and McGloin, M. (1970) *Photochem. Photobiol. 11*, 457.

Kottis, P., and Lefebvre, R. (1963) *J. Chem. Phys. 39*, 393.

Kuwabara, T. and Murata, N. (1982) *Plant Cell Physiol. 23*, 533.

Kuwabara, T. and Murata, N. (1983) *Plant Cell Physiol. 24*, 741.

Lin, C. P., Bowman, M. K., and Norris, J. R. (1985) *J. Magn. Reson. 65*, 369.

LoBrutto, R., Smithers, G. W., Reed, G. H., Orme-Johnson, W. H., Tan, S. L., and Leigh, J. S. Jr. (1986) *Biochem. 25*, 5654.

Lucken, E. A. C., (1961) *Trans. Faraday Soc. 57*, 729.

Magliozzo, R. S., McCracken, J., and Peisach, J. (1987) *Biochem. 26*, 7923.

Maki, A. H., and McGarvey, B. R. (1958) *J. Chem. Phys. 29*, 35.

McCracken, J., Peisach, J., and Dooley, D. M. (1987) *J. Am. Chem. Soc. 109*, 4064.

McCracken, J., Pember, S., Benkovic, S. J., Villafranca, J. J., Miller, R. J., and Peisach, J. (1988) *J. Am. Chem. Soc.* in press.

Mehring, M., and Freysoldt, F. (1980) *J. Phys. E 13*, 894.

Melandri, B. A. and Venturoli, G. (1986) in *Encyclopedia of Plant Physiology, New Series, Volume 19, Photosynthesis III*, ed. L. A. Staehelin and C. J. Arntzen, Springer-Verlag, Berlin, 560.

Metz, J. G., Pakrasi, H., Arntzen, C. J., and Seibert, M. (1987) *Progress in Photosynthesis Research, Vol. 4*, ed. J. Biggins, Martinus Nijhoff Publishers, Dordrecht, 679.

Michel, H., Weyer, K. A., Gruenberg, H., Dunger, I., Oesterhelt, D., and Lottspeich, F. (1986a) *EMBO J. 5*, 1149.

Michel, H., Epp, O., and Deisenhofer, J. (1986b) *EMBO J. 5*, 2445.

Michel, H. and Deisenhofer, J. (1986) in *Encyclopedia of Plant Physiology, New Series, Volume 19, Photosynthesis III*, ed. L. A. Staehelin and C. J. Arntzen, Springer-Verlag, Berlin, 371.

Michel, H. and Deisenhofer, J. (1988) *Biochem. 27*, 1.

Miller, A.-F., de Paula, J. C., and Brudvig, G. W. (1987) *Photosyn. Res. 12*, 205.

Mims, W. B. (1965) *Rev. Sci. Instrum. 36*, 1472.

Mims, W. B. (1972a) *Phys. Rev. B. 5*, 2409.

Mims, W. B. (1972b) *Phys. Rev. B. 6*, 3543.

Mims, W. B. (1972c) in *Electron Paramagnetic Resonance*, ed. by S. Geschwind, (Plenum Press, New York) p. 263.

Mims, W. B. (1974) *Rev. Sci. Instrum. 45*, 1583.

Mims, W. B., and Peisach, J. (1976) *Biochem. 15*, 3863.

Mims, W. B., and Peisach, J. (1978) *J. Chem. Phys. 69*, 4921.

Mims, W. B. and Peisach, J. (1979a) in *Biological Applications of Magnetic Resonance*, ed. by R. G. Shulman, (Academic Press, New York) p. 221.

Mims, W. B. and Peisach, J. (1979b) *J. Biol. Chem. 254*, 4321.

Mims, W. B, Peisach, J., Shaw, R. W., and Beinert, H. (1980) *J. Biol. Chem. 255*, 6843.

Mims, W. B. and Peisach, J. (1981) in *Biological Magnetic Resonance, v. 3*, ed. by L. J. Berliner and J. Reuben, (Plenum Press, New York) p. 213.

Mims, W. B. (1984) *J. Magn. Reson. 59*, 291.

Miyao, M. and Murata, N. (1984) *FEBS Lett. 170*, 350.

Mondoví, B., Graziani, M. T., Mims, W. B., Oltzik, R., and Peisach, J. (1977) *Biochem. 16* 4198.

Muha, G. M. (1980) *J. Chem. Phys. 73*, 4139.

Murata, N. and Miyao, M. (1985) *Trends Biochem. Sci. 10*, 122.

Nanba, O. and Satoh, K. (1987) *Proc. Natl. Acad. Sci. U.S.A.84*, 109.

Norris, J. R., Uphaus, R. A., Crespi, H. L., and Katz, J. J. (1971) *Proc. Natl. Acad. Sci. USA, 68* 625.

Norris, J. R. and Van Brakel, G. (1986) in *Encyclopedia of Plant Physiology, New Series, Volume 19, Photosynthesis III*, ed. L. A. Staehelin and C. J. Arntzen, Springer-Verlag, Berlin, 353.

Nugent, J. H. A. (1987) *Biochim. Biophys. Acta 893*, 184.

Nyholm, R. S., and Turko, A. (1960) *Chem. Ind. (London)* p. 74.

O'Malley, P. J., and Babcock, G. T. (1984) *Proc. Natl, Acad. Sci. USA 81*, 1098.

Ono, T. and Inoue, Y. (1984) *FEBS Lett. 168*, 281.

Ort, D. R. (1986) in *Encyclopedia of Plant Physiology, New Series, Volume 19, Photosynthesis III*, ed. L. A. Staehelin and C. J. Arntzen, Springer-Verlag, Berlin, 143.

Padhye, S., Kambara, T., Hendrickson, D. N., and Govindjee (1986) *Photosyn. Res. 9*, 103.

Parson, W. W., and Ke, B., (1982) in *Photosynthesis: Energy Conversion by Plants and Bacteria*, Govindjee, ed., Academic, New York, 331.

Parson, W. W. (1982) *Annu. Rev. Biophys. Bioeng. 11*, 57.

Pearson, R. G. (1968a) *J. Chem. Ed. 45*, 581.

Pearson, R. G. (1968b) *J. Chem. Ed. 45*, 643.

Pirson, A. (1937) *Z. Bot. 31*, 193.

Plaksin, P. M., Stoufer, R. C., Mathew, M., and Palenik, G. J. (1972) *J. Amer. Chem. Soc. 94*, 2121.

Poole, C. P., Jr. (1983) *Electron Spin Resonance*, 2nd ed., Wiley-Interscience, New York.

Radmer, R., and Cheniae, G. (1977) in *Primary Processes of Photosynthesis*, J. Barber, ed., Elsevier, Amsterdam, p. 303.

Rao, J. K. M., Hargrave, P. A., and Argos, P. (1983) *FEBS Lett. 156*, 165.

Reed, G. H. and Markham, G. D. (1984) in *Biological Magnetic Resonance, V. 6*, L. J. Berliner and J. Reuben, eds., Plenum, New York, p.73.

Rubenacker, G. V. and Brown, T. L. (1980) *Inorg. Chem. 19*, 392.

Robin, M. B. and Day, P. (1967) *Adv. Inorg. Chem. Radiochem. 10*, 247.

Rutherford, A. W. and Heathcote, P. (1985) *Photosynth. Res. 6*, 295.

Sandusky, P. O. and Yocum, C. F. (1984) *Biochim. Biophys. Acta 766*, 603.

Sandusky, P. O. and Yocum, C. F. (1986) *Biochim. Biophys. Acta 849*, 85.

Satoh, K., Fujii, Y., Aoshima, T., and Tado, T. (1987) *FEBS Lett. 216*, 7.

Sauer, K. (1986) in *Encyclopedia of Plant Physiology, New Series, Volume 19, Photosynthesis III*, ed. L. A. Staehelin and C. J. Arntzen, Springer-Verlag, Berlin, 85.

Sayre, R. T., Andersson, B., and Bogorad, L. (1986) *Cell (Cambridge, Mass.) 47*, 601.

Schaffernicht, H. and Junge, W. (1981) *Photochem. Photobiol. 34*, 223.

Scheer, H., Wieschoff, H., Schaefer, W., Cmiel, E., Nitsche, B., Schiebel, H. M., and Schulten, H. R. (1983) in *Proc. 6th Int. Congr. Photosynth., Brussel, V. II*, ed. C. Sybesma, Nijhoff/Junk, The Hague, 81.

Scheer, H. (1986) in *Encyclopedia of Plant Physiology, New Series, Volume 19, Photosynthesis III*, ed. L. A. Staehelin and C. J. Arntzen, Springer-Verlag, Berlin, 327.

Schempp, E., and Bray, P. J. (1968) *J. Chem. Phys. 49*, 3450.

Sétif, P., Mathis, P., and Vänngård, T. (1984) *Biochim. Biophys. Acta 767*, 404.

Sétif, P. and Mathis, P. (1986) in *Encyclopedia of Plant Physiology, New Series, Volume 19, Photosynthesis III*, ed. L. A. Staehelin and C. J. Arntzen, Springer-Verlag, Berlin, 476.

Sibbald, P. R. and Green, B. R. (1987) *Photosyn. Res. 14*, 201.

Staehelin, L. A. (1986) in *Encyclopedia of Plant Physiology, New Series, Volume 19, Photosynthesis III*, ed. L. A. Staehelin and C. J. Arntzen, Springer-Verlag, Berlin, 1.

Stebler, M., Ludi, A., and Burgi, H.-B. (1986) *Inorg. Chem. 25*, 4743.

Styring, S. and Rutherford, A. W. (1987) *Biochem. 26*, 2401.

Styring, S., Miyao, M., and Rutherford, A. W. (1987) *Biochim. Biophys. Acta 890*, 32.

Swarthoff, T., Gast, P., Amesz, J., and Buismann, H. P. (1982) *FEBS Lett. 146*, 129.

Telser, J., Hoffman, B. M., LoBrutto, R., Ohnishi, T., Tsai, A.-L., Simpkin, D., and Palmer, G. (1987) *FEBS Lett. 214*, 117.

Thomann, H., Morgan, T. V., Jin, H., Burgmayer, S. J. N., Bare, R. E., and Stiefel, E. I. *J. Am. Chem. Soc. 109*, 7913.

Thornber, J. P. (1986) in *Encyclopedia of Plant Physiology, New Series, Volume 19, Photosynthesis III*, ed. L. A. Staehelin and C. J. Arntzen, Springer-Verlag, Berlin, 98.

Townes, C. H., and Dailey, B. P. (1949) *J. Chem. Phys. 17*, 782.

Trebst, A. (1986) *Z. Naturforsch 41c*, 240.

Trebst, A. (1987) *Z. Naturforsch 42c*, 742.

Valentine, J. S., Tatsuno, Y., and Nappa, M. (1977) *J. Am. Chem. Soc. 99*, 3522.

Vermeglio, A. (1977) *Biochim. Biophys. Acta 459*, 516.

Wasielewski, M. R., Norris, J. R., Shipman, L. L., Lin, C. P., and Svec, W. A. (1981a) *Proc. Natl. Acad. Sci. USA 78*, 2957.

Wasielewski, M. R., Norris, J. R., Crespi, H. L., and Harper, J. (1981b) *J. Am. Chem. Soc. 103*, 7664.

Wraight, C. A. and Clayton, R. K. (1974) *Biochim. Biophys. Acta 333*, 246.

Wraight, C. A. (1977) *Biochim. Biophys. Acta 459*, 525.

Yachandra, V. K., Guiles, R. D., McDermott, A. E., Britt, R. D., Dexheimer, S. L., Sauer, K., and Klein, M. P. (1986a) *Biochim. Biophys. Acta 850*, 324.

Yachandra, V. K., Guiles, R. D., Sauer, K., and Klein, M. P. (1986b) *Biochim. Biophys. Acta 850*, 333.

Yachandra, V. K., Guiles, R. D., McDermott, A. E., Cole, J. L., Britt, R. D., Dexheimer, S. L., Sauer, K., and Klein, M. P. (1987) *Biochem. 26*, 5974.

Yocum, C. F., Yerkes, C. T., Blankenship, R. E., Sharp, R. R., and Babcock, G. T. (1981) *Proc. Natl. Acad. Sci. USA 78*, 7507.

Youvan, D. C., Bylina, E. J., Alberti, M., Begusch, H., and Hearst, J. E. (1984) *Cell (Cambridge, Mass.) 37*, 949.

Zimmermann, J. L. and Rutherford, A. W. (1984) *Biochim. Biophys. Acta 767*, 160.

Zimmermann, J. L. and Rutherford, A. W. (1986) *Biochem. 25*, 4609.

Zurawski, G., Bohnert, H., Whitfield, P. R., and Bottomley, W. (1982) *Proc. Natl. Acad. Sci. U.S.A.79*, 7699.

Zweier, J. L., Aisen, P., Peisach, J., and Mims, W. B (1979) *J. Biol. Chem. 254*, 3512.

Zweier, J. L., Peisach, J., and Mims, W. B (1982) *J. Biol. Chem. 257*, 10314.

LAWRENCE BERKELEY LABORATORY
TECHNICAL INFORMATION DEPARTMENT
UNIVERSITY OF CALIFORNIA
BERKELEY, CALIFORNIA 94720